

**FINITE ELEMENT ANALYSIS OF FOOTWEAR
AND GROUND INTERACTION**

Zhigang SUN

**Institute for Materials Research
School of Computing, Science and Engineering
University of Salford, Salford, UK**

Submitted for the Degree of Doctor of Philosophy, April 2005

Table of Contents

	Page
Chapter 1 Introduction	1
1.1 Background	1
1.2 Objective of the Research.....	2
1.3 Scope of the Research.....	2
1.3.1 Problem Specification and Literature Review.....	3
1.3.2 Survey of Plasticity Theories in Soil Mechanics.....	3
1.3.3 Cases Validation Study.....	3
1.3.4 Finite Element Analysis of Footwear and Ground Interaction.....	3
1.3.5 Experiment Study.....	4
1.4 Academic Contribution by this Research.....	4
1.5 Chapters of the Thesis.....	4
Chapter 2 Literature Review.....	8
2.1 Introduction.....	8
2.2 Problem Specification.....	9
2.2.1 General Remarks.....	9
2.2.2 Classification of Various Methods/Tools for Soil Mechanics Problems Study.....	10
2.2.2.1 The slip-line method.....	11
2.2.2.2 The limit equilibrium method.....	11
2.2.2.3 The limit analysis method.....	12
2.2.2.4 Numerical analysis methods/tools.....	12
2.2.3 Finite Element Method & Non-Linear Soil Problems.....	12
2.3 Soil-Tillage Tools Interaction.....	13
2.4 Soil-Wheel Interaction.....	19
2.5 Soil-Structure Interaction.....	21
2.6 Limit Analysis.....	25
2.7 Footwear and Ground Interaction.....	28
2.8 Others.....	33
2.9 Summary.....	34

Chapter 3	Investigation about Theories of Plasticity in Soil Mechanics.....	36
3.1	Introduction.....	36
3.2	Elastic-Perfectly Plastic Assumption.....	39
3.3	Theories of Soil Plasticity.....	40
3.3.1	General Remarks.....	40
3.3.2	Flow Theory.....	41
3.3.2.1	Yield criteria.....	42
3.3.2.2	Flow rule.....	43
3.3.2.3	General nature of plastic theory	45
3.3.3	Perfectly Plastic Material Models.....	46
3.3.3.1	Coulomb model	47
3.3.3.2	Extended von Mises model	50
3.3.3.3	Drucker-Prager model	51
3.3.3.4	The Drucker-Prager hardening cap model.....	55
3.4	Summary	56
Chapter 4	Case Study for Two-Dimensional Validation	58
4.1	Introduction.....	58
4.2	Background of Drucker-Prager Material Model in ANSYS Software....	59
4.3	Two-Dimensional Validation for Earth Pressure Problems on the Use of Drucker-Prager in ANSYS.....	60
4.3.1	Soil Properties.....	60
4.3.2	Meshing Scheme.....	61
4.3.2.1	The elements.....	61
4.3.2.2	The plane strain.....	61
4.3.2.3	The meshing.....	62
4.3.3	Boundary Conditions.....	63
4.3.3.1	Constraints.....	63
4.3.3.2	Loading conditions.....	63
4.3.4	Initial Stress.....	64
4.3.4.1	Introduction.....	64
4.3.4.2	Method to calculate initial stress	64
4.3.4.3	Producing initial stress by FORTRAN programming.....	65

4.3.4.4	Initial stress effect.....	66
4.3.5	Numerical Modelling Results.....	68
4.3.6	Results Analysis and Conclusions.....	69
4.4	Summary.....	71
Chapter 5	Three-Dimensional Case Study for Validation.....	72
5.1	Introduction.....	72
5.2	Three-Dimensional Validation for Soil-Tillage Problems on the Use of Drucker-Prager Material Model in ANSYS.....	73
5.2.1	Three-Dimensional Case 1 Study.....	73
5.2.2	Three-Dimensional Case 2 Study.....	78
5.2.2.1	General information of case 2 study reported by Araya and Gao ¹⁰	78
5.2.2.2	FE modelling of 3-dimensional case 2 study in ANSYS.....	79
5.2.2.3	Results analysis and conclusions	82
5.3	Summary.....	85
Chapter 6	Study of Footwear and Ground Interaction by Using Finite Element Method.....	86
6.1	Introduction.....	86
6.1.1	Outdoor Footwear—Boots.....	86
6.1.2	Process of Gait.....	88
6.2	Construction of Interactive Finite Element Model for the First Tread Pattern of Military Boots.....	89
6.2.1	Some Consideration of Building Up Finite Element Models	89
6.2.2	Building Up Finite Element Model of Outsole for the First Tread Pattern.....	91
6.2.3	Construction of Interactive Soil FE Model with Forepart of the First Tread Pattern.....	92
6.2.3.1	Geometry size of the model.....	93
6.2.3.2	Soil properties.....	93
6.2.3.3	Drucker-Prager material model.....	94
6.2.3.4	The element.....	94
6.2.3.5	Meshing scheme.....	95
6.2.4	Construction of Interactive Soil FE Model with Heel of the First	

	Tread Pattern.....	96
6.2.4.1	Geometry size of the model.....	96
6.2.4.2	Soil properties and material model.....	97
6.2.4.3	Meshing scheme.....	97
6.3	Solution of the Soil FE Model Interactive with the First Tread Pattern...	98
6.3.1	<i>Solution of the Soil FE Model Interactive with Forepart.....</i>	<i>98</i>
6.3.1.1	Constraints.....	98
6.3.1.2	Loading conditions.....	98
6.3.1.3	Methodology of applying vertical and transverse loading.....	99
6.3.2	<i>Solution of the Soil FE Model Interactive with Heel.....</i>	<i>103</i>
6.3.2.1	Constraints	103
6.3.2.2	Loading conditions	103
6.4	Modelling Results and Discussion of the First Tread Pattern.....	107
6.4.1	Modelling Results and Discussion of Soil Interactive with Forepart..	107
6.4.1.1	Traction effect	107
6.4.1.2	Soil deformation.....	108
6.4.1.3	Discussion of soil deformation.....	109
6.4.1.3.1	Soil deformation at cross-section perpendicular to the Y-axis.....	109
6.4.1.3.2	Soil deformation at cross-section perpendicular to the Z-axis.....	111
6.4.1.3.3	Soil deformation at cross-section perpendicular to the X-axis.....	113
6.4.1.4	Soil stresses.....	113
6.4.1.5	Soil strains.....	116
6.4.1.5.1	Soil elastic strains.....	116
6.4.1.5.2	Soil plastic strains.....	118
6.4.2	Modelling Results and Discussion of Soil Interactive with Heel.....	120
6.4.2.1	Soil deformation.....	120
6.4.2.2	Discussion.....	121
6.4.2.3	Soil stresses	124
6.4.2.4	Soil strains.....	125
6.5	The Second, Third, Fourth and Fifth Tread Patterns.....	128
6.5.1	Introduction.....	128
6.5.2	Highlights of FE Modelling for the Second, Third, Fourth and Fifth Tread Patterns.....	131
6.5.2.1	FE models.....	132

6.5.2.2	Material model.....	135
6.5.2.3	Solution of soil FE models for the second, third, fourth and fifth tread patterns.....	135
6.6	Analysis of the FE Modelling Results for the Five Tread Patterns.....	137
6.6.1	Introduction.....	137
6.6.2	Traction Effect.....	139
6.6.3	Sinkage Effect.....	141
6.6.4	Lateral Stability.....	142
6.6.5	Soil Deformation.....	143
6.6.6	Soil Stresses.....	144
6.6.7	Soil Strains.....	146
6.6.8	Effects of the Mechanical Parameters of Soil Property.....	155
6.6.8.1	Effect of the dilatation angle.....	155
6.6.8.2	Effect of the Young's modulus.....	165
6.6.8.3	Effect of cohesion.....	165
6.7	Summary	170
Chapter 7	Study of Experimental Validation.....	172
7.1	Introduction.....	172
7.2	Experimental Facility.....	173
7.3	Soil Selection and Its Properties.....	175
7.3.1	Soil Selection.....	175
7.3.2	Soil Properties.....	176
7.3.2.1	Soil density.....	176
7.3.2.2	Soil friction angle.....	177
7.3.2.3	Soil flow angle.....	178
7.3.2.4	Soil cohesion.....	178
7.3.2.5	Young's modulus and Poisson's ratio.....	178
7.4	FE Modelling of Interaction between Scaled Up Model and Soil.....	179
7.4.1	Star-shape Cleat.....	179
7.4.2	FE Modelling of Soil Interactive with Star-Shape Cleat	180
7.4.2.1	Geometry size of the model.....	180
7.4.2.2	Soil properties and material model.....	181

7.4.2.3	The element and meshing scheme.....	183
7.4.3	Solution of the Soil FE Model Interactive with Star-Shape Cleat.....	183
7.4.3.1	Boundary conditions.....	183
7.4.3.2	Loading conditions.....	184
7.5	Procedure of Experimental Validation.....	190
7.5.1	Soil Preparation.....	190
7.5.2	Installation of Scaled up Model.....	191
7.5.3	Positioning of the Model.....	191
7.5.4	Application of Vertical Load.....	191
7.5.5	Application of Horizontal Load.....	192
7.5.6	Observations and Measurements	193
7.6	Results and Discussion	194
7.7	Summary.....	198
Chapter 8	Conclusions and Further Work.....	200
8.1	Introduction	200
8.2	Conclusive Review of Each Chapter of the Thesis.....	200
8.3	Conclusions	205
8.4	Future Work	206
8.4.1	Consideration of Interface Friction	207
8.4.2	Dynamics Analysis of Footwear and Soft Ground Interaction	207
8.4.3	Advancement of Experimental Facility	208
Appendix I	209
Appendix II	211
References	212

List of Figures

	Page
Fig. 2.1 A flowchart of problem specification.....	11
Fig. 3.1 Stress-strain curve for ideal and real soils.....	39
Fig. 3.2 Yield surface of a perfect plastic material.....	43
Fig. 3.3 Representation of flow rule.....	44
Fig. 3.4 Stress path produced by an external agency.....	45
Fig. 3.5 The overall picture of main yield criteria.....	47
Fig. 3.6 Coulomb yield criterion in σ - τ space.....	48
Fig. 3.7 Coulomb failure criterion in the principal stress space.....	50
Fig. 3.8 Extended von Mises yield criterion for soils.....	51
Fig. 3.9 Drucker-Prager failure criterion for soils.....	52
Fig. 3.10 Drucker-Prager & Coulomb yield criterion on the π -plane.....	53
Fig. 4.1 Typical earth pressure problem.....	60
Fig. 4.2 Meshing scheme of 2-D retaining wall reported by Clough and Duncan ⁷	63
Fig. 4.3 Boundary and loading conditions of 2-D earth pressure problems.....	63
Fig. 4.4 A scheme to produce initial stress.....	65
Fig. 4.5 The initial stress distribution sequence on each PLANE82 element.....	66
Fig. 4.6 The initial stress (Y-direction) effect on the soil mass.....	66
Fig. 4.7 Earth pressure distribution in 0.15m wall movement.....	68
Fig. 5.1 The model of case 1 study by estimated geometry parameters.....	75
Fig. 5.2 Deformed shape with undeformed edge of case 1 study.....	77
Fig. 5.3 Three dimensional finite element model of case 2 study.....	80
Fig. 5.4 Vector plots of translation of case 2 study.....	83
Fig. 6.1 Trainer-type sports hiking boot—1)Rand, 2)Insole, 3)Midsole, 4)Outsole,	

5)Uppers, and 6)Lacing system.....	87
Fig. 6.2 The experiment layout for direction of heel strike (From Pisina ¹).....	90
Fig. 6.3 The experiment layout for direction of forepart outsole tread.....	90
Fig. 6.4 Footprint of the first tread pattern.....	91
Fig. 6.5 The first tread pattern of real military boots.....	91
Fig. 6.6 A 3d geometrical model of outsole for the first tread pattern.....	92
Fig. 6.7 Interactive soil FE model with forepart of the first tread pattern.....	93
Fig. 6.8 The meshed main block of soil volumes surrounding and being adjacent to the tread pattern.....	95
Fig. 6.9 Interactive soil FE model with heel of the first tread pattern.....	96
Fig. 6.10 Loading conditions of soil FE model for the first tread pattern.....	100
Fig. 6.11 Loading conditions of FE modeling for heel.....	104
Fig. 6.12 The resultant soil displacement vector.....	109
Fig. 6.13 Soil deformation at a) $Y = 0$, b) $Y = -0.056 \cdot \frac{2}{3}$ m (by referring Fig. 6.7).....	110
Fig. 6.14 Soil deformation at cross-sections, a) $Z = 0.01$ m, b) $Z = 0.04$ m.....	112
Fig. 6.15 Soil deformation at cross-sections, a) $X = 0.08$ m, b) $X = 0.12$ m.....	114
Fig. 6.16 Element solution for stresses in the X-direction.....	115
Fig. 6.17 Element solution of elastic strain in the X-direction.....	117
Fig. 6.18 Element solution of plastic strain in the X-direction.....	119
Fig. 6.19 Soil displacement in the X direction (nodal solution).....	120
Fig. 6.20 Soil deformations in a) top layer of elements, b) the lowest layer of elements.....	123
Fig. 6.21 Nodal solution of soil stresses in the X direction interactive with heel.....	124
Fig. 6.22 Soil strains in Y direction with heel, a) elastic strain, b) plastic strain.....	126
Fig. 6.23 The second tread pattern of military boots (left foot).....	129

Fig. 6.24 The third tread pattern of military desert boot.....	130
Fig. 6.25 The fourth tread pattern of real military boots.....	130
Fig. 6.26 The fifth tread pattern.....	131
Fig. 6.27 The 3D geometry models of for the a) second, b) third, c) fourth and d) fifth tread patterns.....	132
Fig. 6.28 Soil FE models interactive with forepart of the a) second, b) third, c) fourth and d) fifth tread patterns.....	134
Fig. 6.29 The a) first, b) second, c) third, d) fourth, e) fifth tread patterns in plane.	138
Fig. 7.1 Experimental device for validation of numerical modelling results.....	174
Fig. 7.2 Natural friction angle of silica sand.....	177
Fig. 7.3 Real model scaled up 10 times made of natural rubber	180
Fig. 7.4 Soil FE model interactive with star-shape cleat scaled up 10 times	181
Fig. 7.5 Pre-prepared experiment facilities before loading.....	182
Fig. 7.6 Transverse loading conditions for the FE numerical modelling.....	185
Fig. 7.7 Loading conditions applied in the experimental validation.....	193
Fig. 7.8 Experimental results of soil failure in the soil tray test.....	194
Fig. 7.9 The maximum soil failure distances measured in the experiment.....	195
Fig. 7.10 The FE modelling results of soil deformation.....	196
Fig. 7.11 Vector plots of soil deformation with the FEM.....	197

List of Tables

	Page
Table 5.1 Soil properties of case 1 study.....	76
Table 5.2 Soil properties in case 2 study.....	79
Table 6.1 Soil properties for FE modelling.....	94
Table 6.2 The extreme values of soil displacement for the five tread patterns.....	144
Table 6.3 The maximum compressive stresses for the five tread patterns.....	145
Table 6.4 The maximum tensile stresses for the five tread patterns.....	146
Table 6.5a The extreme values of elastic and plastic strains for the five tread patterns.....	149
Table 6.5b Corresponding nodes no. of items in Table 6.5a.....	149
Table 6.6a The extreme values of the total strains (elastic + plastic) and corresponding node no. for the five tread patterns.....	151
Table 6.6b Elastic and plastic strains compositions of the extreme total strains for the five tread patterns.....	152
Table 6.7 Summary of extreme stresses (kPa) versus flow angle (degree).....	162
Table 6.8 Summary of extreme stresses (kPa) versus Young's modulus (kPa).....	166
Table 6.9 Summary of extreme stresses (kPa) versus cohesion (kPa).....	168
Table 7.1 Soil properties for FE modelling in experiment.....	182
Table 7.2 Comparison between FEM and soil tray test.....	198

List of Charts

	Page
Chart 4.1 Flow chart of a user subroutine of producing initial stress.....	67
Chart 4.2 Earth pressure with 0.115m wall displacement.....	69
Chart 4.3 Earth pressure with 0.13m wall displacement.....	69
Chart 4.4 Earth pressure with 0.15m wall displacement.....	70
Chart 5.1 Error percentage of draught force versus convergence norm.....	84
Chart 6.1 Traction effect evaluated by reaction forces in the X direction.....	140
Chart 6.2 Sinkage effect evaluated by reaction forces in the Y direction.....	141
Chart 6.3 Lateral stability evaluated by reaction forces in the Z direction.....	142
Chart 6.4 The extreme values of soil displacements for the five tread patterns.....	143
Chart 6.5 The maximum compressive stresses for the five tread patterns.....	145
Chart 6.6 The maximum tensile stresses for the five tread patterns.....	146
Chart 6.7 The extreme values of elastic and plastic strains in the X direction.....	147
Chart 6.8 The extreme values of elastic and plastic strains in the Y direction.....	147
Chart 6.9 The extreme values of elastic and plastic strains in the Z direction.....	148
Chart 6.10 The maximum and minimum of the total strain in the X direction....	150
Chart 6.11 The maximum and minimum of the total strain in the Y direction.....	150
Chart 6.12 The maximum and minimum of the total strain in the Z direction.....	151
Chart 6.13 Effects of the extreme stresses versus flow angle.....	161
Chart 6.14 Effects of the extreme stress versus cohesion.....	167

Acknowledgements

I would like to record my most sincere gratitude and appreciation to my supervisor Dr Moji Moatamedi, Salford University, for all his guidance, support and help throughout this study. His excellent academic merits, especially in his research methodology about case validation study, have navigated me into the accurate orbit followed by this project and accelerated the growth of my work. His patient reviews and valuable comments have helped to shape the thesis and significantly improve it.

I would also like to thank my advisor Professor David Howard for his continuous useful advice and encouragement throughout this study and that he initiated this project and offered me this opportunity to study. I am also indebted to Mr Andrew Gibbons for his assistance in producing rubber models used in experimental study.

Financial support funded by the Defence Clothing and Textiles Agency of the UK Ministry of Defence through a research contract is gratefully acknowledged.

Finally, I wish to thank my wife Juan for her sacrifice, encouragement, support and understanding during this long period of study, to whom as well as my son Jianjian this thesis is dedicated.

A_{vh}	A hypothesis total area by summing up all transverse surfaces blocking the moving trend of all cleats on forepart of the first tread pattern
A_{vheel}	A hypothesis total area by summing up all transverse surfaces blocking the moving trend of all cleats on heel of the first tread pattern
A_*	The area of horizontal surface of any one star-shape cleat for the first tread pattern
B	The characteristic dimension-- linear dimension
c	Cohesion of soil
$c_3, c_4,$	Constants
D	Material parameter determined by soil test
E	Elastic modulus (Young's modulus)
$d\varepsilon_{ij}$	The total strain increment
$d\varepsilon^e_{ij}$	Elastic strain increment
$d\varepsilon^p_{ij}$	Plastic strain increment
G	Shear modulus
F_t	The total transverse force initiated by forepart of the first tread pattern
$F_{t(heel)}$	The total transverse force initiated by heel of the first tread pattern
F_*	Vertical load acting on by any one star-shape cleat for the first tread pattern
f	Initial yield criterion
f_0	A constant value of the initial yield criterion for a perfect plastic material
I_1	The first stress invariants
I_c	Stress level on the current yield surface
I_c^0	Stress level on the initial yield surface
J_2	The second deviatoric stress invariants
k	Yield stress of material determined from the pure shear test
K_0	Equivalent initial pressure coefficient
M_l	Mass of loose sand
M_c	Mass of compressed sand
P_V	Average vertical pressure for forepart of the first tread pattern
$P_{V(heel)}$	Average vertical pressure for heel of the first tread pattern
P_{SV}	Average vertical pressure for forepart of the second tread pattern
P_{TV}	Average vertical pressure for forepart of the third tread pattern

P_{FV}	Average vertical pressure for forepart of the fourth tread pattern
P_{FifV}	Average vertical pressure for forepart of the fifth tread pattern
P_{at}	Average transverse pressure for forepart of the first tread pattern
$Pat_{(heel)}$	Average transverse pressure for heel of the first tread pattern
P_{Sat}	Average transverse pressure for forepart of the second tread pattern
P_{Tat}	Average transverse pressure for forepart of the third tread pattern
P_{Fat}	Average transverse pressure for forepart of the fourth tread pattern
P_{Fifat}	Average transverse pressure for forepart of the fifth tread pattern
Q	Plastic potential function
V	Volume of mould without collar
W	Material parameter determined by soil test
α	Materials constant relating to the Coulomb's material
α_i	Inclination angle between the i vertical surface of soil model and the plane perpendicular to the X -axis for forepart of the first tread pattern
$\alpha_{heel,i}$	Inclination angle between the i vertical surface of soil model and the plane perpendicular to the X -axis for heel of the first tread pattern
β	Flow angle or dilatancy angle of soil
γ	Bulk unit weight of soil mass
ρ	Wet bulk density of soil
ν	Poisson's ratio
σ_{ij}	The present state of stress
σ^*_{ij}	A homogeneous state of stress
$\sigma_1, \sigma_2, \sigma_3$	The first, second and third principal stresses, respectively
$d\lambda$	A positive scalar of proportionality dependent on the state of stress and load history
ϕ	The angle of internal friction of soil
θ	Lode angle
ϵ^P_v	Plastic volumetric strain of soil

Abstract

Good slip resistant tread patterns of outer-sole of military boots are vital to minimize the risk or severity of slip in combat and physical training situations. This study was aimed at how plastic failure of soil mass develops between the boot outer-sole with cleats and soft soil surfaces, in contrast with the problem between hard surfaces and outer-sole of boot which can be simply modelled using Coulomb-friction representation.

The Drucker-Prager elastic-perfectly plastic material failure criterion is employed to simulate the behaviour of the soil material. A total of five three-dimensional solid soil Finite Element models interactive with the relatively rigid outer-sole of boots with different typical tread patterns have been constructed in the Preprocessor of the ANSYS finite element package. Vertical and transverse loading conditions were acted on the surfaces of soil models interactive with tread patterns. A series of non-linear, three-dimensional FE numerical model have been successfully produced in Solution of the ANSYS. The numerical modelling results were also validated by experiment. These results were analysed and a suitable model was identified to reduce the plastic failure in horizontal direction (X) or provide the best traction force effect.

The comparison of numerical modelling results shows that the first tread patterns among the total five tread patterns designs displays the best traction force effect to resist slip in gaiting direction than the others. The experimental validation study proves the FE numerical modelling provided a good agreement with soil failure pattern and the maximum failure distances. The methodology created in this study can be used as one kind of standard method to judge how performance is for a particular tread patterns design mainly on aspect of traction force provision as well as lateral slip prevention.

Chapter 1

Introduction

1.1 Background

The project “Finite Element Analysis of Footwear and Ground Interaction” was funded by the UK Ministry of Defence (MOD) in 2000, and this research was started on February 2001. The work was carried out in the School of Computing, Science and Engineering (Originally the School of Aeronautical, Civil and Mechanical Engineering) at University of Salford, with the military footwear section within the Defence Clothing and Textiles Agency (DCTA) of the MOD.

The interaction between military footwear and soft ground surfaces is often encountered in combat and physical training situations. The sponsor (MOD) wishes to improve their understanding of how footwear performance is influenced by the tread pattern on the outer-sole, so as to enable improvements in military boot design and hence soldier performance. The military boot is designed to prevent soft tissue and skeleton of the feet from damage under heavy usage which is most likely to result in injuries. Good slip resistant tread pattern of outer-sole of military boot is vital to minimize the risk or severity of slip in these tough situations. Therefore, how to effectively evaluate various tread pattern designs, regarding good slip resistance, is the primary goal of the work. Thereby the possibility of conducting a non-linear three-dimensional finite element analysis of footwear and ground interaction, based upon an elastic-perfectly plastic material model, was investigated in this research.

The Drucker-Prager non-linear material model is widely adopted in computerized numerical modelling for non-linear soil problems and has already been embedded into the ANSYS 5.5-8.1 University High Version. So, we finally select the Drucker-Prager model to simulate soil behaviour in this research, other than the well-known Coulomb criterion which exhibits corners giving rise to difficulties in computer coding.

1.2 Objective of the Research

The main objective of this research is to develop finite element (F. E.) models that can be used to analyse the traction performance of different tread patterns. The information, finite element numerical modelling methodology, results, and improved understanding achieved from this research will be able to help the MOD's military footwear section in their work to judge footwear design, enhance performance and reduce the risk and severity of slip associated with footwear due to the requirements of combat, physical training, ammunition carriage, terrain and climate.

1.3 Scope of the Research

As the aim of this research is to judge traction force performance of different tread patterns by finite element analysis, it was necessary to review existing information on footwear-ground interaction and finite element analysis in this area at the start of this research, although this was ongoing throughout the whole research period. Due to the nature of this research it was also necessary to study many unfamiliar topics such as footwear design, biomechanics, gait of processing, soil mechanics, terramechanics and finite element analysis for nonlinear material of soil, etc. Therefore, the scope of this research can be summarized as follows.

1.3.1 Problem Specification and Literature Review

This part of work is the starting point of this research as well as standard research procedure. This work will be reported in Chapter 2.

1.3.2 Survey of Plasticity Theories in Soil Mechanics

Comprehensive understanding of the theory of soil plasticity, especially failure criteria is essential for this research, because our study mainly deals with plastic failure of nonlinear soil material by employing numerical modelling and experimental study. Detailed information about plastic theory in soil mechanics is reviewed in Chapter 3.

1.3.3 Cases Validation Study

It is important that suitable finite element software with the Drucker-Prager nonlinear material model embedded is used in this research, so that the suitability of the Drucker-Prager nonlinear material model within the ANSYS can be assessed. The purpose of case studies is to validate this suitability. It is also the best means to be familiar with the techniques to deal with finite element analysis of soil-structure interaction in two-dimensional and three-dimensional situations. Chapter 4 presents the two-dimensional case validation study in detail, and the three-dimensional case validation study is reported in Chapter 5.

1.3.4 Finite Element Analysis of Footwear and Ground Interaction

This part of the work is the main achievement of this research. It has been successful in creating interactive soil finite element models for different tread patterns with complex three-dimensional geometry and shape. After successfully meshing the

created volumes, studying loading conditions, conducting numerical modelling and gaining convergent solutions are key aspects of this research we are concerned with. Finally, conclusions are obtained from analysis of finite element modelling results. The work is comprehensively presented in Chapter 6 step-by-step.

1.3.5 Experiment Study

It is necessary to carry out an experimental study to validate the numerical modelling results. Experimental work has been conducted using the prototype soft slip-rig that has been modified in this research. A star-shape cleat scaled up 10 times is used in the experimental study validated against the FE numerical modelling results. The work is reported in Chapter 7 in detail.

1.4 Academic Contribution by This Research

Part of the work was first presented at the Designing for Load Carriage Systems Symposium, 2002, hosted by the UK Ministry of Defence. Then, the continuous work was presented at and compiled, separately, in proceedings of the International Society of Biomechanics XIX th Congress—The human Body in Motion, 2003, New Zealand and Salford's 2nd International Conference “Biomechanics of the Lower Limb in Health, Disease and Rehabilitation”, 2003. A case study paper of this research work is in press with the International Journal—“Strain”.

1.5 Chapters of the Thesis

Chapter 2 of this thesis is devoted to the literature review. The literature survey was set out from the starting point—“Problem Specification”, and followed several main routes: finite element analysis of soil-tillage tools interaction, soil-wheel interaction,

and soil-structure interaction, limit analysis, footwear and ground interaction, etc. Having carried out the background literature study, it was understood that a comprehensive review for soil mechanics and plastic failure theory was required, and that these were the core principles of the mathematical models in this research.

Chapter 3 presents the results of an investigation of plasticity theory in soil mechanics. Firstly, the evolution of plasticity theory is historically reviewed. Then, some fundamentals of solid mechanics are selectively presented so as to make the concepts clear concerning the description of the theory of soil plasticity. In the main part of this chapter, flow theory is explained, and then the highlights of this chapter, that is, perfectly plastic material models. Five typical, perfectly plastic, models are selectively presented, especially the Drucker-Prager material model, which is embedded into ANSYS Finite Element software and employed in this research.

Chapter 4 reports two-dimensional validation by case study in detail. First, the Drucker-Prager material model in ANSYS software is reviewed. Then, a case study of typical earth pressure problems is presented and simulated step by step. The meshing scheme, boundary conditions, and loading conditions are presented and analysed. The initial stress is comprehensively studied in this 2-D validation and this methodology achieved can also be used as a useful means to deal with initial stress effect in geotechnical engineering. A series of numerical modellings has been conducted under different loading conditions. Finally, these results are analysed, and conclusions revealed that the 2-D validation is successful and the ANSYS FE package is suitable for modelling soil material.

Chapter 5 presents three-dimensional validation by two case studies in detail. First, the application of FE numerical modelling in the soil tillage process is briefly reviewed. Then, case 1 study is introduced step by step as well as case validation in ANSYS software. And then, the results are analysed for case 1 study. Thereafter, case 2 validation study is presented. The meshing scheme, boundary conditions, and loading conditions are introduced one by one. Finally, the modelling results are presented and analysed. The influence of convergence norm versus the draught force is intentionally studied. Conclusions are drawn showing that 3D validation about soil-structure interaction problems in ANSYS FE software is satisfied and the Drucker-Prager soil material model, in ANSYS can be used for FE numerical modelling of footwear and soft ground—soil interaction at the next stage.

Chapter 6 intensively reports the study of finite element analysis of tread patterns and soft ground interaction. In total, five tread patterns are studied by using Finite Element Method with ANSYS FE package—University High Option. The outdoor boots as well as military boots are firstly reviewed. Then, the methodology of constructing soil FE model interactive with the first tread pattern is presented in detail. The soil FE models interactive with forepart or heel of the first tread pattern are constructed separately for different transient times in process of gait. The meshing scheme, boundary conditions, and loading conditions are introduced in detail as well. The modelling results of the first tread pattern are presented and discussed. In total, five soil FE models interactive with the forepart of five tread patterns are built up and successfully numerically modelled. Finally, traction performance of each tread pattern as well as soil deformation, stresses and strains, etc. are comparatively analyzed and conclusive comparative results are achieved.

Chapter 7 presents details of the experimental validation studies. First, the methodology of the experimental studies is introduced. Then, the experiment device and the soil selected in this study are reported in detail. And then, FE modelling of interaction between scaled up 10 times model with star-shape and soil is presented step by step. Loading conditions are intensively studied and the vertical loading condition is derived and determined by similarity theory and dimension analysis of mechanics. The procedure of experimental validation is then described. Finally, results of the experimental study are presented and discussed with comparison of the FE modelling results, and a good agreement is achieved between the FE modelling and experimental validation studies.

Chapter 8 presents conclusions arisen from this research. First, each chapter of the thesis is conclusively reviewed with the conclusions achieved in the relevant studies. Then, general conclusions arisen in this research are summarized. Finally, some suggestions for future work are proposed.

Chapter 2

Literature Review

2.1 Introduction

The literature survey is the starting point for the research and an opportunity to obtain a general understanding of the related subjects and relevant academic areas. As the main objective of this research is to develop finite element models that can be used to analyse the traction performance of different tread patterns, it is necessary to investigate existing works on numerical modelling methods such as the Finite Element Method in the soil mechanics domain and works existing on the topic of footwear and ground interaction with soft surfaces. However, before starting the research it was already known that little work existed on the topic of footwear and ground interaction with soft surfaces, reported by Pisani¹ (2002). After an initial background literature survey, it was also found that there is still little work existed related to finite element numerical modelling of footwear issues.

In the initial background literature study, we have understood the problem specification of this research and we are interested in load conditions when plastic failure of the soil mass occurs, that is, what the condition is when shear failure of soil mass happens between the cleats on the bottom of the footwear.

As little work existed on the topic of footwear and ground interaction with soft surfaces, and there is also little work existed related to finite element numerical modelling of footwear issue, we must have to refer to similar relevant mechanisms. The literature survey was focussed on several relevant topics, such as soil-tillage tools

interaction, soil- wheel interaction, soil-structure interaction, limit analysis, etc.

2.2 Problem Specification

2.2.1 General Remarks

As the purpose of this research is to improve the understanding of how footwear performance is influenced by the tread pattern on the outer-sole of military boot, it is necessary to first make clear the problem specification.

As mentioned before, the military boot is designed to prevent soft tissue and skeletal of the feet from damage under heavy usage. Besides, boot design should offer customers the flexibility, comfort, shock absorption and lighter weight to operate regardless of the ground surface texture and various weather conditions. Good slip resistant tread pattern of outer-sole are vital to minimize the risk or severity of slip under the situations that are most likely to result in accidents. Vertical compressive and transverse shear forces are applied to the ground via the footwear during the process of gait, regardless of the surface texture. For a hard surface, no sinkage occurs, the interaction between footwear and ground can be modelled using the Coulomb friction mechanism. It is obvious that this research is not focused on this issue, that is, soft surfaces are the main concern. So, soil properties, soil shear failure, sinkage, tread pattern, etc, are dominating factors affecting the interaction. Therefore, the theories of soil mechanics, plastic failure, etc, will be applied to the study throughout this research.

The problems of soil mechanics are divided into two distinct groups, stability problems and elasticity problems. Stability problems deal with the conditions of

ultimate failure of a mass of soil. Problems of earth pressure, bearing capacity, stability of slopes and shear failure of a soil mass are most often classified in this category. The most important feature of such problems is the determination of the loads which cause failure of the soil mass. Solutions to these problems are often obtained using the theory of perfect plasticity. The elasticity problems on the other hand deal with stress or deformation of the soil when no failure of the soil is involved. Stresses at points in a soil mass under a footing, and all settlement problems belong in this category. Solutions to these problems are often obtained by using the theory of linear elasticity. The problem of progressive failure lies in between the elasticity and stability problems. Progressive failure problems address the elastic-plastic transition from the initial linear state to the ultimate failure state of the soil. For our research purposes, we are interested in load conditions when plastic failure of the soil mass occurs and are also concerned with elastic deformation of the soil mass at the same time. Obviously, the issue of footwear and ground interaction of this research can be classified as the traditional stability problems category of soil mass and solutions to it can be obtained using the theory of perfect plasticity. So, elastic-perfectly plastic theory was adopted in this study and the Drucker-Prager non-linear material model was chosen to model soil property.

2.2.2 Classification of Various Methods/Tools for Soil Mechanics Problems Study

There are several analysis methods/tools existing and used in soil mechanics. They are the slip-line method, the limit equilibrium method, the limit analysis method and numerical analysis methods/tools, such as Finite Difference Method and Finite Element Method, etc. A direct visual classification is shown in Fig. 2.1.

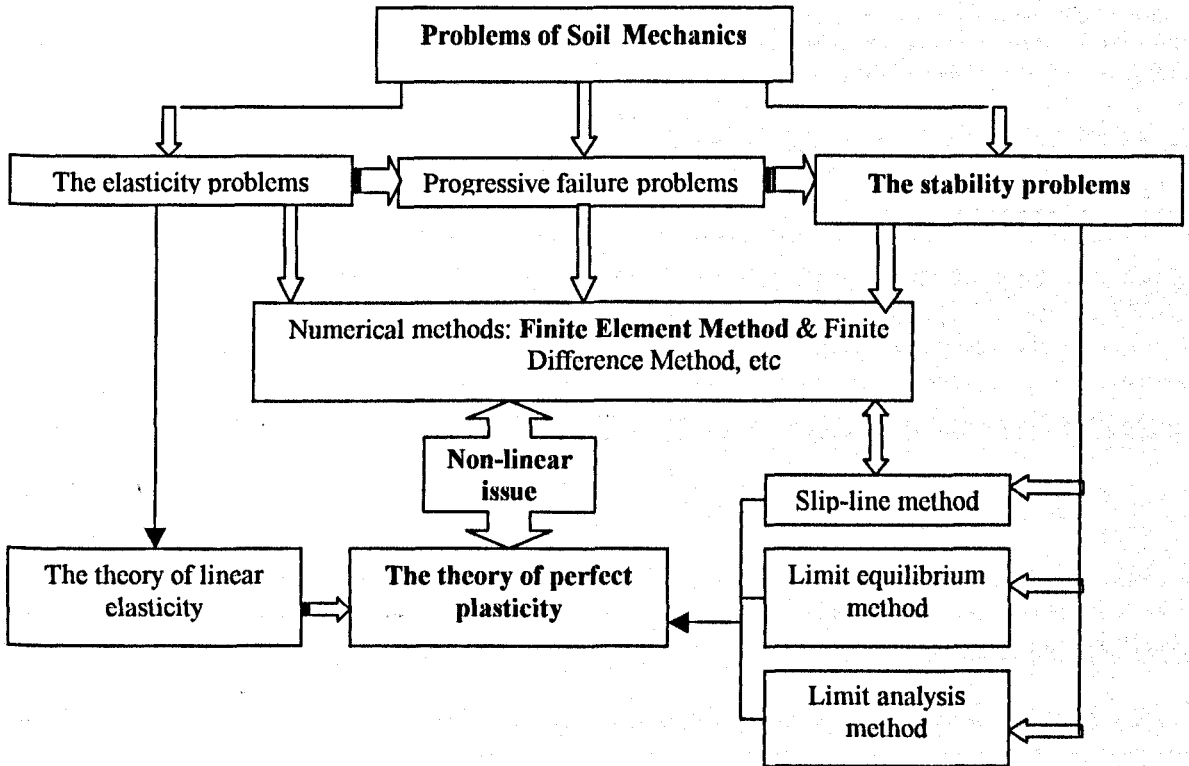


Fig. 2.1 A flowchart of problem specification

2.2.2.1 The slip-line method

The slip-line method is a method that derives the basic differential equations that then make it possible to obtain the solutions of various problems by the determination of the so-called slip-line network. One simplification of the slip-line method is that it omits the stress-strain relationship of the soil. In general, in a slip-line solution, only a part of the soil mass near a footing or behind a retaining wall is assumed to be in the state of plastic equilibrium.

2.2.2.2 The limit equilibrium method

The equilibrium method is a method that creates a simplified mode of failure that then makes it possible to solve various problems by simple static analysis. In this method,

it is necessary to make sufficient assumptions regarding the stress distribution along the failure surface so that an overall force equilibrium equation can be derived and solved for a given problem in terms of stress resultants.

2.2.2.3 The limit analysis method

The limit analysis method is a method that is used for computing the collapse load in a more direct manner. The most distinct characteristic of the limit analysis method is that no matter how complex the geometry of a problem or loading condition, it is always possible to obtain a realistic value of the collapse load. It provides a clear physical picture of the mode of failure. Limit analysis method enables a definite statement to be made about the collapse load without carrying out the step-by-step elastic-plastic analysis.

2.2.2.4 Numerical analysis methods/tools

Numerical analysis methods/tools that are popular computer-based solution technique nowadays are rather effective when applied with proper caution. When it is impossible to obtain the exact answer to problems of engineering analysis and design, the answers of numerical solution are the best estimation for them. The basic philosophy of numerical analysis methods is to reduce the complex continuum from infinite degrees of freedom to a finite number of unknowns. The Finite Difference Method first successfully performed such a process of discretization. The Finite Element Method acts as an alternative to such a process.

2.2.3 Finite Element Method & Non-Linear Soil Problems

The Finite Element Method is essentially a numerical method for the approximate solution of practical problems arising in engineering and scientific analysis. It is now firmly accepted as a most powerful general technique for the numerical solution of a variety of problems from linear to non-linear analysis.

For the increased numerical calculations associated with non-linear problems, considerable computing power is needed. However, rapid developments in the last decades have ensured that high-speed computing facilities that meet this need are now available and the reductions in unit computing costs will continue.

The development of more efficient non-linear solution algorithms and the experience gained in their application to engineering and scientific analysis has ensured that non-linear finite element analysis can now be performed with less barriers than before. The Finite Element Method is especially powerful for a numerical solution of progressive failure non-linear soil problems.

Nowadays, plenty of commercial packages for finite element analysis are available for university campus and industry area. For this research, we have been using Finite Element Method CAE (Computer-Aided-Engineering) software--ANSYS 5.5-8.1 University High Version, which is network supported by the Information Services Division (ISD) at University of Salford.

2.3 Soil-Tillage Tools Interaction

Initially, the theoretical approach to the soil cutting problem was based on Terzaghi's passive earth pressure theory. When the computer became more and more popular and

powerful, the numerical method was developed to solve the cutting problem of soil. The effectiveness of the Finite Element Method in modelling interaction between soil and tillage tool has been proved by some relevant publications.

Yong and Hanna² (1977) first proposed a finite element model for a two-dimensional soil failure under a wide blade. Chi and Kushwaha^{3,4} (1988) developed a three-dimensional finite element model for a narrow cutting blade. This sort of finite element analysis not only gives the soil forces, it also provides stress field, displacement field, failure zone, and force distribution.

Chi and Kushwaha^{3,4} constructed the mathematical model in their study for simulating soil-tool interaction by using the partial difference equation derived by Harr⁵ (1966), which can be expressed in a matrix form. As the soil is a non-linear material, the hyperbolic stress-strain equation reported by Duncan and Chang⁶ (1970) was used in their finite element model. The incremental method was utilized in the non-linear analysis. The change in loading is analysed in a series of increments. At the beginning of each new increment of loading an appropriate modulus value is selected for each element. Thus, the stress-strain relationship is approximated by a series of straight lines. The accuracy of the incremental procedure may be improved if each load increment is analysed more than once. The weighed residual method was used to develop the finite element model that the exact theoretical solution of the differential equation is usually unavailable. By using the Galerkin's weighted residual method, the weighing functions are selected to weight the residual function. As a result, an approximate solution of differential equation is obtained with certain boundary conditions. The authors adopted a hyperbolic model proposed by Clough and Duncan⁷

(1971) for the interface between the soil and the surface of cutting blade. The tetrahedral constant strain element was used during the analysis because of its simplicity and convenience for non-linear material and large displacement. Only half of the total region was considered in the analysis as the soil failure for a narrow blade is symmetric about the centre line of the blade. A total of 996 nodes and 4206 elements, including 18 interface elements, were used for a vertical blade. Laboratory tests were also conducted in the soil bin. The values from the finite element modelling were smaller than that from the lab test because some acceleration forces have introduced some errors while the tests were conducted at a travel speed of 2 km/h.

Nakashima⁸, *et al* developed the simulation program for soil-lug system interaction by Rigid Plastic Finite Element Method (RPFEM). They focused on the problems between lug plate of multiple lugged wheels and its surrounding soil. Firstly they applied soil deformation analysis by mixed formulation with no consideration on large deformation of the soil to investigate the possibility of RPFEM analysis, and then further analysed soil reaction by penalty formulation with mesh rezoning method to decrease the calculation time while enlarging the calculation steps in the analysis. They developed a FORTRAN program with 180 maximum nodes and 130 maximum elements. Two special methods, 1) mesh rezoning and 2) observation markers were employed in their program of tracing large deformation within soil. The calculated result reflected the better performance of numerical procedures for soil reaction and behaviour prediction. The simulated lug reaction showed similar behaviour derived from experiments.

Godwin and Spoor⁹ studied soil failure mechanisms with narrow tines. Studies were carried out using a glass-sided box to observe the soil failure pattern in the vertical plane containing the centre line of the tine. The soil failure mechanism below the critical depth was considered to be purely two-dimensional in a horizontal plane. They developed a force prediction model for tines for a wide range of working depth/width ratios. The predictions showed useful agreement with experimental data for the horizontal force components with high angles of shearing resistance. Two failure mechanisms were identified:

- a) an upper failure zone where the displaced soil has forward, sideways and upward components, termed crescent failure.
- b) a lower failure zone where the displaced soil has components both in the direction of travel and sideways, termed lateral failure.

The soil can deform by crescent failure, lateral failure, or a combination of both. The critical depth can be estimated using minimizing technique, that is, by iteration or by differentiation. The predictions of the curves were closer in the compacted soil than in the loose soil when comparing to the experimental data.

K. Araya and R. Gao¹⁰ (1995) reported a non-linear three-dimensional finite element analysis of subsoiler cutting with pressurized air injection. In their study, a hardening cap model was proposed for hysteresis and plastic bulk deformation of soil and being as the soil yield criterion. The soil properties of sand as an elastic-plastic body were experimentally determined by a triaxial compression test and used in the analysis. The experiments in a soil bin were carried out for comparison with the FEM analysis. The finite element mesh consists of 315 elements and 480 nodes. The load was applied by a 100mm subsoiler movement resulting in the maximum draught force. Air injection

loading was imposed on the soil assumed that there is an empty element without soil at the nozzle port. As flow velocity on soil failure was only one-tenth of static pressure, the effect of kinematic pressure was neglected. Only one-half of the region was considered in the analysis owing to the subsoiler system is symmetric about the central plane. The motion was assumed frictionless, so interface friction between the subsoiler and the soil is zero. This study showed the rake angle affected the rupture distances dramatically. Good agreement was achieved with FEM prediction and soil bin test for forward aspect, vertical soil movements prediction by FEM were smaller than those measured in the tests. Little soil failure is observed for the air injection and the stress around the cavity zone decreases rapidly.

A. M. Mouazen and M. Nemenyi^{11, 12, 13, 14, 15} (1998-2000) reported tillage tool design with the Finite Element Method by numerical modelling soil plastic behaviour and experimental validation with soil bin test. A non-linear, three-dimensional finite element analysis of the soil cutting process by a variety of shank angles and chisel angles combinations were conducted. The Drucker-Prager elastic-perfectly plastic material model was used and an incremental technique was adopted to deal with the material non-linearity of soil. The geometrical non-linearity was solved by using the small strain assumption. A commercial package COSMOS/M 1.71 finite element program was to perform the numerical modelling. Linear rectangular prism elements with eight nodes were selected to represent the soil material and the total number of nodal points and elements were 1374 and 963. The subsoiler was assumed to be a rigid body. A uniform horizontal displacement of 15cm was applied for all subsoiler interfacial nodes. Interface elements were placed between soil-subsoiler bodies to simulate soil-subsoiler interaction by utilizing the Coulomb criterion of dry friction.

The theoretical results showed that a combination of a shank angle of 75° and a chisel angle of 15° made a large reduction in the draught force and vertical forces of the subsoiler. A wedge-shaped soil upheaval was produced owing to deformation in front of the shank. Concentration of normal pressure at the outer linking edges between shank and chisel as well as the bottom corners of the chisel indicated that these locations should be better treated against wear and deformation during manufacturing. Laboratory soil bin tests proved finite element numerical modelling results agreed well with these measurements for the subsoiler draught force and the extent of surface soil failure, the over prediction error ranged from 11.76 to 20.04 %.

Renon¹⁶, *et al* reported their study of "Numerical Modelling of soil ploughing for military breaching". In this study, the soil is modelled as a continuous compressible plastic medium using 3D FEM. A FEM software developed by CEMEF (*Ecole des Mines de Paris*) has been chosen for this study. The tetrahedral element is used in modelling. To handle strong non-linearity, the iterative Newton-Raphson method with linear search is used, so that one linear system has to be solved at each step of iteration. As a first step, the Drucker-Prager model has been implemented in the FEM software. The simulations, involving one single tine, were performed for three different rake angles: 45, 75 and 90 degree. 26 hours CPU for 330 time steps including 122 remeshings on a SUN E4000/5000 computer (processors SUN UltraSPARC-II, 248 Mhz). The average number of Newton-Raphson iterations per increment is 7.8, and each one increment takes an average 289s. Simulations results express two very different flow modes: a chip in front of the tine (75 and 90 degree) and larger bulges (lateral spread, 45 degree).

2.4 Soil-Wheel Interaction

Since the literature survey of foot-ground interaction has shown little suitable research on soft surfaces, it is necessary to investigate other relevant fields, terra-mechanics for example. Soil-wheel interaction belongs to this category. Terra-mechanics is the study of the performance of a machine in relation to its environment, the terrain. It can be divided into two main branches, terrain-vehicle mechanics and terrain-implement mechanics. Much research has been carried out on the interaction between soil and wheels.

M.G. Bekker carried out soil-wheel interaction study in the 1950's. He investigated the effect of thin and wide wheels on sand and clay and was able to show that the behaviour of soil beneath a rolling wheel conforms to the basic principles of soil mechanics. Bakker's theory¹⁷, applicable to all soils, was based on some simple tests and semi-empirical equations. It does not take into consideration the flow of soil. The underlying soil theory of Bakker used in terra-mechanics was actually based upon the soil mechanics works of Terzaghi¹⁸ used in civil engineering.

Oida and Satoh¹⁹ reported their results for three dimensional stress distributions on tyre-sand contact surface. By using a forced-slippage test apparatus and a small three axial force transducer attached on a tyre surface, the distributions of normal, longitudinal and lateral stresses along the tire-soil contact area were precisely measured on standard sand in the laboratory and processed by a personal computer. Stress distribution patterns, positions of maximum stresses, relations between thrust and side force with parameters of slippage and side slip angle and so on were presented.

Ueno, etc²⁰ developed a sub-loading surface model of plasticity by Finite Element Method to analyse the problems of soil deformation by the rotation of a rigid wheel. The points of this FEM were to express suitably the plastic deformation of soil, to represent the boundary conditions at the contact surface between the wheel and the soil, and to deal with the rolling condition. The FEM numerical modelling is performed with two stages, in the first stage a wheel drops down vertically, and in the next stage it rolls keeping the axle load constant. Controlled displacement increments were given as boundary conditions at the contact surface of the soil and the wheel. The concept of relative slip and the Coulomb's frictional criterion were employed to control these displacement increments. The basic equations were formulated by the incremental method in elastic-plasticity and the FEM based on it. The strain and stress increments were calculated from the nodal displacement increments. The stress and strain of each element, the force and displacement of each node were obtained by accumulating these increments. The same process was repeated until reaching to the prescribed state. The results by this elastic-plastic FEM analysis for a soil-wheel interaction represented some of the fundamental tendencies observed in experiments.

Aubel²¹ studied the interaction between an elastic tyre and soft soil by FEM-Simulation. A new FEM simulation concept VENUS (VEHICLE NATURE SIMULATION) is developed. It consists of a soil model, a tyre model and a combination of both. The tyre model takes into consideration the different elastic properties as a function of the inflation pressure, and the lateral expansion of the tyre cross section seems to be neglectable. The soil model is based on the Mohr-Coulomb hypothesis and Drucker-Prager's modified version of the flow criterion by V. Mises. The simulation examples

in this research are calculated with the FEM program ABAQUS. The numerical solution of the interaction is based on a contact algorithm, which works during every calculation step. The new FEM simulation model VENUS has the advantage that it does not need to estimate any parameters acting in the contact area between tyre and soil, opens up a promising field of investigation for the interaction between elastic tyres and soft soils.

2.5 Soil-Structure Interaction

The finite element analysis of soil-structure interaction has been applied to a number of types of soil mechanics and soil engineering problems since 1960s. The method has been used for analysis of stresses and deformations in embankments (Clough and Woodward²², 1967), (Finn²³, 1967); for the modelling of movements around excavations (Duncan and Dunlop²⁴, 1969) (Chang and Duncan²⁵, 1970); for analysis of stresses and settlements resulting from footing loads (Girijavallabhan and Reese²⁶, 1968), (Desai and Reese²⁷, 1970), (D'Appolonia and Lambe²⁸, 1970), (Smith²⁹, 1970); and for the modelling of the relationship between earth pressures and wall movements (Morgenstern and Eisenstein³⁰, 1970), (Lambe³¹, 1970), and so on. Most of the studies mentioned above have been carried out employing one of two limiting assumptions about the characteristics of the soil-structure interface: (1) that the interface is perfectly smooth, with no possibility for shear stresses which would retard relative movements between the structure and the soil; or (2) that the interface is perfectly rough, without possibility for slip between the structure and the soil.

Clough and Duncan⁷ (1971) developed a procedure for representing the interface between a structure and the adjacent soil in finite element analyses of soil-structure

interaction. The stress-deformation and strength characteristics of interfaces between a backfill sand and concrete were investigated by means of direct shear tests on composite specimens. Analyses of retaining walls were performed in their studies using finite elements to simulate the interface between the wall and the backfill. The analyses were performed in a series of increments, adjusting the properties of the interface and the backfill in accordance with the stresses for each increment to approximate non-linear behaviour. The minimum active and maximum passive pressures calculated in these analyses were in good agreement with the results of classical earth pressure theory. These incremental finite element analyses provide an effective means of analysing soil-structure interaction problems and the procedures in this study also show that it has considerable potential for the analysis of complex soil-structure problems.

Girijavallabhan and Reese²⁶ reported their study results for finite element method applied to soil mechanics. They claimed the basic procedure used in finite element analysis to solve foundation problems consists of representing each element as a homogeneous, isotropic linear material, which is defined by two pseudo-elastic constants, the secant modulus of elasticity and Poisson's ratio. The solution of a load-deformation problem for a soil with a given set of boundary conditions can be achieved by finite element analysis. The computational procedure used to solve stress problems for soil starts with an assumed pseudo-elastic constant, E . The components of strains are computed for a given set of boundary forces and deflections, and then a new value for the pseudo-elastic constant is obtained for each element. Iteration is continued until the difference between the new and the previous value of the pseudo-elastic constant for each element is less than a specified small quantity. The results of

the problems solved for non-linear media agree closely with experimental results. The experiment was performed in the laboratory, where a rigid steel plate was pushed into the sand in a way that produced a state of plain strain.

Duncan and Chang²⁵ developed a simple, practical procedure for representing the non-linear stress-strain relationship of soils, which is convenient for use with the finite element method of analysis. Kondner³² claimed that the non-linear stress-strain curves of both clay and sand might be approximated by hyperbolae with a high degree of accuracy. Experimental studies by Janbu³³ had shown the relationship between initial tangent modulus and confining pressure. The authors discussed two techniques in their study for approximate non-linear analyses, the iterative procedure and incremental procedure. Both of these methods have both advantages and shortcomings. The expression for the equation for tangent modulus is derived and employed conveniently in incremental stress analyses, and constitutes the essential portion of the stress-strain relationship in these studies. A number of experiments have been conducted to determine the parameters used in the equation of tangent modulus and to evaluate the usefulness of this equation for representing non-linear soil behaviour. The authors also discussed a footing in sand and a footing on clay examples based upon results of finite element analysis.

Potts and Fourie³⁴ reported their study of the effects of wall deformation on earth pressures (1986). The Finite Element Method was used to investigate the effect of the mode of wall movement on the generation of earth pressure. Both smooth and rough walls were considered. Results proved that the distribution of earth pressure is mainly dependant on the assumed mode of deformation. The finite element equations were

solved using an accelerated incremental form of the initial stress approach. An elastoplastic constitutive law using a Mohr-Coulomb yield surface had been employed to model the soil behaviour. A number of conclusions arose from their investigation. They also studied the effect of soil dilatation, the initial horizontal stress, the distribution of soil stiffness with depth, wall translation, rotation about the top and rotation about the bottom of a wall. Their results clearly stated that the finite element approach is more exact and has considerable advantage comparing with those from the other approximate methods, and to be a viable potential alternative for design of earth retaining structure.

Schweiger³⁵ discussed the use of different forms of Drucker-Prager failure criterion for a simple earth pressure problem (1994). Active and passive earth pressure problems were simulated in this study under plane strain conditions by applying prescribed horizontal displacements to a rigid wall in front of a soil subjected to initial stresses. The finite element mesh consists of 300 eight-noded isoparametric elements and a viscoplastic algorithm was employed for solving the non-linear equations. A smooth wall was assumed in this series analyses and no geometric nonlinearities were considered. The results of this study demonstrated importance for elastic-perfectly plastic analyses in geomechanics. The internal and extension cone of failure criteria produce approximately the correct pressure distribution other than wall displacements compared to Mohr-Coulomb criterion. Neither the compression nor the compromise cone can predict the active and passive pressure to an accuracy that is acceptable for practical purposes. Even though the Drucker-Prager models are popular used for engineering problems owing to its simplicity and easiness for the implementation into finite element codes, the author suggested a proper Mohr-Coulomb failure criterion

should be used when it is impossible to use other more refined models.

Jean-Francois⁶¹, etc. published their work (2004) about a micromechanical approach to the strength criterion of Drucker-Prager materials reinforced by rigid inclusions. The paper proposes a theoretical approach to the strength criterion of such a composite material. It is shown that the macroscopic stress states on the yield surface can be obtained from the solution to non-linear viscous problems defined on a representative volume element. The practical determination of the yield surface implements a non-linear homogenization scheme based on the modified secant method. Two extreme cases of perfect bonding and non-frictional interfaces are modelled. In both cases, the method yields a macroscopic strength criterion of the Drucker-Prager type. The macroscopic friction angle is a function of that of the matrix and of the volume fraction of the inclusions. In the case of perfect bonding, the inclusions have a reinforcing effect. In contrast, this may not be true for a non-frictional interface.

2.6 Limit Analysis

Limit analysis method was established in 1950s. There have been an enormous number of applications with it in a wide field from metal deformation processing to the design of reinforced concrete structures. A great deal of effort practicing the limit analysis method has been paid to soil mechanics problems since 1970s in addition to concrete and rock, accompanying the development of numerical methods in the meantime.

Drucker³⁶ (1953) reported his study about limit analysis of soil mechanics problems.

A brief discussion is given of suitable general forms of the yield or sliding criterion for soils. Coulomb's equation is interpreted in terms of a modified Tresca as well as a modified Mises rule. Particular attention is paid to a soil unable to take tension but exhibits both cohesion and internal friction in sliding action. The author claims that a modified Tresca criterion is probably more in the spirit of the Coulomb postulate for soils than is the modified Mises. Two main limit theorems, that is, the upper bound theorem and the lower bound theorem are discussed as well as the dissipation function.

Chen³⁷ (1975) carried out comprehensive studies with limit analysis as presented in his works "Limit Analysis and Soil Plasticity". He claims that 'perhaps the most striking characteristic of the limit analysis method is that no matter how complex the geometry of a problem or loading condition, it is always possible to obtain a realistic value of the collapse load'³⁷. The limit analysis method is an effective method for computing the collapse load in a more direct manner. It enables definite statement to be made about the collapse load without carrying out the step-by-step elastic-plastic analysis. This method provides a clear physical picture of the mode of failure and considers the stress-strain relationship of a soil in an idealized manner. This idealization, termed normality or flow rule, establishes the limit theorems on which limit analysis is based. The plastic limit theorems of Drucker³⁸ (1952) may conveniently be employed to obtain upper and lower bounds of the collapse load for stability problems. The author also emphasized that limit analysis is not the only method of assessing the collapse load of a stability problem in soil mechanics. The other standard and widely known techniques used in the solution of soil mechanics problems are the slip-line method and the limit equilibrium method.

Lyamin and Sloan³⁹ reported in their study that, a robust numerical scheme for upper bound limit analysis could be used for two- and three-dimensional problems. They stated the technique generates the stress and velocity fields at collapse and can be implemented using finite element theory and mathematical programming algorithms.

By adopting linear finite elements and a polyhedral approximation of the yield surface, the finite-dimensional optimisation problem can be solved using classical linear programming techniques. The solution procedure does require the yield function to be both convex and smooth. Numerical results show that the new algorithm demonstrates fast convergence to the optimum solution and is effective for a broad spectrum of stability problems.

Pontes⁴⁰, etc. presents an algorithm for limit analysis with mixed approach by finite elements with application to geo-technical problems. The approach is based on the direct application on the sub-differential concept to the flow law and is essentially different from the Lagrange multipliers technique. The case of a Drucker-Prager model is particularly considered, as well as the Mohr-Coulomb model in plane strain conditions. The algorithm is applied to a footing and a shallow tunnel.

Ponter⁴¹, etc. describes a generalisation of the programming method for the evaluation of optimal upper bounds on the limit load of a body composed of a rigid perfectly plastic material. The method is based upon similar principles to the "Elastic Compensation" method. The method is demonstrated through an application to a Drucker-Prager yield condition in terms of the Von Mises effective stress and the

hydrostatic pressure. Implementation is shown to be possible using the user routines in a commercial finite element code, ABAQUS.

Babakov⁴², etc. states (1994) that, we know of no studies that have analysed the problem when a transverse load is applied to a die embedded in soil. The solution of such a problem would require consideration of the irreversible strains undergone by the soil, i.e. require the use of a mathematical model of plasticity for the soil. They use an established method of solving problems of plasticity theory that is based on one of the theorems of limit analysis -- the theorem of the upper bound of the limit load.

2.7 Footwear and Ground Interaction

During the whole process of this research information concerning footwear and ground interaction was constantly searched for. As presented in "Problem Specification" section in Chapter 2, we are interested in the issue of footwear and soft surfaces ground interaction. Based upon this basic point, the following information is useful for this research.

Barry and Milburn^{43, 44} reported their study on a mechanism of explaining traction of footwear on natural surfaces and a footwear traction-measuring device. They review and discuss the mechanism associated with footwear-natural surfaces interaction at a molecular level and carried out their research based upon tribology and soil mechanics. At the molecular level, solid smooth surfaces of a pair of contacted solids have valleys and ridges, respectively. These asperities respond to each other when sliding happens. Analytical research classifies this contact into a complex molecular-

mechanical interaction between the contacting surfaces. This interaction was considered to be a result affected by various factors, such as the combined effects of asperity deformation, ploughing by hard surface asperities and wear particles, and adhesion between flat surfaces. This mechanism used to explain how dry friction could be treated as a basis to illustrate the mechanism of footwear-natural surfaces interaction, even though 'The classical laws of friction do not apply to footwear sliding on artificial and natural surfaces' (Valiant⁴⁵, 1993).

The tread pattern or cleat configuration of footwear outsoles interact with natural turf surfaces made of particles of soils and grass. Soil consists of discrete particles that are not strongly bonded together and are relatively free to move with respect to each other. When the soil surface is subjected to a load via the outsole and cleats, the soil resists the applied load by developing resistant forces through the responded particles in three ways: compressing, bending and sliding. Deformation due to sliding is usually the most significant, and is nonlinear and irreversible, making the load-deformation behaviour of soil nonlinear and irreversible as well (Lambe & Whitman⁴⁶, 1979). When the applied external become large enough, failure of the soil mass may occur when the resistance force reaches its limit and the soil mass as whole slides. This mechanism discussed by Barry and Milburn is the same or similar to the soil plasticity theory adopted in the work reported in this thesis.

Barry and Milburn also introduced a computer-controlled device to measure traction load-deformation properties at the footwear-natural surfaces interface. This device is designed based on the traditional methods used in soil mechanics to determine the direct shear force of a soil where a horizontal displacement is imposed at the interface

while its vertical displacement is measured. A number of methods have been used to measure the translation or rotational traction between court shoes and artificial surfaces and little research has tested the traction of footwear on natural surfaces only an exception that the Nike Sports Research Laboratory (NSRL) tested footwear while separately translating or rotating (Valiant⁴⁷, 1990). The method used by Barry and Milburn to measure translation or rotation to the footwear was similar to the NSRL device, however, its slide rate and displacement were precisely controlled and vertical displacement of the boot was measured as it slid over the test surface. The measured traction data was fitted by a non-linear regression analysis technique by using exponential model used by Wong⁴⁸ to obtain the maximum traction force in a similar way in 1989. The nonlinear load-deformation curves provide the maximum traction force, the displacements corresponding to relevant traction forces, and the overall stiffness of the interface materials. In the case of footwear sliding on sand, the failure surface was clearly observed at the end of test. The experiment showed that the foremost cleats of the outsole 'piggybacked' on the failure wedge of sand. This observation was not obvious for the turf samples, as the binding of the grass roots would affect the traction mechanism. Each footwear-surface combination has unique interface properties. Typical traction results for football boots bearing on sand and turf were studied.

Baroud⁴⁹, D. etc. presented a non-linear hyper-elastic finite element model of energy return enhancement in sport surfaces and shoes. They developed a 3-D F. E. model of a sport shoe and surface using a generalized compressible hyper-elastic material model. The material parameters were identified based on quasi-static uniaxial compression, confined compression, and tension tests. The energy return of the

structural surface-shoe combination was determined under actual loading. The 3-D reaction forces used in the F. E. simulation were measured from one subject during forepart of foot running over a Kistler force platform. The numerical results were experimentally verified. The agreement between numerical and experimental results for a sport surface and /or shoe is much better using the proposed hyper-elastic than linear elastic materials models. The generalized 3-D material model, together with F. E. modelling provides a means to theoretically examine different designs of sport surfaces and/or shoes with respect to their energy storage and return and/or cushioning potential.

Garcia⁵⁰, etc. developed a method for measuring horizontal forces of soccer boots studs during skills performance. The author argued that even though some studies about ground reaction forces in different skills have been made by using a force platform, no studies show the reaction forces in the studs themselves. Therefore, a new system to analyze the action of each studs based on strain gauge technology has been developed. The system allows measuring horizontal forces in every stud during a movement. Thirteen studs instrumented with strain gauges were employed to measure the forces in lateral and direction in every stud in real soccer actions. Five male semi-professional soccer players have participated in this work. The results measured have a very good level in the reliability of modulus in turning movements and starting run, but in zigzag movement shows low reliability. The measuring system could be considered as a useful training and sports shoe design tool concerning stud behaviour.

Douglas⁵¹, etc. studied cleat-surface friction on new and old AstroTurf by a cleat platform device. Three cleats taken from a shoe are fastened in a triangular array on a

platform paved by Astro turf. Normal loading was applied symmetrically on the array with weights. The array is then pulled across the Astro turf using the crank tower affording the polling or friction force that is recorded on a chart recorder. More weight can be added and the test is repeatable. This ensures the cleats contact the surface in a uniform manner and allows one to observe the static and dynamics friction as well as the amount of 'chatter' during the sliding. Three types of cleat were tested: the Riddell 78 polyurethane screw-on type cleat, the Riddell 391 red-molded urethane slightly worn cleat and a very worn Riddell 391 cleat. Experiments shows: The Riddell 78 type cleat produces more friction on five year old used and exposed Astro turf than on the unused and unexposed Astro turf, the Riddell 391 type cleat reverse this behaviour; In general, the 391 cleat has greater friction than the 78 on the unused and unexposed Astro turf; Cleat wear of the shoe, the Riddell 391 most commonly used on Astro turf, has little effect on friction.

Robert⁵², etc. reported their investigation about differences in friction and torsional resistance in athletic shoe--turf surface interfaces. By using a specially designed pneumatic testing system, the shoe-surface interaction of 15 football shoes made by 3 manufacturers was evaluated in both anterior translation and rotation. The surface sample was secured to the turf platform on the testing apparatus. Rotation of a loaded shoe on the apparatus was accomplished by rotating the surface using a rotary pneumatic actuator, and translation was performed by a linear pneumatic actuator acting on the frame. Load was applied with free weights placed on the tibial shaft. The shoes included traditional cleated football shoes, court shoes, molded-cleat shoes, and turf shoes. All shoes were tested on natural stadium grass and synthetic turf under dry and wet conditions. The values on translation with wet versus dry surface were

significantly different for rotation about the tibial axis. No overall difference between shoes on grass versus Astroturf. However, there were significant differences for cleated and turf shoes. The authors strongly suggested, on the basis of this study, for manufacturers to display suggested indications and playing surface conditions for which their shoes were recommended.

2.8 Others

A study about experiment and analysis of the interaction between camel foot and sand ground was reported by Xu⁵³, etc. With the use of a footprint measuring instrument, a high-speed camera system and a multi-channel data synchronous collecting system, the area and shape of interaction between camel foot and sand ground, and the varying process of three-dimensional stress of sand beneath a camel foot were measured and analyzed. The study of interaction between camel foot and sand is very meaningful to develop ideal running gear on sand. The results from footprint measurement shows that a camel foot swings with hoof as pivot when it is about to leave sand ground, this way of interaction makes the shear capacity of sand under the foot be fully utilized, and traction performance improved. The area-increasing characteristics of camel foot makes the sand beneath its foot has a small stress with little change.

During the process of literature study and project research, a number of texts and/or books were found to be very helpful and benefited for our research. As the soil mechanics is the fundamental theory to carry out this our research, a few popular texts and/or books about soil mechanics, authored by Craig⁵⁴, Smith and Smith⁵⁵, Jumikis⁵⁶, and Yong and Warkentin⁵⁷ were addressed. The Finite Element Method is the sole numerical modelling technique used by us to perform the finite element analysis of

footwear and ground interaction, so three books describing FEM, written by Rao⁵⁸, Cook⁵⁹, Lewis and Ward⁶⁰, were referred to. For the study of theory of soil plasticity and failure criterion the following texts were most valuable: Chen³⁷, Hill⁶², and Chakrabarty⁶³ where the basic principles of theory of plasticity and failure criteria of soil were derived in detail. The texts by Smith⁶⁴, and Chen⁶⁵ were most helpful to carry out nonlinear finite element analysis in soil mechanics and civil engineering. The books by Duncan⁶⁶, and Sedov⁶⁷ were very useful to guide us building up the mechanism of experimental validation. A book authored by Johnson⁶⁸ was also referred to when sorting out contacting problem.

2.9 Summary

The literature survey was initiated from 'Problem Specification'. Little work existed on the topic of footwear and ground interaction with soft surfaces, especially on work related to finite element numerical modelling; the literature survey was focussed on several relevant topics, such as soil-tillage tools interaction, soil-wheel interaction, soil-structure interaction, limit analysis, etc. besides the issue of footwear and soft ground interaction.

Plenty of studies concerning soil-tillage tools interaction had been performed, and quite a few practices of them were by using FEM since 1970s. Literatures reported by K. Araya and R. Gao¹⁰ (1995), A. M. Mouazen and M. Nemenyi^{11, 12, 13, 14, 15} (1998-2000) are typically selected as the candidates for 3D case study of this research reported in Chapter 5; Soil-wheel interaction study began from 1950's and a number of researches by using FEM and Drucker-Prager nonlinear material model are very helpful for forming the idea of our research about footwear and ground interaction;

The finite element analysis of soil-structure interaction has been applied to a number of types of soil mechanics and soil engineering problems since 1960s. Works by Schweiger³⁵ is specially chosen to be two-dimensional case validation in Chapter 4; Being a sort of analytical methods opposite to numerical methods, limit analysis method was widely applied in soil mechanics problems since it was established in 1950s.

A few researches concerning about footwear and ground interaction with soft surfaces were mainly by means of experiment methods with respect to artificial surfaces, such as Astroturf, and natural surfaces, for instance, football field. The study carried out by Barry and Milburn^{43, 44} was representative and focused on employing experimental methods to investigate traction performance of footwear on the soft and natural surfaces. The mechanism discussed by them is the same or similar to the soil plasticity theory adopted in our work reported in this thesis. We carried out experiments to validate the numerical modeling results presented in Chapter 7. Only one works by Baroud⁴⁹, D. etc. was founded by using FEM to study footwear. However, they use hyper-elastic material model to simulate footwear behaviour, other than the methodology created by us by using DP material model to model interactive soil properties, which is reported in Chapter 6 as the main part of this research reported in this thesis.

Texts by Chen^{37, 65}, Smith⁶⁴ were founded to be most helpful for comprehensive understanding of soil plasticity, failure criterion, nonlinear analysis, and FEM in soil mechanics. They are reviewed in detail in Chapter 3.

Chapter 3

Investigation about Theories of Plasticity in Soil Mechanics

3.1 Introduction

As stated in previous chapters, little literature can be found concerning about study of interaction between footwear and soft surfaces of natural ground, especially by using Finite Element Method. We, therefore, have to investigate some relevant research areas by using Finite Element Method, such as soil-tillage tool interaction, soil-wheel interaction and soil-structure interaction, etc. at the stage of literature survey. However, all of these relevant studies were based upon the fundamental theories of soil plasticity and failure criteria that we also employ in this research and are embedded in the ANSYS finite element analysis software we used. So, a clear understanding of soil plasticity and failure criteria is necessary and important to carry out this research.

The theories of soil plasticity and failure criteria were generally considered as early as in 1773 originated by Coulomb¹¹⁰ who put forward the Coulomb failure criterion for soil. He also proposed the important concept of limiting plastic equilibrium and applied it to a fill on a retaining wall to determinate the earth pressure. Rankine¹¹¹ introduced the concept of slip surfaces in 1857 through studying about limit plastic equilibrium of a half-infinite body. In 1899, Massau¹¹² established the basic geometric property of the net of slip-line field. The works of Kötter¹¹³ was published in 1903 to obtain a set of differential equations of plastic equilibrium and transform them to curvilinear co-ordinates (slip-line method). In 1926, Fellenius¹¹⁴ described a simplified theory of plastic equilibrium (limit equilibrium method). Subsequently

many of researchers including Terzaghi developed further Fellenius's works and that were summarized in the Terzaghi's book¹⁸ on soil mechanics in 1943. Sokolovskii applied the Kötter's equations (slip-line method) to various soil stability problems and his works was summarized in book¹¹⁵ (1965).

The development relation between the theory of metal plasticity and the theory of soil plasticity has been close and interactive. The development of metal plasticity had been strongly influenced by the earliest theory of earth pressure. For instance, Tresca's yield condition of metal material presented in 1864, and thereafter¹¹⁶, is a special case of Coulomb's yield condition (1773) which is 95 years before Tresca; Rankine's (1857) theory of plastic states of equilibrium in loose earth preceded De Saint Venant's¹¹⁷ (1870) investigation of such equilibrium states in plastic solids. Von Mises, in 1913, introduced a new yield criterion—the von Mises criterion for metals to be more convenient for numerical solutions. During the period from 1950s to 1960s the theory of metal plasticity has been intensively developed. The fundamental theorems of limit analysis about perfect plasticity, the concept of normality condition or associated flow rule, and the Drucker's postulate³⁸ formed the core and most extensively developed part of the theory of metal plasticity. The development of the modern theory of soil plasticity was also strongly influenced by the well-established theory of metal plasticity. Modern researchers have been preoccupied with extending these concepts to answer the complex problems in soil mechanics.

The first major advance in the extension of metal plasticity to soil plasticity was reported by Drucker and Prager⁷³ in 1952. The authors extended the Coulomb criterion to three-dimensional soil mechanics problems. In 1953, Drucker³⁶ interpreted

the Coulomb criterion as a modified Tresca as well as an extended von Mises yield criterion. The latter yield criterion is known as the Drucker-Prager model or the extended von Mises model, which was embedded into ANSYS finite element software and has been employed by us in this research to study footwear and ground interaction. An important advance was achieved reported by Drucker, etc.⁷⁷ in 1955 in the paper “Soil Mechanics and Work-Hardening Theories of Plasticity”. The authors introduced the concept of work-hardening plasticity into soil mechanics. The idea of a work-hardening cap added to perfectly plastic yield surface, such as the Coulomb type or Drucker-Prager type of yield criterion, was a important innovation and has led to in turn to the generation of many soil models. Notably, Roscoe and his colleagues¹¹⁸ introduced the concept of critical state soil mechanics in 1958, and thereafter Cam-clay model¹¹⁹ in 1963 with additional experimental data having been gathered, interpreted, and matched. ‘This extension marks the beginning of the modern development of a consistent theory of soil plasticity’ (Chen³⁷, 1975). From around 1970s to up to date, the studies focused on constitutive models of soil problems have still been being blooming. In the meantime, the rapid development of computing technology on the aspects of both “hardware” and algorithm has been playing an important role in advancing the theory of soil plasticity. Numerical analysis specialist, for instance, Zienkiewicz¹²⁰ suggested the concept of generalized plasticity, and established the system of generalized plasticity theory. He indicated that, comparing to the traditional theory of plasticity—the theory of metal plasticity, the theory of soil plasticity is a sort of generalized theory of plasticity, and the former is just a special case of the generalized theory of plasticity.

This chapter does not aim to review the whole field of theories of plasticity in soil mechanics. A few fundamental concepts of soil plasticity and relevant material models related to the model employed in our research, i.e. the Drucker-Prager material model, are presented.

3.2 Elastic-Perfectly Plastic Assumption

From the investigation of plasticity theories and failure criteria in soil mechanics, it has been realized that the mechanical behaviour of soil materials is much more complicated than that described by classical elasticity and/or plasticity theories. However, the modern theories of plasticity and failure criteria in soil mechanics have been notably based on the classical elasticity and plasticity theories developed in structural and continuum mechanics, especially the theory of metal plasticity. In the most of real cases, the soil behaves as an elastic-plastic material, and its stress-strain behaviour is 'characterized by an initial linear portion and a peak or failure stress followed by work softening to a residual stress'³⁷, seen Fig. 3.1. However, the necessity of a good simplification in engineering problems makes it available that to ignore the work softening and peak features and to take the stress-strain relationship to be consisted of two straight lines as shown by the dashed lines, *oa* and *ab* in

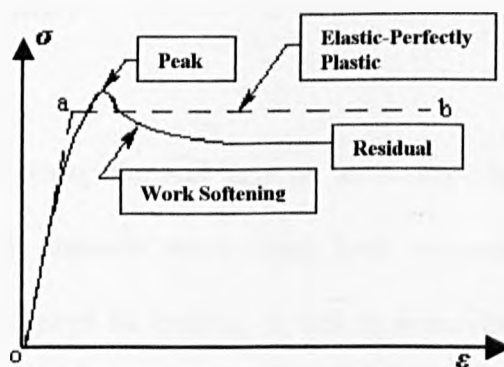


Fig. 3.1 Stress-strain curve for ideal and real soils (From Chen³⁷)

Fig. 3.1. A material hypothetically exhibiting this property of continuing or unrestricted plastic flow at constant stress, i.e. $\sigma = \sigma_a = \sigma_b = \text{Constant Stress}$, is called an ideally plastic or perfectly plastic material. Of course, a material assumed to have a stress-strain relationship as straight lines oa and ab shown in Fig. 3.1 is an elastic-perfectly plastic material, where the yield stress level ($\sigma = \sigma_a = \sigma_b = \text{Constant Stress}$) that the perfect plasticity assumption is made may be chosen to present the average stress in an appropriate range of strain.

The stress-strain diagram shown in Fig. 3.1 is associated with a simple shear test or a tri-axial compression test. To realize the behaviour of the soil for a complex stress state requires a solution where conditions characterize the change of the soil material from an elastic state to a yield or flow state (the horizontal line ab , Fig. 3.1). This condition was created and developed, called yield criteria (perfect plasticity condition), to answer this arisen question of a possible form of the condition that characterizes the transition of a soil from an elastic deformation state to a plastic failure state. The yield criteria will be narrated in the following sections.

3.3 Theories of Soil Plasticity

3.3.1 General Remarks

In the most fundamental case, the soil acts as an elastic-plastic material, i.e., soil deformations are basically inelastic since upon load removal, unloading follows a different path from that followed by loading, as well as irrecoverable strains.

Elasticity-based model can be used to describe the soil behaviour, but a special loading criterion must be defined for loading and for unloading. Such a formulation is known as the deformation theory of plasticity. The variable modulus models are generalized in this kind of theory to deal with incremental stress-strain relationships.

There are some limitations for the deformation theory of plasticity and the variable modulus, which can be overcome by the flow theory of plasticity.

The flow theory of plasticity is based on three basic assumptions: (a) the existence of an initial failure surface; (b) the evolution of subsequent loading surfaces (hardening rule); and (c) the formulation of an appropriate flow rule. For soils, as for metals, perfect plasticity is an ideal design simplification. For more complex stress-strain behaviour of soil, it may be simulated by more sophisticated hardening plasticity theory. For this research, only the theory of perfect plasticity and perfect plasticity material model—Drucker-Prager are mainly employed.

The formulation based on the flow theory of plasticity gives a good fit to data from laboratory tests. Existing plasticity models including the Drucker-Prager model can represent important soil characteristics such as dilatation, dependency of strength on stress or strain history and non-linear behaviour, etc. These models such as Drucker-Prager, Coulomb, Tresca and von Mises, etc. rigorously satisfy the basic requirements of continuum mechanics such as uniqueness, stability and continuity.

3.3.2 Flow Theory

In the theory of stress increment--strain increment relationship, the total strain increment $d\varepsilon_{ij}$ is composed of the elastic strain increment $d\varepsilon_{ij}^e$ and the plastic strain increment $d\varepsilon_{ij}^p$, i.e.:

$$d\varepsilon_{ij} = d\varepsilon_{ij}^e + d\varepsilon_{ij}^p \quad (3.1)$$

The elastic strain increment obeys Hook's law where two material parameters such as the elastic modulus, E , and the shear modulus, G , are either constants or a function of stress invariants and/or strain invariants. On the other hand, the plastic strain increment is estimated by the following two concepts of flow/incremental theory of plasticity for perfect plastic materials:

1. The existence of a yield surface that is yield criteria.
2. Flow rule that determinates the general form of the stress to the incremental plastic strain relationship.

3.3.2.1 Yield criteria

Yield criteria define the stress conditions over which plastic deformation will occur for a material element and also separate zones of elastic behaviour from those of elastic-plastic behaviour. Stress paths within the yield surface result in pure recoverable deformations, while paths that intersect the yield surface produce both recoverable and permanent deformations (plastic strains). In general, the initial yield function f (or criterion) can be written down as:

$$f(\sigma_{ij}) = f_c \quad (3.2)$$

where f_c is a constant value for a perfect plastic material.

In a biaxial stress space, the yield surface for a perfect plastic material is fixed, and plastic deformation occurs only when the stress path moves on the yield surface (See Fig. 3.2).

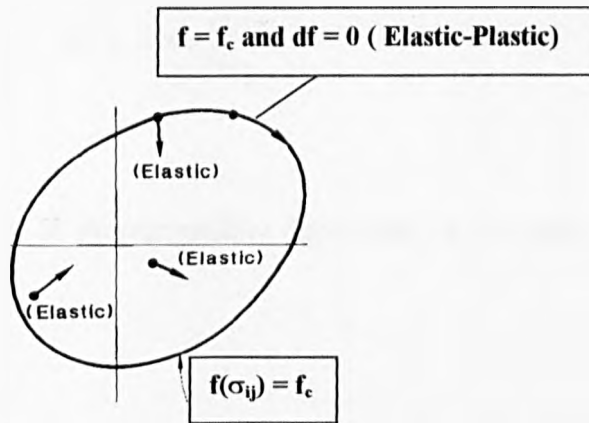


Fig. 3.2 Yield surface of a perfect plastic material (From Chen⁶⁵)

Thus, the loading condition for plastic flow is given by:

$$f = f_c \quad \text{and} \quad df = \frac{\partial f}{\partial \sigma_{ij}} d\sigma_{ij} = 0 \quad (3.3)$$

If the new state of stress is within the elastic domain after an increment of stress, the material is in elastic state, that is:

$$f < f_c \quad (3.4)$$

3.3.2.2 Flow rule

The flow rule is related to the relationship between the next increment of the plastic strain increment $d\varepsilon^{p}_{ij}$, and the present state of stress σ_{ij} for a yielded element subjected to further loading. This relationship is established by the concept of plastic potential function Q . According to the theory of plasticity, the direction of the plastic strain increment is defined by the plastic potential function Q in the form:

$$d\varepsilon^{p}_{ij} = d\lambda \frac{\partial Q}{\partial \sigma_{ij}} \quad (3.5)$$

where $d\lambda$ is a positive scalar of proportionality dependent on the state of stress and load history.

If the potential and yield surfaces coincide with each other ($f = Q$), the flow rule is called the associated type, otherwise it is the non-associated type. From equation (3.5), we can find that the direction of the plastic strain increment vector, $d\varepsilon^{p}_{ij}$, is normal to the surface of plastic potential Q at the current stress point, σ_{ij} . This normality condition is displayed in Fig. 3.3.

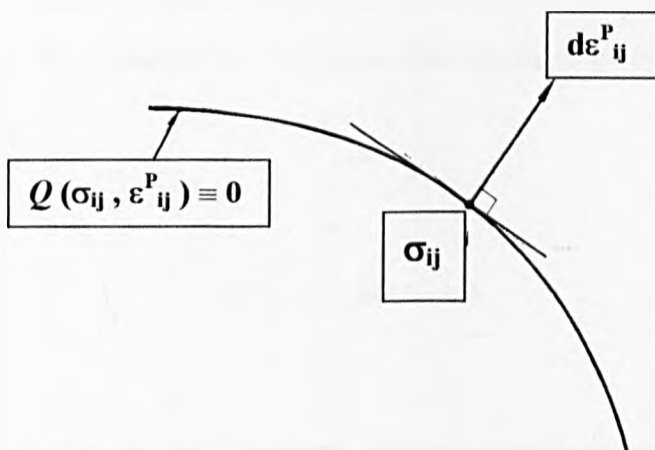


Fig. 3.3 Representation of flow rule (From Chen⁶⁵)

3.3.2.3 General nature of plastic theory

The irreversible character of plastic deformation implies that the work done by stress on the change of plastic strain is positive. Suppose a unit volume of perfect plastic

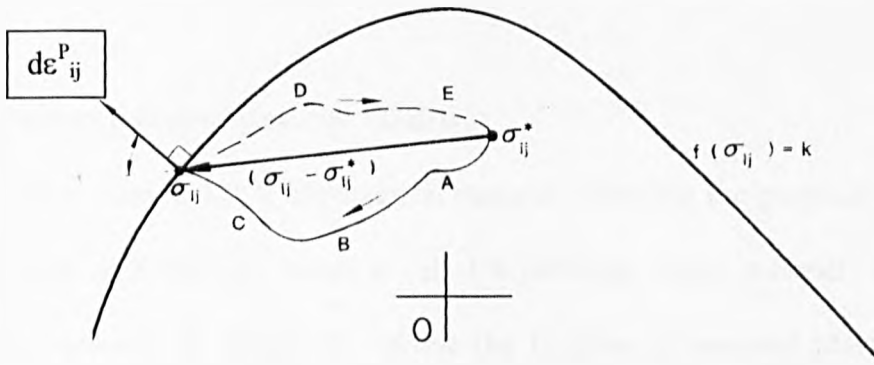


Fig. 3.4 Stress path produced by an external agency (From Chen⁶⁵)

material subjected to a homogeneous state of stress σ_{ij}^* on or inside the yield surface (see Fig. 3.4).

In Fig. 3.4, all purely elastic changes are completely reversible and independent of the path from σ_{ij}^* to σ_{ij} and return to σ_{ij}^* , all the elastic energy is recovered. The plastic work done by the external load on this loading and unloading cycle is the scalar product of the stress vector $(\sigma_{ij} - \sigma_{ij}^*)$ and the plastic strain increment vector $d\epsilon_{ij}^p$. It is obvious that:

$$(\sigma_{ij} - \sigma_{ij}^*)d\epsilon_{ij}^p \geq 0 \quad (3.6)$$

The positive scalar product requires an acute angle between the stress vector $(\sigma_{ij} - \sigma_{ij}^*)$ and the plastic strain increment vector $d\epsilon_{ij}^p$. As the plastic strain increment

vector $d\varepsilon^{P_{ij}}$ is normal to the yield surface if the normality condition for plastic flow is taken, and since equation (3.6) must be satisfied for all stress vectors, $(\sigma_{ij} - \sigma^*_{ij})$, this condition requires that the yield surface be convex. The normality condition for the plastic strain increment vector $d\varepsilon^{P_{ij}}$ and the convexity property of the yield surface imposed on the plastic stress-strain relations are of general nature for plastic theory.

3.3.3 Perfectly Plastic Material Models

As stated in section 3.2, a hypothetical material exhibiting the property of continuing plastic flow at a constant stress is called a perfectly plastic material. Similar to the historical account in section 3.1 about the theories of classical plasticity and soil plasticity, the Coulomb failure criterion¹¹⁰ is a well know perfectly plastic material model in soil mechanics. This criterion was proposed in 1773 for geo-technical materials much earlier than the Tresca and von Mises yield criteria for metals, and it is the first type of failure criterion to take into account the effect of the hydrostatic pressure on the strength of granular materials.

The first proposed yield criterion for metals is known as the Tresca criterion¹¹⁶ (or the maximum shear stress criterion) dating back to 1864, and thereafter. Von Mises, in 1913, introduced a new yield criterion for metals that is more convenient for numerical solutions than the Tresca criterion. This yield criterion condition is known as the von Mises criterion. In 1928, von Mises¹²¹ used this criterion and developed a constitutive relation based on the normality concept that relates the plastic strain rate to the yield surface.

On the other hand, the concept of perfect plasticity based on the Coulomb criterion, the Tresca criterion, and the von Mises criterion has been used broadly in the conventional soil mechanics to assess the collapse load in stability problems. Drucker and Prager³⁶, in 1953, discussed a modified Tresca yield criterion as well as an extension of the von Mises yield criterion that included the hydrostatic component of the stress tensor. The extension of the von Mises yield criterion is the Drucker-Prager perfectly plastic material model (or the extended von Mises model).

The overall picture of these models can be seen in Fig. 3.5.

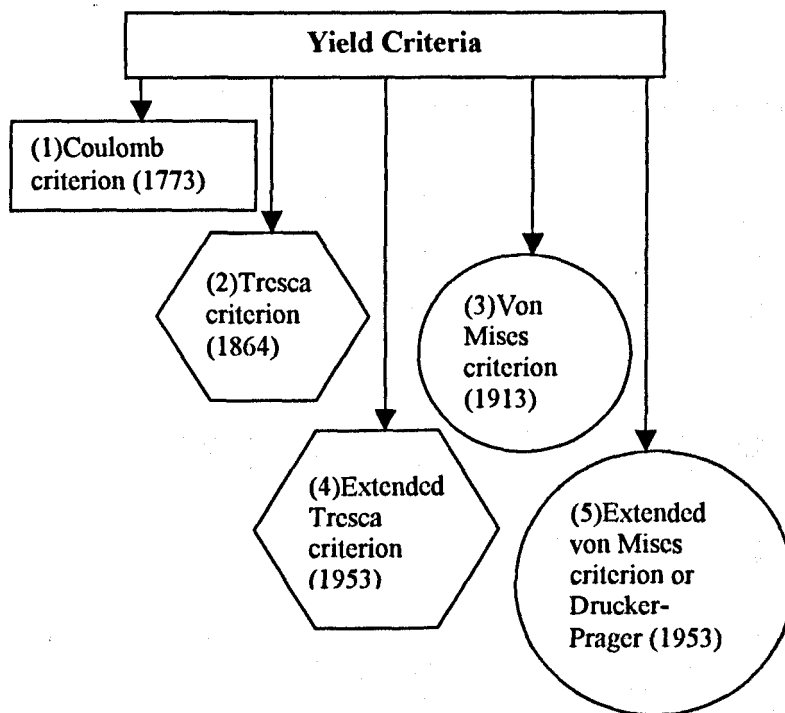


Fig. 3.5 The overall picture of main yield criteria

3.3.3.1 Coulomb model

Coulomb criterion states that failure occurs when the shear stress τ and the normal stress σ acting on any element in the material satisfy the linear equation:

$$\tau = c + \sigma \tan \phi \quad (3.7)$$

where c and ϕ denote the cohesion and the angle of internal friction, respectively. Coulomb criterion in $\sigma - \tau$ space is expressed in Fig. 3.6. For frictionless materials which $\phi = 0$, equation (3.7) reduces to the maximum shear stress criterion of Tresca, $\tau = c$, that is the cohesion becomes equal to the yield stress in pure shear $c = k$.

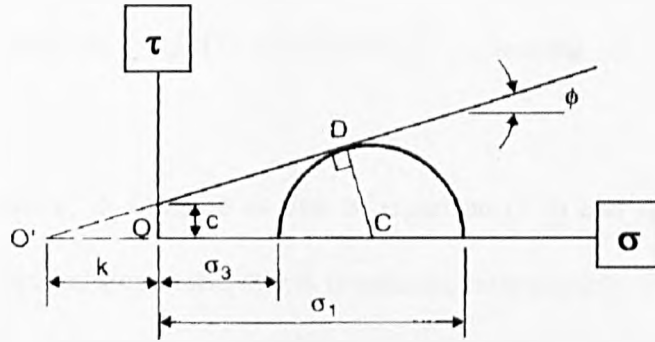


Fig. 3.6 Coulomb yield criterion in σ - τ space (From Smith⁵⁵)

If the condition of stress state is $\sigma_1 > \sigma_2 > \sigma_3$, the Coulomb criterion can be expressed as:

$$\frac{1}{2}(\sigma_1 - \sigma_3) = \frac{1}{2}(\sigma_1 + \sigma_3) \sin \phi + c \cos \phi \quad (3.8)$$

Each principal stress can be represented in terms of $I_1, \sqrt{J_2}, \theta$ (Lode angle) as follow:

$$\sigma_1 = \frac{2}{\sqrt{3}} \sqrt{J_2} \cos \theta + \frac{1}{3} I_1 \quad (3.9)$$

$$\sigma_2 = \frac{2}{\sqrt{3}} \sqrt{J_2} \cos\left(\theta - \frac{2}{3}\pi\right) + \frac{1}{3}I_1 \quad (3.10)$$

$$\sigma_3 = \frac{2}{\sqrt{3}} \sqrt{J_2} \cos\left(\theta + \frac{2}{3}\pi\right) + \frac{1}{3}I_1 \quad (3.11)$$

Therefore, from equations (3.8), (3.9), (3.10) and (3.11) the Coulomb criterion can be expressed by stress invariant as:

$$I_1 \sin \phi + \frac{1}{2} \left[3(1 - \sin \phi) \sin \theta + \sqrt{3}(3 + \sin \phi) \cos \theta \right] \sqrt{J_2} - 3c \cos \phi = 0 \quad (3.12)$$

where θ is Lode angle, c , ϕ is same as that of equation (3.7) and I_1 , J_2 is the first stress invariants, the second deviatoric stress invariants, respectively. Equation (3.12) represents an irregular hexagonal pyramid (Fig. 3.7) in the principal stress space whose cross-sectional shape on the π -plane is an irregular hexagon.

Even though the Coulomb criterion is certainly the best-known failure criterion in soil mechanics and generally simple in two-dimensional graphical form, the Coulomb model exhibits corners or singularities in three-dimensional generalization. Some difficulties in numerical modelling cannot be avoided as the general yield or failure function with singularities. In addition to this limitation, the Coulomb criterion neglects the influence of intermediate principal stress on shear strength. Nevertheless, the Coulomb criterion is the first type of failure criterion that takes into consideration the effect of the hydrostatic pressure on the strength of granular materials, and has in the past been well established for important and practical soils problem to obtain reasonable solutions.

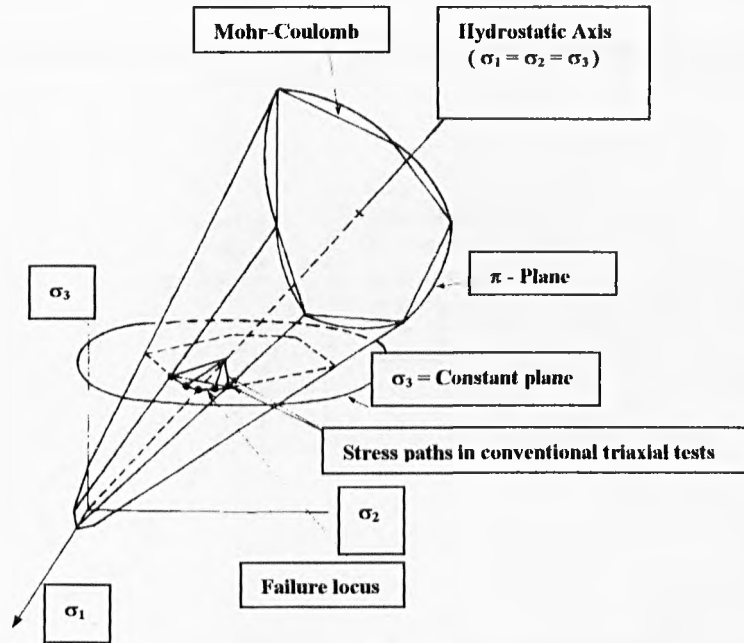


Fig. 3.7 Coulomb failure criterion in the principal stress space (From Yong⁵⁷)

3.3.3.2 Extended von Mises model

Since the von Mises yield criterion is mainly used for metal which yield strength is insensitive to the hydrostatic pressure, it is not suitable for stability problems in soil mechanics. To consider the hydrostatic pressure effect on soil strength, the von Mises criterion can be extended to so-called extended von Mises criterion as follows:

$$\frac{\sqrt{J_2}}{I_1 + c_3} = c_4 \quad (3.13)$$

or in the form of Drucker-Prager model as follows:

$$\alpha I_1 + \sqrt{J_2} = k \quad (3.14)$$

where I_1, J_2 are same as that of above the Coulomb's model, c_3, c_4, α and k are constants, in which the constants α and k relates to the Coulomb's material constants

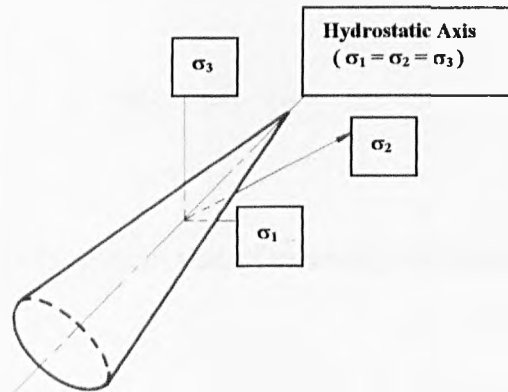


Fig 3.8 Extended von Mises yield criterion for soils (From Chen⁶⁵)

c and ϕ in several ways, as described later. Equation (3.13) or (3.14) represents a right circular cone in three-dimensional principal stress space, as be shown in Fig. 3.8, which intersection of the π -plane is a circle. It is obvious that equation (3.14) is a special case of equation (3.12) when the Lode angle $\theta=0$.

3.3.3.3 Drucker-Prager model

As presented in section 3.3.3.2, Drucker-Prager model is also called extended von Mises model, and was first proposed by Drucker and Prager in 1953 to describe the internal cone in applying the limit theorems to perfectly plastic soils. For practical application, a smooth surface is often adopted to approximate the Coulomb yield surface with singularities in elastic-plastic Finite Element analyses. The Drucker-Prager perfect plastic model is the first attempt to approximate the well-known Coulomb criterion by a simple smooth function. This criterion, which neglects the influence of J_3 on the cross-sectional shape of failure surface, is represented by a

simple stress invariant function of the first invariant of stress tensor, I_1 , and the second invariant of deviatoric stress tensor, J_2 , together with two material constants α and k . It has the simple form:

$$f = \alpha I_1 + \sqrt{J_2} = k \quad (3.15)$$

where the constants α and k is same as that of extended von Mises model.

The yield or failure surface of equation (3.15) in the principal stress space depicts a right-circular cone with the symmetry about the hydraulic axis as shown in Fig. 3.9. If α becomes zero, equation (3.15) reduces to the von Mises yield criterion for metal.

In the three dimensional stress space, the Drucker-Prager criterion can be matched with the apex of the Coulomb criterion for either point A or B on its π -plane as shown in Fig. 3.10.

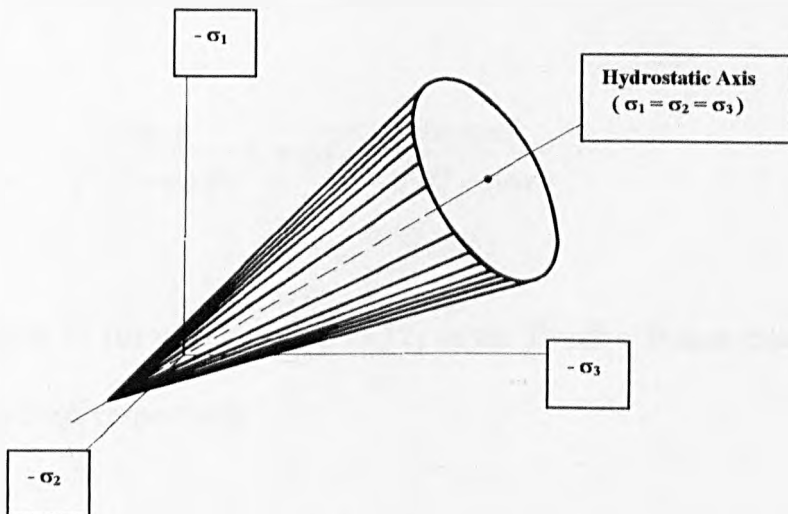


Fig. 3.9 Drucker-Prager failure criterion for soils (From Chen⁶⁵)

For point A case, the cone circumscribes the hexagonal pyramid. A compressive meridian line element connecting the apex O with the point A contains the same line

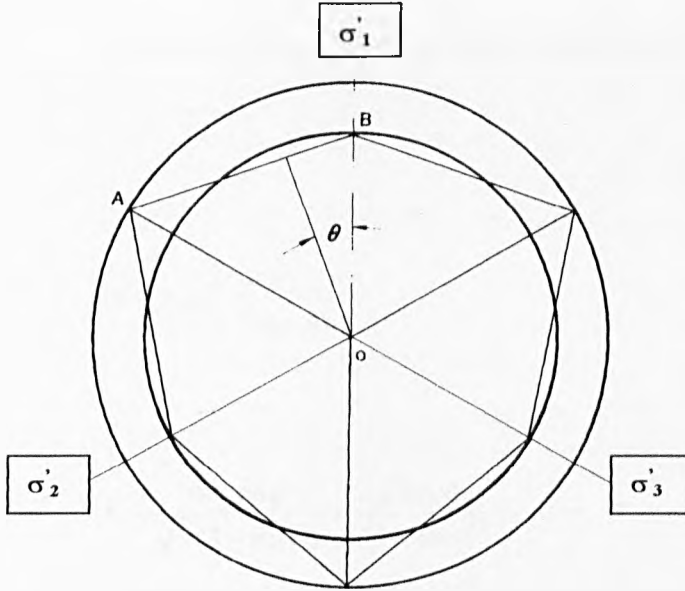


Fig. 3.10 Drucker-Prager & Coulomb yield criterion on the π -plane (From Chen⁶⁵)

for both criteria. So, the relations between α , k , and c , ϕ can be found. Substituting $\theta = \pi/3$ into equation (3.12), the line element OA is governed by:

$$\frac{2 \sin \phi}{\sqrt{3}(3 - \sin \phi)} I_1 + \sqrt{J_2} = \frac{6c \cos \phi}{\sqrt{3}(3 - \sin \phi)} \quad (3.16)$$

Comparing equation (3.16) with equation (3.12) of the Drucker-Prager criterion, the parameters α and k are, respectively:

$$\alpha = \frac{2 \sin \phi}{\sqrt{3}(3 - \sin \phi)} \quad (3.17a)$$

$$k = \frac{6c \cos \phi}{\sqrt{3}(3 - \sin \phi)} = \frac{2\sqrt{3}c \cos \phi}{(3 - \sin \phi)} \quad (3.17b)$$

For the point B case, the corresponding constants for a tensile meridian ($\theta = 0$ degree) are:

$$\alpha = \frac{2 \sin \phi}{\sqrt{3}(3 + \sin \phi)} \quad (3.18a)$$

$$k = \frac{6c \cos \phi}{\sqrt{3}(3 + \sin \phi)} = \frac{2\sqrt{3}c \cos \phi}{(3 + \sin \phi)} \quad (3.18b)$$

For the internal cone of the Drucker-Prager inscribing the Coulomb yield criterion, as shown in Fig. 3.10, the corresponding constants are:

$$\alpha = \frac{\sin \phi}{\sqrt{3}\sqrt{3 + \sin^2 \phi}} = \frac{\tan \phi}{\sqrt{9 + 12 \tan^2 \phi}} \quad (3.19a)$$

$$k = \frac{\sqrt{3}c \cos \phi}{\sqrt{3 + \sin^2 \phi}} = \frac{3c}{\sqrt{9 + 12 \tan^2 \phi}} \quad (3.19b)$$

The Drucker-Prager model has both advantages and shortcomings. It is simple to use and available for computer coding, resulting in gained popularity and for analysing challenging projects, such as the channel tunnel project; it can be matched with the Coulomb model by a set of suitable selection s of constants; limit analysis techniques

can be used with it; and it satisfies the associated flow rule. On the other hand, the Drucker-Prager model exceeds plastic dilatancy at yielding, for instance, the compression cone of the Drucker-Prager approximation over-predicts the strength of soils, whereas the internal cone of it results in equivalent friction angles lower than intended; it can not predict plastic volumetric strain or compaction of soil materials during hydrostatic loading.

An explicit correlation between the Mohr-Coulomb friction angle and the equivalent friction angle produced by circular, such as Drucker-Prager criterion, and other smooth criteria have been established in Griffiths's work⁷⁵, and it was shown that the DP compression cone over-predicts the strength of soils. A comparison using various Drucker-Prager models has been reported by Zienkiewicz¹²², *et al*, for a footing problem, and the important conclusion from this study was that the ultimate bearing capacity might be grossly overestimated depending on the Drucker-Prager cone used.

3.3.3.4 The Drucker-Prager hardening cap model

Drucker *et al.*⁷⁷ first suggested in 1955 that soil might be treated as a work hardening or strain-hardening material which may reach the perfectly plastic state. A spherical end-cap was added to the Drucker-Prager model in order to control the plastic dilatancy of soil. The innovative idea of the spherical cap fitted to the cone of the Drucker-Prager model made a major step to more realistically represent soil behaviour. As the soil strain-hardens, both the cone and cap expand. The innovation of a cap model introduces the use of current soil density as the strain hardening parameter to determine the successive loading surfaces for a particular value of soil

density. Such successive surfaces are all geometrically similar, but of different sizes for different densities.

With the Drucker-Prager strain hardening cap model, for the elastic-plastic state of soil, the yield criterion is same as that of the Drucker-Prager model expressed by formula (3.15). The cap-hardening function is controlled by I_c , the stress level on the current yield surface. I_c is given by the following equation:

$$I_c = -\frac{1}{D} \ln \left(1 - \frac{\varepsilon_V^P}{W} \right) + I_c^0 \quad (3.20)$$

where I_c^0 is the stress level on the initial yield surface, ε_V^P is the plastic volumetric strain of soil, and D, W are material parameters determined by soil tests¹⁰.

3.4 Summary

The theory of perfectly plasticity is the simplest type of flow theory. An existing yield surface $f(\sigma_{ij})$ is postulated for elastic-perfectly plastic materials in the development of stress-strain relations. Each stress point inside the fixed surface represents an elastic state of stress and each stress point on the yield surface expresses a plastic state. The strain in the plastic state is assumed as the sum of the reversible elastic strain and the permanent plastic strain. Plastic flow occurs when $f = 0$ and $df = 0$, which is used as the criterion for loading for a perfectly plastic material. During loading, both elastic and plastic strain occurs. Plastic flow is developed along the exterior normal of the fixed yield surface, that is, the normality principle for the associated flow rule material.

Perfect plasticity models such as the best-known failure model—the Coulomb criterion is well established for hydrostatic pressure sensitive soils. However, it is not mathematically convenient in three-dimensional modelling situation owing to the existence of corners. The Tresca and von Mises criteria for metals are used for determining the collapse or limiting state of a structure, but can not describe the shear strength of soils except the total stress analysis of saturated undrained soil of clay type. The extended Tresca and extended von Mises criteria consider the effectiveness of mean normal stress, but the former still has the disadvantage of singularities. The latter, also called the Drucker-Prager model, is the simplest perfectly plasticity model approximating the well-known failure criterion—the Coulomb model. The Drucker-Prager model may give reasonable results for progressive failure analysis of soil, with adequate assumption of the material constants, α and k for the particular problems.

Chapter 4

Case Study for Two-Dimensional Validation

4.1 Introduction

As the final target of this project is to numerically model the soil deformation between outer sole of the footwear and the soft surfaces of ground using FEM, to determine the limit loading condition which causes plastic failure of soil mass, and to judge which kind of tread pattern of military boots displays the best performance of traction forces, it is necessary to certify if the ANSYS—University High Option Finite Element software supported at Salford University is valid for numerical modelling soil problems regarding the use of the Drucker-Prager material model inherently embedded in the ANSYS software. For the necessity as mentioned above, we must study it step by step from simple two-dimensional soil problems by FE numerical modelling.

As the issue of footwear and soft ground surfaces interaction is mainly associated with earth pressure problems, so a two-dimensional numerical modelling case for earth pressure problem published works by Schweiger³⁵ is selected for validation. For the first stage, we use the ANSYS software to conduct two-dimensional finite element model construction, applying loading conditions and nonlinear numerical modelling of this sort of plane strain situation with the exact same geometry sizes, soil properties, material model—Drucker-Prager model and loading conditions as that of selected case. Then the numerical modelling results are compared to that of hand calculation using typical earth pressure theory as it has been widely used and cited,

and at the same time to numerically model results by Schweiger on the use of Drucker-Prager model supported in another different software³⁵ (TDV, Graz, Austria).

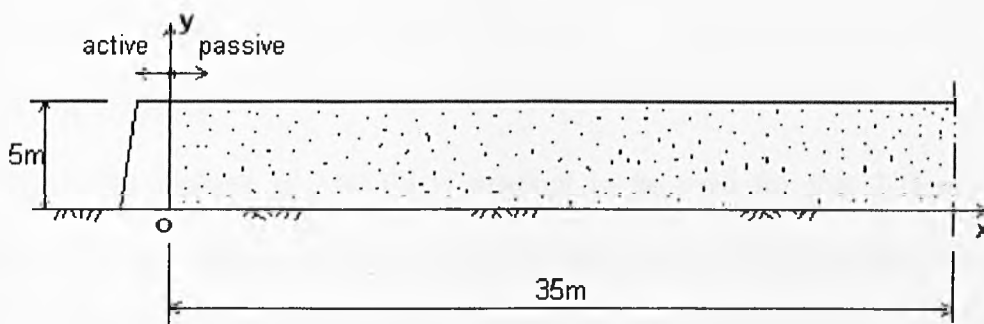
4.2 Background of Drucker-Prager Material Model in ANSYS Software

Through the literature survey and plasticity theory studied in detail, we understand and become focused on the topic of perfect plasticity theory and theoretical models based on it, as we are interested in limit load conditions when plastic failure of the soil mass occurs. So, what is the condition, when plastic failure of soil mass happens under vertical loading and transverse loading conditions acted by tread pattern and the outer-sole of footwear. The Drucker-Prager nonlinear material model having been embedded in the ANSYS finite element software supplied an effective means to carry out this research.

The Drucker-Prager model in ANSYS is applicable to granular (frictional) material such as soils, rock, and concrete and uses the outer cone (compressive cone) approximation to the Mohr-Coulomb law. This option uses the Drucker-Prager yield criterion with either an associated or non-associated flow rule. The yield surface does not change with progressive yielding, hence there is no hardening rule and the material is elastic-perfectly plastic. The Drucker-Prager yield criterion is a modification of the von Mises yield criterion that accounts for the influence of the hydrostatic stress component. The higher the hydrostatic stress, the higher the yield strength. The Drucker-Prager yield surface is a circular cone with the Mohr-Coulomb material parameters chosen such that it corresponds to the outer aspires of the hexagonal Mohr-Coulomb yield surface, that is, it is the compressive cone in ANSYS software same as that governed by equations (3.16), (3.17a) and (3.17b).

4.3 Two-Dimensional Validation for Earth Pressure Problems on the Use of Drucker-Prager in ANSYS

For this two-dimensional case study, earth pressure problems are simulated under plane strain conditions. Loading conditions are acted on by applying prescribed horizontal displacements to a rigid wall in left front of a soil mass. The soil mass is subjected to initial stresses. A general picture of this earth pressure problem is shown in Fig. 4.1. Only a translation of the wall is considered for this validation. The wall is assumed to be smooth, that is, no friction. Geometric nonlinearity is not taken into account i.e. small strains have been considered.



Soil parameters:

$E = 75000 \text{ kPa}$	{ E — Young's modulus }
$\nu = 0.3$	{ ν — Poisson's ratio }
$\gamma = 18 \text{ kN/m}^3$	{ γ — Bulk unit weight }
$\phi = 30^\circ$	{ ϕ — Friction angle }
$c = 0.1 \text{ kPa}$	{ c — Cohesive strength }

Fig. 4.1 Typical earth pressure problem

4.3.1 Soil Properties

The soil material parameters are chosen to be the same as that of published works by Schweiger³⁵ except the cohesive strength, see also in Fig. 4.1. Cohesion values in both cases are originally considered as zero. However, the inputting requirement of the

cohesion value in ANSYS must not be zero, otherwise, the numerical modelling can not proceed further. So, a relative small value, 0.1, close to zero is selected to be the approximation of the cohesive strength of model by Schweiger³⁵. Three material constants of Drucker-Prager non-linear material model in ANSYS are inputted:

- The cohesion value (= 0.1)
- The angle of internal friction (= 30°)
- The dilatation angle (= 30°)

For this case, the dilatation angle is equal to the friction angle, which means the flow is associative.

4.3.2 Meshing Scheme

4.3.2.1 The elements

The PLANE82 element in ANSYS is selected to be used for this 2-D numerical modelling of soil structure. The PLANE82 element is a 2-D 8-node structural solid element. It is a higher order version of the two-dimensional, four-node element (PLANE42) and provides more accurate results for mixed automatic meshes and can tolerate irregular shapes without as much loss of accuracy. The 8-node elements have compatible displacement shapes and are well suited to model curved boundaries. The 8-node element has two degrees of freedom at each node: translations in the nodal x and y directions. The element has plasticity, creep, swelling, stress stiffening, large deflection, and large strain capabilities and can be used as a plane element (plane stress or plane strain) or as an axis-symmetric element.

4.3.2.2 The plane strain

In the case of analysis of dams, foundations, cylinders and retaining walls, the boundaries are not clearly defined in the longitudinal direction (z direction), and whose geometry shapes and loading do not vary significantly in the length direction. Therefore, a unit slice or a cross section of these long bodies can be considered for idealization and analysed as a plane strain problem and the dependent variables are therefore to be functions of only the x and y coordinates in two-dimensional stress-strain space, provided the cross section of the body is away from the ends of the body. So, the two-dimensional case validation of earth pressure problem in our studies is simulated under plane strain conditions.

4.3.2.3 The meshing

4 key points, 4 lines, 1 area, 981 nodes and 300 equivalent eight-node PLANE82 elements are created and shown in Fig.4.3.

Normally, the size of elements influences the convergence of the solution. The final solution is expected to be more accurate if the size of the elements is small or the number of elements is large. Even though the use of elements of smaller size traditionally means more computational time and cost, Nowadays fast and remarkable advancement in both “hardware” and algorithm of computing technology has greatly reduced the sensitivity of rising computational time and cost resulting from using a finer meshing scheme.

Comparing to an example of meshing scheme in a paper reported by Clough and Duncan⁷ in 1971, as shown in Fig. 4.2, the average meshing density shown in Fig. 4.3 is much finer than that of Fig. 4.2. However, there is no costing computational time

met even though by using a usual desktop PC.

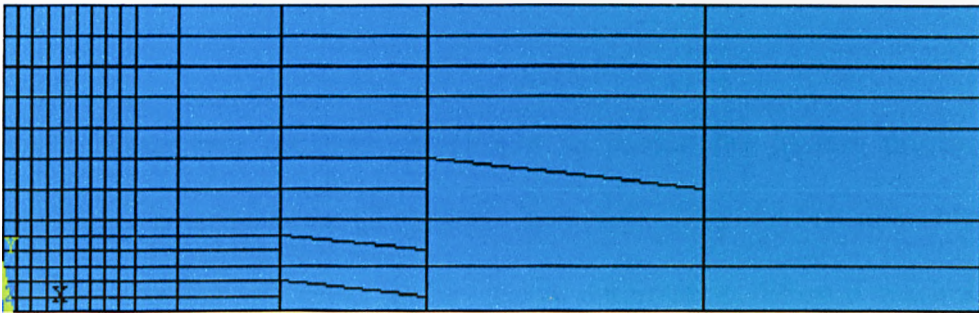


Fig. 4.2 Meshing scheme of 2-D retaining wall reported by Clough and Duncan⁷

4.3.3 Boundary Conditions

4.3.3.1 Constraints

For this two-dimensional earth problem, boundary conditions were applied to this model on bottom and right ends, the top is left free of any constraints, the left ends is left to be applied by loading conditions. The constraints on the right ends are supposed to be on rollers as shown in Fig. 4.3, i.e. the horizontal movement has to be restrained and vertical movement is not constrained. The bottom boundary is constrained only against vertical movement.

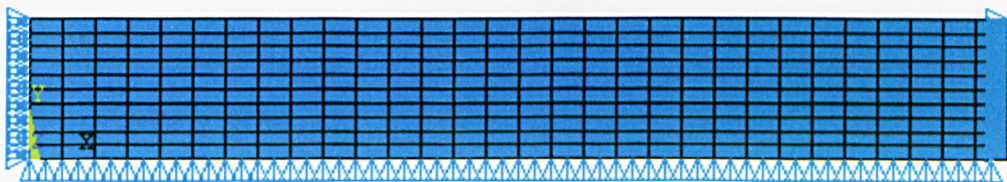


Fig. 4.3 Boundary and loading conditions of 2-D earth pressure problems

4.3.3.2 Loading conditions

As also shown in Fig.4.3, horizontal wall displacements in the positive x direction were applied to left hand side of soil mass at rigid interface between retaining wall and soil mass as a loading condition to simulate effect of passive earth pressure.

The wall displacement necessary is 11.5cm to predict the passive pressure with Drucker-Prager criterion when all elements have yielded for the first time. Increasing the wall displacement will cause further plastic deformation. When it reaches 15cm, the predicted passive pressure by this validation studies will be very close to the results by Schweiger³⁵, see also in section 4.3.5 and 4.3.6 for details.

4.3.4 Initial Stress

4.3.4.1 Introduction

Initial stress was formulated in the geotechnical structure, especially soil structure, owing to natural factors, such as gravity, consolidation, etc. In geotechnical engineering, the initial stress has a significant effect on a structural analysis. Loading initial stress in ANSYS is only allowed in a static or full transient analysis, and the analysis can be linear or nonlinear. In a structure analysis, the initial stress can be applied only in the first load step of this analysis with ANSYS. The user subroutine can be used to input initial stresses. Initial stress can be read from an input file and constant initial stresses can be specified using the command. This initial stress capability is supported by the following element types, such as PLANE42, PLANE82, SOLID45, and SOLID95, etc.

4.3.4.2 Method to calculate initial stress

Initial stress was assumed to act in the soil prior to loading and a FORTRAN routine

was written to produce initial stress file for this model.

The initial stress in vertical direction and horizontal direction are σ_y and σ_x , respectively. They are represented by the following equation:

$$\sigma_y = \gamma(5 - y) = 18000(5 - y) \quad (4.1a)$$

$$\sigma_x = K_0\sigma_y = 0.5\sigma_y \quad (4.1b)$$

where γ is bulk unit weight of soil mass, K_0 is the equivalent initial pressure coefficient and y is the vertical height of soil mass from its bottom.

4.3.4.3 Producing initial stress by FORTRAN programming

A general form FORTRAN routine was created to produce an initial stress file for this model in ANSYS. The sequence of a scheme to produce initial stress for $(n \times n)$ elements of a 2D structure in FORTRAN programme is shown in Fig. 4.4.

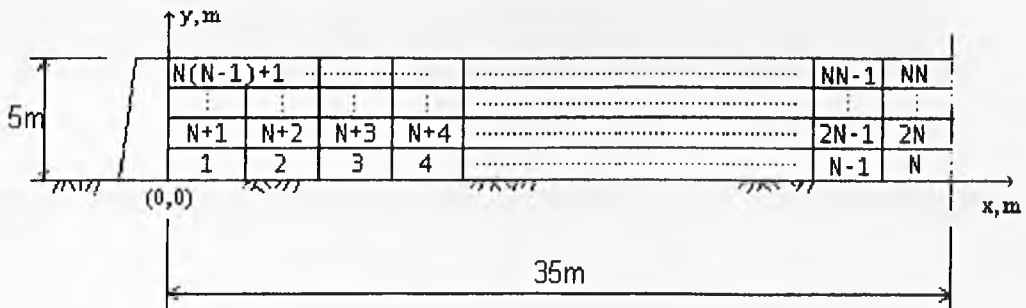


Fig. 4.4 A scheme to produce initial stress

For each PLANE82 element, the initial stress distribution on eight nodes of it in

FORTRAN routine is shown in Fig. 4.5 and the sequence of the nodes' distribution is ruled in counter-clockwise direction, see also in Fig. 4.5.

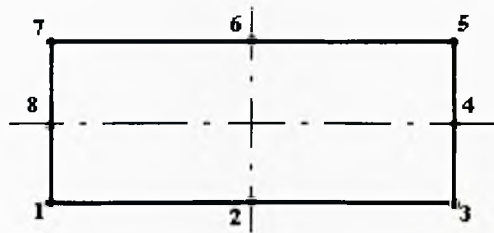


Fig. 4.5 The initial stress distribution sequence on each PLANE82 element

A flow chart of a user subroutine is displayed in Chart 4.1 as follow. The FORTRAN programme is presented in Appendix I.

4.3.4.4 Initial stress effect

The initial stress effect on the soil mass is shown in Fig. 4.6. As seen in Fig. 4.6, the deformation due to initial stress is significant. About 95% regions of the whole soil

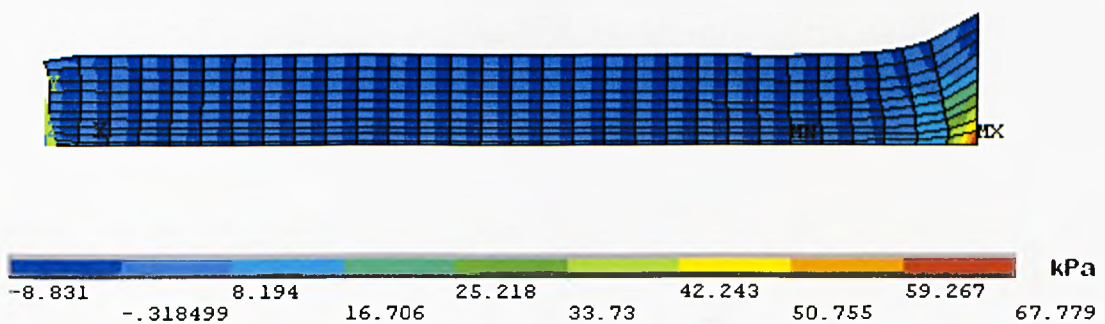


Fig. 4.6 The initial stress (Y-direction) effect on the soil mass

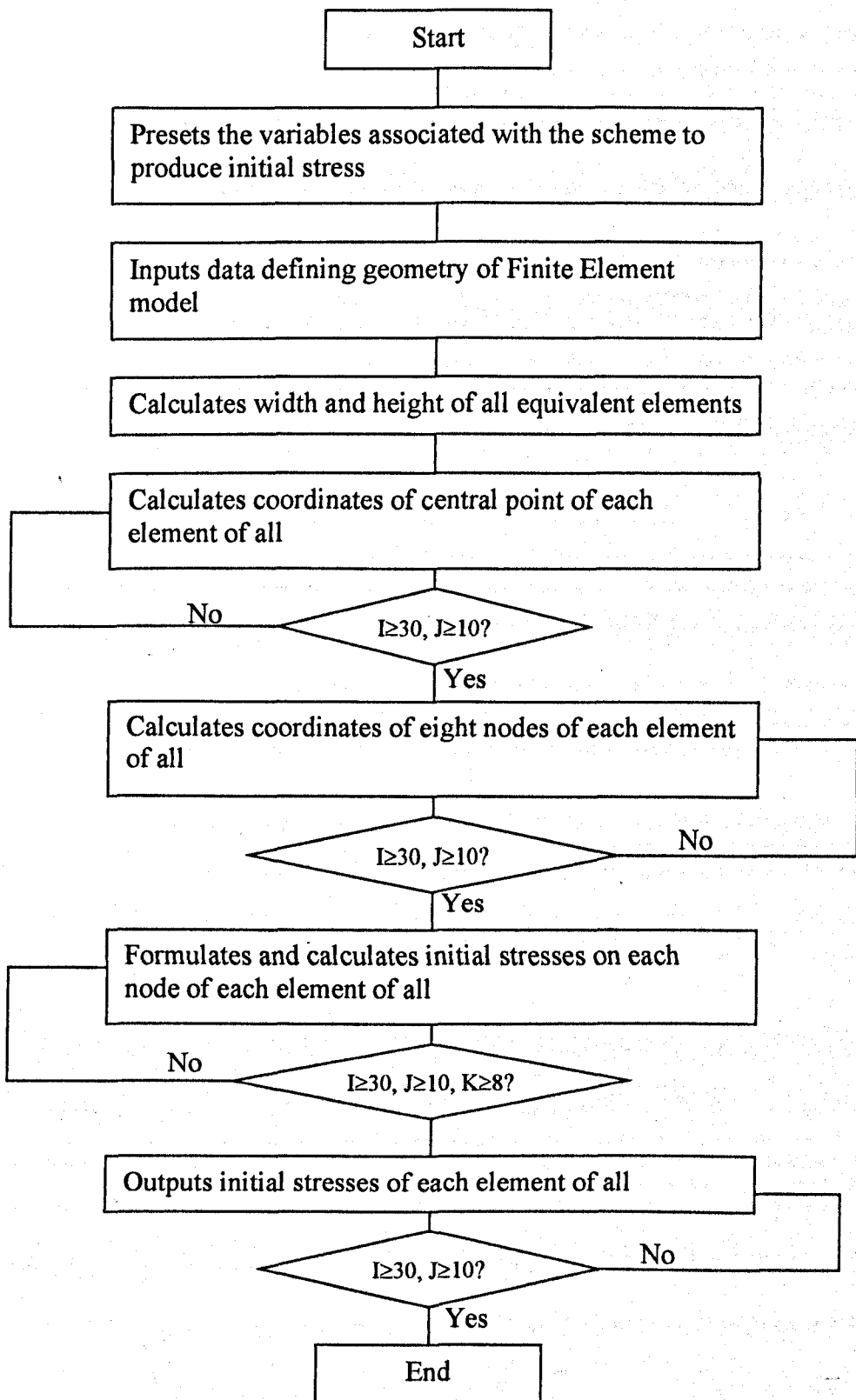


Chart 4.1 Flow chart of a user subroutine of producing initial stress

mass are in compressive state in the Y-direction. The soil deformation at location close to upper right ends is gradually decreased in the Y direction. The reason of this is due to influence of constraint condition applied at right ends. Even though vertical movement is not constrained at right ends, constraints in the X direction could still interfere soil deformation in the Y direction. The initial stress in the X-direction is distributed in two main regions, the upper half part of the soil mass is in compressive state and the lower half part of the soil mass is in tensile stresses. This can be explained that the soil element in the upper half part of the soil mass is subjected to compressive pressure in both X and Y directions as the effect of gravity is not significant as the depth is less than half of height of soil mass. The lower part of soil is subject to higher compressive pressure in Y direction as deeper depth, and the soil element is tend to expand in the X direction under tensile stresses.

4.3.5 Numerical Modelling Results

After initial stress was acted on the soil mass, the loading condition—wall displacement was applied, the model solved and a non-linear convergent solution was obtained. A series of solutions were obtained for different loading conditions (wall displacements). Numerical modelling results under 0.15m wall displacements are shown in Fig. 4.7.

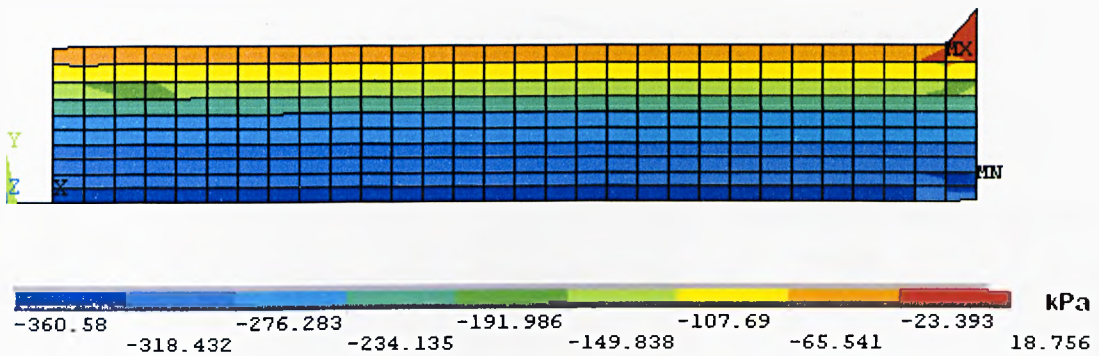


Fig. 4.7 Earth pressure distribution in 0.15m wall movement

4.3.6 Results Analysis and Conclusions

As shown in Chart 4.2, Chart 4.3 and Chart 4.4 by referring Fig. 4.1, we can find that both earth pressure values with Drucker-Prager model used by both in ANSYS and Schweiger's work³⁵ are higher than theoretical limit of typical theory (Coulomb criterion).

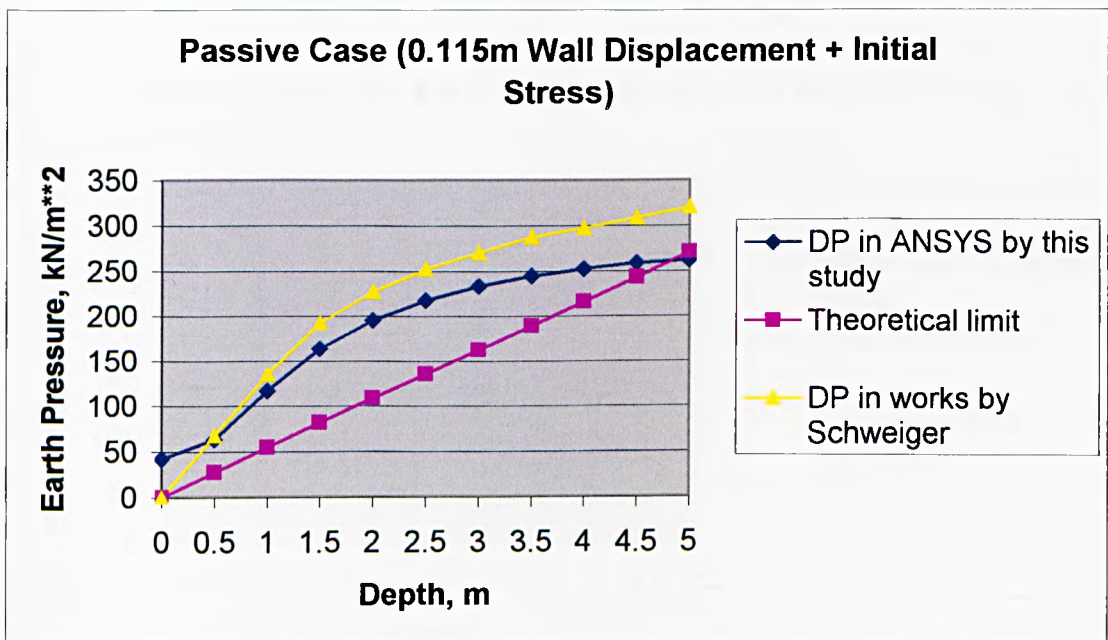


Chart 4.2 Earth pressure with 0.115m wall displacement

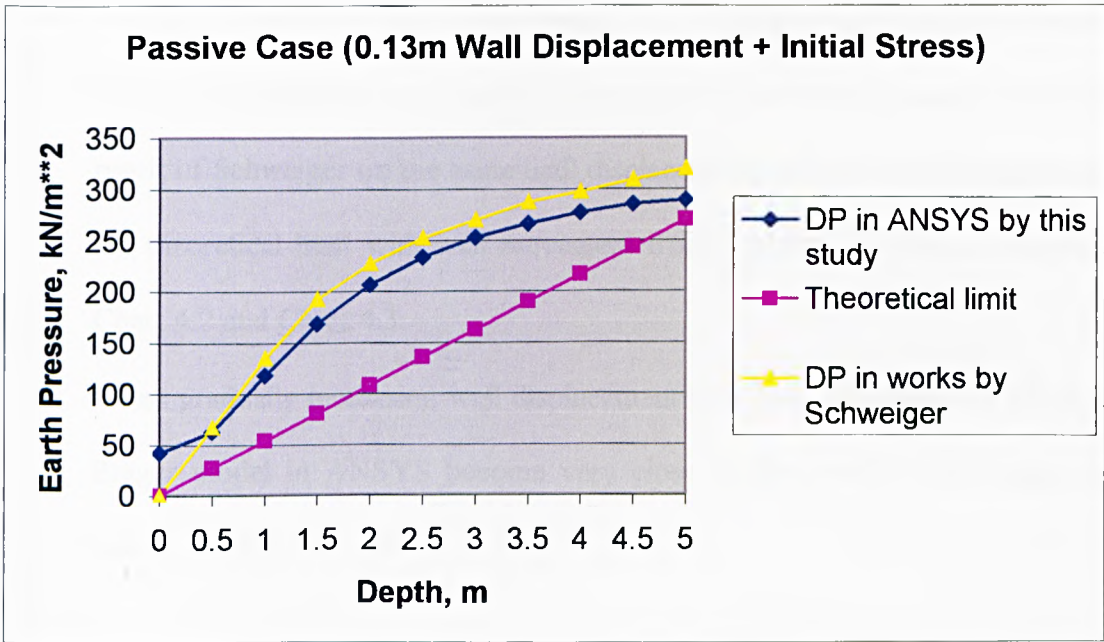


Chart 4.3 Earth pressure with 0.13m wall displacement

From various comparison charts of numerical modelling results conducted by us, it shows that:

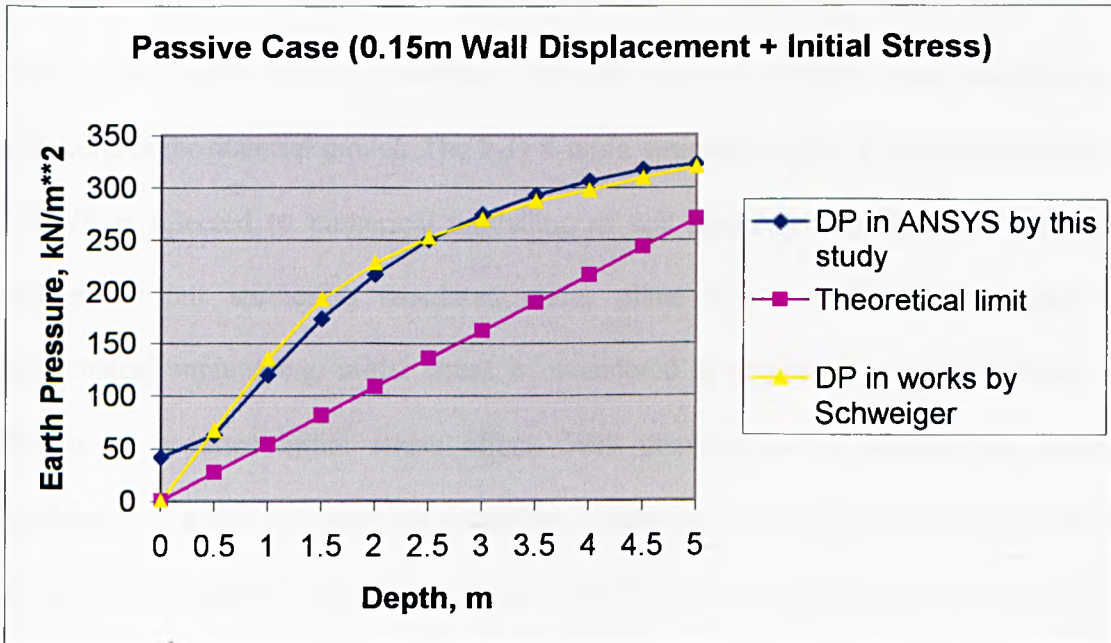


Chart 4.4 Earth pressure with 0.15m wall displacement

- For $U_y = 0$ (Bottom of soil mass) and $U_x = 0$ (Right-hand side of soil mass) boundary constraints, the results of our study has a better agreement with the result of Schweiger on the same wall displacement, but the latter is higher than the theoretical limit with wall movement from 0.115m to 0.13m as shown in Chart 4.2 and Chart 4.3.
- When gradually increasing wall displacement to 0.15m, the results of Drucker-Prager model in ANSYS become very close to the result of Schweiger, as shown in Chart 4.4.

From the result analysis, we can reach a conclusion that two-dimensional validation of numerical modelling earth pressure problem in ANSYS is successful, that is, ANSYS software is suitable for two-dimensional numerical modelling with soil material.

4.4 Summary

Two-dimensional validation was focused on a case study reported by Schweiger³⁵ about typical earth pressure problems. The soil material properties are simulated by Drucker-Prager material model. The 2-D 8-node structural solid PLANE82 element in ANSYS is selected to numerical modelling of soil structure and this earth pressure problem in our studies is simulated under plane strain conditions. As usual in geotechnical engineering, initial stress is considered in this study and user routine is created to produce initial stress effect. Wall displacement is applied as loading conditions. A series of numerical modelling results shows that good agreement with works of Schweiger³⁵ has achieved and ANSYS software is applicable to 2-D FE numerical modelling for soil problems.

Chapter 5

Case Study for Three-Dimensional Validation

5.1 Introduction

We have successfully conducted a two-dimensional validation about numerical modelling for earth pressure problems on the use of Drucker-Prager failure criterion comparing the modelling results to hand calculating results using typical theory of lateral earth pressure, and the results reported by H. F. Schweiger. So we are confident in the effectiveness of the commercial package—ANSYS in numerical modelling for two-dimensional soil structure failure issue. Therefore, we can continue to undergo validation of numerical modelling for more complex soil structure failure problems in three-dimensions with ANSYS FE commercial package, comparing to the results of published works, so as to make sure that ANSYS FE commercial package is available to model soil failure problem in three-dimensional situation.

Numerical modelling methods have become a standard tool for analysing complex problems in geo-technical engineering and in agricultural soil ploughing process. After an initial literature survey in the domain of soil-tillage tools interaction, soil-wheel interaction and soil-structure interaction, etc., we concentrated on the studies of finite element modelling for three-dimensional soil-tillage problems in more depth.

The Finite Element Method is being widely used to investigate the soil tillage process. This method is employed to evaluate soil stress distribution, soil deformation, positions of soil failure and the effects of tool's horizontal draught forces and vertical uplift forces, etc. For instance, Yong and Hanna² conducted their finite element

modelling for cutting of a clay soil with simple tillage tool by adopting the non-linear curve-fitting approach considering the soil as elastic material; Chi and Kushwaha⁷⁶ reported that the hyperbolic formulate were used to simulate the behaviour of soil in the FE modelling. In FE numerical modelling, many of constitutive elastic-perfectly plastic material models such as the Drucker-Prager, critical state and cap models, etc. were employed to simulate soil behaviour either in practical applications or in theoretical research due to its simplicity. For example, Mouazen and Nemenyi¹²³ proposed a sandy loam soil to be simulated as an elastic-perfectly plastic material, and the Drucker-Prager material model was employed in the FE numerical modelling; Araya and Gao¹⁰ carried out three-dimensional FE modelling of subsoiler cutting with pressurised air injection. In their study, the Drucker-Prager harden material model was used to treat the soil as elastic-perfectly plastic material. The last two examples^{123, 10} will be selected as objects of case study for three-dimensional validation in detail in the following sections.

5.2 Three-Dimensional Validation for Soil-Tillage Problems on the Use of Drucker-Prager Material Model in ANSYS

5.2.1 Three-Dimensional Case 1 Study

First of all, a published paper authored by Mouazen and Nemenyi¹²³ was focused on, which is titled as “APPLICATION OF THE DRUCKER-PRAGER ELASTIC-PERFECTLY PLASTIC MATERIAL MODEL FOR PERFORMING FINITE ELEMENT ANALYSES OF DEEP TILLAGE”. In this reported study, the soil cutting process by medium-deep subsoiler was investigated by conducting a non-linear, three-dimensional finite element analysis.

From the point of view of agricultural production, the quality of soil cultivation is of great importance. Comparing to topsoil, subsoil is also required to be well cultivated. 'subsoil' is explained as 'the layer of earth which is under the surface level' in Cambridge Advanced Learner's Dictionary', as well as 'the stratum of weathered material that underlies the surface soil' as a *noun* dated from 1799, and 'to turn, break, or stir the subsoil of' as a *transitive verb* dated from 1840 in Merriam-Webster Dictionary. 'subsoiler' is a nounal format of the *transitive verb* – 'subsoil'. Obviously, 'subsoiler' is equal to 'tillage tool' in meaning to some extent.

In this published works, the mathematical construction of the Drucker-Prager model was reviewed. An incremental technique was used to deal with the material non-linearity of soil. Inside each step the Newton-Raphson iteration method was applied. In order to study the friction and sliding characteristics of the soil-subsoiler system, two nodes gap elements were placed between soil-subsoiler bodies. The subsoiler was assumed as a rigid body and a three-dimensional FEM mesh was generated for the soil domain in front of the medium-deep subsoiler. From the authors' report, the finite element predictions of subsoiler draught force as well as surface failure dimensions agreed with those measured in a soil bin experiment.

However, this paper¹²³ did not give geometry parameters of three-dimensional finite element model of soil-subsoiler system in detail, so the 3D FE model of soil-subsoiler system of this case study is reconstructed in ANSYS software based upon estimation of geometry parameters of that, and is shown in Fig. 5.1. Since the soil cutting is symmetric about the centric plane ABCD (Fig. 5.1), only one-half of the total region is reconstructed in this case study.

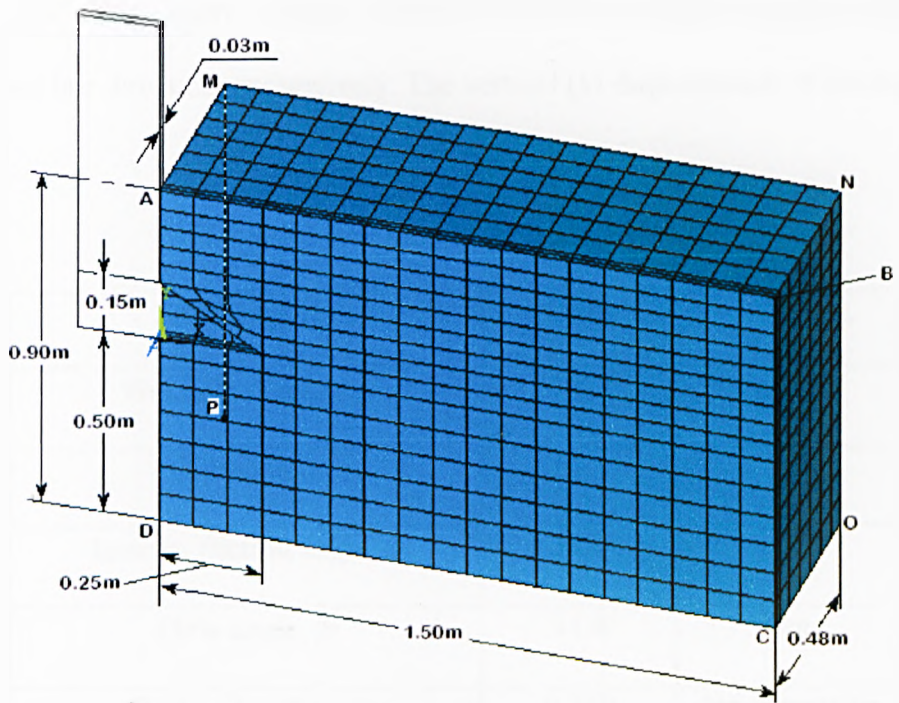


Fig. 5.1 The model of case 1 study by estimated geometry parameters

Eight nodes, linear, isoparametric three-dimensional solid elements, that is SOLID45 element type in ANSYS software, are selected to represent the soil material. The element nodes are located at the corners of the rectangular prism. Each node has three degrees of freedom: translations in the nodal x , y , and z directions. Description of SOLID45 element in ANSYS software is presented in detail in three-dimensional case 2 studies. As shown in Fig. 5.1, the total number of nodes and elements are 2961 and 2158, respectively.

The properties of soil material assigned to this FE model are summarised in table 5.1 and used as input data for FEA modelling in ANSYS software.

Boundary and loading conditions are applied to the meshed FE model. As shown in Fig. 5.1, the front lateral surface ABCD and the rear lateral surface MNOP are constrained in z direction, respectively. The vertical (y) displacement of the bottom

Table 5.1 Soil properties of case 1 study

Soil Property	Value	Unit
Wet bulk density, ρ	1.731	$\text{k}\cdot\text{kg}/\text{m}^3$
Cohesion, c	15.5	kPa
Internal friction angle, ϕ	31.8	deg.
Flow angle, β	31.8	deg.
Poisson's ratio, ν	0.359	No dimension
Young's modulus, E	8067	kPa

surface DPOC is also constrained. The right lateral surface BNOC is constrained against displacement in the x direction. The upper surface ANMB and the left lateral surface AMPD are left free of any constraints. The subsoiler is assumed to be a rigid body, and its Young's modulus is remarkably greater than that of the soil. So, the loading acting on the soil by the subsoiler is prescribed by a uniform horizontal displacement in positive x direction of 15cm for all subsoiler interfacial nodes of soil mass. The total displacement is not divided into many small increments.

Then finite element modelling is successfully conducted. The modelling results of it are presented in Fig. 5.2. Fig. 5.2 displays the soil deformation situation after 15cm

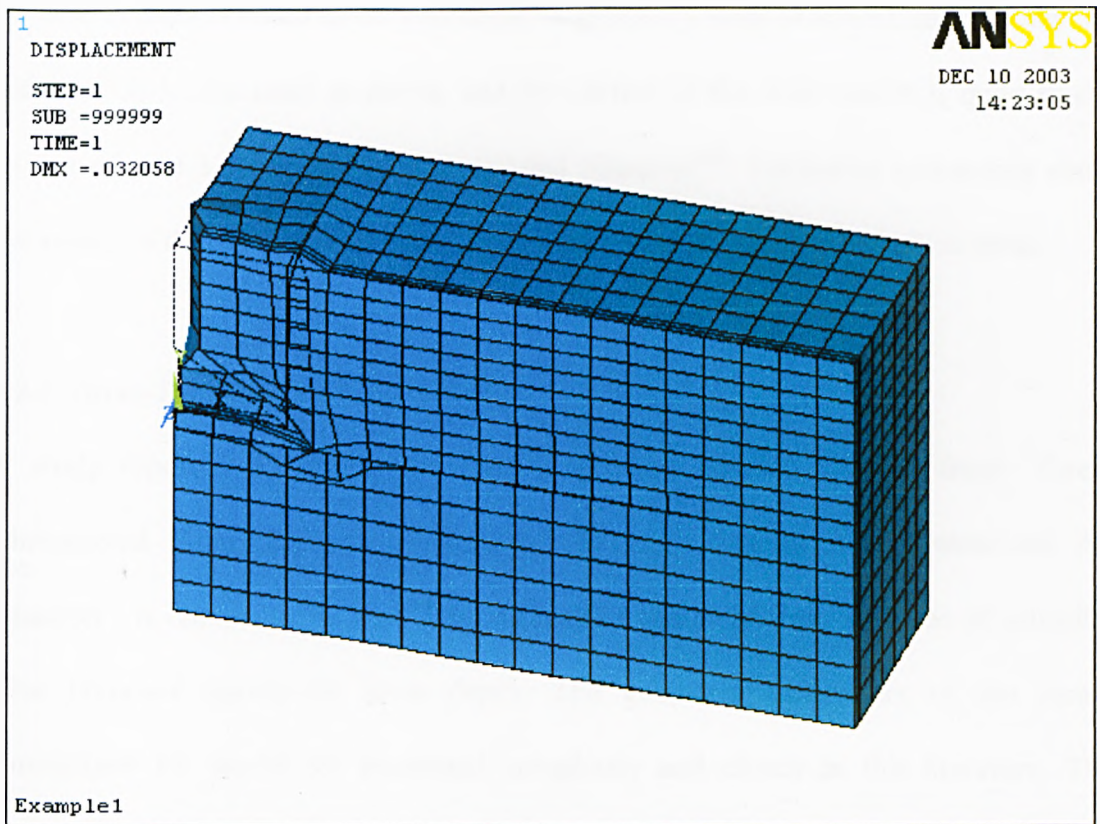


Fig. 5.2 Deformed shape with undeformed edge of case 1 study

horizontal displacement was acted on it as loading conditions. As seen in Fig. 5.2, the soil is deformed to form a wedge-shaped soil upheaval on the soil surface in front of shank of the subsoiler. In the region of above chisel of the subsoiler, in front of the shank, the soil is forced to move upward, forward and sideways comparing to the original position of the subsoiler. The soil below this region experienced small movement except the part of zone in front of the tip of the chisel. The stresses distribution in subsoiler travel direction is complex due to complexity in nature of the type of loading and the tool geometry. Most zones show compressive stresses and few regions display tensional stresses.

As case 1 study is based upon estimation of geometry sizes of soil FE model, only soil deformation is discussed as above, and the pattern of the deformation is quite similar to that of case 1 reported by Mouazen and Nemenyi¹²³. Validation concerning about the aspect of draught force of subsoiler will be conducted in case 2 study in detail.

5.2.2 Three-Dimensional Case 2 Study

A study reported by Araya and Gao¹⁰, which is entitled “A Non-linear Three-Dimensional Finite Element Analysis of Subsoiler Cutting with Pressurized Air Injection”, is chosen to be case 2 for validation about the draught force of subsoiler after literature survey in more depth. The geometry parameters of the three-dimensional FE model are presented completely and clearly in this literature. The mathematical model of soil material in this study is the Drucker-Prager hardening cap model, which is a little different from the Drucker-Prager model adopted in ANSYS software. The Drucker-Prager hardening cap model has been briefly reviewed in the Chapter 3, section 3.3.3.4.

5.2.2.1 General information of case 2 study reported by Araya and Gao¹⁰

The published paper of case 2 reports experiments in a movable soil bin and a theoretical analysis using Finite Element Method of soil failure by a pan-breaker and an injector with or without pressurized air injection. A Drucker-Prager's strain hardening cap model was adopted to simulate the soil material and to be as the soil yield criterion. A commercial package — ADANA was used for finite element modelling, and a subroutine program was written by the authors. The soil properties of sand as an elastic-plastic body were experimentally measured by a tri-axial compression test and used in the FEM analysis, as shown in table 5.2. The results by

subsoiler tests in laboratory showed good agreement with the numerical modelling results by FEM.

Table 5.2 Soil properties in case 2 study

Soil Property	Value	Unit
Wet bulk density, ρ	1.43	$\text{k}\cdot\text{kg}/\text{m}^3$
Cohesion, c	9.13	kPa
Internal friction angle, ϕ	23.8	deg.
Flow angle, β	23.8	deg.
Poisson's ratio, ν	0.248	No dimension
Young's modulus, E	83360	kPa
Material parameter, D	335	kPa^{-1}
Material parameter, W	0.10	No dimension

5.2.2.2 FE modelling of 3-dimensional case 2 study in ANSYS

The three-dimensional case 2 validation study in ANSYS is conducted for analyses of soil cultivated by a shank with 90 degrees rake angle without chisel and air injection, as shown in Fig. 5.3.

The parameters of soil material are selected as same as that of "A Non-linear Three-Dimensional Finite Element Analysis of Subsoiler Cutting with Pressurized Air Injection" reported by Araya and Gao¹⁰, seen also in table 5.2.

The Drucker-Prager material model of inelastic model of non-linear model in ANSYS is chosen to represent soil material in this validation. A SOLID45 element type in ANSYS software is selected to represent the soil material. The SOLID45 element is used for the three-dimensional modelling of solid structure. The element is defined by

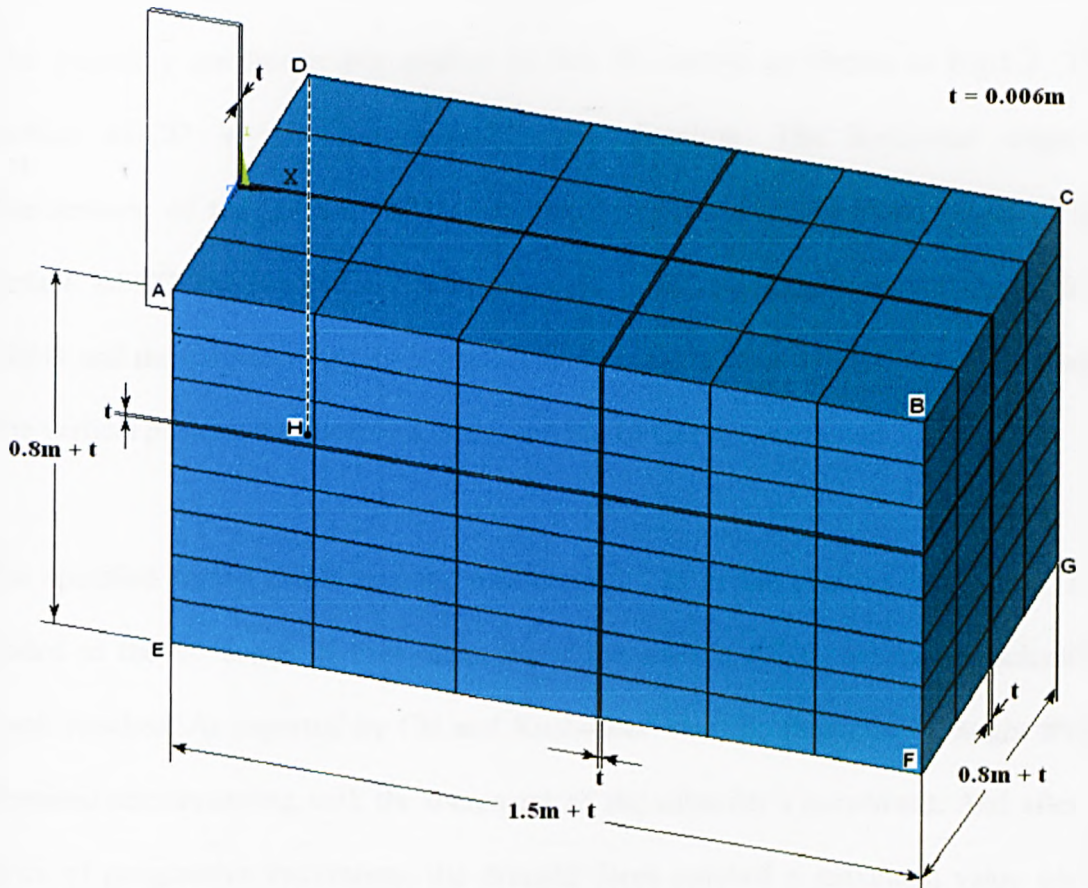


Fig. 5.3 Three dimensional finite element model of case 2 study

eight nodes having three degrees of freedom at each node in the x , y , and z directions. The element has plasticity, creep, swelling, stress stiffening, large deflection, and large strain, etc. capabilities. Pressures may be input as surface loads on the element faces and positive pressures act into the element.

Total 64 keypoints, 144 lines, 108 areas, 27 volumes, 480 nodes, and 315 eight nodal SOLID45 elements are created, as shown in Fig. 5.3. The subsoiler-soil system is symmetric about the vertical central plane in Fig. 5.3. In order to determine stress caused in the plane where the subsoiler passes, the whole symmetrical region in Fig. 5.3 is constructed and numerical analysed.

The boundary conditions are applied to this FE model as shown in Fig.5.3. The surface ABCD is not constrained in any direction. The horizontal negative displacement of the surface AEHD and the horizontal positive displacement of the surface BFGC are constrained. The sideways positive displacement of the surface AEFB and the sideways negative displacement of the surface DHGC are constrained. The vertical positive displacement of the surface EFGH is constrained.

The specified forced displacements, maximum 0.1 m in the positive x-direction, are loaded at the 10 nodes of four elements of the surface AEHD where the subsoiler shank touched. As reported by Chi and Kushwaha³ that the theoretical draught force increased accompanying with the increment of the subsoiler's movement. And after a series of progressive increments, the draught force reached a maximum value when the tool's movement is at 0.05 m to 0.1 m because the failure of the soil structure occurred. As a result, 0.1 m subsoiler movement is determined to be loaded in this validation to analyse the draught force, and the stress and deformation fields. The movement of the subsoiler is assumed to be frictionless, that is, interface friction between the subsoiler and the soil is zero.

Finally, numerical modelling of this case is conducted and non-linear convergent

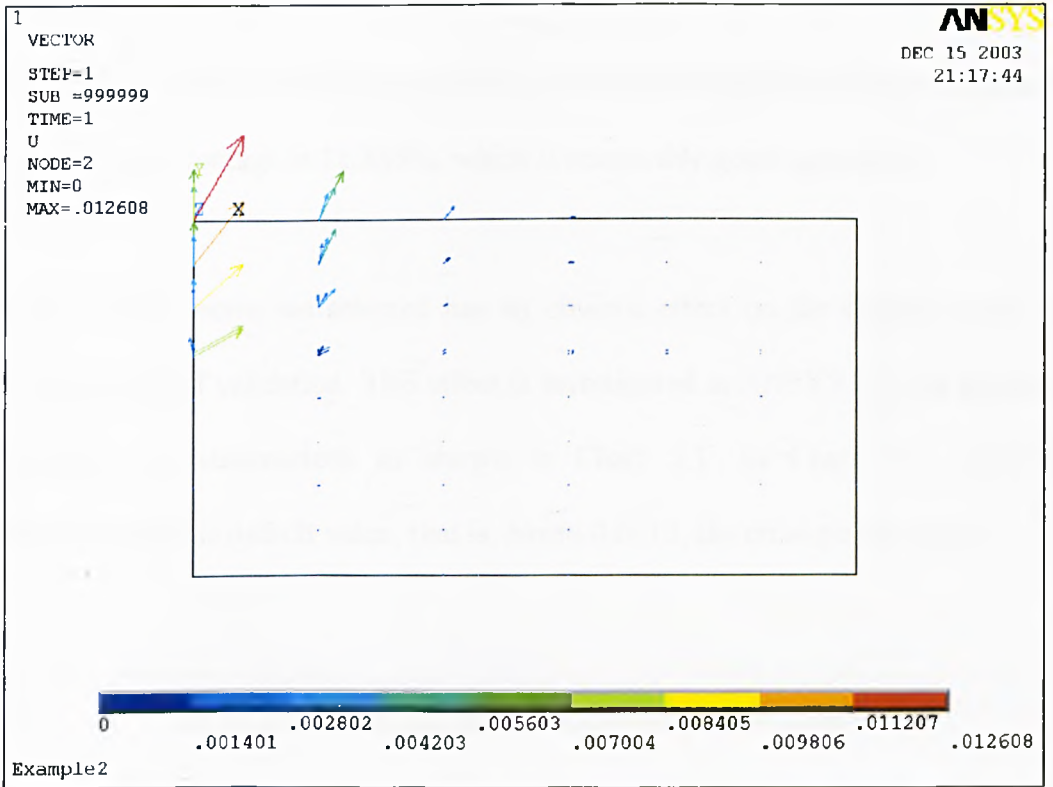
solutions are obtained. The results will be presented and analysed in the following section.

5.2.2.3 Results analysis and conclusions

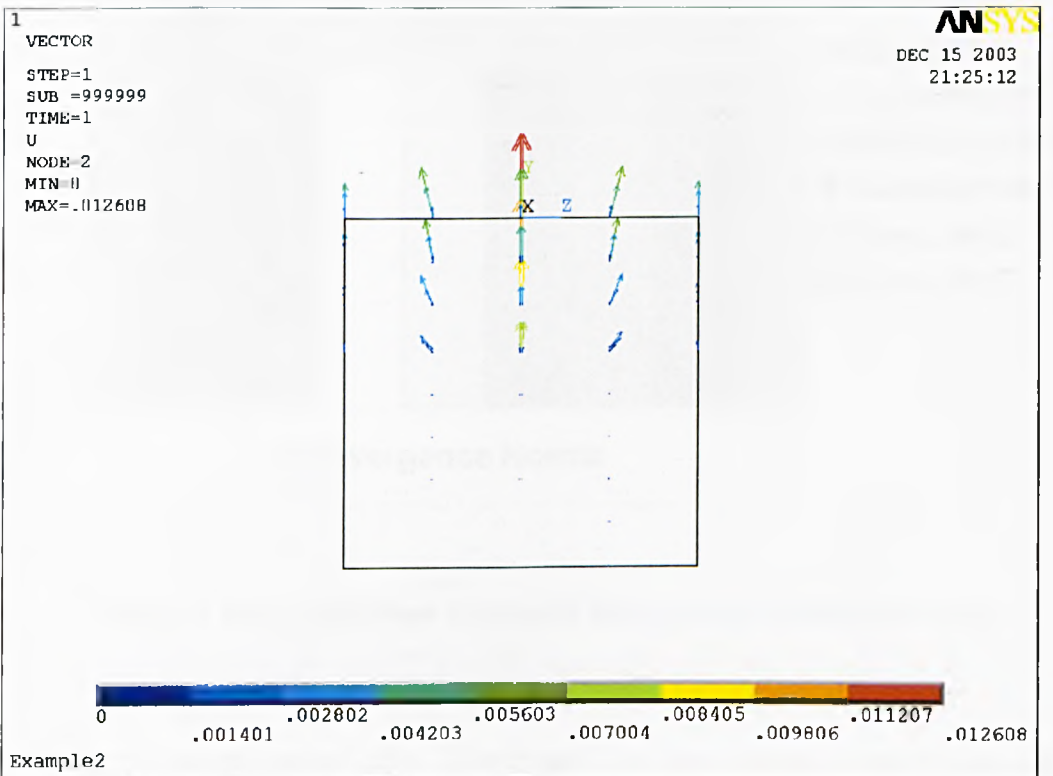
Parts of the FE modelling results about soil deformation are shown in Fig. 5.4 by vector plots of translation. Fig. 5.4 (a) is the front perspective drawing of three-dimensional oblique vector plot; Fig. 5.4 (b) is the left perspective drawing of the three-dimensional oblique vector plot. As seen in Fig. 5.4 (a) and (b), the soil is forced to move upward, forward and sideways. The closer the region is near to the shank, the greater the soil deformation is. Soil upheaval on the soil surface in front of shank of the subsoiler is formed. The soil below the horizontal plane contacting by the bottom of the shank experienced very small movement. It is obvious that the soil deformation is symmetrical to the central plane being cut by the subsoiler as demonstrated in Fig. 5.4 (b).

The FE analysis results of this vertical shank-soil system are compared to the results reported in literature¹⁰, and the contours of plastic strain and deformation situation of these two numerical modelling are similar or close to each other.

For soil-subsoiler system, the draught force is a dominating factor in assessing the function of tillage. In the report of “A Non-linear Three-Dimensional Finite Element Analysis of Subsoiler Cutting with Pressurized Air Injection” authored by Araya and Gao¹⁰, the draught force from FE numerical modelling results was 3.2 kN for 90 degree shank case without air injection and chisel.



(a)



(b)

Fig. 5.4 Vector plots of translation of case 2 study

From our FE numerical modelling results in ANSYS software, the draught force is 3.6 kN. The error percentage is 11.245%, which is reasonably good agreement.

The convergence norm we selected has an obvious effect on the draught force and error percentage of validation. This effect is investigated in ANSYS and the results of investigation are summarized as shown in Chart 5.1. In Chart 5.1, when the convergence norm is default value, that is, Norm 0.0010, the error percentage is

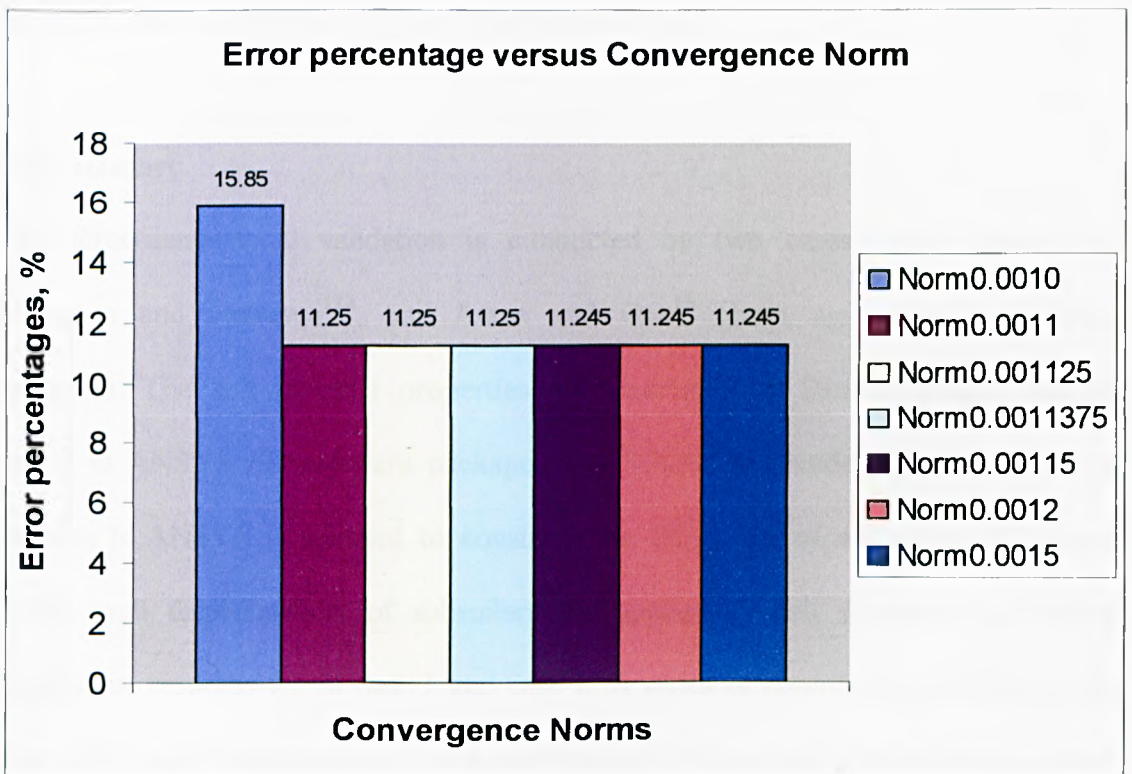


Chart 5.1 Error percentage of draught force versus convergence norm

15.85%, that is the maximum value. If enlarging the convergence norm by one step (0.0001), the error percentage drops down dramatically to 11.25%, therefore the corresponding Norm 0.0011 can be considered as a threshold value. Continuously

increasing the convergence norm step by step, there is no improvement for error percentage until it equals to Norm 0.00115, the error percentage reaches to a limited minimum value, 11.245%. Further enlarging convergence norm after Norm 0.00115 by two steps, the error percentage of each step remains same value. So, it means Norm 0.00115 is the optimum convergence norm for conducting this particular case of FE modelling.

From the above analyses of 3D validation of case 2 study, it can be concluded that there is a reasonable good agreement for the draught force comparison. Therefore, the three-dimensional validation of case study is successful.

5.3 Summary

The three-dimensional validation is conducted by two cases study reported by Mouazen and Nemenyi¹²³, and Araya and Gao¹⁰ about agricultural soil tillage problems. The soil material properties are simulated by Drucker-Prager material model in ANSYS FE software package. The SOLID45 8-node 3D structural solid element in ANSYS is selected to construct the FE model of soil mass. 0.15m and 0.10m wall displacements of subsoilers are applied to soil structures as loading conditions, respectively, in case 1 and case 2. A series of numerical modelling results shows that good agreement with the deformation contour and draught force of cases has achieved, and ANSYS software is suitable to 3D FE numerical modelling for problems of soil and structure interaction.

Chapter 6

Study of Footwear and Ground Interaction by Using Finite Element Method

6.1 Introduction

Having successfully conducted cases validation studies for two-dimensional and three-dimensional soil-structure interaction by finite element numerical modelling in ANSYS package—University High Option, we are confident in employing Drucker-Prager material model in study of footwear and soft ground interaction, by using Finite Element Method with the same ANSYS package. Before moving to the issue of FE modelling of footwear and ground interaction, a general understanding of footwear, especially military boots, and human gait is essential to inform the construction of the finite element model.

6.1.1 Outdoor Footwear—Boots

Outdoor footwear development over the past thirty years more has seen that the traditional heavy leather boot of the 1970's was replaced by the "lightweight" comfortable boot of the 1980's with the addition of the synthetic fabric boot boom; technological advances in the 1990's aid the return of leather, with many new characteristics such as lighter weight, easy care and more fashionable appearances. The trainer-type sports hiking boot has been developed over recent decade to be suitable for many terrains. A well-constructed trainer-type sports hiking boot is showed in Fig. 6.1.

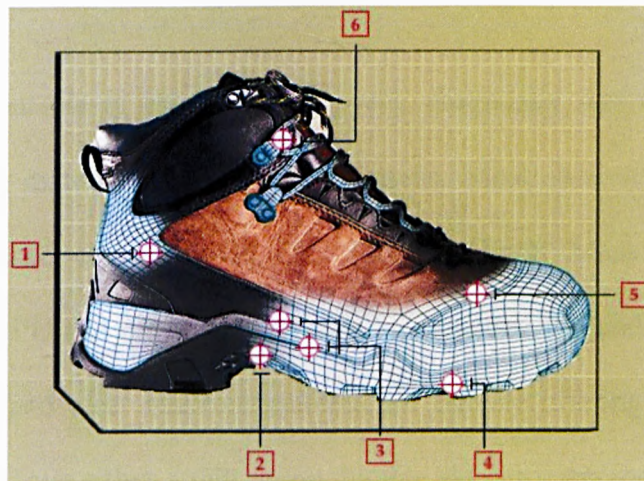


Fig. 6.1 Trainer-type sports hiking boot—

1)Rand, 2)Insole, 3)Midsole, 4)Outsole, 5)Uppers, and 6)Lacing system

The natural environment of ground varies from grass pastures and soft soil to snow, ice and rugged rock. Therefore outdoor activities can be differentiated, for instance, walking; hiking; scrambling and climbing. In order to meet these environment requirements, the high quality and versatile design of boots is always demanded and advanced. The desired characteristics of good boot design are comfort, insulation, maximized traction and lateral stability, lightness, water resistance, crampon compatibility, flexibility, wear resistance, breathing-ability, adaptability and easy care, etc. The boot types may be classified as several groups, such as walking, hiking boot, climbing boot, and special purpose boot, etc. Depending on how the boot is used, not all of these characteristics are achievable in any one design. The military boot is used for the special situations of combat and physical training. Apart from the general characteristics of boot design, it is subjected to much more emphases on good traction performance, lateral stability, comfort, adaptability and prevention of water and granular debris invading into boot, etc.. Therefore these characteristics help to enhance soldier performance and reduce injures due to the high demands of load carriage, terrain and climate.

A good, grippy outsole is essential in slippery, frequently wet environments. This depends on soling materials and the tread pattern. Most shoe soles are made from rubber, thermoplastic or vulcanised, PU (polyurethane). Many leading footwear manufacturers use PU and rubber compounds for outsoles. PU and vulcanised rubbers are good durable and wear resistant material for outsole offering traction. Moulded PU sole units may have either a thin, more durable skin on a microcellular structure or a thicker skin on a lower density partly open cell structure. For the UK Ministry of Defence, the outsole of one sort of military boots is made from two densities of reaction-moulded polyurethane. The soling compounds are hydrolysis resistant and to comply with the physical properties, such as that hardness is 60-70 IRHD, and density on whole mouldings is 1.05-1.15 g/cm³ for facer part.

For the natural soft surfaces, as reported in chapter 2, so little information is available about the interaction of footwear and soft ground. In this situation, good traction should be provided by well-designed tread pattern, producing the maximum shear resistant force by cleats and arrangement of cleats. So, how to effectively judge a tread pattern design of military boots respect to traction performance have been the most concerns in this study. FEM has been selected to be a powerful means to accomplish this mission of this project. This study will be presented in detail in the latter sections.

6.1.2 Process of Gait

During walking, the body passes over the supporting leg, the other swings forward in preparation for its next support phase. In the single support phase, the body tends to

shift laterally over the weight-bearing limb. One foot is always on the ground, and during the period when the support of the body is transferred from one leg to the other, there is a brief period when both feet are on the ground. As the speed of walking increases, the period of double support decreases. When running, it disappears and period of neither foot being on the ground occurs.

During normal walking, a consistent cycle of heel strike and toe-off occurs. Between these two extremities, there is foot strike, opposite toe-off, opposite foot strike and toe-off. With each step, the body speeds up or slows down, rises and falls, and gently sways from side to side. The motion of the body during walking decreases vertical displacement of the centre of gravity to conserve energy. Any deviation from normal walking pattern and comfortable speed increases energy expenditure. Increased gradient or weight by loading affects oxygen intake and energy consumption. The nature of terrain has a considerable effect on the metabolic demand of walking. Therefore a sort of suitable footwear, especially with well-designed tread pattern, will effectively improve the process of gait as well as energy conservation.

6.2 Construction of Interactive Finite Element Model for the First Tread

Pattern of Military Boots

6.2.1 Some Consideration of Building Up Finite Element Models

By considering the same direction of layout for both existing experimental device and finite element model to be built up, it is required that the layout of finite element model with tread pattern is identical to that of experiment facility. The experiment layout is showed in Fig. 6.2 and Fig. 6.3.

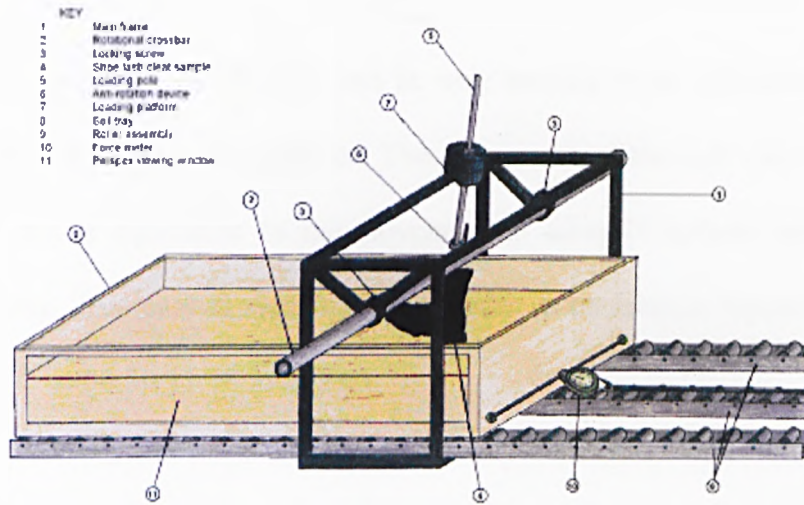


Fig. 6.2 The experiment layout for direction of heel strike (From Pisina¹)

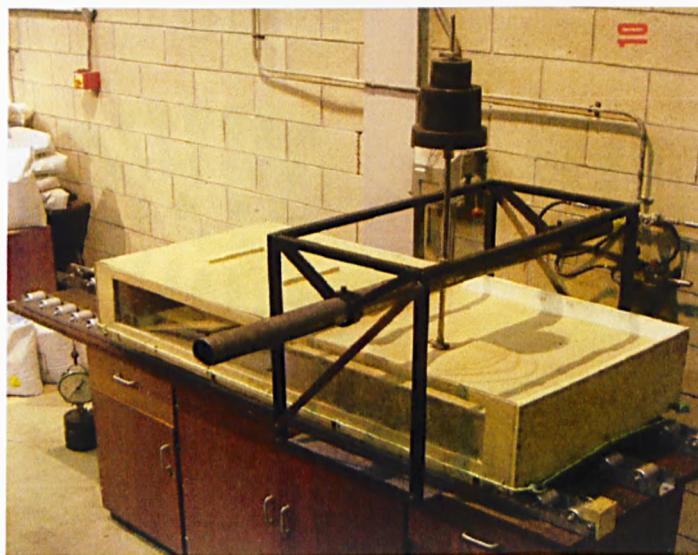


Fig. 6.3 The experiment layout for direction of forepart outsole tread

In Fig. 6.2, the soil tray can be only sliding from left-hand side to right-hand side, in regard to static boot sample. According to the principle of relative motion in physics, the movement of the soil tray relative to static boot sample is equal to the movement of heel strike relative to static soil tray, which is natural soft ground in real world. This situation is similarly corresponding to a transient state reported by Fendley and Marpet¹⁰⁶ at 00:30:21:08 in its FIG. 1a.

Similarly, the soil tray, in Fig. 6.3, can be only moving from right-hand side to left-hand side by measured pulling forces. The movement of the soil tray relative to the static shoe last is equivalent to the movement of forepart outsole tread relative to static soil tray. This case is similar to a transient circumstance reported by Fendley and Marpet¹⁰⁶ at 00:30:21:18 in its FIG. 1b.

6.2.2 Building Up Finite Element Model of Outsole for the First Tread Pattern

A footprint of the first tread pattern of military boots is shown in Fig. 6.4 and the real military boots (Sizes: M 10) is displayed in Fig. 6.5.



Fig. 6.4 Footprint of the first tread pattern



Fig. 6.5 The first tread pattern of real military boots

A 3d geometrical model of outsole for the first tread pattern has been successfully, step by step, constructed and the final version is shown in Fig. 6.6. This geometry was used to create the corresponding geometrical depression in the finite element model of the soil—as explained in the following sections.

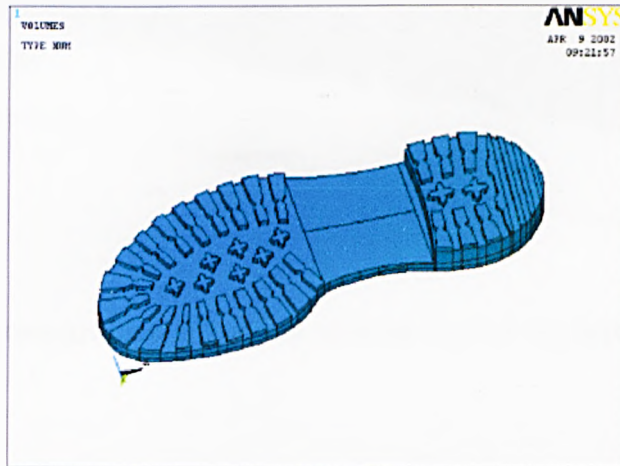


Fig. 6.6 A 3d geometrical model of outsole for the first tread pattern

6.2.3 Construction of Interactive Soil FE Model with Forepart of the First Tread Pattern

As reported in section 6.1.1, the hardness of outsole is 60-70 IRHD for military boots. Comparing to soft soil, the outsole including forepart, heel and all cleats is assumed to be a rigid body. Loads initiated by foot on insole will be transferred by supposed rigid outsole with tread pattern on the soft ground, which will be simulated by soil material. As discussed in section 6.2.1 associated with Fig. 6.3, an interactive soil FE model with forepart of the first tread pattern has been successfully constructed and as shown in Fig. 6.7.

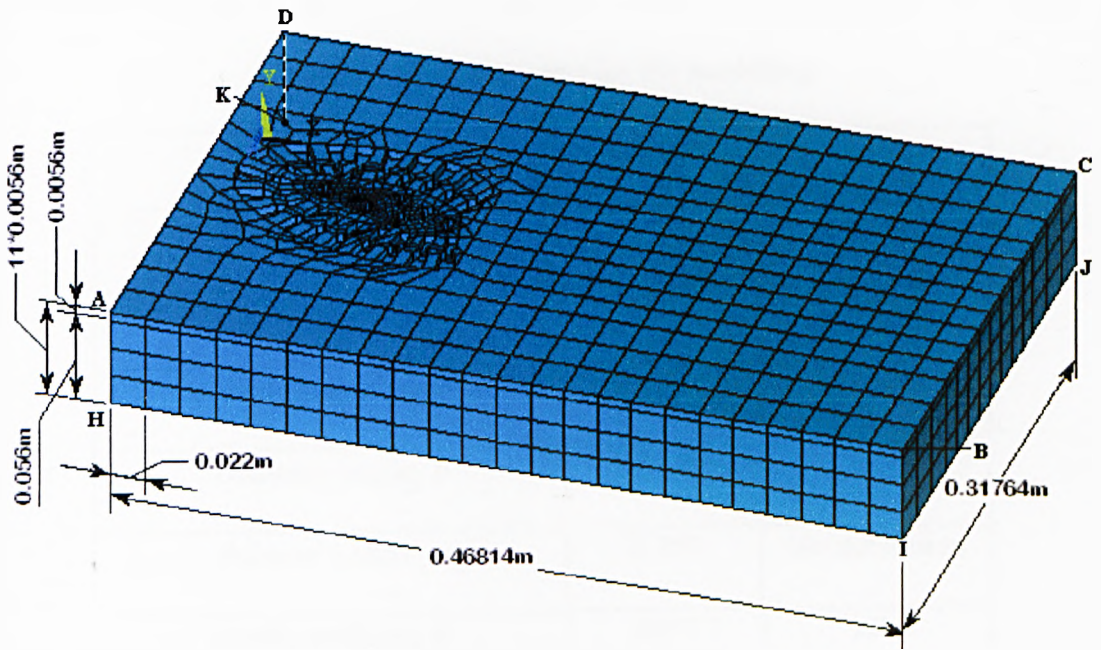


Fig. 6.7 Interactive soil FE model with forepart of the first tread pattern

6.2.3.1 Geometry size of the model

The soil is assumed fully compressed before loading. Full sinkage is applied to all cleats of forepart of outsole, that is, the depth of full sinkage equals to the height of cleats (= 0.0056 m). As seen in Fig. 6.7, overall depth of the FE model is designed to be 11 times greater than the height of cleat. Overall length and width of the FE model are considered to be 3 times plus greater than the maximum length and width of forepart contour of the first tread pattern, respectively. The basic element size is optimized as 0.022m, which will be explained in the following sections.

6.2.3.2 Soil properties

The soil material parameters in this study are chosen to be the same as that of published works by Mouazen and Nemenyi¹²³ and used as input data for FE modelling interaction of outsole with tread pattern and soft ground in ANSYS package. These parameters are presented in table 6.1.

Table 6.1 Soil properties for FE modelling

Soil Properties	Value	Unit
Wet bulk density, ρ	1.731	k•kg/m ³
Cohesion value, c	15.5	kPa
Internal friction angle, ϕ	31.8	deg.
Dilatancy angle, β	31.8	deg.
Poisson's ratio, ν	0.359	No dimension
Elastic modulus, E	8067	kPa

6.2.3.3 Drucker-Prager material model

The Drucker-Prager material model is employed to simulate the behaviour of elastic perfectly plastic soil material in this study. It is governed by a yield criterion—the Drucker-Prager criterion and an associated flow rule. The increase in material volume due to yielding—The amount of dilatancy can be controlled by the dilatancy angle. As shown in table 6.1, the dilatancy angle, β is equal to the internal friction angle, ϕ , the flow rule is associative and there is a material volume increase. If the dilatancy angle is zero or less than the internal friction angle, there is no or less of an increase in material volume when yielding and the flow rule is non-associated.

6.2.3.4 The element

SOLID45 element in ANSYS package is selected to construct the three-dimensional soil FE model. This type of element has been used for 3D cases validation studies as described in section 5.2.1 and 5.2.2.2 of Chapter 5 in detail.

6.2.3.5 Meshing scheme

A basic element size, that is 0.022 m, is optimized to firstly mesh the main block of soil volumes surrounding and being adjacent to the first tread pattern, as displayed in Fig. 6.8 as follows. After this key step of meshing is successful, the other parts of soil volumes are meshed and complete meshing is finalized as in Fig. 6.7.

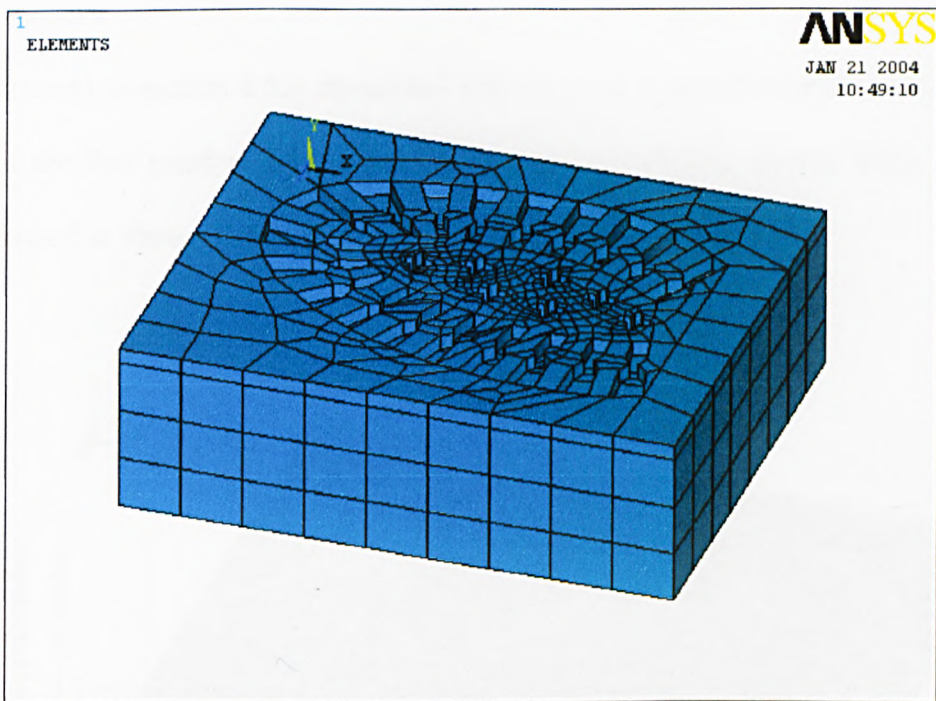


Fig. 6.8 The meshed main block of soil volumes surrounding and being adjacent to the tread pattern

Total 961 key-points, 1642 lines, 749 areas, 40 volumes, 4325 nodes, and 3186 eight-node SOLID45 elements are created, respectively.

A finer meshing scheme had been tried by selecting the basic element size being 0.01m. However, this finer meshing scheme was finally abandoned. There are two

main reasons to give up this scheme. First, the total element number of this finer meshing FE model is 8516, which is close to the maximum limit of elements number of ANSYS University High Vision. Secondly, shape testing for this finer meshing reveals that 506 of the total 5258 modified elements violate shape-warning limits. This may lead to numerical modelling failure.

6.2.4 Construction of Interactive Soil FE Model with Heel of the First Tread Pattern

As discussed in section 6.2.1 associated with Fig. 6.2, a soil FE model interactive with heel of the first tread pattern, similar to forepart reported in section 6.2.3, has been constructed as shown in Fig. 6.9.

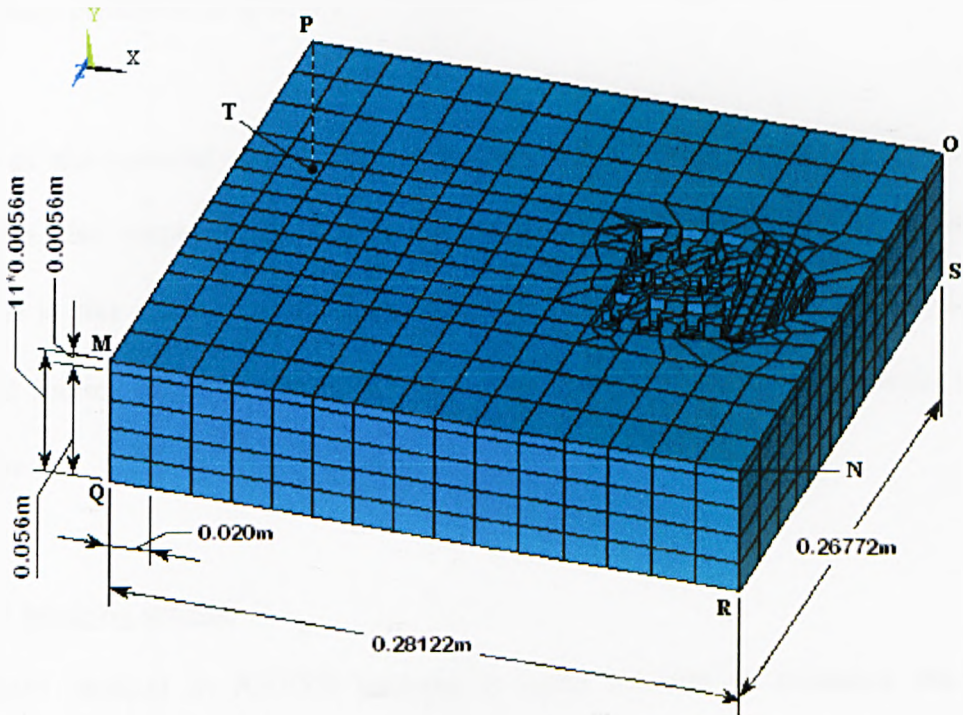


Fig. 6.9 Interactive soil FE model with heel of the first tread pattern

6.2.4.1 Geometry size of the model

Similar to the methodology used in section 6.2.3.1, the soil is assumed fully compressed before loading. Full sinkage is applied to all cleats of heel of outsole, that is, the depth of full sinkage equals to the height of cleats ($= 0.0056$ m). As seen in Fig. 6.9, overall depth of the FE model is designed to be 11 times greater than the height of cleat. Overall length and width of the FE model are designed to be 3 more times greater than the maximum length and width of heel tread pattern's contour, respectively. The basic element size is optimized as 0.020m.

6.2.4.2 Soil properties and material model

The soil material properties in this study are also chosen to be the same as that of in section 6.2.3.2, and used as input data for FE modelling about interaction between heel of the first tread pattern and soft ground in ANSYS software. These parameters are already presented in table 6.1.

Same as the material model used in section 6.2.3.3, the Drucker-Prager material model is also employed to simulate the behaviour of elastic perfectly plastic soil material in this study. As shown in table 6.1, the dilatancy angle, β is equal to the internal friction angle, ϕ , the flow rule is associative and there is a material volume increase.

6.2.4.3 Meshing scheme

SOLID45 element in ANSYS package is again selected to construct the three-dimensional soil FE model interactive with heel of the first tread pattern. This type of element has been used for 3D cases validation studies as described in Chapter 5 in detail.

A optimized element size (0.020m), which is different from that of forepart interactive soil FE model, is employed to mesh main block of soil volumes surrounding and being adjacent to heel of the first tread pattern. After successfully conducting this key step of meshing, the other parts of soil volumes are meshed and complete meshing is accomplished as shown in Fig. 6.9. Total 460 key-points, 811 lines, 406 areas, 38 volumes, 2954 nodes, and 2235 eight-node SOLID45 elements are created, respectively.

6.3 Solution of the Soil FE Model Interactive with the First Tread Pattern

6.3.1 Solution of the Soil FE Model Interactive with Forepart

6.3.1.1 Constraints

For this three-dimensional soil problem, boundary conditions are applied to this FE model interactive with forepart of the first tread pattern. Referring to Fig. 6.7, the top surface ABCD is left free of any constraints in any direction, the lateral surfaces AHIB and DCJK are constrained in positive and negative z directions, respectively. The vertical y displacement of the bottom surface HIJK is also constrained. The horizontal negative displacement (x) of the surface ADKH and the horizontal positive displacement (x) of the surface BIJC are constrained, respectively.

6.3.1.2 Loading conditions

Vertical compressive and transverse shear forces are applied to the ground via the footwear during the process of gait.

For static analysis of a transient state in Fig. 6.3, the vertical compressive force is mainly a result of the weight of the soldier's body and ammunition in his backpack. Although the weight of the human body is not linearly distributed over the inner sole in a particular time instant and position of gait¹⁰⁵, the vertical compressive force distribution applied to the soft ground via the outer-sole of boot is more even, owing to rigidity of outer-sole, than the distribution of body weight over the inner sole.

The most promising tests applied a vertical force equivalent to at least 50% (single foot on the ground) of bodyweight and the bodyweight ranges from 400 to 830 N¹⁰⁷. For this study, vertical force is considered as 50%* ("body + ammunition" weight). Soldier's body weight is assumed as 800N and ammunition weight is 200N. Friction force in vertical direction is assumed to be zero due to contact is considered as frictionless.

The transverse force consists of a shear force due to the vertical areas of cleats and friction forces due to contact between the cleats and the soil surfaces in the horizontal direction. For this study, the contact between the cleats and the soil surface is also assumed to be frictionless, so the transverse force, F_t , is only composed of a shear force. A ratio of 0.35 of transverse shear force to vertical compressive force is used to calculate the transverse shear force.

6.3.1.3 Methodology of applying vertical and transverse loading

The applied vertical and transverse loadings—pressures are displayed in Fig. 6.10. The methodology of applying loading conditions is presented, step-by-step, as following in detail.

i) Calculating average vertical pressure: The average vertical pressure equals to the total vertical forces, which is 500N as described in section 6.3.1.2, divides by total area sustaining the total forces. The total area is equal to the sum of two groups of

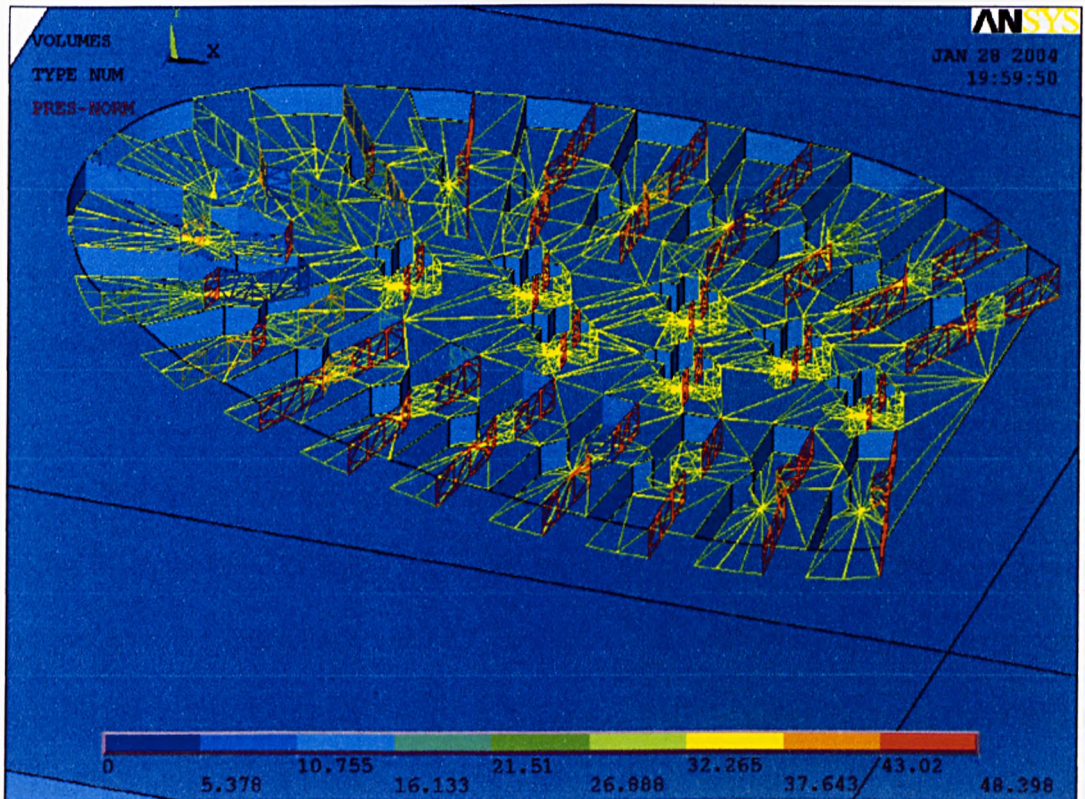


Fig. 6.10 Loading conditions of soil FE model for the first tread pattern

area. One group of area is a single area (A_{387}) at top surface of the soil FE model between the cleats. The another group of area is the sum of areas ($A_2, A_3, \dots, A_i, A_{i+1}, \dots, A_{26}, A_{27}$) occupied and contacted with bottom surface of all the cleats at forepart of the first patterns as shown in Fig. 6.10. Hence, the average vertical pressure, P_V , is:

$$P_V = \frac{\text{Vertical Forces}}{\sum (A_{387} + A_2 + A_3 + \dots + A_i + A_{i+1} + \dots + A_{26} + A_{27})} \quad (6.1)$$

$$= \frac{500N}{0.01503679m^2} = 33.252kPa$$

ii) Applying vertical loading—the average vertical pressure, P_V , on all the areas in Fig. 6.10. The applied vertical loading is shown in Fig. 6.10 at two levels of horizontal planes.

iii) Applying transverse loading on specified areas interactive with lateral vertical areas of all cleats. The applied transverse loading is also displayed in Fig. 6.10. How the transverse loading acts on the specified areas will be presented in next subsection.

iiii) Method of acting transverse loading on specified vertical areas: As mentioned before, forepart tread effect is simulated by vertical and transverse force or pressure. The moving or slipping tendency of forepart with cleats is horizontally from left to right, which is the positive X -direction in Fig. 6.10. In this process, transverse loading is acted, by all cleats, on only vertical surfaces of soil model that blocking the moving trend of cleats and being interactive with vertical surfaces of cleats. Corresponding to Fig. 6.10, these vertical surfaces of soil model are straight lines from the top of view.

How to judge which vertical surface of soil model horizontally blocking the moving trend of cleat is to select any a vertical surface of soil model. From the top of view in Fig. 6.10, the selected vertical surface becomes a line. If the line is at right hand side or up-right hand side or down-right hand side to a corresponding cleat which is adjacent to the line, the vertical surface, therefore, blocks the moving or slipping trend

horizontally forward to right direction. Otherwise, the line which is at left hand side or up-left hand side or down-left hand side to a corresponding cleat being adjacent to the line does not block the moving or slipping trend forward to right direction.

After selection of all vertical surfaces obstructing moving trend of cleats, average transverse pressure, P_{at} , acted by cleats on all vertical surfaces of soil model is calculated. The total transverse force, F_t , initiated by forepart of outer-sole with cleats is assumed as 0.35 times greater than the total vertical force, which is 500N as described in section 6.3.1.2. As the F_t is assumed to be acting on in the direction of paralleling the X -axis, a hypothesis total area, A_{vh} , is calculated by summing up all projected areas perpendicular to the X -axis of all transverse surfaces blocking the moving trend of all cleats. Total 131 such vertical surfaces are founded as shown in Fig. 6.10. So, the A_{vh} can be calculated as:

$$\begin{aligned} A_{vh} &= A_{vh1} + A_{vh2} + \dots + A_{vh,i} + A_{vh,i+1} + \dots + A_{vh131} \\ &= A_{v1} \cos \alpha_1 + A_{v2} \cos \alpha_2 + \dots + A_{v,i} \cos \alpha_i + A_{v,i+1} \cos \alpha_{i+1} + \dots + A_{v131} \cos \alpha_{131} \end{aligned} \quad (6.2)$$

where $A_{v1}, A_{v2}, \dots, A_{v,i}, A_{v,i+1}, \dots, A_{v131}$ is the areas of all the selected vertical surfaces, respectively, as shown in Fig. 6.10. The angle $\alpha_1, \alpha_2, \dots, \alpha_i, \alpha_{i+1}, \dots, \alpha_{131}$ is the inclination angles between the selected vertical surfaces and the plane perpendicular to the X -axis, respectively. These angles are determined by coordinates of two key-points of the selected vertical surfaces of soil model at the same depth. Finally, the average transverse pressure is solved as:

$$P_{at} = \frac{F_t}{A_{vh}} = \frac{0.35 * 500N}{0.00359201893m^2} = 48.719kPa \quad (6.3)$$

Then the average transverse pressure is acted on each selected vertical surface, as shown in Fig. 6.10. The method of acting on is by selecting each surface i , which area is $A_{v,i}$, of the total 131 selected vertical surfaces, and multiplying it by P_{at} , and cosine of its inclination angle α_i , one by one.

6.3.2 Solution of the Soil FE Model Interactive with Heel

6.3.2.1 Constraints

Similar to the scheme of boundary conditions for the soil FE model interactive with forepart presented in section 6.3.1.1, the boundary conditions are applied to soil FE model interactive with heel. By referring to Fig. 6.9, the top surface MNOP is left free of any constraints in any direction, the lateral surfaces MQRN and OPTS are constrained in the positive and negative z directions, respectively. The vertical y displacement of the bottom surface QRST is also constrained. The horizontal negative displacement (x) of the surface MPTQ and the horizontal positive displacement (x) of the surface NOSR are constrained, respectively.

6.3.2.2 Loading conditions

Similar to the methodology employed in section 6.3.1.2 and 6.3.1.3, loading conditions are applied for this FE model as shown in Fig. 6.11.

Vertical compressive and transverse shear forces are applied to the ground via the footwear during the process of gait. For static analysis of a transient state in Fig. 6.2, the vertical compressive force is mainly a result of the weight of the soldier's body and ammunition in his backpack plus the tread effect. Due to the rigidity of outer-sole

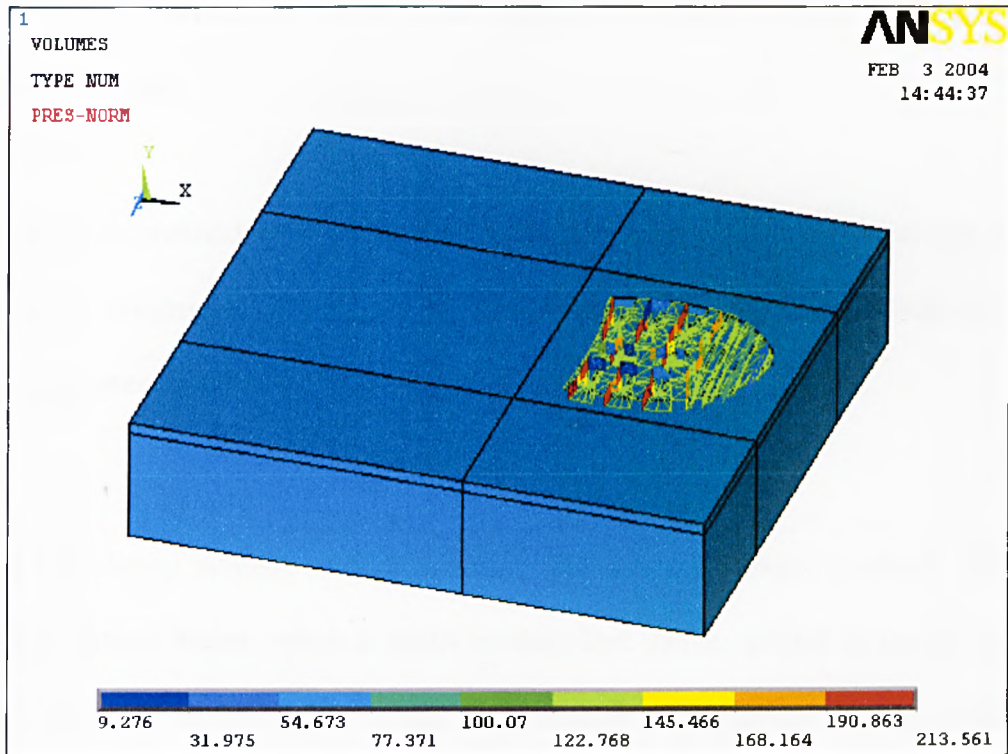


Fig. 6.11 Loading conditions of FE modeling for heel

the vertical compressive force distribution applied to the soft ground via the outer-sole of boot is more even than the distribution of body weight over the inner sole. The soldier's body weight is also considered as 800N and ammunition weight is 200N. Due to the tread effect by heel, a vertical force equivalent to 80% of (800N+200N), is assumed. Friction force in vertical direction is also assumed to be zero due to contact is considered to be frictionless in this study.

The transverse force consists of a shear force due to the vertical surfaces of cleats and friction forces due to contact between the cleats and the soil surfaces in the horizontal direction. For this study, the contact between the cleats and the soil surface is also assumed to be frictionless, so the transverse force, $F_{t(heel)}$, is only composed of a shear

force. A ratio of 0.50 of transverse shear force to vertical compressive force is used to calculate the transverse shear force due to the severity of possible injury resulting from heel slip.

The same methodology as that of used in section 6.3.1.3 is employed to act the loading conditions on the soil FE model interactive with heel. It will be presented step-by-step as follows.

a) Calculating average vertical pressure: The average vertical pressure equals to the total vertical forces, which is 800N as described above, divides by total areas bearing the total vertical forces. The total area is equal to summing up areas on the top surface of soil FE model bearing the average vertical pressure, and areas on the soil surface contacting the bottom surfaces of cleats with full depth sustained the same average vertical pressure, and areas on the soil surfaces contacting the bottom surfaces of cleats with 0.8 times, 0.6 times, 0.4 times and 0.2 times heights, separately, of full depth (0.0056m) of tread patterns of heel.

Hence, the average vertical pressure, $P_{V(heel)}$, is:

$$\begin{aligned}
 P_{V(heel)} &= \frac{\text{Vertical Forces}}{\sum (A_{107} + A_{96} + A_{98} + A_{101} + A_{104} + A_{12} + \dots + A_{16} + A_{21} + \dots + A_{24} + A_{39} + A_{44} + A_{49})} \\
 &= \frac{800N}{0.00625642m^2} = 127.869kPa
 \end{aligned}
 \tag{6.4}$$

b) Applying vertical loading—the average vertical pressure, $P_{V(heel)}$, on all the areas in Fig. 6.11. The applied vertical loading is shown in Fig. 6.11.

c) Applying transverse loading—the average transverse pressure, $P_{at(heel)}$, on all the surfaces blocking slipping trend of cleats of heel horizontally from right to left, that is the negative X-direction in Fig. 6.11.

From top of view in Fig. 6.11, these vertical soil surfaces are all at left hand side or the upper-left hand side or the lower-left hand side of the corresponding cleats being adjacent to these surfaces. The methodology of applying transverse loading for soil FE model interactive with heel is same as that of for soil FE model interactive with the forepart as presented in section 6.3.1.3, part iii).

After selection of all vertical surfaces obstructing moving trend of cleats of heel, average transverse pressure, $P_{at(heel)}$, acted by cleats on all vertical surfaces of soil model is calculated. The total transverse force, $F_{t(heel)}$, initiated by heel of outer-sole with cleats is assumed to be 0.50 times greater than the total vertical force, which is 800N. As the $F_{t(heel)}$ is assumed to be acting on in the direction of paralleling the X-axis, a hypothesis total area, A_{vheel} , is calculated by summing up all projected areas perpendicular to the X-axis of all vertical surfaces blocking the moving trend of all cleats. Total 58 such vertical surfaces are founded. So, the A_{vheel} can be calculated as:

$$\begin{aligned}
 A_{vheel} &= A_{vheel1} + A_{vheel2} + \dots + A_{vheel,i} + A_{vheel,i+1} + \dots + A_{vheel58} \\
 &= A_{vheel1} \cos\alpha_{heel1} + A_{vheel2} \cos\alpha_{heel2} + \dots + A_{vheel,i} \cos\alpha_{heeli} + A_{vheel,i+1} \cos\alpha_{heel,i+1} + \dots + A_{vheel58} \cos\alpha_{heel58}
 \end{aligned}$$

(6.5)

where $A_{vheel1}, A_{vheel2}, \dots, A_{vheel,i}, A_{vheel,i+1}, \dots, A_{vheel58}$ is the areas of all the selected vertical surfaces, respectively. The angle $\alpha_{heel1}, \alpha_{heel2}, \dots, \alpha_{heel,i}, \alpha_{heel,i+1}, \dots, \alpha_{heel58}$ is the inclination angles between the vertical surfaces of soil model and the plane perpendicular to the X -axis, respectively. These angles are determined by coordinates of two key-points of the vertical surfaces of soil model at the same depth. Finally, the average transverse pressure, $P_{at(heel)}$, is solved as:

$$P_{at(heel)} = \frac{F_{t(heel)}}{A_{vheel}} = \frac{0.50 * 800N}{0.001873m^2} = 213.561kPa \quad (6.6)$$

Then the average transverse pressure is acted on each selected vertical surface, as shown in Fig. 6.11. The method of acting on is same as that of forepart soil FE model.

6.4 Modelling Results and Discussion of the First Tread Pattern

After the loading conditions are applied and the solution controls are determined, a nonlinear numerical modelling is successfully conducted. The modeling results and discussion are presented as follows in detail.

6.4.1 Modelling Results and Discussion of Soil Interactive with Forepart

6.4.1.1 Traction effect

As mentioned in section 6.1.1 above, a good grippy outsole, which is depended upon the tread pattern of outsole and soling materials, is essential in slippery, frequently wet environment. The effect of traction is an important factor in judging how good one kind of particular tread pattern design is to resist slip. After having obtained the numerical solutions of forepart of the first tread pattern, its traction effect can be

evaluated. In order to conveniently compare the traction effects associated with the other four tread patterns, this section—6.4.1.1 will be presented in section 6.6.2 in detail.

6.4.1.2 Soil deformation

The resultant soil displacement vector of soil FE model is shown in Fig. 6.12. As shown in Fig. 6.12, the most of large displacements occurs within regions contacted by the tread pattern and under the tread pattern, that is, the deformation of soil mass contacting forepart with cleats is magnificent other than the other regions far away from the forepart.

The distributions of the soil displacements in the X, Y and Z directions are complex in nature because of the complex tread pattern geometry and transverse loading conditions. However, the situation of soil displacement in each coordinate direction can still, generally, be the maximum translation in traction direction (the positive X direction) takes place in regions interactive with rear cleats of forepart; the maximum translation in vertical loading direction (the negative Y direction) occurs within regions at and under the center zone of tread pattern. The other regions' translations decrease progressively along the radial direction from the center zone. The translation in vertical loading direction in regions far away from the tread pattern decreases to the minimum absolute value being nearly the same; the maximum translation in the negative Z direction happens in regions interactive with right hand side of toe part of cleats. Most regions of soil experience moderate translation in either the positive Z direction or the negative Z direction.

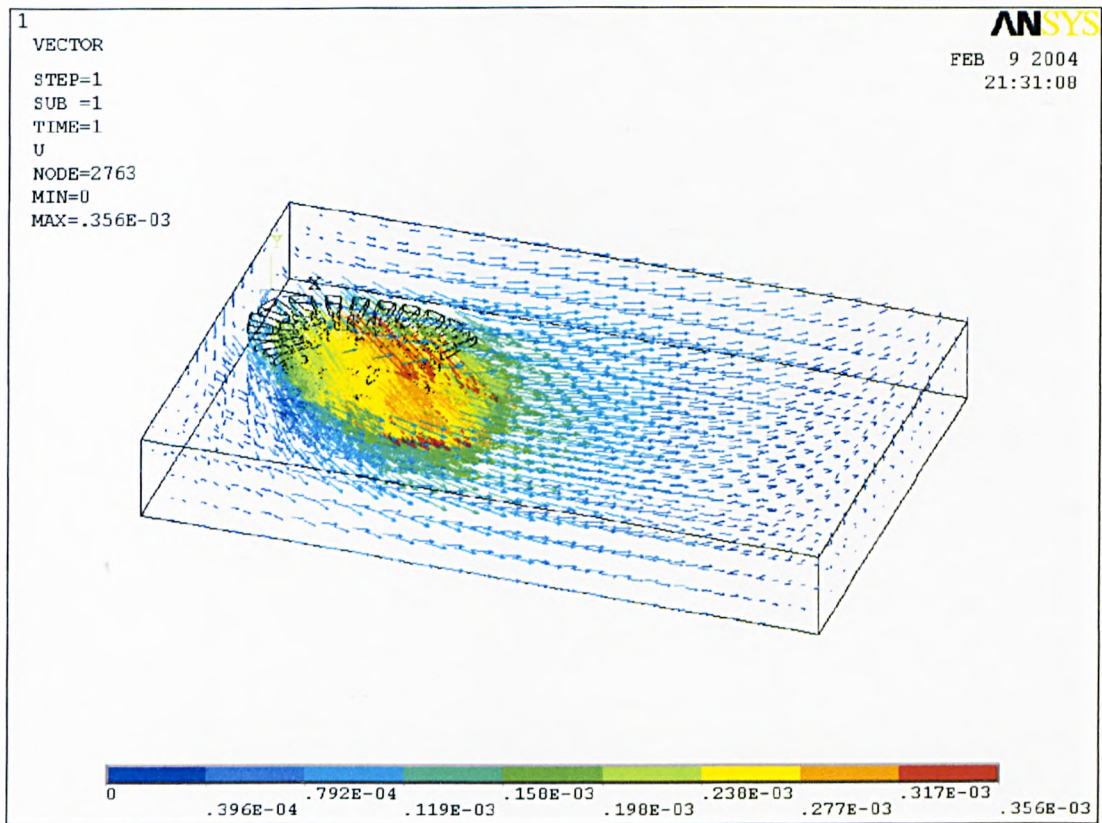


Fig. 6.12 The resultant soil displacement vector

6.4.1.3 Discussion of soil deformation

A series of cross-sections of the soil model are captured to observe and discuss soil deformation in detail. These cross-sections are perpendicular to the Y, Z and X-axis, respectively.

6.4.1.3.1 Soil deformation at cross-section perpendicular to the Y-axis

First, the group of cross-sections perpendicular to the Y-axis is shown in Fig. 6.13. By observing Fig. 6.13 a), and b), it is obvious that soil deformation in the positive X-direction (the dash lines are undeformed shape or edge before loading), that are located in regions interactive with toe of forepart, decreases progressively from depth

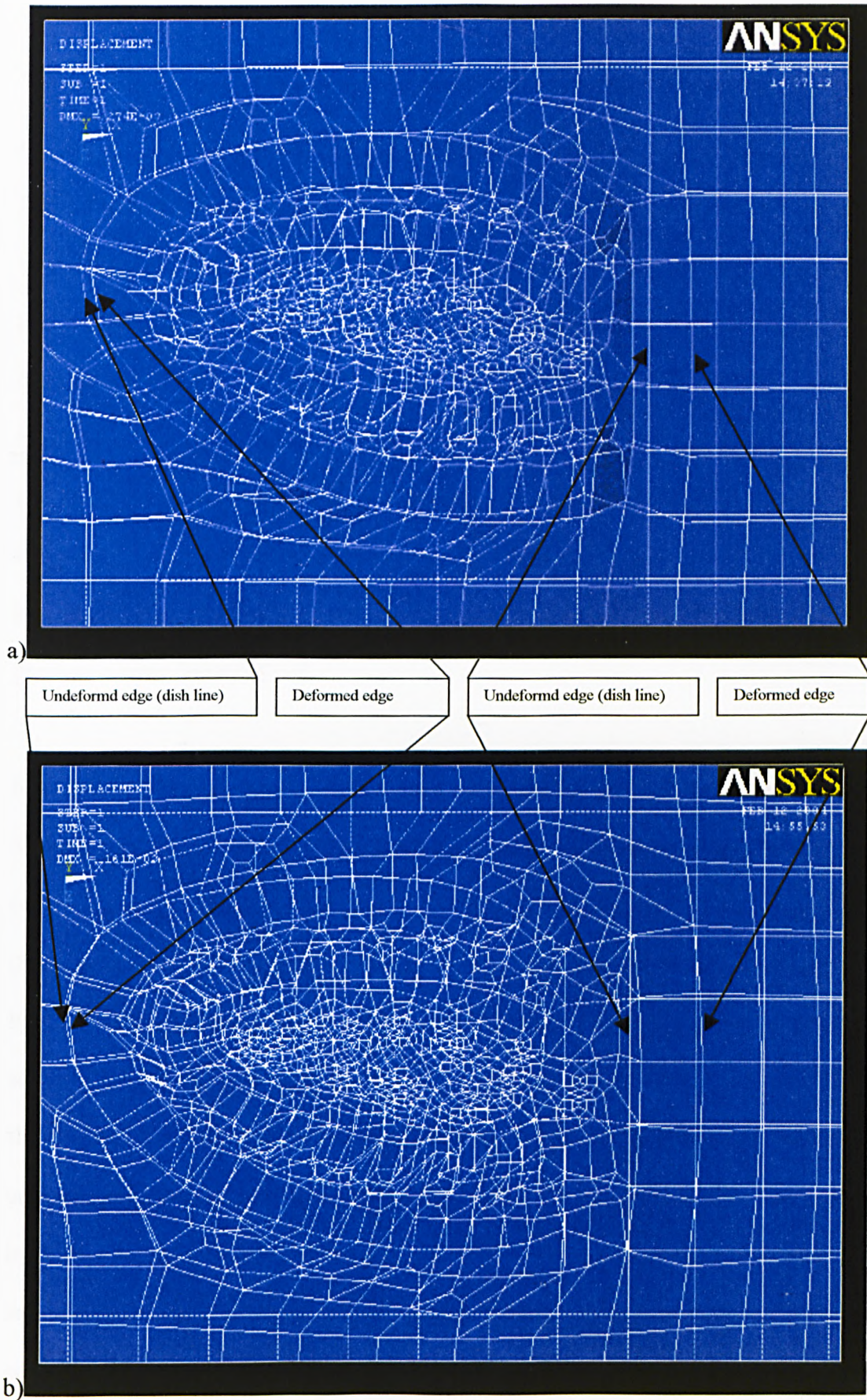
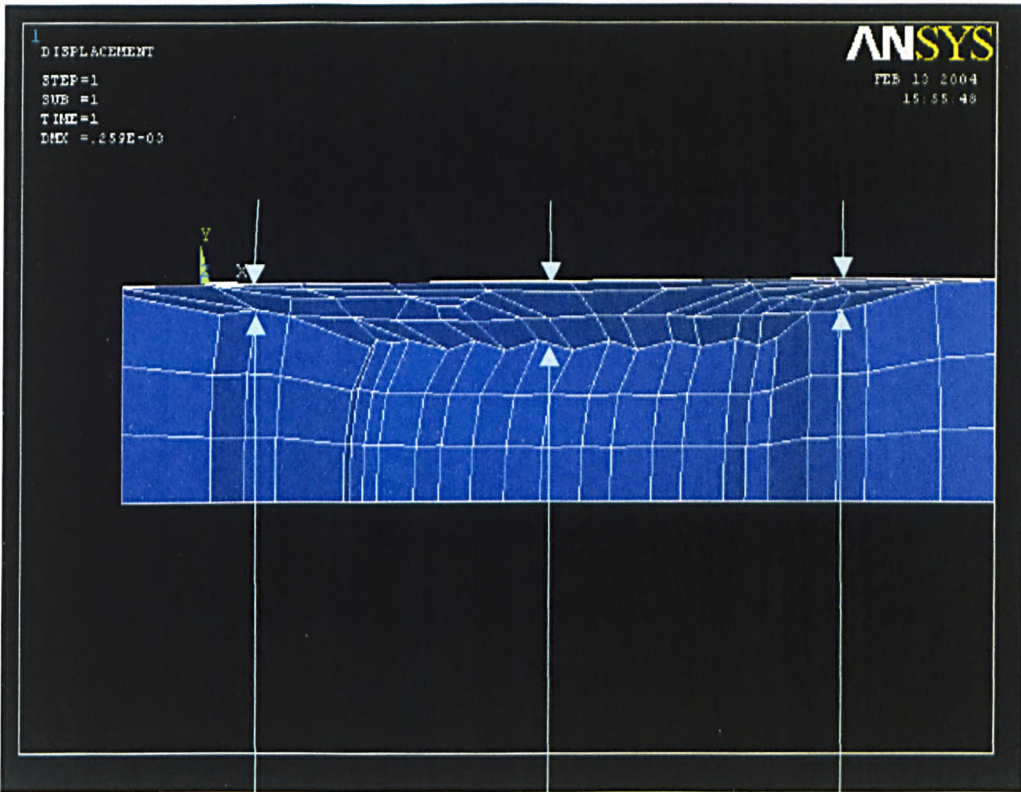


Fig. 6.13 Soil deformation at a) $Y = 0$, b) $Y = -0.056^2/3$ m (by referring Fig. 6.7)

$Y = 0$ to $Y = -0.056^{*2}/3$ m), as indicated by arrows on the left hand side in Fig. 6.13 a), and b). The dish lines indicated by arrows are at the same position in the X-Z plane, but at different depth in the Y direction. Deformed edges reflect the difference of soil deformation extent in the positive X direction. However, at areas related to rear part of forepart, the soil deformation increase progressively in depth at the negative Y direction as indicated by arrows on the right hand side in Fig. 6.13 a), and b). It implies that soil deformation on the top surface interactive with toe part with cleats is greater than the other deeper layers beneath toe of forepart. This FE modelling result is consistent with a phenomenon in a process of gait that slipping occurs firstly at toe part at top soil surfaces if transverse shear load subjected to soil is great enough to produce plastic failure of soil.

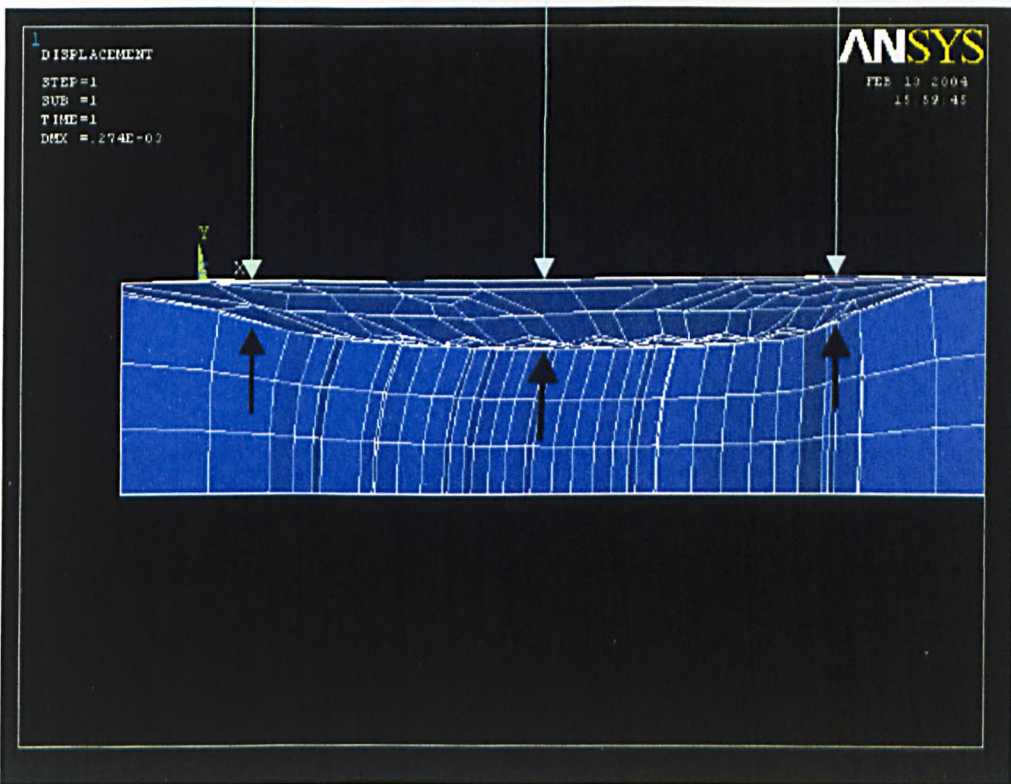
6.4.1.3.2 Soil deformation at cross-section perpendicular to the Z-axis

Secondly, two cross-sections perpendicular to the Z-axis are shown in Fig. 6.14. In order to clearly observe soil deformation in the Y direction, soil model is cut by these cross-sections after removing top layer of elements as shown in Fig. 6.7. Comparing Fig. 6.14 a) to b), soil deformation in depth (the negative Y direction) at middle cross section ($Z = 0.04\text{m}$) is greater than that of at cross section ($Z = 0.01\text{m}$) far away from the middle cross section. Three locations along the X-direction are selected to compare soil deformation in the Y-direction at these two cross sections, as indicated by arrows in Fig 6.14. It is obvious that the soil deformation in the Y-direction at the selected positions at b) cross section is, respectively, greater than that of at a) cross section. This conclusive remark is based on comparison of most positions located at the bottom contour along the X coordinate.



a)

Comparison of soil deformation in depth at the same position in X-direction



b)

Fig. 6.14 Soil deformation at cross-sections, a) $Z = 0.01\text{m}$, b) $Z = 0.04\text{ m}$

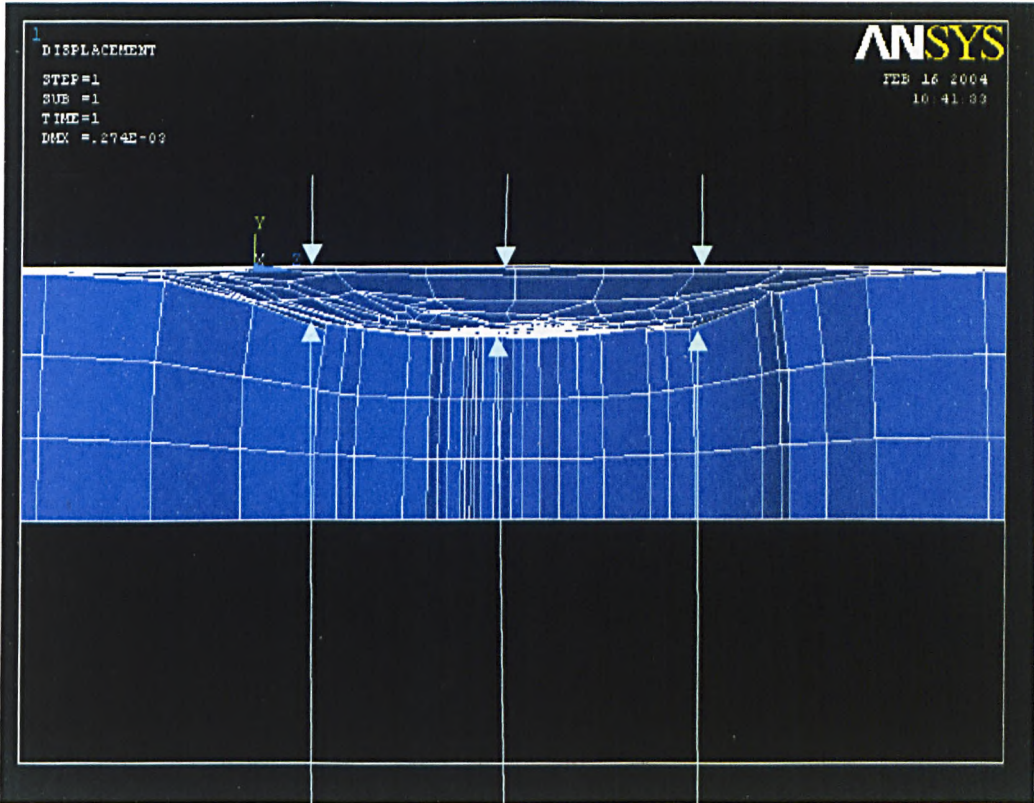
6.4.1.3 Soil deformation at cross-section perpendicular to the X-axis

Finally, two cross-sections perpendicular to the X-axis, as shown in Fig. 6.15 a) and b), are selected to compare soil deformation from left view of the soil model. Similar to the soil deformation patterns shown in Fig. 6.14 a) and b), three locations along the Z-direction are selected to compare soil deformation in depth at these two cross sections, as indicated by arrows in Fig 6.15. It is obvious that the soil deformation in the negative Y-direction at the selected positions at middle cross section ($X = 0.08\text{m}$), as shown in Fig. 6.15 a), is greater than that of at another rear cross section ($X = 0.12\text{m}$) shown in Fig. 6.15 b). This is concluded from comparison of most points located at the bottom contour along the Z coordinate.

Based on the results of soil deformation discussed in Fig. 6.14 and Fig. 6.15, it makes clear that soil mass experiences the maximum deformation in the negative Y direction under and interacting with the central part of forepart of the first tread pattern.

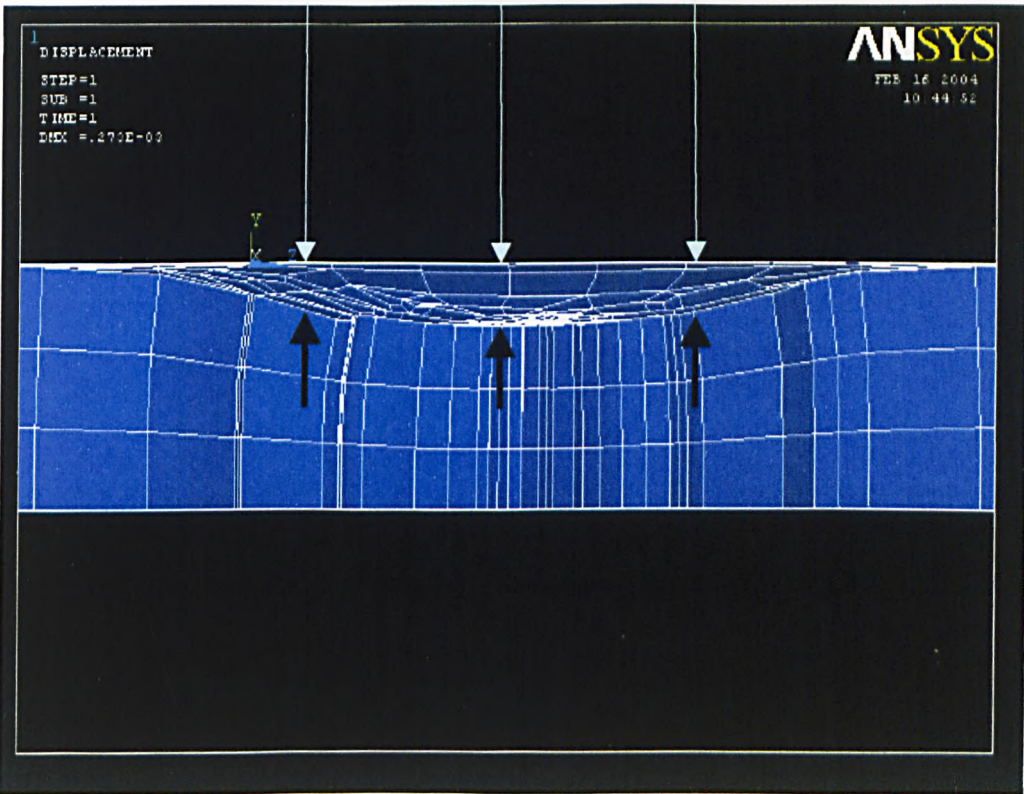
6.4.1.4 Soil stresses

Fig. 6.16 shows the stress fields caused in the whole soil mass in the direction of traction force (the X-direction) after the particular loading conditions applied as described in section 6.3.1.2. As shown in Fig. 6.16, much greater compressive stresses in traction force direction were distributed at regions contacting middle and rear part of tread pattern in the top elements layer of the F. E. model. Tensile stresses are emerged, as shown in brown in Fig. 6.16, in the zone between left boundary ADKH of the soil FE model (referring Fig. 6.7) and toe part of outsole in the X direction.



a)

Comparison of soil deformation in depth at the same position in Z-direction



b)

Fig. 6.15 Soil deformation at cross-sections, a) $X = 0.08$ m, b) $X = 0.12$ m

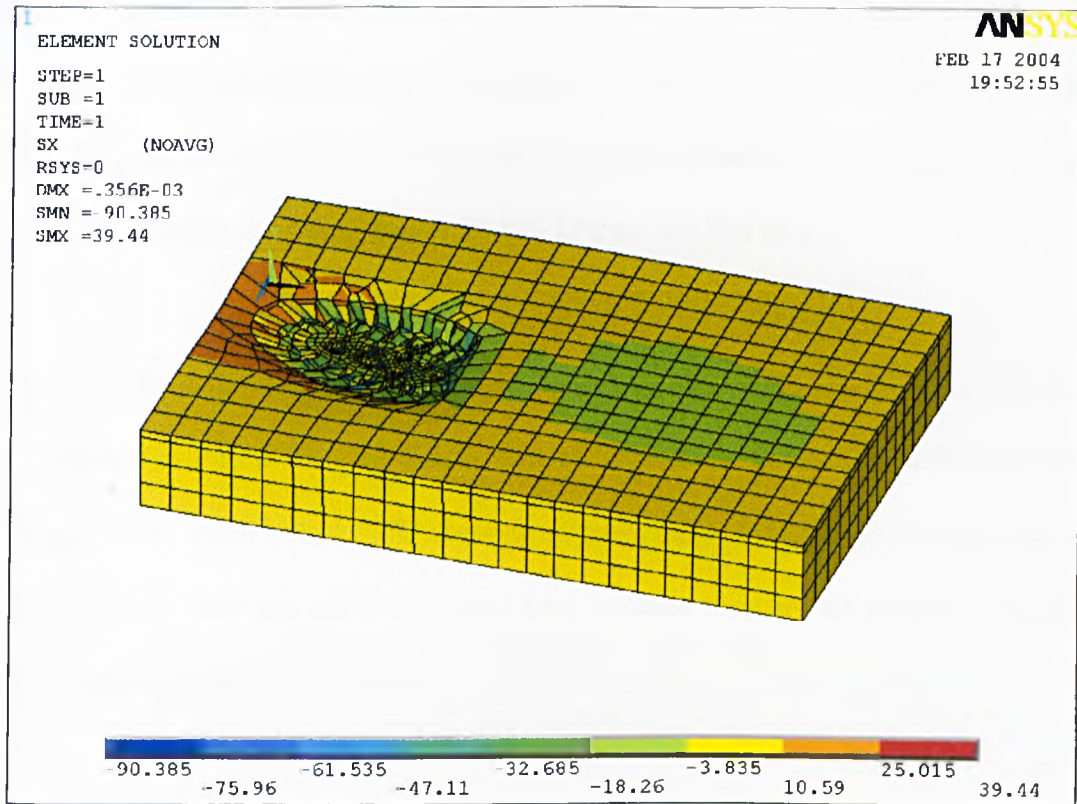


Fig. 6.16 Element solution for stresses in the X-direction

The stress distribution for the first tread pattern is unique and there is a stress image similar to the first tread pattern contour on the top layer of elements.

Stress fields caused on the whole soil mass in vertical direction (Y coordinate direction) is different from that of in X coordinate direction. Plastic yielding exists in negative Y direction within all elements in the whole soil mass, therefore the stresses in negative Y direction within most of all elements in the zone of plastic yielding are nearly the same, that is -8.96 kPa. The stresses within elements under forepart of outsole are ranging from -21.057 kPa to -69.533 kPa.

Stress distribution on the whole soil mass in the Z direction is also different from above. The stresses within in elements surrounding to contour of forepart are positive. Whereas, the stresses within other elements in most of zone of soil mass are negative and same, that is -12.125 kPa. The stresses within elements around cleats of forepart are also negative but varying from -12.125 kPa to -67.104 kPa.

The hydraulic static stresses are equal to $\frac{1}{3}(S_X + S_Y + S_Z)$. The S_X component has been shown in Fig. 6.16. The distribution of hydrostatic stresses is similar to that of S_X and S_Z to some extent. The shearing stresses caused within all elements are also calculated, but they are not commented here because they are all smaller or equal to the minimum compressive stresses.

As discussed above, the stresses distributions in the X, Y and Z direction indicates that the stresses field around cleats of forepart is complex in nature owing to complicated geometry shapes and configuration of tread pattern, and the stress field in other zone of soil mass displays particular pattern and law. These will be analyzed by comparing with the other four tread patterns in section 6.6.

6.4.1.5 Soil strains

Since the soil undergoes elastic and plastic deformation under loading conditions in transverse and vertical directions, the resulting total strain is composed of elastic strains and plastic strains.

6.4.1.5.1 Soil elastic strains

The element solution of soil elastic strains in the X direction is shown in Fig. 6.17 for forepart of the first tread pattern. As shown in Fig. 6.17, elastic strains in the X direction reaches a maximum tensile strain, 0.004337 on toe position; the regions between left boundary and contour of toe as well as some small regions contacting cleats experiences peak tensile strains within top layer of elements between 0.000109

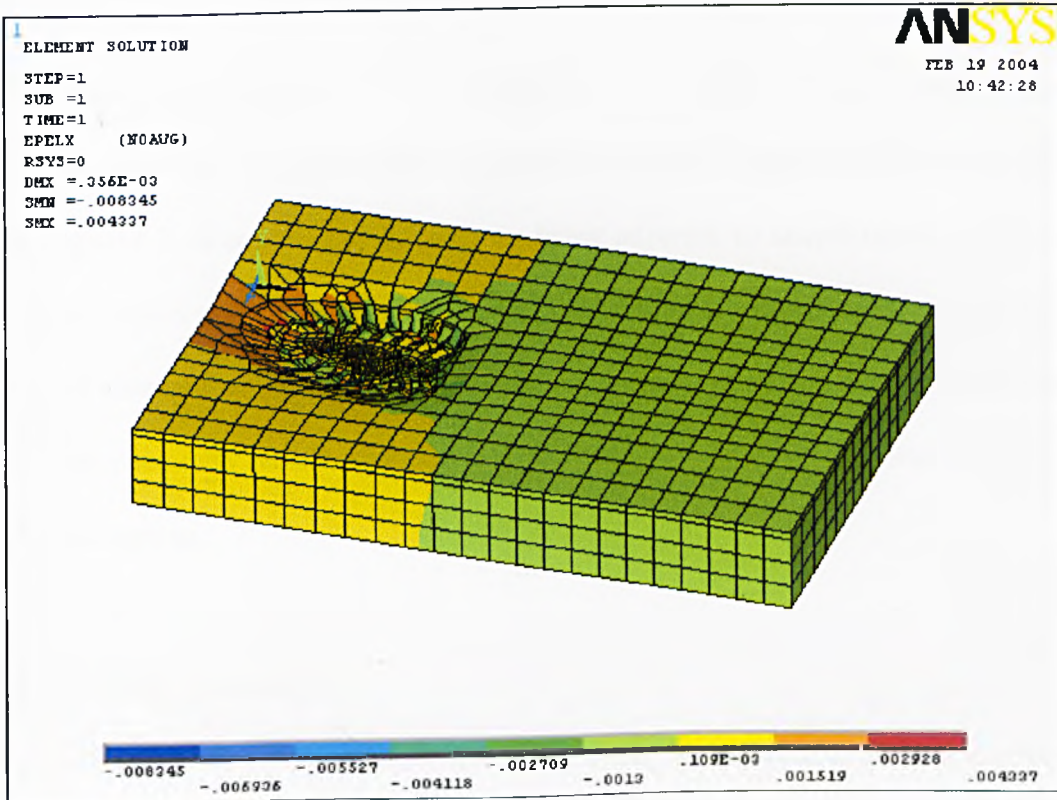


Fig. 6.17 Element solution of elastic strain in the X-direction

and 0.001519. This result is consistent with stress distribution in Fig. 6.16. The strain distribution in most of other regions is more uniform as compressive strains, -0.002709, and smaller tensile strains, 0.000109 affected by local tensile stresses as distribution shown in Fig. 6.16.

Elastic strains distribution in the Y direction is similar to that of stresses distribution in the Y direction. That is to say the regions under the forepart experiences peak strains in the negative Y direction, and the other parts within left half of entire soil model reaches an uniform compressive strains, -0.001618. An exception for this case is that all elements within right half of whole soil model slightly experiences uniform tensile strains, 0.000151. This maybe results from squeeze of left half of soil mass.

Elastic strains distribution in the Z direction is also similar to stresses distribution in the Z direction that most of regions experiences smaller uniform strains, -0.001002, in the negative Z direction, and the regions being adjacent to lateral contour of forepart of tread pattern undergoes smaller strains in the positive Z direction. However, the top layer of elements within regions between left boundary and toe part of tread pattern does not encounter tensile strains, which is contrary to stresses distribution pattern in only this regions.

6.4.1.5.2 Soil plastic strains

Fig. 6.18 shows situation of plastic strains in the X direction. It is obvious that plastic yielding does not occur within most of elements, that is plastic strain is zero in the X direction under certain loading conditions in vertical and traction force directions as presented in section 6.3.1.2. However, a few small regions still experience plastic yielding in the X direction as shown in Fig. 6.18, a magnified top view of soil model respect to plastic strains in the X direction. All plastic strains are in the positive X direction, that is traction force direction, and to range between 0.000152 and 0.001372. The maximum plastic strain reaches 0.001372 within one element among all elements at the top layer of and is located at left hand side of tread pattern's

contour. It is expected that further plastic yielding will develop in other elements until whole elements reach a state of plastic yielding or failure, if loads in traction force direction are intentionally applied greater than the prescribed value described in section 6.3.1.2.

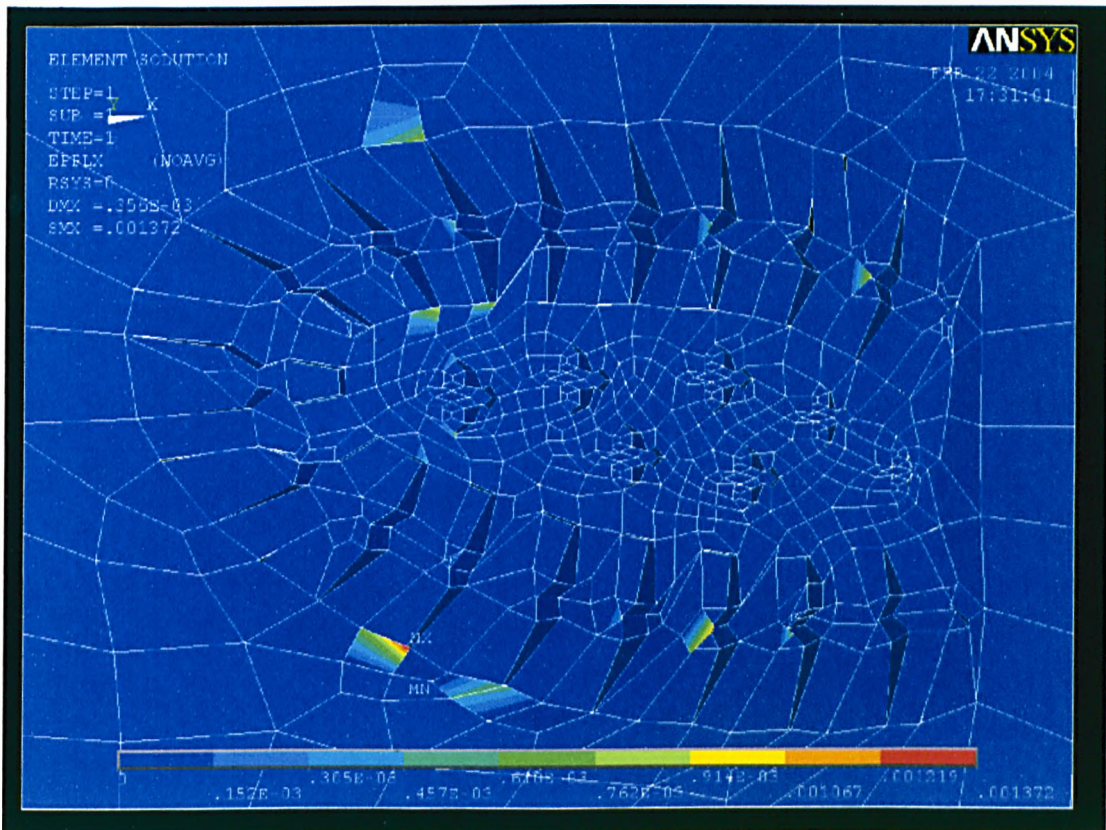


Fig. 6.18 Element solution of plastic strain in the X-direction

Plastic strains in the Y direction are rather uniform. Because the vertical load is greater enough, the entire elements of soil model experience plastic strains, and finally reach a uniform value, -0.0000475, in direction of vertical loading, that is the negative Y direction. Plastic strains at only a few locations are greater than this uniform value in the negative Y direction, and one location shows plastic strain in the positive Y direction. However, these tiny differences do not violate the entire situation of plastic strains in the Y direction.

Most of the elements experience plastic strains in the negative Z direction, and reach a consistent value -0.0000289 . Only a few regions develop plastic strains in the positive Z direction ranging between 0.0000907 and 0.001047 . It is anticipated that plastic strains in the negative Z direction will continue to develop if the Z-component of transverse loading increases after the first load step or it is greater enough than the prescribed loading conditions presented in section 6.3.1.2.

6.4.2 Modelling Results and Discussion of Soil Interactive with Heel

6.4.2.1 Soil deformation

The nodal solution of soil displacement in the X direction interactive with heel of the first tread pattern is shown in Fig. 6.19. From Fig. 6.19, it can be seen that all soil

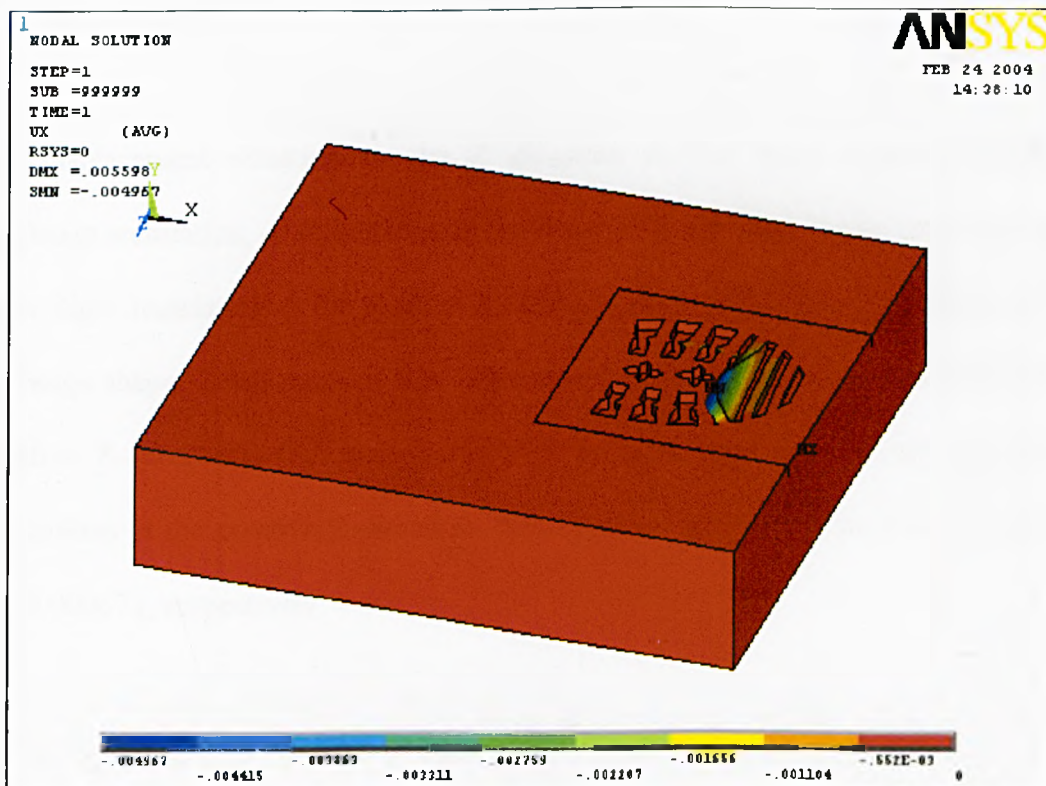


Fig. 6.19 Soil displacement in the X direction (nodal solution)

displacements occurs in the traction direction (the negative X direction), and the maximum translation, -0.004967m , in the traction direction takes place in regions in front of the third column straight cleat counting from right end-side of heel. All other regions experience uniform minimum translations, -0.000552m .

The situation of soil deformation in the Y direction is that most regions occurs uniform translation, -0.000501m , in the negative Y direction (the vertical loading direction). Regions under central part of heel experience greater translation, -0.001041m , that is two times greater than the uniform translation in the negative Y direction. Magnificent translation in the positive Y direction happens within soil in front of the third column straight cleat counting from right end-side of heel. It indicates that plastic failure remarkably occurs within this regions and the slip surface has a bulge shape.

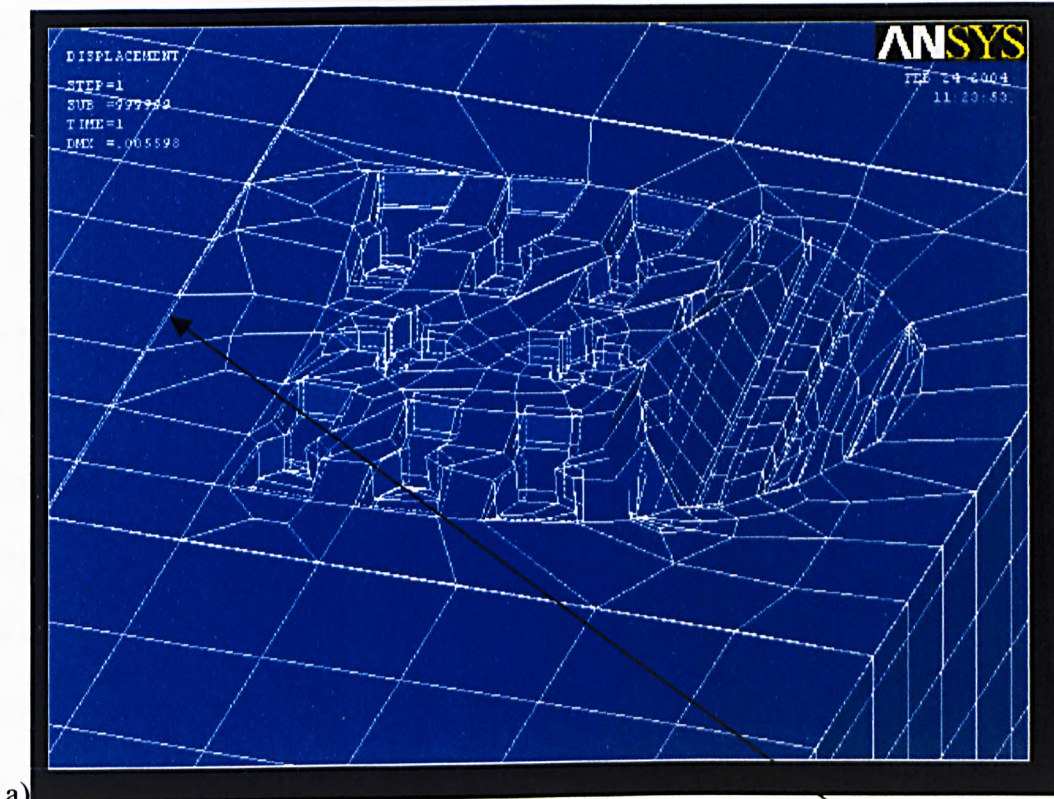
Soil displacement situation in the Z direction is that most regions experience consistent translation, -0.0000816m , in the negative Z direction except that some parts show slight translation in the positive Z direction. Opposite translations occurs within the bulge shape. Small parts of it at left position show progressive translations in the negative Z direction, and most parts of it at right hand side display progressive translations in the positive Z direction. The extreme values of them reach -0.000296 and 0.000671 , respectively.

6.4.2.2 Discussion

A group of different horizontal layers of elements are selected and as shown in Fig. 6.20 a) and b). Fig. 6.20 a) and b) shows soil deformation on top layer of elements and the lowest layer of elements, respectively.

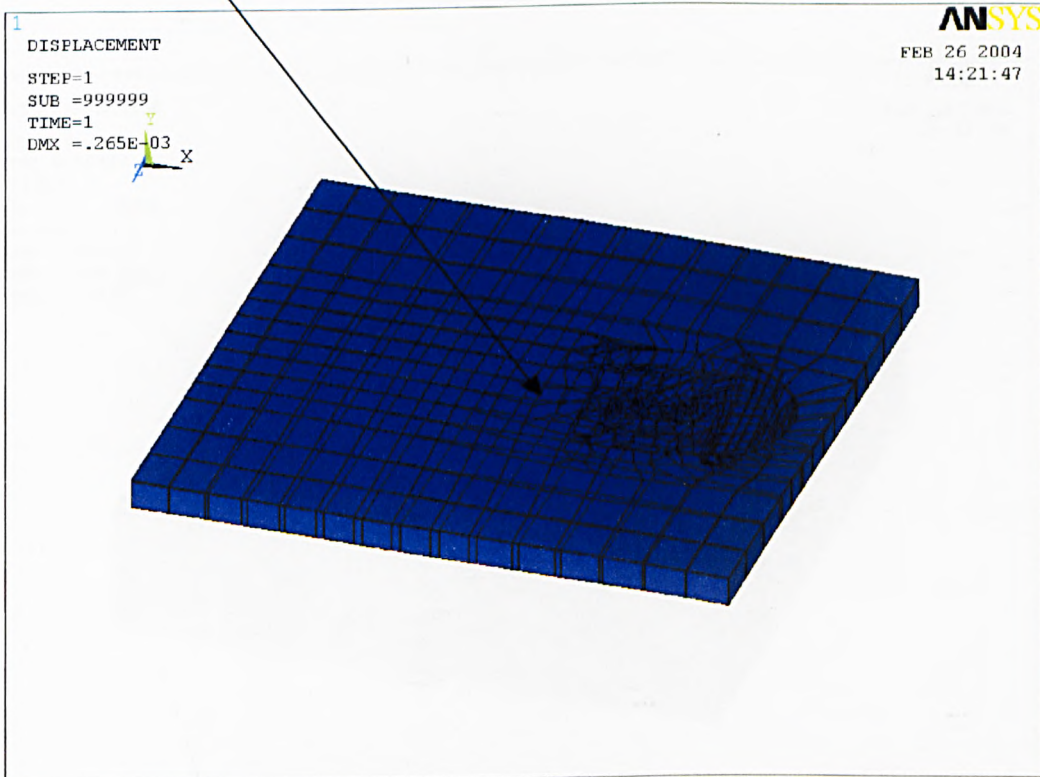
It is obvious that soil deformations in the horizontal plane progressively become larger in the direction of the negative Y coordinate (dash lines are original shapes before applying load). Soil deformation at the lower layer of elements is greater than that of the upper layer of elements as indicated by arrows in Fig. 6.20. In general, the situation of soil deformation interactive with heel is different from that of forepart of the first tread pattern. For instance, the tendency of soil deformation at toe part shown in Fig. 6.20 is opposite to that of in Fig. 6.13. That is soil deformation interactive with forepart at the lower layer of elements is less than that of the upper layer of elements. The loading condition is the main cause of this difference in soil deformations. Loads acted on the soil-heel FE model is much greater than that on the soil-forepart FE model as described in section 6.3.1.2 and 6.3.2.2. Different geometry sizes between soil-heel FE model and soil-forepart FE model maybe affect the soil deformation situations as well.

Generally, the deformation of the soil contacting heel with cleats is greater than the other regions far away from the heel, and magnificent plastic failure occurs within soil mass in front of the third cuboid cleat counting from right end-side of heel. The resultant vector results show that the maximum displacement occurs within regions in front of the third cuboid cleat counting from right end-side of heel, and reaches peak of 0.005598 comparing to 0.000356 of soil-forepart modeling results. Most large



a)

Soil deformation at the same location but different layers



b)

Fig. 6.20 Soil deformations in a) top layer of elements, b) the lowest layer of elements

displacements happen within regions contacted by the tread pattern and under the tread pattern. The other regions of soil experience very small uniform displacement.

6.4.2.3 Soil stresses

The nodal solution of soil stresses in the direction of traction force (the X direction) is shown in Fig. 6.21 for heel of the first tread pattern. Fig. 6.21 shows the stress fields in the whole soil FE model, caused by the prescribed loading conditions as described in section 6.3.2.2. Most regions experience uniform stresses to range between -53.932 kPa and 25.031 kPa. Regions beneath tread pattern undergo progressive compressive stresses ranging from -132.895 kPa to -685.639 kPa. The extreme value, -685.639 kPa, emerges at top position of the regions in front of the third column straight cleat counting from right end-side of heel.

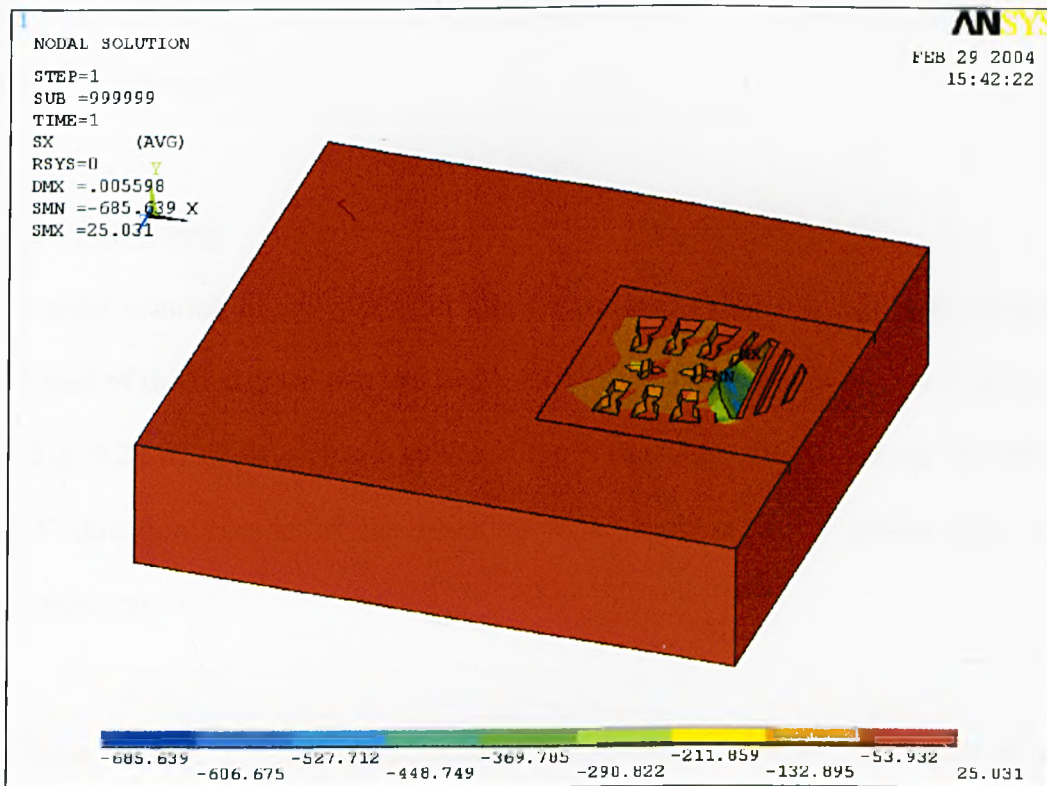


Fig. 6.21 Nodal solution of soil stresses in the X direction interactive with heel

Stresses distribution pattern in the Y direction is similar to that of in the X direction as shown in Fig. 6.21. That is most regions experience uniform stresses, but the distribution range is wider from -121.549 kPa and 24.756 kPa. Only a few regions, including the region in front of the third column straight cleat counting from right end-side of heel, develop greater compressive stresses in magnitude and the extreme reaches -1292 kPa at same location as that of peak value of the total strain in the Y direction (see subsection 6.4.2.4).

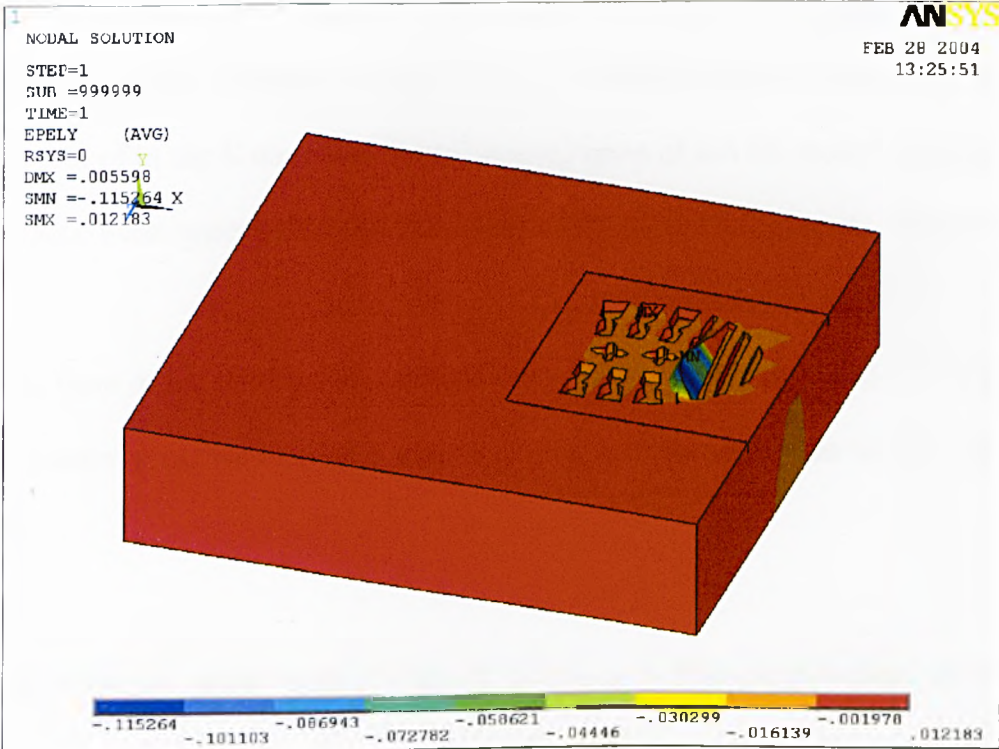
The distribution patterns of stresses in the Z direction is quite similar to that of in the X direction displayed in Fig. 6.21, and these stresses level is close to each other in magnitude.

The hydraulic static stress's distribution pattern is also very similar to that of in the X or Y or Z directions.

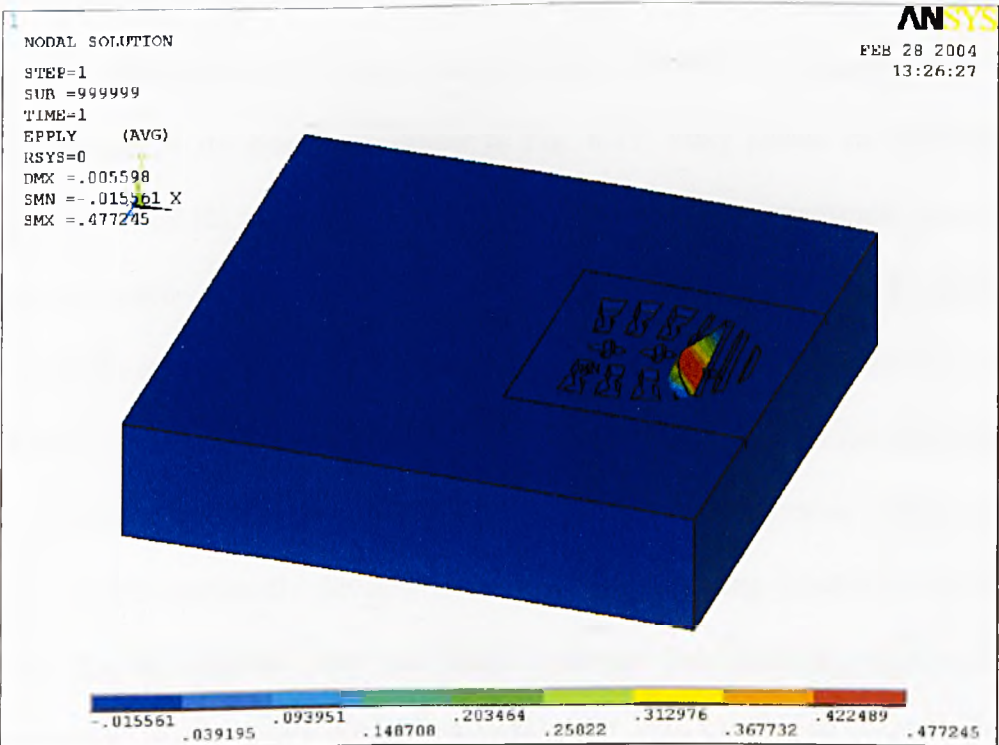
6.4.2.4 Soil strains

The nodal solution of soil strains in the Y direction is shown in Fig. 6.22 interactive with heel of the first tread pattern. Fig. 6.22 a) shows elastic strains in the Y direction, and Fig. 6.22 b) displays plastic strains in the Y direction. Elastic and plastic strains in the Y direction consist of the resulting total strain in the Y direction by linear superposition.

As shown in Fig. 6.22 a), elastic strains reach a uniform value, -0.001978 , in most regions. Regions around cleats experience further compressive elastic strains and the



a)



b)

Fig. 6.22 Soil strains in Y direction with heel, a) elastic strain, b) plastic strain

maximum value, -0.115264, appears in the region where the maximum translation occurs. The situation of plastic strains in the Y direction shown in Fig. 6.22 b) is similar to that of in the X direction. That is entire region of soil FE model experiences plastic strains. Most regions undergo consistent compressive plastic strain, -0.015561.

Regions in front of the third column straight cleat counting from right end-side of heel develop greater progressive tensile plastic strains and the maximum value reaches 0.477245.

The distribution of elastic strain in the X direction is that most regions develop uniform compressive elastic strains, -0.008312. Regions around cleats experience either further compressive elastic strains or tensile elastic strains. Tensile elastic strains also develop in regions between right-hand side boundary and around rear part of heel. The maximum tensile elastic strain reaches 0.046605 in region where the maximum translation developed as shown in Fig. 6.19. Fully plastic strains exist in whole regions of soil FE model in the X direction. Most regions experience consistent compressive plastic strain, -0.003294. Regions, where progressive translations develop until the maximum translation reached, as shown in Fig. 6.19, develop greater tensile plastic strains and the maximum value reaches 0.13383. It indicates that plastic yielding or failure has happened in the regions where the maximum plastic strain exists, and it will continually develop if the prescribed loading conditions are kept acting on. This is consistent with the failure criterion from plasticity theory of an elastic-perfectly plastic material—Drucker-Prager material model reviewed in Chapter 3.

The situation of elastic strains and plastic strains in the Z direction is presented as follows. Most regions experience uniform elastic strains, -0.003924 , in the negative Z direction. Regions around or close to cleats undergo elastic strains either in the negative Z direction or the positive Z direction ranging between -0.027784 and 0.015164 . The two extreme values appear in the regions in front of the third column straight cleat counting from right end-side of heel. Most regions experience consistent plastic strain, -0.003717 , in the negative Z direction. A few regions around or close to cleats develop plastic strains either in the negative Z direction or the positive Z direction, and the extreme value in the negative Z direction also occurs in same region as where the extreme elastic strain happens. But the maximum plastic strain in the positive Z direction emerges in some other small regions other than region where the maximum elastic strain develops.

6.5 The Second, Third, Fourth and Fifth Tread Patterns

6.5.1 Introduction

Having successfully conducted FE modelling for soil material interactive with forepart and heel of the first tread pattern, it becomes a reality to model more tread patterns based upon the methodology achieved in the study of the first tread pattern. In total, five tread patterns are investigated in this study by using Finite Element Method, so as to judge which tread pattern can provide with the best traction force effect as well as other good effects. Therefore, the study for the second, third, fourth and fifth tread patterns will be briefly presented in this section.

Since the main purpose of this study is to identify which kind of tread pattern is the best concerning traction force effect and the tread pattern on the forepart of the outsole dominates the main features of tread pattern design, only the forepart and the interactive soil FE models are built up for the second tread pattern, the third tread pattern, the fourth tread pattern and the fifth tread pattern. Analyses of traction force effects about the five tread patterns will be presented in section 6.6 based upon soil FE numerical modelling results interactive with forepart of outsole of the five tread patterns.

The second tread pattern of a military boots is shown in Fig. 6.23. It is a picture of real left-foot boots with the second tread pattern.



Fig. 6.23 The second tread pattern of military boots (left foot)

The third tread pattern of military boots is shown in Fig. 6.24. It is supplied by the UK Ministry of Defence. The third tread pattern is specially designed for military in desert terrain. As seen in Fig. 6.24, area of each cleat is generally greater than that of

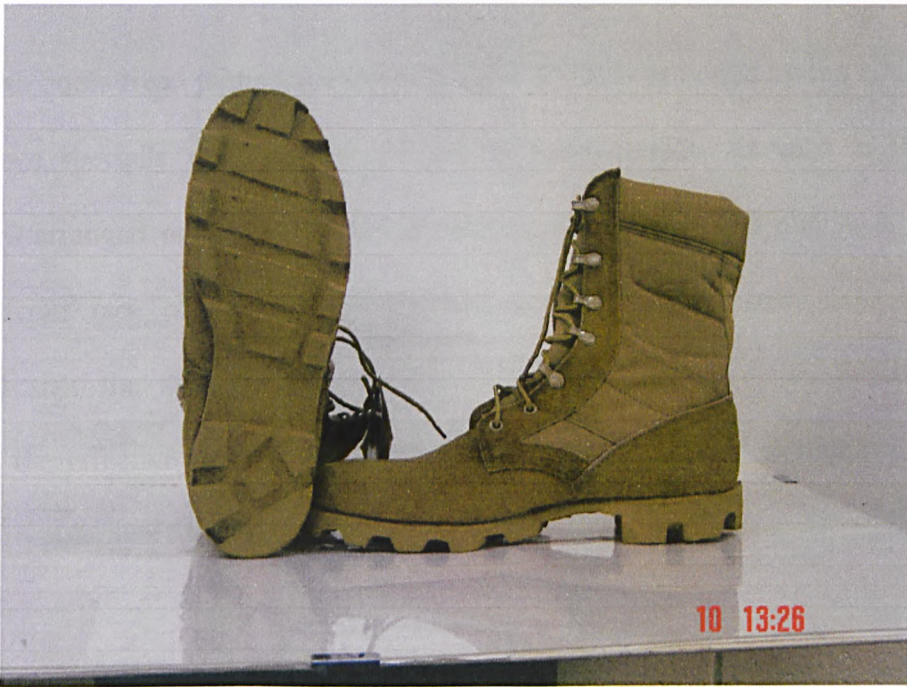


Fig. 6.24 The third tread pattern of military desert boot



Fig. 6.25 The fourth tread pattern of real military boots

conventional boots, so as to prevent sinkage that easily occurs on soft sand surfaces in desert.

The fourth boots tread pattern is shown in Fig. 6.25. It is provided by the UK Ministry of Defence specially designed for military in rough-terrain. As seen in Fig. 6.25, cleats are arranged circumferentially on center points of forepart and heel. Vertical, inner, barrier face of cleats gives traction in every linear, radial direction. It is expected that the staggered positioning between concentric rows of cleats will increase the effective area of the inner, vertical, barrier face of the cleat to engage surface irregularities for grip.

The fifth tread pattern of military boots is supplied by the UK Ministry of Defence. As shown in Fig. 6.26, it is a scanned picture of a drawing specially designed by the UK Ministry of Defence to evaluate various tread pattern designs for using in natural soft ground surfaces.

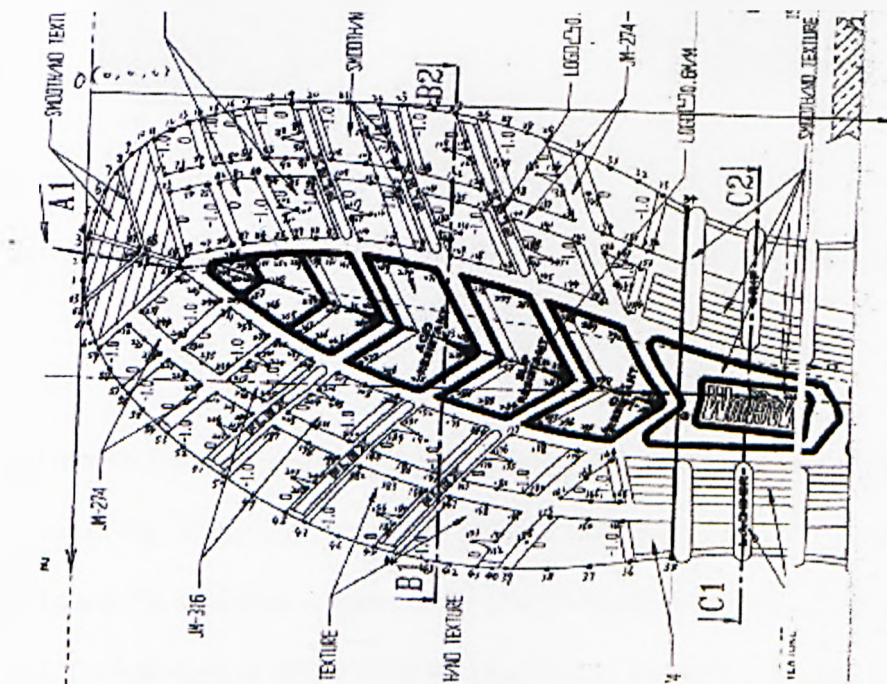


Fig. 6.26 The fifth tread pattern

6.5.2 Highlights of FE Modelling for the Second, Third, Fourth and Fifth Tread

Patterns

6.5.2.1 FE models

Models of forepart of outsole with the second, third, fourth and fifth tread patterns are constructed in ANSYS pre-processor and shown in Fig. 6.27. The soil FE models

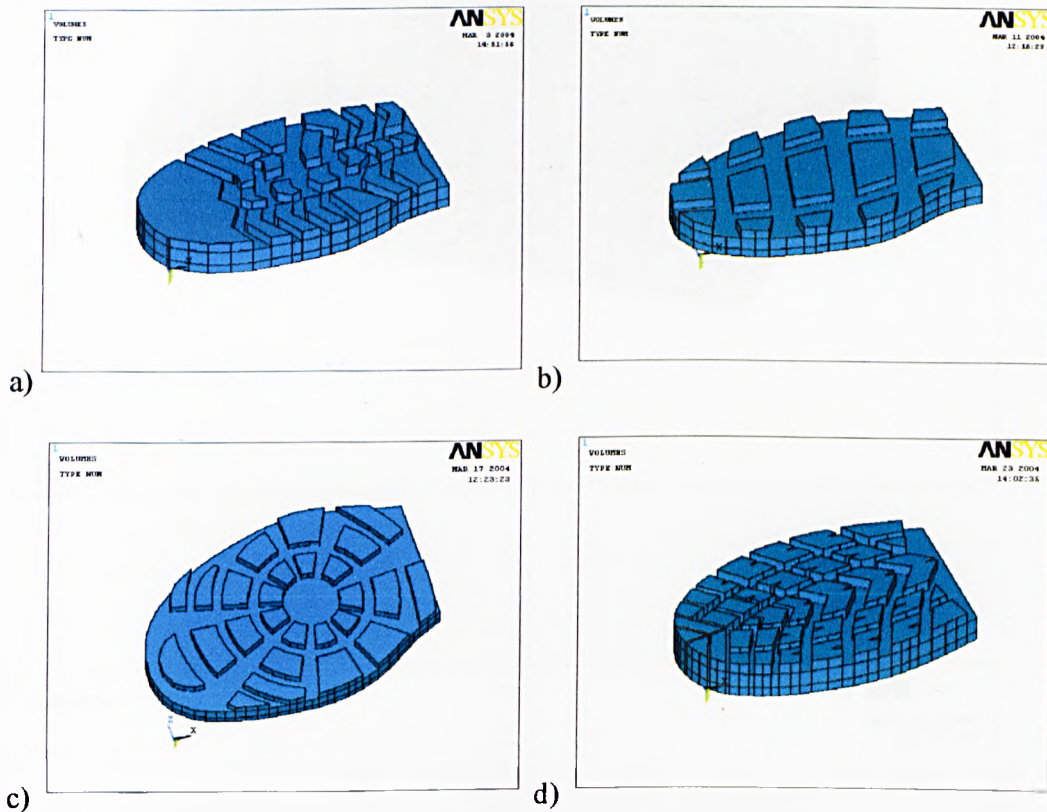
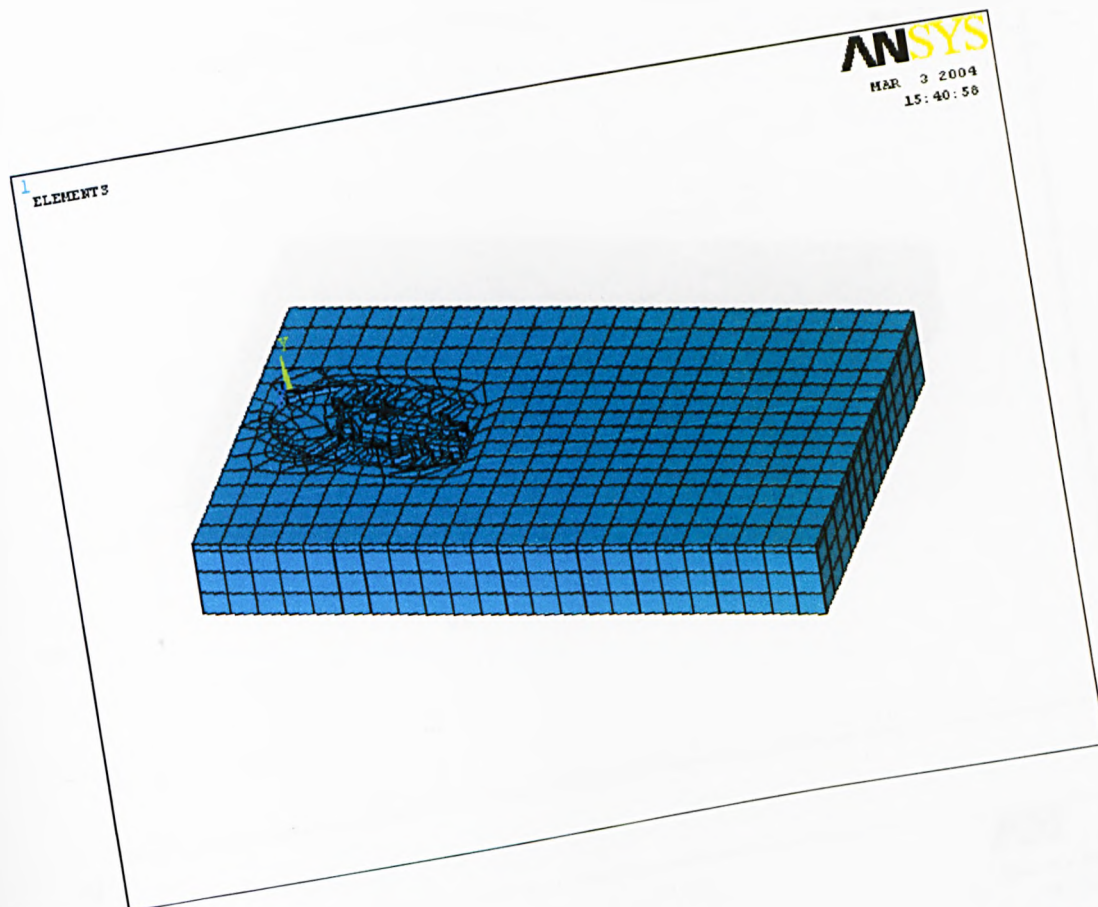


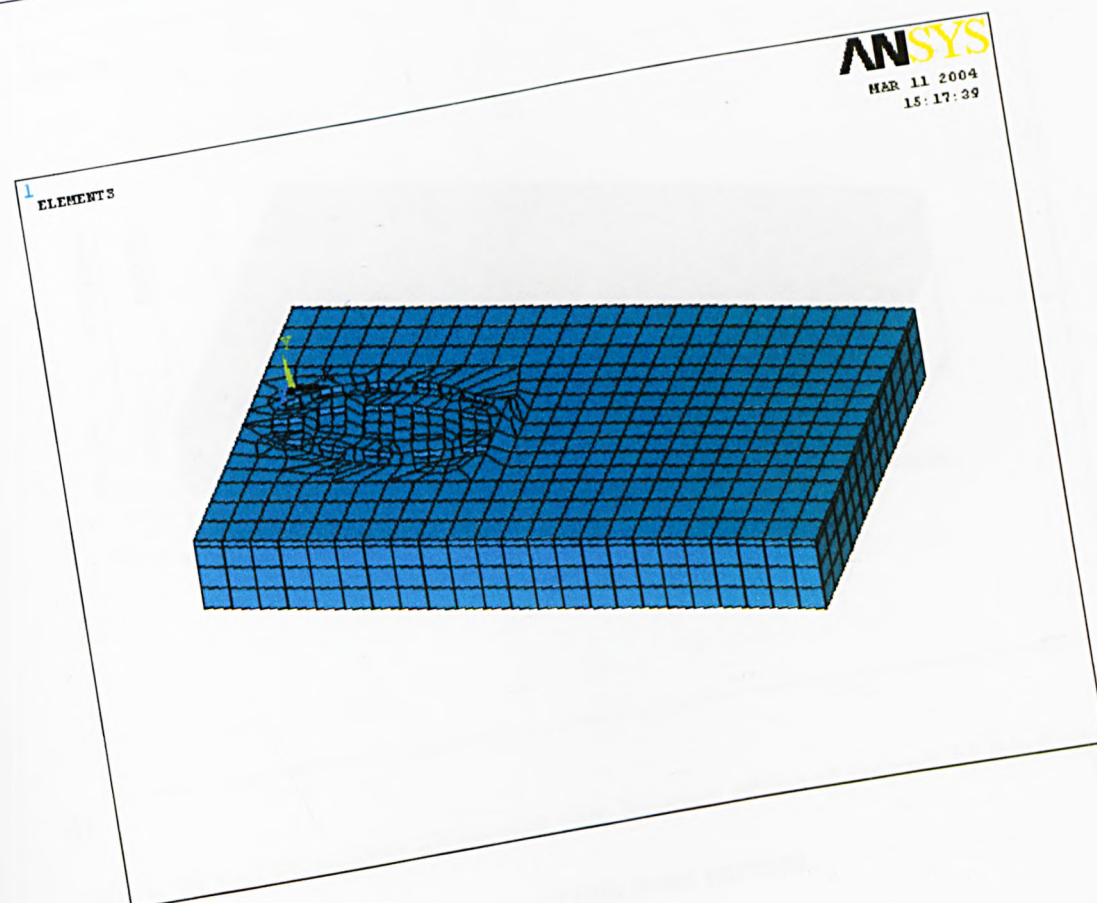
Fig. 6.27 The 3d geometry models of forepart for the a) second, b) third, c) fourth and d) fifth tread patterns

interactive with forepart of outsole of the second, third, fourth and fifth tread patterns are shown in Fig. 6.28. Geometry sizes of these soil FE models are exactly same as that of the soil FE model for forepart of the first tread pattern as shown in Fig. 6.7.

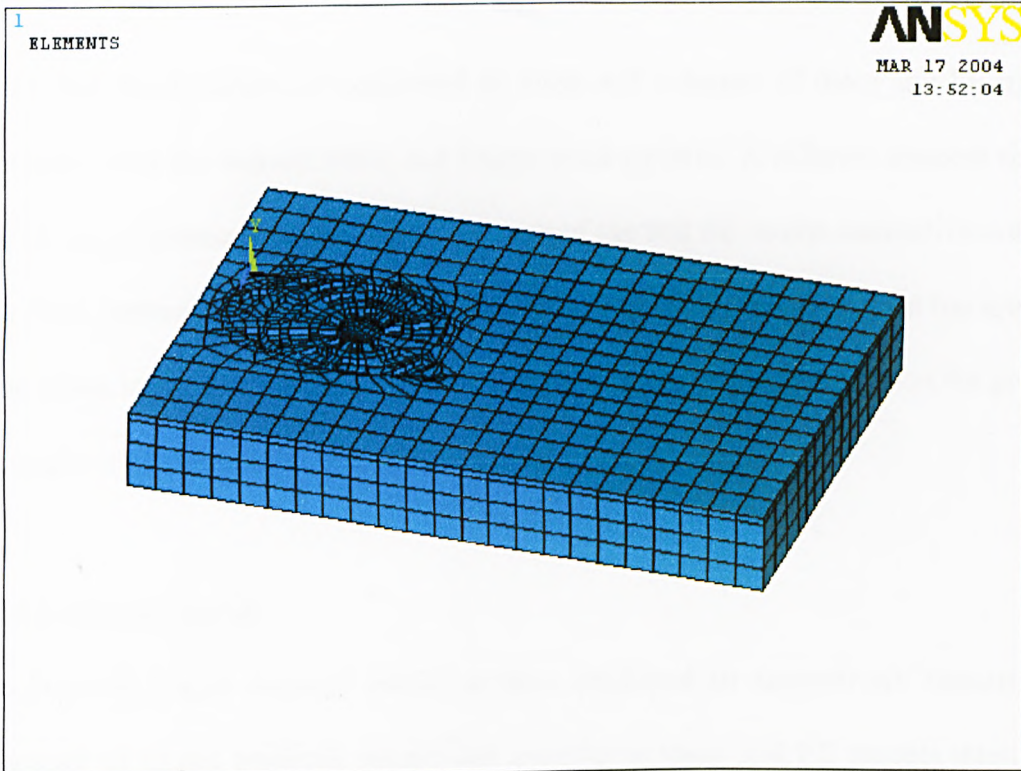
The SOLID45 element in ANSYS FE package is also selected to construct the three-dimensional soil FE model. Also, a basic element size, 0.022m that is same as that



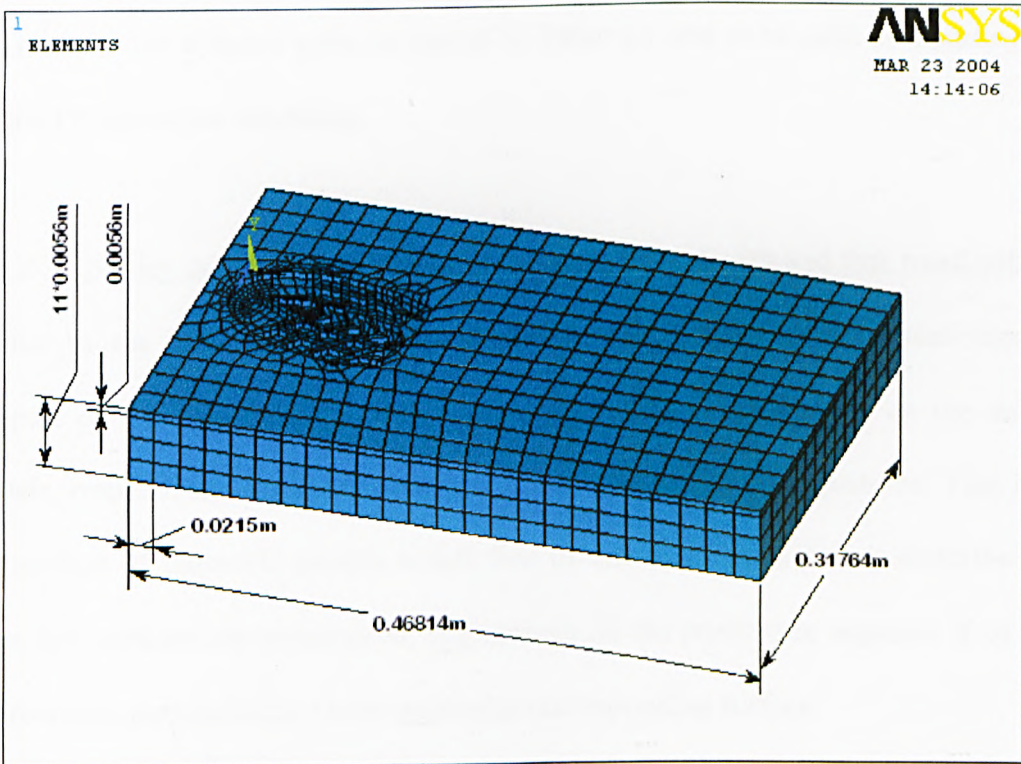
a)



b)



c)



d)

Fig. 6.28 Soil FE models interactive with forepart of the a) second, b) third, c) fourth and d) fifth tread patterns

of the first tread pattern, is optimized to mesh soil volumes of these soil FE models interactive with the second, third, and fourth tread patterns. A different element size, 0.0215 m, is optimized to mesh soil volumes of the soil FE model interactive with the fifth tread pattern. For the second and fifth tread patterns, shallow slots at toe area and some cleats located at middle area of forepart are treated as flat surfaces in the process of constructing the soil FE models.

6.5.2.2 Material model

The Drucker-Prager material model is also employed to respectively simulate the behaviour of elastic perfectly plastic soil material in these soil FE models interactive with forepart of the second, third, fourth and fifth tread patterns. The properties of the soil material are selected same as that of in Table 6.1 and to be used as inputting data for the FE numerical modelling.

6.5.2.3 Solution of soil FE models for the second, third, fourth and fifth tread patterns

Similar to the boundary conditions applied on the soil FE model constructed for forepart of the first tread pattern, boundary conditions are applied on the soil FE models, respectively, for the second, third, fourth and fifth tread patterns. That is the top surface of these FE models is left free of any constraints in any direction. The other five surfaces are constrained, respectively, in the positive or negative X or Y or Z directions, perpendicular to the particular corresponding surface.

Loading conditions are then applied on the constrained soil FE models, respectively, for the second, third, fourth and fifth tread patterns. The methodology of applying

loading conditions used in these numerical modelling processes is same as that of used in for the first tread pattern as reported in section 6.3.1.3. Since the total area of the surfaces sustaining vertical forces of the second, third, fourth and fifth tread patterns is different from each other and also different from that of the first tread pattern as well as item of the total area bearing transverse shear forces, the resulting loads—total vertical and transverse pressure of the second, third, fourth and fifth tread patterns are, therefore, different from each other and also different from that of the first tread pattern, even though the total vertical force and transverse force are purposely set to be identical for the five tread patterns so as to compare their traction force effect based upon identical comparison criterion. As results, the average vertical pressures for the five tread patterns are listed below:

The first tread pattern: $P_V = 33.252 \text{ kPa}$

The second tread pattern: $P_{SV} = 34.283 \text{ kPa}$

The third tread pattern: $P_{TV} = 30.303 \text{ kPa}$

The fourth tread pattern: $P_{FV} = 20.661 \text{ kPa}$

The fifth tread pattern: $P_{FfV} = 36.232 \text{ kPa}$

From the list, the average vertical pressure of the third tread pattern is 8.9% smaller than that of the first tread pattern, 11.6% smaller than that of the second tread pattern and 16.4% smaller than that of the fifth tread pattern. It is obvious that the smaller average vertical pressure of load for the third tread pattern design will improve effect to reduce sinkage extent of the military boots in desert terrain as mentioned in section 6.5.1.

The average transverse shear pressures for the five tread patterns are grouped below:

The first tread pattern: $P_{at} = 48.719 \text{ kPa}$

The second tread pattern: $P_{Sat} = 37.254 \text{ kPa}$

The third tread pattern: $P_{Tat} = 82.547 \text{ kPa}$

The fourth tread pattern: $P_{Fat} = 52.553 \text{ kPa}$

The fifth tread pattern: $P_{Fifat} = 65.299 \text{ kPa}$

Comparing to the first tread pattern, the average transverse pressure of the second tread pattern is 76.5% of it, 169.4% of it for the third tread pattern, 107.9% of it for the fourth tread pattern, and 134.0% of it for the fifth tread pattern. As shown in above list, the third tread pattern acts on the maximum average transverse pressure to the soil. It is, therefore, anticipated that much greater elastic and plastic strains of soil interactive with the third tread pattern will occur than that of the first tread pattern.

After vertical and transverse pressures are loaded, numerical modelling is successfully carried out for the second, third, fourth and fifth tread patterns, and convergent solutions are obtained respectively. These modelling results will be comparatively analysed in the following section.

6.6 Analysis of the FE Modelling Results for the Five Tread Patterns

6.6.1 Introduction

Having successfully conducted numerical modelling for the five tread patterns, it is available to comparably analyze the modelling results. Analyses are undertaken associated with the forepart of outsole of these five tread patterns. Traction effect,

sinkage effect, lateral stability, soil deformation, stress and strain distribution, etc. are, respectively, evaluated in detail in the following sub-sections. The five tread patterns in plane are grouped as shown in Fig. 6.29, so as to conveniently compare and refer them.



Fig. 6.29 The a) first, b) second, c) third, d) fourth, e) fifth tread patterns in plane

6.6.2 Traction Effect

As mentioned in section 6.4.1.1, traction effect will be analyzed in this section for the five tread patterns. Traction effect is one of most important factors to judge how good a particular military boots is designed. In case of assumption that no friction exists or friction factor is neglected, the designed tread pattern dominantly influence on the traction effect or function of resisting slip on soft ground due to plastic failure of soil resulting mainly from transverse shear loads initiated by cleats of tread pattern. Having obtained the numerical solutions of the five tread patterns, the traction effect of them can be evaluated by means of reaction forces in the X direction of soil FE model.

Reaction forces are sum of nodal reaction force at all constrained nodes. These reaction solutions consist of the X, Y and Z components, respectively, in global coordinates. The mechanism of using reaction force in the X direction to judge the traction effect of tread pattern is based upon consistency of between soil FE model construction and experiment scheme shown in Fig. 6.2 and/or Fig. 6.3. In these experimental validation studies, the pulling force applied to the soil mass tray is measured in the X direction (traction direction) when plastic failure of soil mass begins to occur. The soil mass tray is mounted on a nearly frictionless roller assembly. The pulling force is, therefore, equally transferred to constrained boundary surfaces of soil mass by the tray containing the soil mass. Equivalent in the FE modelling, all boundary surfaces of soil mass are constrained except the top surface which is left free of any constraints. All constrained nodes involved in these constrained surfaces generate reaction forces reacted to the loading conditions. Under the same certain loading conditions, the soil interacts with tread pattern of different designs and

experiences different deformation processes from elastic deformation to perfectly plastic deformation (Drucker-Prager material model). Comparing to other tread patterns, a particular tread pattern design with best traction effect should have function of producing plastic failure of soil to the minimum extent when plastic failure of soil occurs or produce the maximum reaction forces in the X direction, under the same loading conditions. In other words, the greater the reaction force generated in the X direction is, the better traction effect of the tread pattern design is.

The traction effects represented by reaction forces in the X direction are displayed in Chart 6.1. As seen in Chart 6.1, it is obvious that reaction force in the X direction of the first tread pattern is the greatest of the five tread patterns. Therefore, the first tread pattern demonstrates the best traction effect of these five tread patterns, under the same loading conditions. The third and the fourth tread patterns also show relative better traction effect than the second and the fifth ones. The second tread pattern shows the poorest traction effect of all five tread patterns.

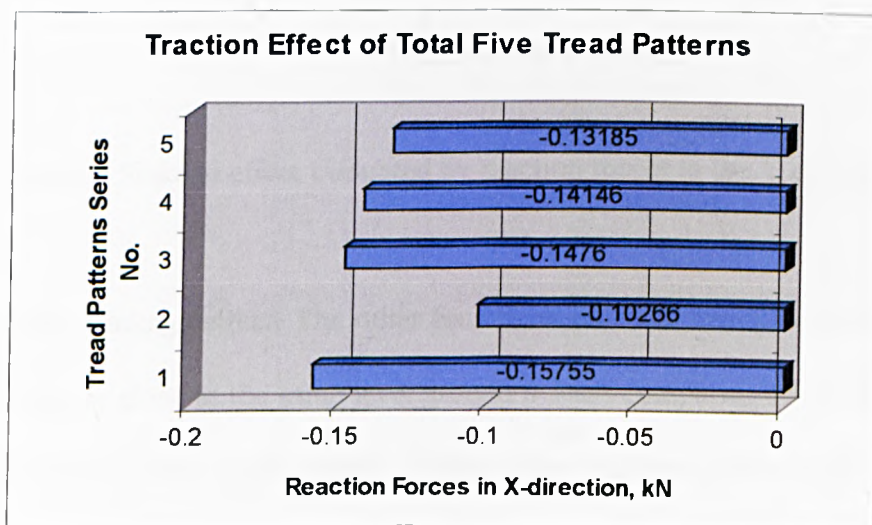


Chart 6.1 Traction effect evaluated by reaction forces in the X direction

6.6.3 Sinkage Effect

For soft surfaces ground, the sinkage effect of tread pattern is also an important factor to judge how the particular tread pattern's function is on the aspect of slip resistance by means of shear capacity of soil. Generally, the more sinkage there is, the more area there is for all transverse surfaces of cleats to sustain shear forces. So, the reaction force in the Y direction is employed to evaluate how the sinkage effect is for the five tread patterns. As shown in Chart 6.2, the fourth tread pattern demonstrates the smallest reaction force in the Y direction under the same loading conditions, and therefore the best sinkage effect. So the fourth tread pattern is the best one of the five tread patterns to utilize shear capacity of soil as well as to enable gripping and

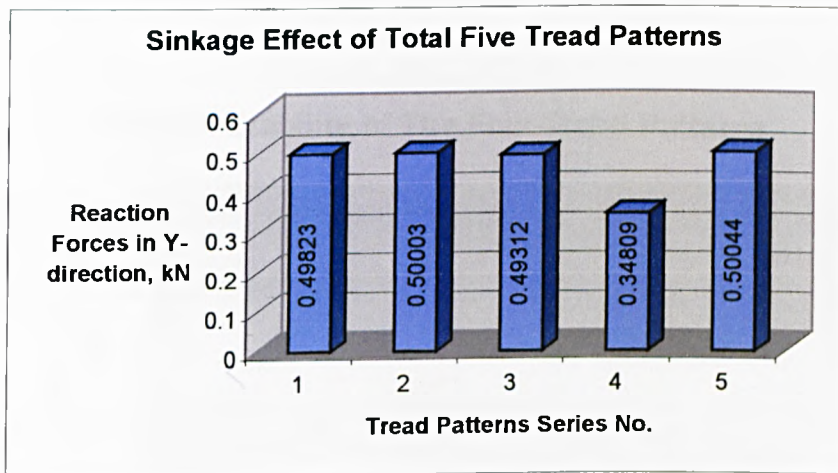


Chart 6.2 Sinkage effect evaluated by reaction forces in the Y direction

pivoting due to sinkage effect. The other four tread patterns' reaction forces in the Y direction are very close at the same level around 0.5 kN comparing to the fourth tread pattern. Therefore, they have similar or the same sinkage effect under the same loading conditions.

6.6.4 Lateral Stability

Good lateral stability of tread pattern design is also an important factor to ensure that injuries caused by lateral slip are reduced to minimum degree. The lateral stability is evaluated by reaction forces in the Z direction. As the lateral slip may occur either in the positive Z direction or negative Z direction, it is obvious that a tread pattern design without lateral slip either in the positive Z direction or negative Z direction is the ideal design. Therefore, the less reaction force in either Z direction is, the better lateral stability is for this tread pattern design. Chart 6.3 shows the FE numerical modelling results of reaction forces in the Z direction for the five tread patterns. As seen in Chart 6.3, the fourth tread pattern obviously demonstrates the best lateral stability of the five tread patterns. The first tread pattern is more prone to lateral slip

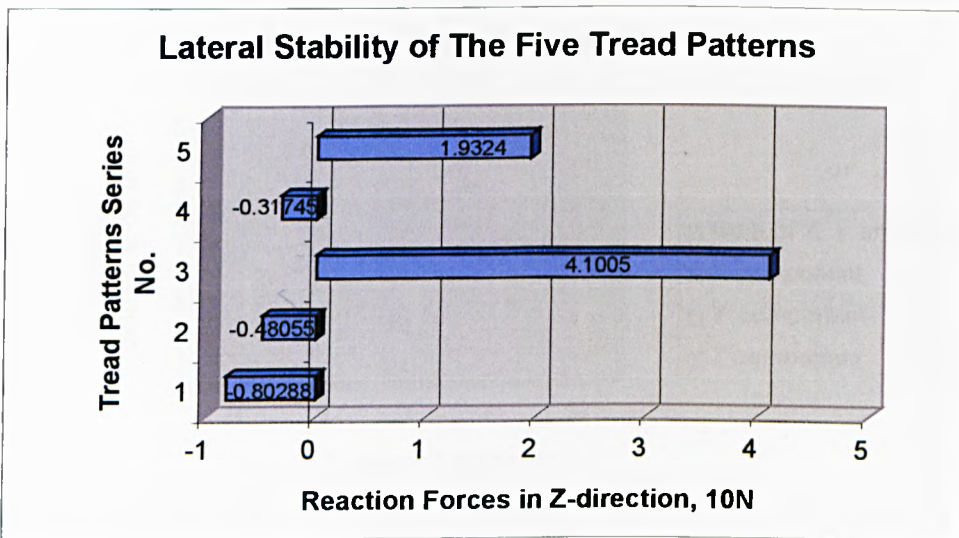


Chart 6.3 Lateral stability evaluated by reaction forces in the Z direction

in the positive Z direction that is outward lateral direction of left foot. The third tread pattern is likely to generate greater lateral slip in the negative Z direction.

6.6.5 Soil Deformation

The soil deformation in this study is complex in nature because of the complex tread pattern geometry and transverse loading conditions. Detailed deformed shape and distribution of the horizontal, vertical and lateral soil displacements have been reported and discussed in sub-sections 6.4.1.2 & 6.4.1.3 in this Chapter 6 for the first tread pattern. Generally, most of greater soil displacements in vector point to the positive X direction, negative Y direction and either positive or negative Z direction for the five tread patterns. It can also be concluded that the maximum soil displacement of them take place within regions contacted by or nearby cleats of the tread pattern and zones straight under the tread pattern. The extreme values of soil displacements for the five tread patterns are summarized in Chart 6.4 and Table 6.2.

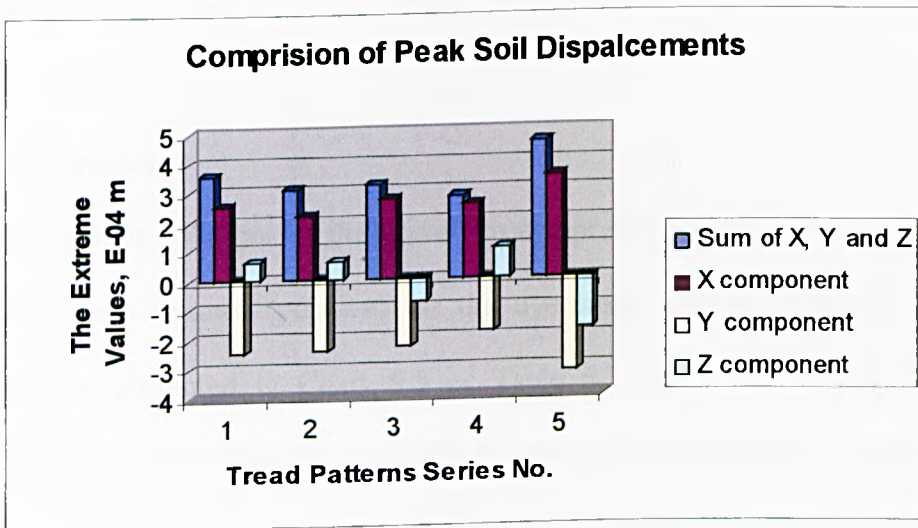


Chart 6.4 The extreme values of soil displacements for the five tread patterns

As seen in Chart 6.4 or Table 6.2, the fifth tread pattern experiences the maximum extreme soil displacement in absolute value of vector of the five tread patterns, as well as in absolute value for the X, Y and Z components. The fourth tread pattern undergoes the minimum extreme soil displacement in absolute value of vector and in

Table 6.2 The extreme values of soil displacement for the five tread patterns

Soil displacements Tread patterns	U, m, sum of soil displacement	Ux, m, soil displacement in X direction	Uy, m, soil displacement in Y direction	Uz, m, soil displacement in Z direction
The first tread patterns	0.35631 E-03	0.25868 E-03	-0.24556 E-03	0.64678 E-04
The second tread patterns	0.31227 E-03	0.22437 E-03	-0.24042 E-03	0.61954 E-04
The third tread patterns	0.32757 E-03	0.27960 E-03	-0.22156 E-03	-0.73644 E-04
The fourth tread patterns	0.28547 E-03	0.25659 E-03	-0.17734 E-03	0.10699 E-03
The fifth tread patterns	0.46734 E-03	0.35093 E-03	-0.31456 E-03	-0.17254 E-03

absolute value for the Y component of the five tread patterns. The second tread pattern encounters the minimum extreme soil displacement in absolute value for the X and Z component of the five tread patterns.

6.6.6 Soil Stresses

The finite element solutions of the maximum compressive stresses (negative) and the maximum tensile stresses (positive) for the five tread patterns in the X, Y and Z directions are presented in Chart 6.5 or Table 6.3 and Chart 6.6 or Table 6.4, respectively. As seen in Chart 6.5 or Table 6.3, the third tread patterns experiences the maximum compressive stress in the X direction. The fifth tread pattern causes the greatest compressive stress in the Y direction as well as in the Z direction; The third tread pattern undergoes the minimum compressive stresses for the Y component as well as the Z component. The second tread pattern shows the minimum compressive stress in the X direction. Chart 6.6 or Table 6.4 shows that the third tread pattern displays the maximum tensile stresses with the X component. The fifth tread pattern causes the greatest tensile stresses in the Y and Z directions; The minimum tensile

stresses in the Y and Z directions emerges in the modelling result for the second tread pattern. The minimum tensile stress of the X component appears in the modelling results for the fourth tread pattern.

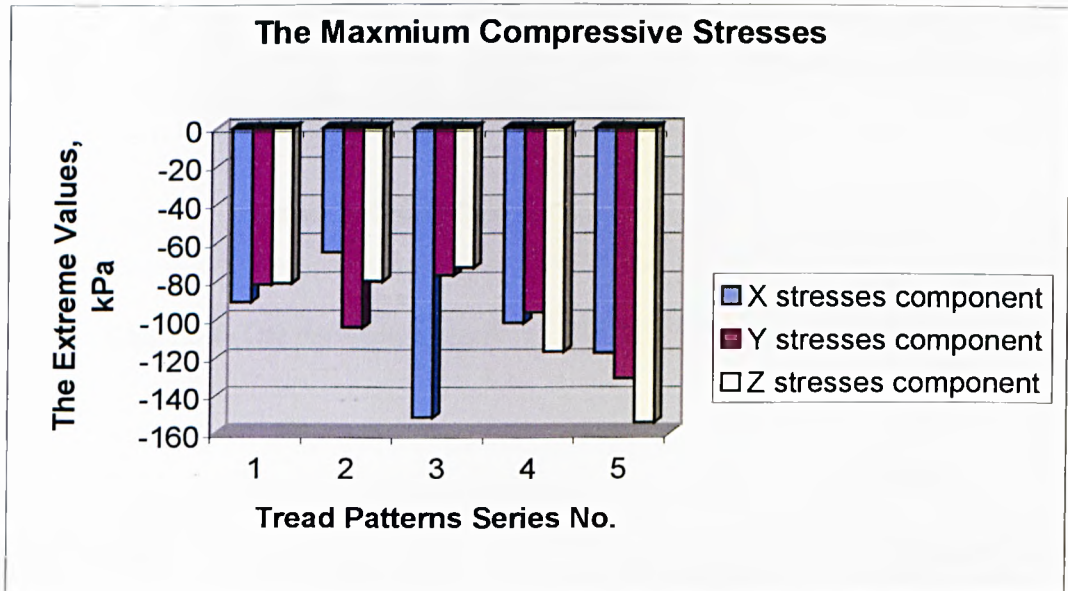


Chart 6.5 The maximum compressive stresses for the five tread patterns

Table 6.3 The maximum compressive stresses for the five tread patterns

Stresses Tread Patterns	Sx, Stresses in X direction, kPa	Sy, Stresses in Y direction, kPa	Sz, Stresses in Z direction, kPa
	The maximum compressive stresses	The maximum compressive stresses	The maximum compressive stresses
The first tread patterns	-90.385	-81.648	-80.848
The second tread patterns	-64.939	-103.912	-79.813
The third tread patterns	-151.21	-76.745	-72.646
The fourth tread patterns	-101.50	-95.882	-116.43
The fifth tread patterns	-117.26	-130.70	-153.95

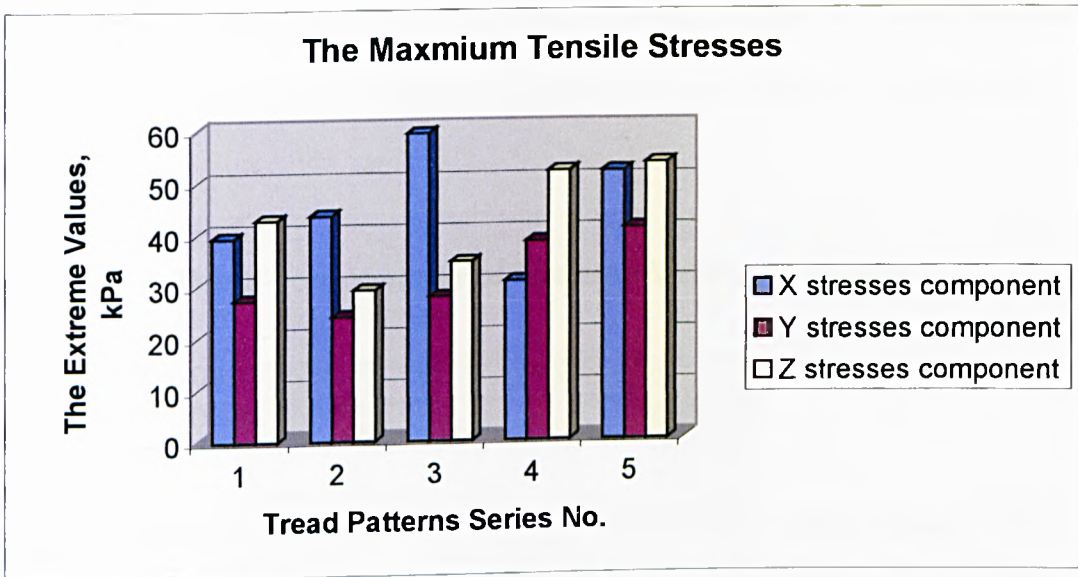


Chart 6.6 The maximum tensile stresses for the five tread patterns

Table 6.4 The maximum tensile stresses for the five tread patterns

Stresses Tread Patterns	Sx, Stresses in X direction, kPa	Sy, Stresses in Y direction, kPa	Sz, Stresses in Z direction, kPa
	The maximum tensile stresses	The maximum tensile stresses	The maximum tensile stresses
The first tread patterns	39.44	27.384	42.855
The second tread patterns	43.676	24.185	29.229
The third tread patterns	59.37	27.908	34.647
The fourth tread patterns	30.747	38.488	51.917
The fifth tread patterns	51.931	41.047	53.488

6.6.7 Soil Strains

The finite element solutions of the maximum and minimum of elastic strain, plastic strain for the five tread patterns in the X, Y and Z directions are presented in Chart 6.7, Chart 6.8 and Chart 6.9 or Table 6.5, respectively. The extreme total strains

(elastic strain + plastic strain) for the five tread patterns in the X, Y and Z directions are, respectively, presented in Chart 6.10, Chart 6.11, and Chart 6.12 or Table 6.6.

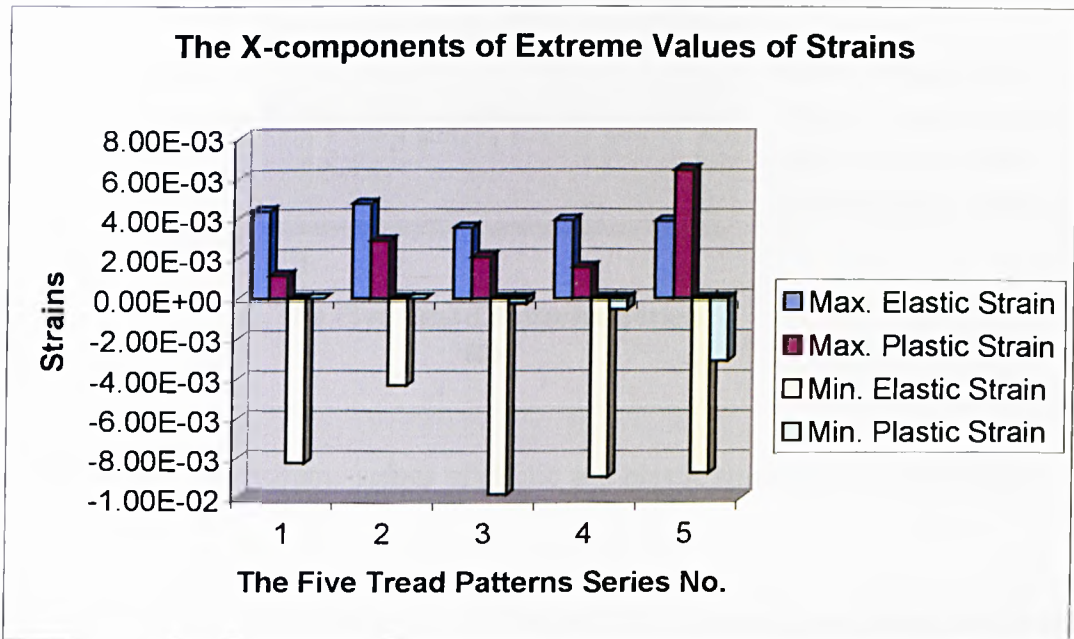


Chart 6.7 The extreme values of elastic and plastic strains in the X direction

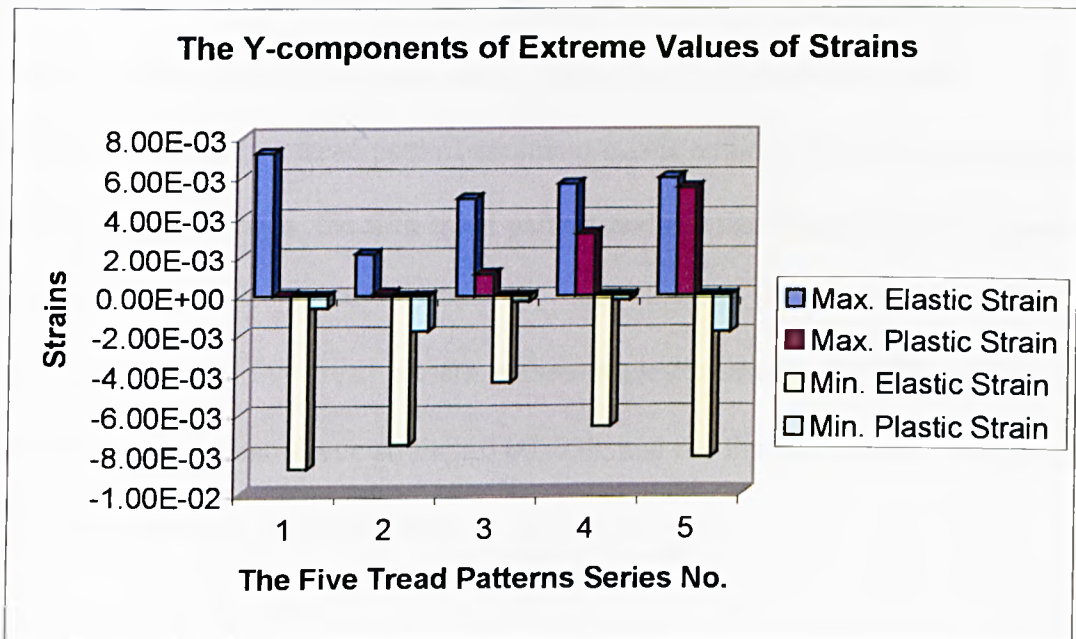


Chart 6.8 The extreme values of elastic and plastic strains in the Y direction

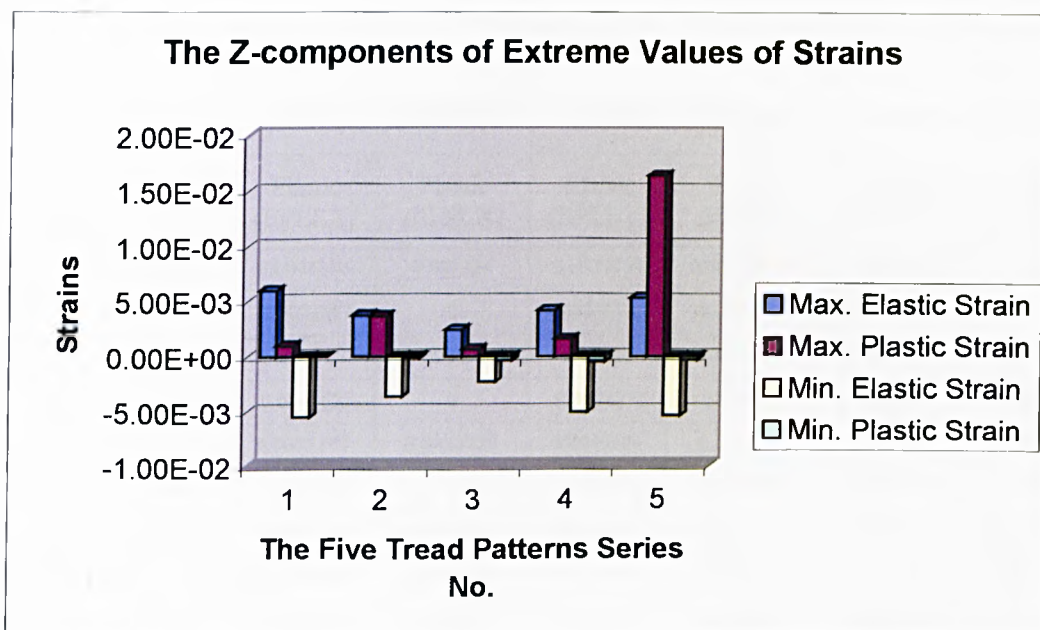


Chart 6.9 The extreme values of elastic and plastic strains in the Z direction

As shown in Chart 6.7 or Table 6.5, the second tread pattern experiences the greatest elastic strain, 0.004706, in the X direction of the five tread patterns maximum elastic strains, and the lowest elastic strain, -0.0042872, of the five tread patterns' minimum elastic strains; The third tread pattern undergoes the lowest elastic strain, 0.0035147, of the five tread patterns maximum elastic strains, and the least elastic strain, -0.0097453, of the five tread pattern minimum elastic strains. Of the five tread pattern maximum plastic strains, the fifth tread pattern and the first tread pattern experiences the greatest plastic strain, 0.0064159, and lowest plastic strain, 0.001134, respectively. Of the five tread pattern minimum plastic strains, the fifth tread pattern experiences the lowest plastic strain, -0.003059, and the first and second tread pattern undergoes zero-level plastic strains.

Table 6.5a The extreme values of elastic and plastic strains for the five tread patterns

Strains The tread patterns No.		Strains in X direction		Strains in Y direction		Strains in Z direction	
		Elastic (EPELX)	Plastic (EPPLX)	Elastic (EPELY)	Plastic (EPPLY)	Elastic (EPELZ)	Plastic (EPPLZ)
1	Max. values	0.0043366	0.001134	0.0072251	0.000029472	0.0060263	0.0010474
	Min. values	-0.0081891	0	-0.0086922	-0.00062631	-0.0054716	-0.0000022782
2	Max. values	0.004706	0.0028715	0.00216	0.0001535	0.0037768	0.0036893
	Min. values	-0.0042872	0	-0.0074872	-0.0017926	-0.0035914	-0.00012393
3	Max. values	0.0035147	0.0020727	0.0049359	0.0011179	0.002448	0.00066919
	Min. values	-0.0097453	-0.00027008	-0.0044132	-0.00029218	-0.0023169	-0.00033449
4	Max. values	0.0038836	0.0015345	0.0056494	0.0031738	0.0041581	0.0015926
	Min. values	-0.0088998	-0.000546	-0.0066332	-0.00021571	-0.0050351	-0.00045437
5	Max. values	0.0038586	0.0064159	0.0059586	0.0054567	0.0053151	0.016399
	Min. values	-0.0087047	-0.003095	-0.0081639	-0.0018999	-0.0053411	-0.00026121

Table 6.5b Corresponding nodes no. of items in Table 6.5a

The node No. corresponding to the extreme strains above		Strains in X direction		Strains in Y direction		Strains in Z direction	
		Elastic (EPELX)	Plastic (EPPLX)	Elastic (EPELY)	Plastic (EPPLY)	Elastic (EPELZ)	Plastic (EPPLZ)
1	To the max.	2753	2686	2768	1098	2866	2686
	To the min.	2893	1	2753	2686	2768	2758
2	To the max.	2437	2390	788	768	2462	2396
	To the min.	2410	1	2397	2390	2421	797
3	To the max.	536	906	949	949	195	949
	To the min.	949	949	921	947	999	999
4	To the max.	707	1180	665	665	540	685
	To the min.	671	769	656	815	665	1180
5	To the max.	703	1821	1816	1814	1804	1814
	To the min.	1876	1814	1836	1821	1826	2157

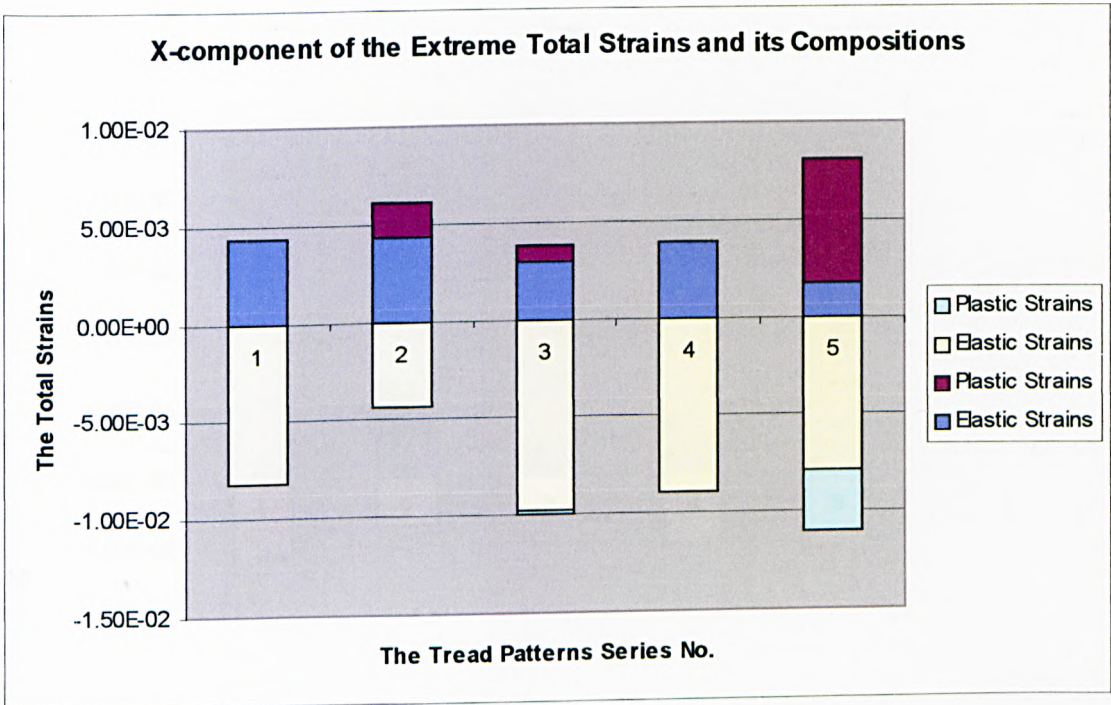


Chart 6.10 The maximum and minimum of the total strain in the X direction

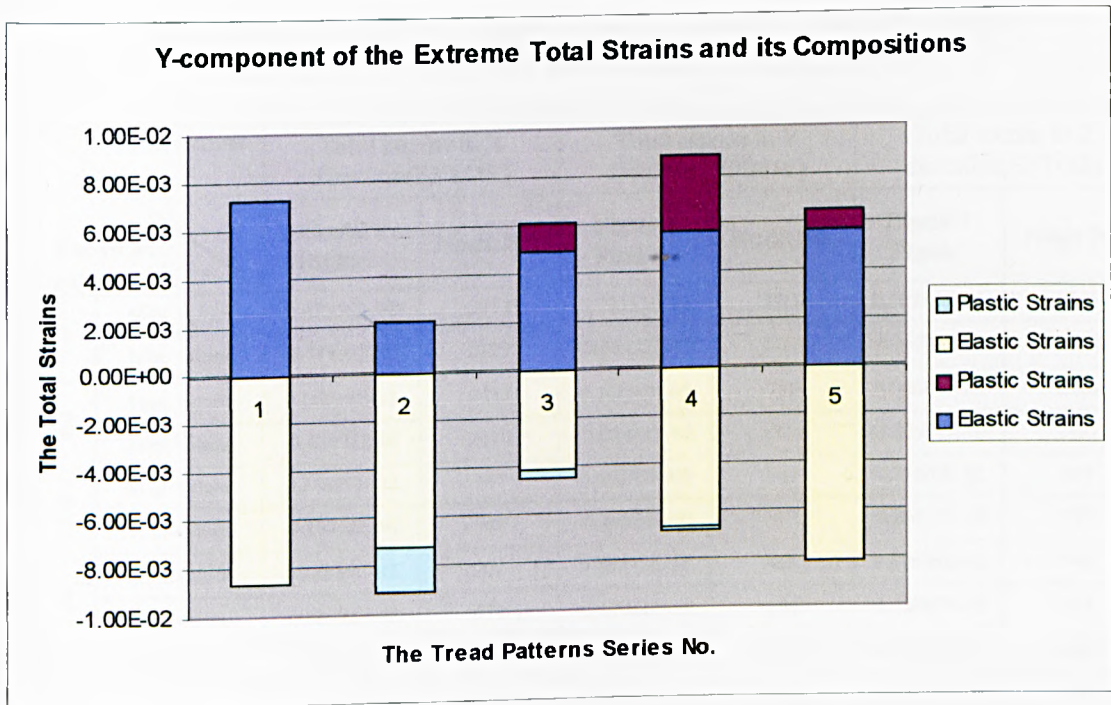


Chart 6.11 The maximum and minimum of the total strain in the Y direction

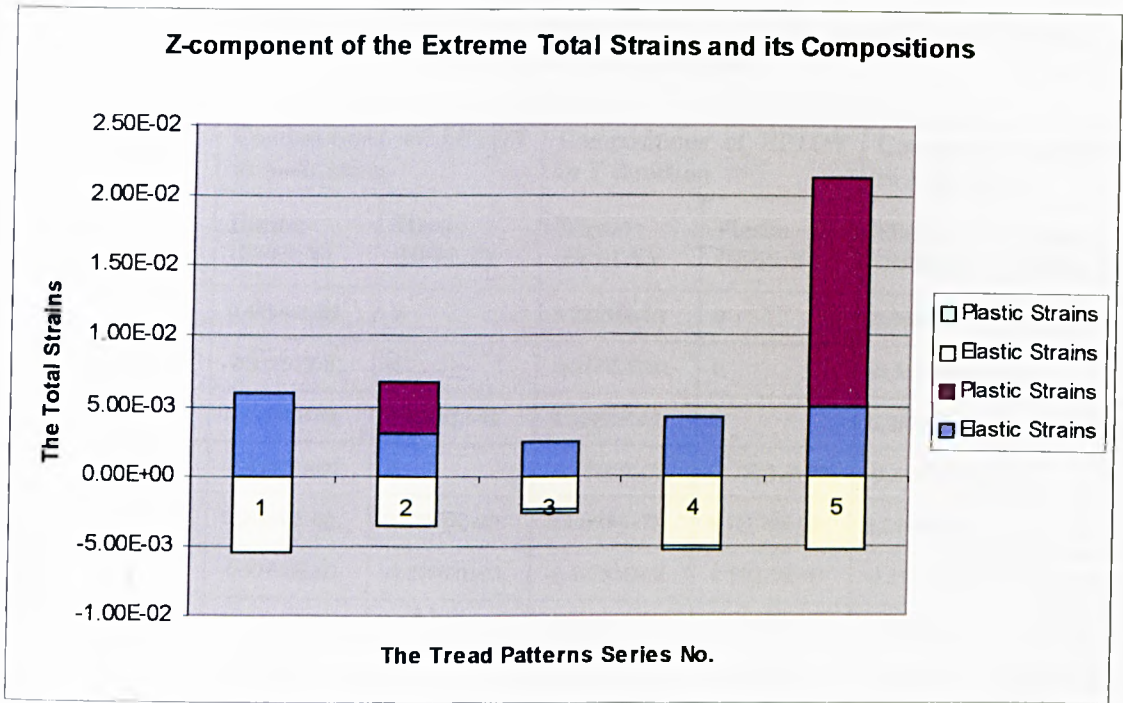


Chart 6.12 The maximum and minimum of the total strain in the Z direction

Table 6.6a The extreme values of the total strains (elastic + plastic) and corresponding node no. for the five tread patterns

Total strains The tread patterns No.		Total strains in X direction(EPTOX)		Total strains in Y direction(EPTOY)		Total strains in Z direction(EPTOZ)	
		Elastic+ Plastic	Node No.	Elastic+ Plastic	Node No.	Elastic+ Plastic	Node No.
1	Max. values	0.43366E-02	2753	0.72251E-02	2768	0.60263E-02	2866
	Min. values	-0.81891E-02	2893	-0.86922E-02	2753	-0.54716E-02	2768
2	Max. values	0.60939E-02	2433	0.21600E-02	788	0.66684E-02	2396
	Min. values	-0.42872E-02	2410	-0.90468E-02	2390	-0.35914E-02	2421
3	Max. values	0.38629E-02	947	0.60537E-02	949	0.24480E-02	195
	Min. values	-0.10015E-01	949	-0.44674E-02	947	-0.26514E-02	999
4	Max. values	0.38836E-02	707	0.88232E-02	665	0.42656E-02	540
	Min. values	-0.88998E-02	671	-0.67961E-02	656	-0.52908E-02	665
5	Max. values	0.81415E-02	1821	0.64612E-02	1817	0.21305E-01	1814
	Min. values	-0.11020E-01	1814	-0.81639E-02	1836	-0.53411E-02	1826

Table 6.6b Elastic and plastic strains compositions of the extreme total strains for the five tread patterns

Total trains The tread patterns No.		Compositions of EPTOX in X direction		Compositions of EPTOY in Y direction		Compositions of EPTOZ in Z direction	
		Elastic (EPELX)	Plastic (EPPLX)	Elastic (EPELY)	Plastic (EPPLY)	Elastic (EPELZ)	Plastic (EPPLZ)
1	To the max.	0.43366E-02	0	0.72251E-02	0	0.60263E-02	0
	To the min.	-0.81891E-02	0	-0.86922E-02	0	-0.54716E-02	0
2	To the max.	0.43538E-02	0.17401E-02	0.21600E-02	0	0.29791E-02	0.36893E-02
	To the min.	-0.42872E-02	0	-0.72543E-02	-0.17926E-02	-0.35914E-02	0
3	To the max.	0.29890E-02	0.87390E-03	0.49359E-02	0.11179E-02	0.24480E-02	0
	To the min.	-0.97453E-02	-0.27008E-03	-0.41752E-02	-0.29218E-03	-0.23169E-02	-0.33449E-03
4	To the max.	0.38836E-02	0	0.56494E-02	0.31738E-02	0.41581E-02	0.10752E-03
	To the min.	-0.88998E-02	0	-0.66332E-02	-0.16288E-03	-0.50351E-02	-0.25571E-03
5	To the max.	0.17256E-02	0.64159E-02	0.56556E-02	0.80560E-03	0.49056E-02	0.16399E-01
	To the min.	-0.79250E-02	-0.30950E-02	-0.81639E-02	0	-0.53411E-02	0

For the Y-components shown in Chart 6.8 or Table 6.5, the first tread pattern experiences the greatest elastic strain, 0.0072251, of the five tread pattern maximum elastic strains, and the lowest elastic strain, -0.0086922, of the five tread pattern minimum elastic strains; In contrast, the second tread pattern undergoes the lowest elastic strain, 0.00216, of the five tread pattern maximum elastic strains, and the third tread pattern has the least elastic strain, -0.0044132, of the five tread pattern minimum elastic strains. Of the five tread pattern maximum plastic strains, the fifth tread pattern dominates the greatest, 0.0054567, and the first tread pattern has the lowest, 0.00002229472. Of the five tread pattern minimum plastic strains, the fifth tread pattern experiences the lowest, -0.0018999, and the fourth tread pattern undergoes the smallest, -0.00021751.

For the extreme elastic or plastic strains in the Z direction shown in Chart 6.9 or Table 6.5, the first tread pattern experiences the greatest elastic strain, 0.0060263, of the five tread pattern maximum elastic strains, and the lowest elastic strain, -0.0054716, of the five tread pattern minimum elastic strains; On the contrary, the third tread pattern undergoes the lowest elastic strain, 0.002448 of the five tread pattern maximum elastic strains, as well as the least elastic strain, -0.0023169, of the five tread pattern minimum elastic strains. Of the five tread pattern maximum plastic strains, the fifth tread pattern experiences the greatest, 0.016399, and the third tread pattern has the lowest, 0.00066919. Of the five tread pattern minimum plastic strains, the fourth tread pattern experiences the lowest, -0.00045437, and the first tread pattern undergoes the least, -0.0000022782.

When soil is in a plastic state, the stress-strain relationship is non-linear and the total strain is composed of elastic and plastic strain as⁶⁵

$$d\varepsilon_{ij} = d\varepsilon_{ij}^e + d\varepsilon_{ij}^p \quad \dots \quad (6.19)$$

where $d\varepsilon_{ij}$ is the incremental total strain tensor, $d\varepsilon_{ij}^e$ is the incremental elastic strain tensor, and $d\varepsilon_{ij}^p$ is the incremental plastic strain tensor. The extreme total strains for the five tread patterns have been summarized in Table 6.6 and shown in Chart 6.10, chart 6.11 and Chart 6.12, respectively. As seen in Chart 6.10 or Table 6.6, the fifth tread pattern dominates both the greatest and lowest total strains, 0.0081415 and -0.011020, of the five tread pattern maximum and minimum total strains in the X direction; On the contrary, the fourth tread pattern experiences the smallest total

strain, 0.0038629, in the X direction of the five tread pattern maximum total strains, and the second tread pattern undergoes the least total strain, -0.0042872 , of the five tread pattern minimum total strains.

For the Y-component of the extreme total strains shown in Chart 6.11 or Table 6.6, the fourth tread pattern and the second tread pattern experience, respectively, the greatest and lowest total strains, 0.0088232 and -0.0090468 , of the five tread patterns maximum and minimum total strains; In contrast, the second tread pattern experiences the smallest total strain, 0.0021600, of the five tread patterns maximum total strains, and the third tread pattern undergoes the least total strain, -0.0044674 , of the five tread pattern minimum total strains.

Similarly, for the Z-component of the extreme total strains shown in Chart 6.12 or Table 6.6, the fifth tread pattern and the first tread pattern respectively experience the greatest and lowest total strains, 0.021305 and -0.0054716 , of the five tread pattern maximum and minimum total strains; In contrast, the third tread pattern undergoes both the smallest total strains, 0.0024480 and -0.0026514 , of the five tread pattern maximum total strains and minimum total strains.

As seen in Table 6.5b and Table 6.6a, four nodes reach both peak elastic strain and peak plastic strain as well as the peak total strain at the same time. These are node 949 with the third tread pattern in the Y direction for positive peak values, node 949 with the third tread pattern in the X direction for the negative peak values, node 999 with the third tread pattern in the Z direction for the negative peak values, and node 665 with the fourth tread pattern in the Y direction for the positive peak values. The

corresponding peak values can be found in Table 6.5a and Table 6.6b. Seen also in Table 6.6a and Table 6.6b, the extreme total strains on node 2753, 2768, 2866, 2893 with the first tread pattern consist of zero-level plastic strains, that is the extreme total strains on these nodes equals to the extreme elastic strains of corresponding nodes, as seen in Table 6.5a. The same situation exists on node 788, 2410 and 2421 with the second tread pattern; node 195 with the third tread pattern; node 707 and 671 with the fourth tread pattern; and node 1836 and 1826 with the fifth tread pattern. In a word, respect to the extreme elastic strain, plastic strain and the total strain, most of nodes existing extreme strain experience only either peak elastic strain or peak plastic strains. Some nodes undergo both peak elastic strains and the total strains. A few nodes encounter both peak elastic strains and peak plastic strains as well as the extreme total strains.

As seen in Table 6.5b and Table 6.6a, most of nodes show extreme strains only either in the X direction or Y direction or Z direction. Some nodes exist peak strains for both components of the X or Y or Z, such as node 2753, 2768 for the first tread pattern; node 2390 for the second tread pattern; node 947 for the third tread pattern; node 665, 1180 for the fourth tread pattern; and node 1821 for the fifth tread pattern. Three nodes experience peak strains in three directions of the X, Y and Z coordinates, they are node 2686 for the first tread pattern, node 949 for third tread pattern and node 1814 for the fifth tread pattern.

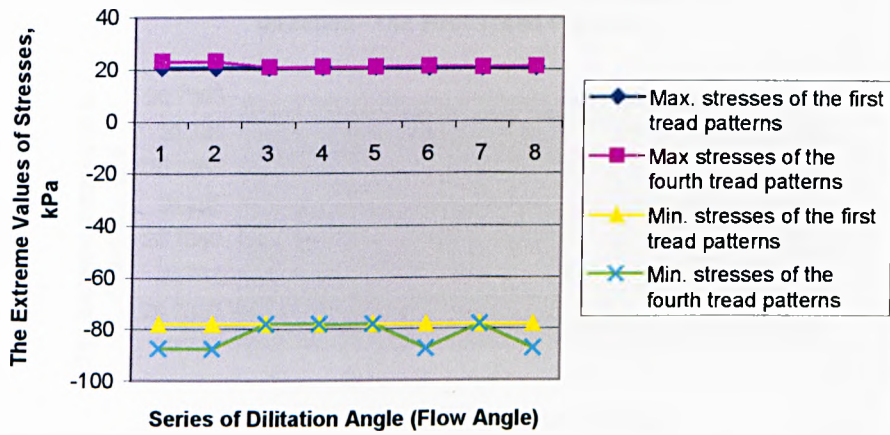
6.6.8 Effects of the Mechanical Parameters of Soil Property

6.6.8.1 Effect of the dilatation angle

In accordance with classical plasticity theory, soil deformation causes no further changes to the stresses in the soil for elastic-perfectly plastic soil material failure model, and the elastic strain increments is zero if limiting conditions being reached. (Seen also in Fig. 3.1 and Fig. 3.3) The stress direction is assumed to be coincident with plastic strain increment direction. The angle of soil dilatation, β , allows the direction of principal plastic strain increments to be determined. A flow rule is applied to describe state of plastic flow. If the dilatation angle or flow angle, β , is equal to the angle of internal friction (ϕ) of soil, the plastic flow is fully associated. If the β is zero, then it is non-associated plastic flow. The plastic flow is associated for case of that the flow angle (β) is in between zero and the ϕ . In this study, analyses have been carried out using a series of values of β ranging from zero to ϕ . The effects of β to the extreme values of stresses are now examined for the selected first and fourth tread patterns.

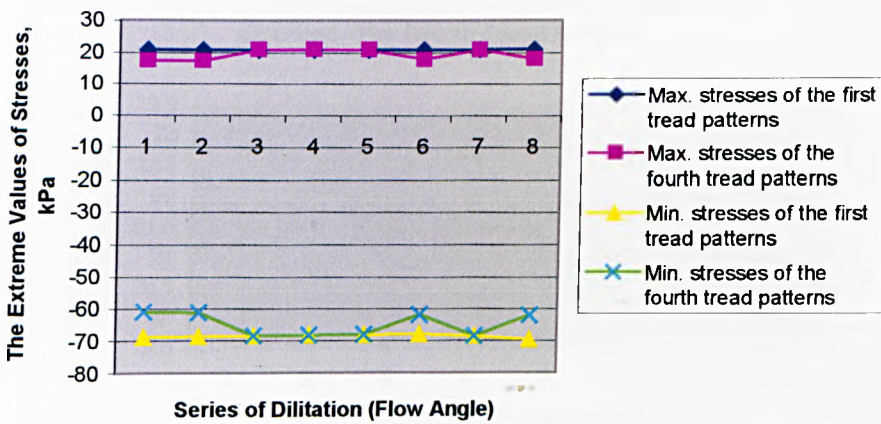
The FE models and loading conditions used in the analyses of the effects of β are same as that reported in sections 6.2.3 & 6.3.1 for the first tread pattern and that for the fourth tread pattern. Modelling results of the effects of β to the extreme values of stresses are presented in Chart 6.13 and Table 6.7. Only the extreme stresses versus the dilatation angle or flow angle are evaluated. Chart 6.13 reflects same results as that of Table 6.7, but the former is focused on visualization of varying tendency, and the latter emphasizes readability of raw data. Chart 6.13 a, b and c gathers information of both the first and fourth tread patterns in the X, Y and Z direction, respectively.

The X-components of Extreme Stress for the First & Fourth Tread Patterns Versus Flow Angle



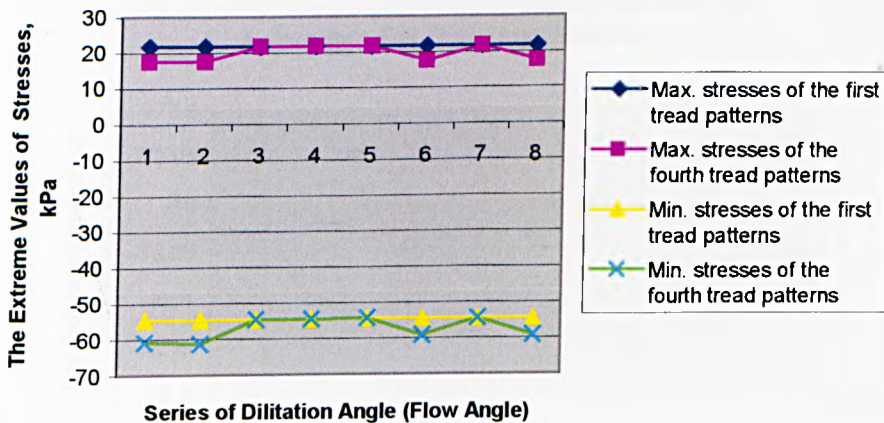
a)

The Y-components of the Extreme Stress for the First & Fourth Tread Patterns Versus Flow Angle

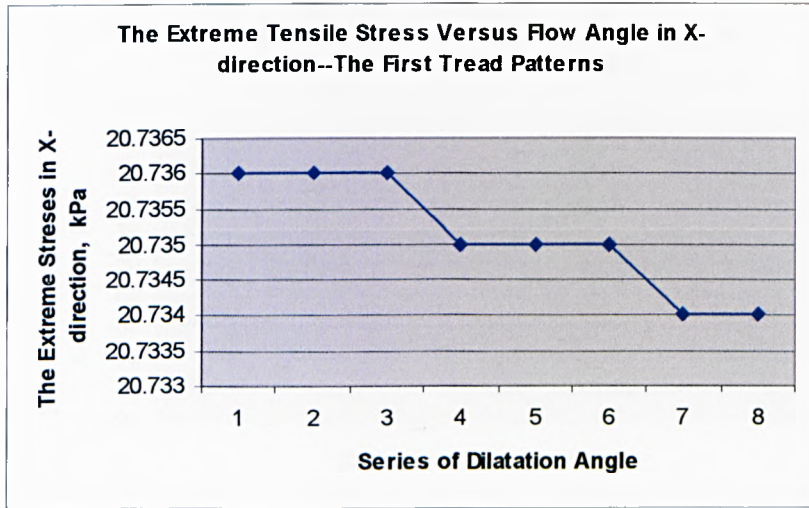


b)

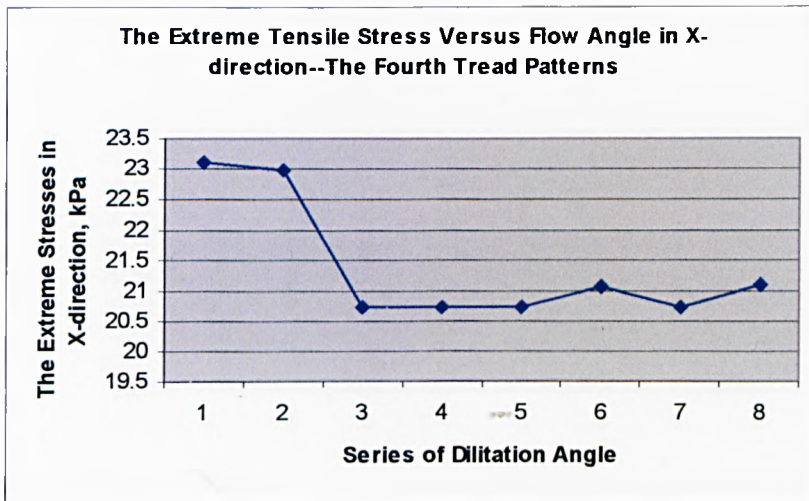
The Z-components of Extreme Stress for the First & Fourth Tread Patterns Versus Flow Angle



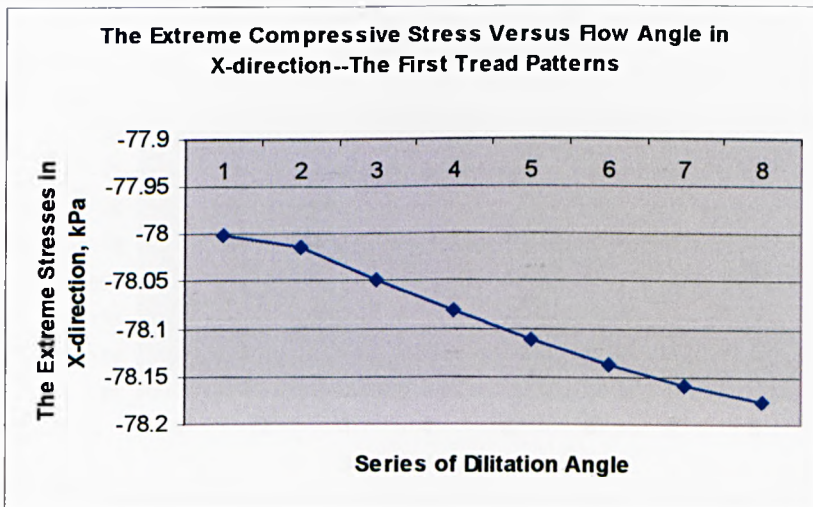
c)



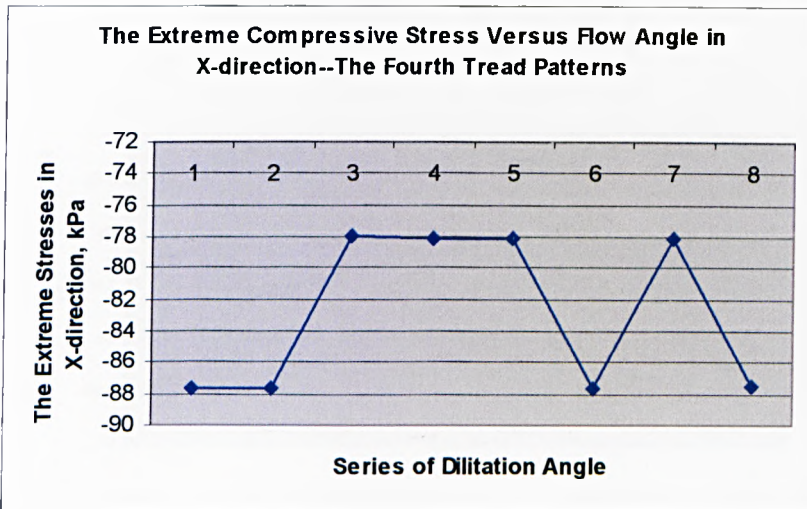
d)



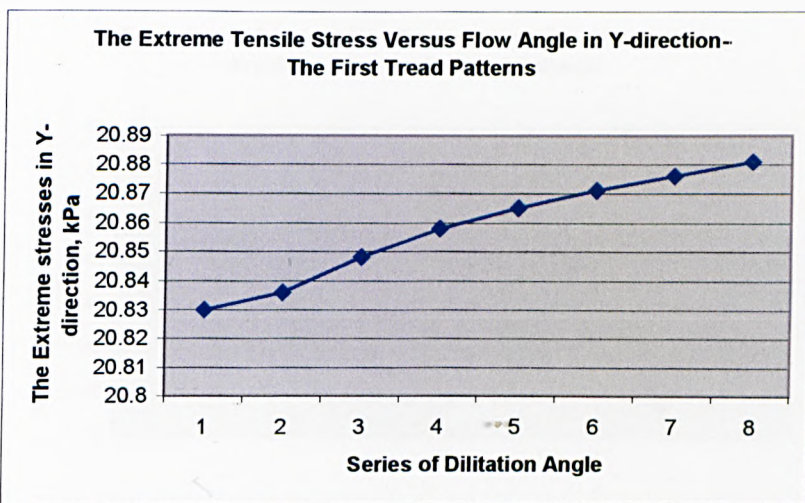
e)



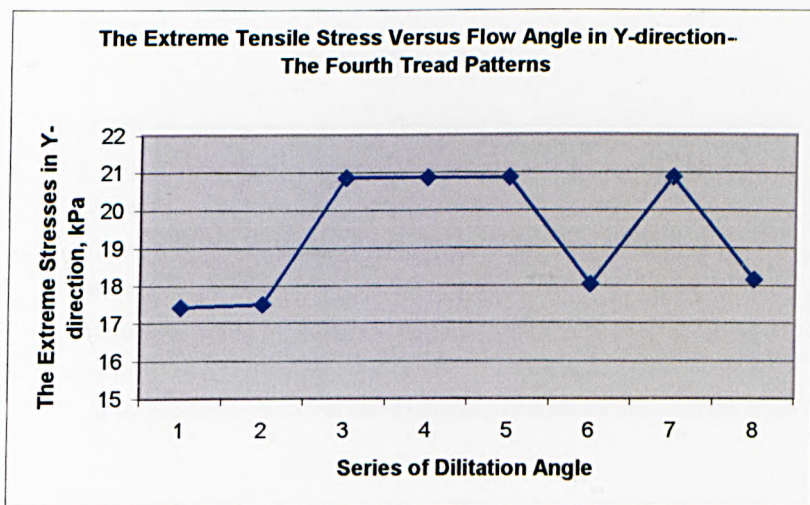
f)



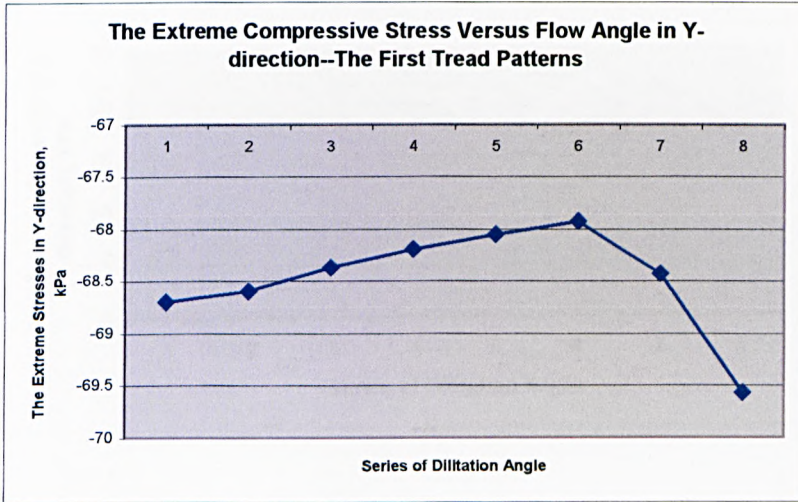
g)



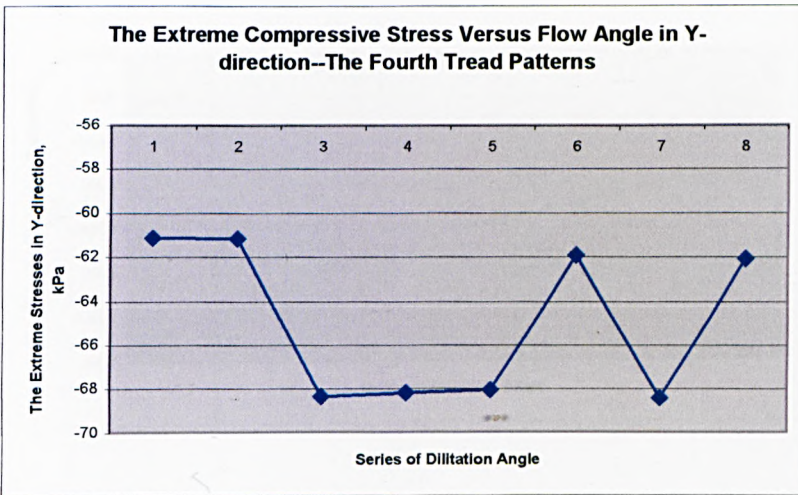
h)



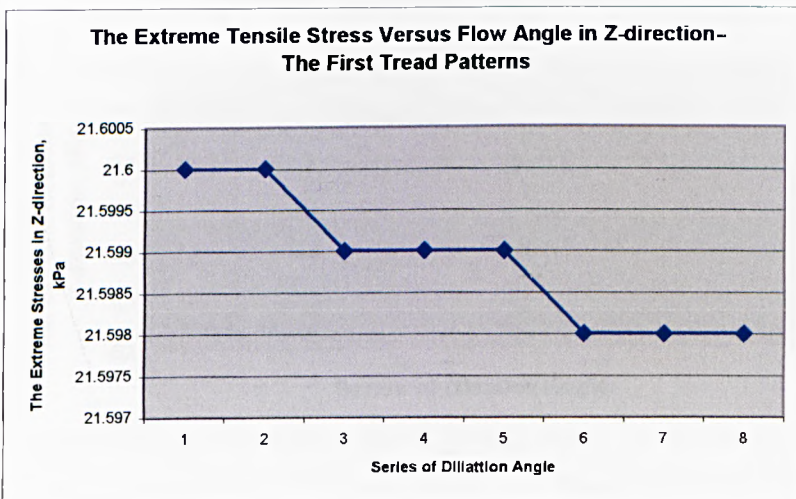
i)



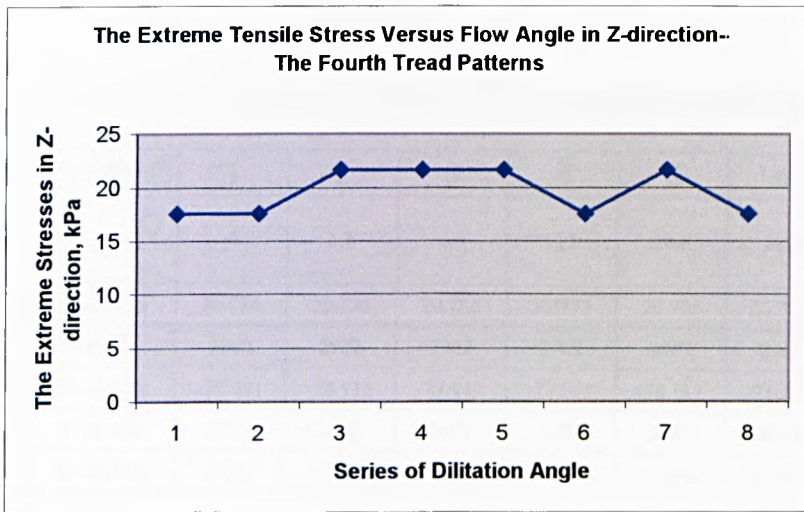
j)



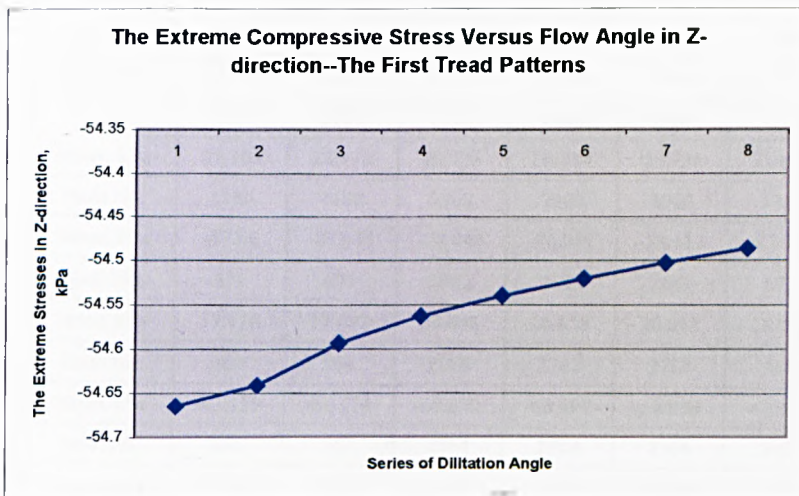
k)



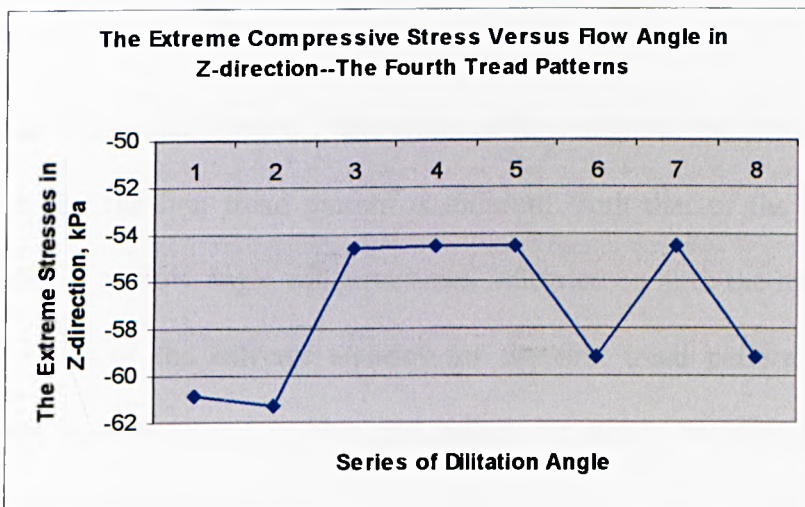
l)



m)



n)



o)

Chart 6.13 Effects of the extreme stresses versus flow angle

Table 6.7 Summary of extreme stresses (kPa) versus flow angle (degree)

Items		Flow Angle, β		1	2	3	4	5	6	7	8
		(°)		0	1.8	6.8	11.8	16.8	21.8	26.8	31.8
The First Tread Patterns	X-components	Max.	Stress, kPa	20.736	20.736	20.736	20.735	20.735	20.735	20.734	20.734
			Node No.	2962	2962	2962	2962	2962	2962	2962	2962
		Min.	Stress, kPa	-78.081	-78.112	-78.049	-78.081	-78.112	-78.138	-78.16	-78.177
			Node No.	2682	2682	2682	2682	2682	2682	2682	2682
	Y-components	Max.	Stress, kPa	20.83	20.836	20.848	20.858	20.865	20.871	20.876	20.881
			Node No.	2768	2768	2768	2768	2768	2768	2768	2768
		Min.	Stress, kPa	-68.703	-68.6	-68.372	-68.197	-68.054	-67.933	-68.431	-69.572
			Node No.	2764	2764	2764	2764	2764	2764	2686	2686
	Z-components	Max.	Stress, kPa	21.6	21.6	21.599	21.599	21.599	21.598	21.598	21.598
			Node No.	2866	2866	2866	2866	2866	2866	2866	2866
		Min.	Stress, kPa	-54.665	-54.641	-54.594	-54.563	-54.54	-54.521	-54.503	-54.487
			Node No.	2768	2768	2768	2768	2768	2768	2768	2768
The Fourth Tread Patterns	X-components	Max.	Stress, kPa	23.104	22.978	20.736	20.735	20.735	21.076	20.734	21.11
			Node No.	1180	1180	2962	2962	2962	1238	2962	1238
		Min.	Stress, kPa	-87.66	-87.653	-78.049	-78.081	-78.112	-87.595	-78.16	-87.578
			Node No.	671	671	2682	2682	2682	671	2682	671
	Y-components	Max.	Stress, kPa	17.418	17.492	20.848	20.858	20.865	18.028	20.876	18.153
			Node No.	804	804	2768	2768	2768	804	2768	804
		Min.	Stress, kPa	-61.119	-61.174	-68.372	-68.197	-68.054	-61.934	-68.431	-62.086
			Node No.	655	747	2764	2764	2764	747	2686	747
	Z-components	Max.	Stress, kPa	17.542	17.535	21.599	21.599	21.599	17.515	21.598	17.511
			Node No.	802	802	2866	2866	2866	802	2866	802
		Min.	Stress, kPa	-60.887	-61.277	-54.594	-54.563	-54.54	-59.239	-54.503	-59.237
			Node No.	665	665	2768	2768	2768	544	2768	544

As seen in Chart 6.13a and Table 6.7, the effect of flow angle to the extreme stress in the X direction for the first tread pattern is different from that of the fourth tread pattern. The choice of flow angle will have small influence on both the maximum and the minimum stress or the extreme stresses for the first tread pattern for the X-component, that is, both curves in blue and yellow are nearly horizontally flat. The maximum and the minimum stresses are constantly located at node 2962 and 2682, respectively. However, the dilatation angle has a considerable effect on the extreme

stresses for the fourth tread pattern in the X direction as showed by curves in pink and green. The minimum stress fluctuates more violently than the maximum stress as shown in Chart 6.13e and 6.13g. The locations of the extreme stresses have been shifted to-and-fro between node 1180, node 2962 and node 1238 for the maximum stress, and node 671, node 2682 for the minimum stress. Varying tendency of the extreme stresses for the first tread pattern is shown in Chart 6.13d and 6.13f with enlarged scale at coordinate axis of stress. The maximum tensile stress slightly discontinuously decreases from 20.736 kPa to 20.734 kPa along with the increasing of flow angle from zero to 31.8° , but absolute value of the extreme compressive stress continuously increases slightly from 78.081 kPa to 78.177 kPa when flow angle rises from zero to 31.8° .

The effect of flow angle versus the extreme stress in the Y direction for the first tread pattern is also different from that of the fourth tread pattern as shown in Chart 6.13b and Table 6.7. The flow angle has little influence on both the maximum and the minimum stress or the extreme stresses for the first tread pattern for the Y-component, but the influence is a little stronger than that for the X-component. Both curves in blue and yellow are not nearly horizontally flat as seen in Chart 6.13b. The maximum stresses are still constantly located at node 2768, but the minimum stresses have been shifted between node 2764 and node 2686. However, the dilatation angle has a significant effect on the extreme stresses for the fourth tread pattern in the Y direction as showed in Chart 6.13b by curves in pink and green. The minimum stress fluctuates stronger than the maximum stress in amplitude as shown in Chart 6.13i and 6.13k. The locations of the extreme stresses existing have been shifted to-and-fro between node 804 and node 2768 for the maximum stress, and node 655, node 747, node 2686

and node 2764 for the minimum stress. Varying tendency of the extreme stresses in Y the direction for the first tread pattern is shown in Chart 6.13h and 6.13j with enlarged scale at coordinate axis of stress. The maximum tensile stress slightly continuously increases from 20.83 kPa to 20.881 kPa along with the increasing of flow angle from zero to 31.8° , but the extreme compressive stress varies discontinuously. The maximum absolute value occurs at a flow angle of 31.8° and the minimum occurs with a flow angle of 21.8° .

As seen in Chart 6.13c, fluctuation pattern of the extreme compressive stress versus the flow angle for the Z-component is similar to that of the X-component shown in Chart 6.13a, and situation of the extreme tensile stress versus the flow angle in the Z direction is similar to that of the Y-component shown in Chart 6.13b. That is that, the choice of flow angle will have small influence on both the maximum and the minimum stress or the extreme stresses for the first tread pattern in the Z direction as seen in Chart 6.13c. Both curves in blue and yellow are nearly horizontally flat unaffected by the varying of flow angle. The maximum and the minimum stresses are constantly located at node 2866 and 2768, respectively. However, the flow angle has an obvious effect on the extreme stresses for the fourth tread pattern in the Z direction as shown by curves in pink and green. The extreme compressive stress fluctuates a little stronger than the extreme tensile stress in amplitude as shown in Chart 6.13o and 6.13m. The locations of the extreme stresses have been shifted to-and-fro between node 544, node 665 and node 2768 for the extreme compressive stress, and node 802, node 2866 for the extreme tensile stress. Chart 6.13l and 6.13n shows the varying tendency of the extreme stresses for the first tread pattern with larger scale coordinate axis of stress. The maximum tensile stress slightly discontinuously drops from 21.6

kPa to 21.598 kPa along with the increasing of flow angle from zero to 31.8° , but the extreme compressive stress continuously decreases slightly from 54.665 kPa to 54.487 kPa in absolute value of them as flow angle varies from zero to 31.8° .

6.6.8.2 Effect of the Young's modulus

To investigate whether the elastic stiffness might affect the extreme stresses, analyses have been carried out using a series of Young's modulus, E , ranging from 8000 kPa to 88000 kPa that were commonly used to simulate the soil behaviour. The first and fourth tread patterns are also selected to test the effects of E to the extreme stresses. The soil FE models and loading conditions used in the analyses of the effects of E are also same as that reported in sections 6.2.3 & 6.3.1 for the first tread pattern. The simulation results of the effects of E to the extreme stresses are summarized in Table 6.8.

As seen in Table 6.8, the extreme stresses for both the first and the fourth tread patterns are not affected by variation of the Young's modulus as well as the locations of the extreme stresses occurring. Therefore, the effect of the Young's modulus appears to be negligible.

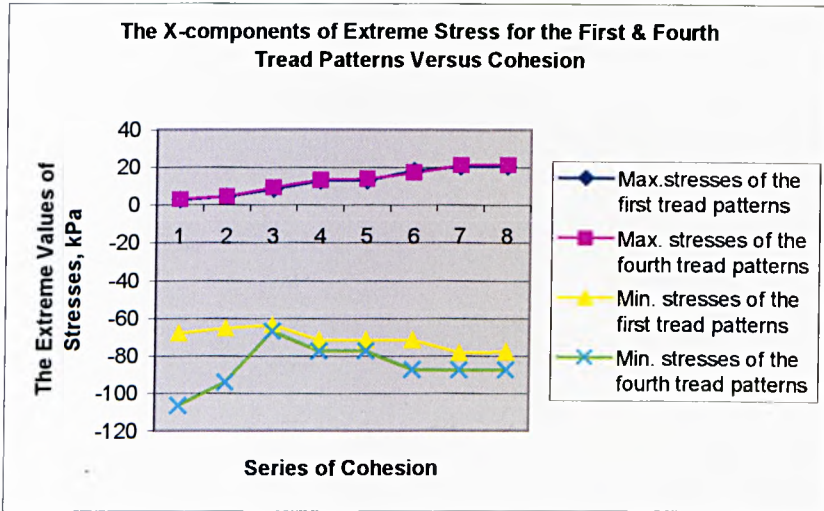
6.6.8.3 Effect of cohesion

The effect of cohesion, c , to the extreme stresses is also studied for both the first and the fourth tread patterns. Cohesion value ranges from 2 kPa to 15.5 kPa, that is, the soil type is varying from nearly cohesion-less to sandy loam of the texture. The soil FE models and loading conditions used in the analyses of the effects of c are still same as that reported in sections 6.2.3 & 6.3.1 for the first tread pattern. The effect of

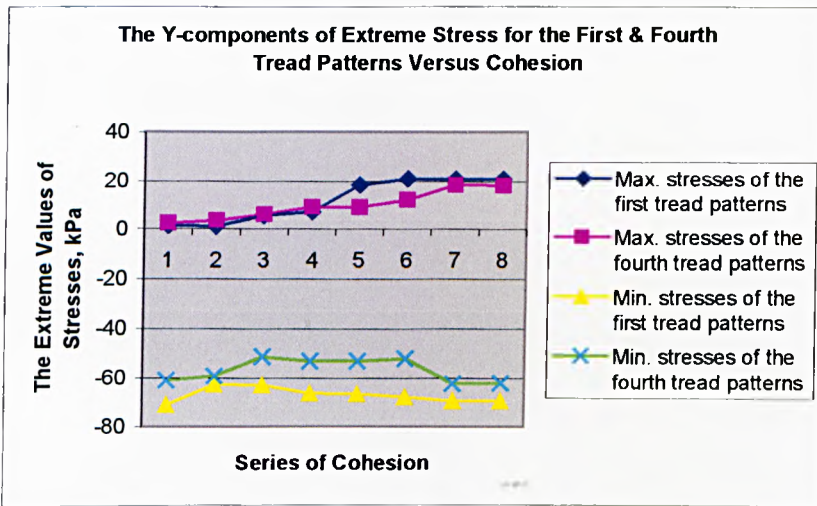
Table 6.8 Summary of extreme stresses (kPa) versus Young's modulus (kPa)

Items		Young's Modulus, E		1	2	3	4	5	6	7
		(kPa)		8000	8067	28000	48000	68000	83360	88000
The First Tread Patterns	X-components	Max.	Stress, kPa	20.734	20.734	20.734	20.734	20.734	20.734	20.734
			Node No.	2962	2962	2962	2962	2962	2962	2962
		Min.	Stress, kPa	-78.177	-78.177	-78.177	-78.177	-78.177	-78.177	-78.177
			Node No.	2682	2682	2682	2682	2682	2682	2682
	Y-components	Max.	Stress, kPa	20.881	20.881	20.881	20.881	20.881	20.881	20.881
			Node No.	2768	2768	2768	2768	2768	2768	2768
		Min.	Stress, kPa	-69.572	-69.572	-69.572	-69.572	-69.572	-69.572	-69.572
			Node No.	2686	2686	2686	2686	2686	2686	2686
	Z-components	Max.	Stress, kPa	21.598	21.598	21.598	21.598	21.598	21.598	21.598
			Node No.	2866	2866	2866	2866	2866	2866	2866
		Min.	Stress, kPa	-54.487	-54.487	-54.487	-54.487	-54.487	-54.487	-54.487
			Node No.	2768	2768	2768	2768	2768	2768	2768
The Fourth Tread Patterns	X-components	Max.	Stress, kPa	21.110	21.110	21.110	21.110	21.110	21.110	21.110
			Node No.	1238	1238	1238	1238	1238	1238	1238
		Min.	Stress, kPa	-87.578	-87.578	-87.578	-87.578	-87.578	-87.578	-87.578
			Node No.	671	671	671	671	671	671	671
	Y-components	Max.	Stress, kPa	18.153	18.153	18.153	18.153	18.153	18.153	18.153
			Node No.	804	804	804	804	804	804	804
		Min.	Stress, kPa	-62.086	-62.086	-62.086	-62.086	-62.086	-62.086	-62.086
			Node No.	747	747	747	747	747	747	747
	Z-components	Max.	Stress, kPa	17.511	17.511	17.511	17.511	17.511	17.511	17.511
			Node No.	802	802	802	802	802	802	802
		Min.	Stress, kPa	-59.237	-59.237	-59.237	-59.237	-59.237	-59.237	-59.237
			Node No.	544	544	544	544	544	544	544

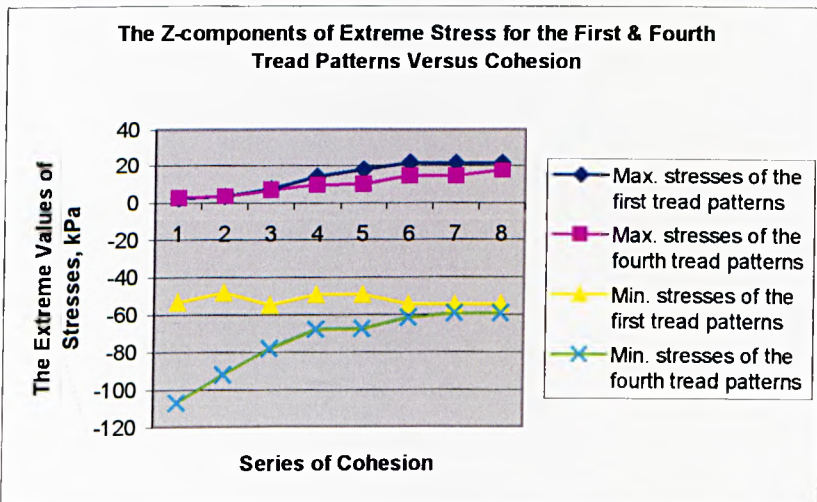
cohesion to the extreme stresses is presented in Chart 6.14 and Table 6.9. Chart 6.14 a), b) and c) gathers information of both the first and fourth tread patterns in the X, Y and Z direction, respectively. Table 6.9 summarizes all the raw data presented in Chart 6.14. No charts with enlarged scale of coordinate axis are made as it is clear to observe varying tendency of the extreme stress versus cohesion by Chart 6.14 a), b) and c).



a)



b)



c)

Chart 6.14 Effects of the extreme stress versus cohesion

Table 6.9 Summary of extreme stresses (kPa) versus cohesion (kPa)

Items		Cohesion, c (kPa)		1	2	3	4	5	6	7	8
				2	3	6	9	9.13	12	15	15.5
The First Tread Patterns	X-components	Max.	Stress, kPa	2.7295	4.3031	8.5289	12.836	13.018	18.147	20.734	20.734
			Node No.	2960	2614	2962	2962	2962	2961	2962	2962
		Min.	Stress, kPa	-68.021	-65.240	-63.615	-71.612	-71.611	-71.585	-78.199	-78.177
			Node No.	2865	2865	2738	2894	2894	2894	2682	2682
	Y-components	Max.	Stress, kPa	1.4545	1.1896	5.4905	7.0846	18.176	20.812	20.879	20.881
			Node No.	3798	3774	2681	2681	2703	2768	2768	2768
		Min.	Stress, kPa	-71.227	-62.799	-63.085	-66.578	-66.771	-67.997	-69.613	-69.572
			Node No.	2840	449	2733	2763	2763	2763	2686	2686
	Z-components	Max.	Stress, kPa	2.2915	3.4484	7.2134	13.912	17.808	21.588	21.597	21.598
			Node No.	1856	1846	2619	2925	2913	2866	2866	2866
		Min.	Stress, kPa	-53.468	-48.281	-54.846	-49.301	-49.287	-54.745	-54.517	-54.487
			Node No.	2935	2935	2919	2661	2661	2768	2768	2768
The Fourth Tread Patterns	X-components	Max.	Stress, kPa	2.8449	4.3011	8.9116	13.182	13.798	17.263	21.110	21.110
			Node No.	969	2146	1245	875	2152	873	1238	1238
		Min.	Stress, kPa	-106.75	-94.211	-67.083	-77.889	-77.874	-87.517	-87.575	-87.578
			Node No.	540	540	482	671	671	671	671	671
	Y-components	Max.	Stress, kPa	2.4121	3.5563	6.0225	8.9649	9.0917	12.074	18.344	18.153
			Node No.	2173	2173	2167	2167	2167	2165	804	804
		Min.	Stress, kPa	-60.986	-59.255	-51.514	-53.210	-53.171	-52.079	-62.294	-62.086
			Node No.	623	655	656	656	656	656	747	747
	Z-components	Max.	Stress, kPa	2.5062	3.3189	6.5550	9.5844	9.6754	14.607	14.375	17.511
			Node No.	2117	2117	688	953	953	1144	540	802
		Min.	Stress, kPa	-107.07	-92.084	-78.518	-68.187	-67.804	-61.755	-59.243	-59.237
			Node No.	807	665	665	665	665	665	544	544

As seen in Chart 6.14a and Table 6.9, the effect of cohesion to the maximum tensile stress in the X direction for the first tread pattern is same as that of the fourth tread pattern. Both curves of varying tendency overlap to the most extent (see curves in blue and pink). However, the locations of the maximum tensile stresses existing have been shifted to-and-fro between node 2960, node 2614, node 2962 and node 2961 for the first tread pattern, and altered from node 1238 to node 671, 873, 2152, 875, 1245,

2146 and node 2682 for the fourth tread pattern. The effect of cohesion to the extreme compressive stress in the X direction for the first tread pattern is different from that of the fourth tread pattern (see curves in yellow and green), but the peak values emerge at the same point of cohesion (No. 3, cohesion 6 kPa) for both tread patterns. The locations of the extreme compressive stresses existing have also been shifted to-and-fro between node 2682, node 2894, node 2738 and node 2865 for the first tread pattern, and from node 671 to node 482 and node 540 for the fourth tread pattern. In general, the maximum tensile stresses increase for both tread patterns along with rising of cohesion. The extreme compressive stresses reduce in absolute values before reaching the peak point, and then increase in absolute value after passing the peak point for both tread patterns following increasing of cohesion.

In general, the varying tendency of the maximum tensile stress versus cohesion in the Y direction for both tread patterns is same as that of in the X direction, i. e. the maximum tensile stress gradually increase along with increasing of cohesion (see in Chart 6.14b and Table 6.9). However, the situation of the extreme compressive stress versus cohesion for the Y-component is complicated and no regularity. The locations of the extreme stresses occurring are also altered to-and-fro for both tread patterns (see node no. in Table 6.9 for the Y-components).

Similarly, the varying tendency of the maximum tensile stress versus cohesion in the Z direction for both tread patterns is same as that of in the X and Y directions, i.e. the maximum tensile stress gradually increase along with increasing of cohesion except one point at curve in pink where cohesion is 15 kPa (see in Chart 6.14c and Table 6.9). The extreme compressive stress versus cohesion in the Z direction for the fourth

tread pattern monotonously decreases in absolute value along with increasing of cohesion, but for the first tread pattern it fluctuates without regularity. The locations of the extreme stresses occurring are still shifted to-and-fro for both tread patterns (see node no. in Table 6.9 for the Z-components).

6.7 Summary

The study of footwear and soft ground interaction has been successfully conducted for the five tread patterns by using Finite Element Method. A methodology of numerical modelling for footwear and soft ground interaction has been created with ANSYS FE package and can be applied to footwear industry on the aspect of tread pattern design and assessment. The Drucker-Prager elastic-perfect plastic material model is adopted in this study to simulate soil behaviour. The DP failure criterion is with an associated flow rule, i.e. flow angle of soil material is equal to its internal friction angle, 31.8° . A series of standard soil FE models interactive with forepart of various tread patterns has been constructed and the SOLID45 eight-nodal element type in ANSYS is selected for modeling three-dimensional soil structure. A general size, 0.022m or around it, for successful meshing has been optimized for the five tread patterns. Boundary conditions are acted on all boundary surfaces of the soil FE model except the top surface being left free to any constraints. Loading conditions are applied to the soil model by average vertical and transverse pressures. The FE numerical solutions have been successfully carried out and a series of modeling results have achieved. The results demonstrate that, the first tread pattern has the best traction performance of the five tread patterns, but the fourth tread pattern is the best one having lateral stability and to utilize shear capacity of soil as well as to enable gripping and pivoting due to sinkage effect. Soil deformation, distribution of soil

stresses and strains are complex due to complicated tread pattern geometry size, configuration and transverse loading conditions. In general, the significant deformation of soil occurs in the regions contacted by cleats of the tread pattern or nearby and under them. Analyses of the extreme stresses and strains are presented. All the comparisons for the five tread patterns are based upon the exact same soil properties and material model, geometry sizes of FE models and external loads initiated by left foot. A soil FE model interactive with heel of the first tread pattern is also constructed and solved by acting on transverse loading condition which is different from that of forepart. Effects of soil properties are also investigated and founded that flow angle and cohesion have influence on the extreme stresses with different regularity respect to the X or Y or Z components and particular tread patterns, but the Young's modulus has no influence on them.

Chapter 7

Study of Experimental Validation

7.1 Introduction

After having successfully conducted 2-dimensional and 3-dimensional case validation study, we are confident in that Drucker-Prager material model in ANSYS Finite Element package is suitable for simulating soil behaviour in similar problems regarding soil failure. Therefore, the Drucker-Prager material model is employed in our study by using ANSYS Finite Element package. By far, FE numerical modellings of footwear and soft ground (soil) interaction have been successfully carried out with the total five different tread patterns of military and hiking boots. In the meantime, we have been carrying out experimental validation study against the FE numerical modelling results.

Since complexity of the tread pattern geometry shape and cleats configuration, it is difficult and expensive in cost to make experimental model containing the whole tread pattern with all cleats by using natural rubber, as well as unrealistic to clearly observe and measure soil deformation and failure caused by the whole tread pattern. Finally, a particular star shape cleat located at central area of forepart of the first tread pattern (see Fig. 6.6) is selected as prototype that will be employed in the process of experimental validation. Ideally, the physical model in experimental validation with real size against those employed in FE numerical modelling is the best choice. However, we have to use the scaled up model for experimental validation as the real cleat of tread pattern is too small in size and it would not be possible to clearly observe and record soil deformation and failure with the normal scale. In order to best

observe the soil deformation and failure, a standard scaled up physical model which is 10 times greater as the prototype was adopted, by considering factors about as much as possible to utilize the maximum inner width of soil tray, and to reduce frequency of the soil tray preparation.

On the other hand, a same scaled up FE model which 10 times greater as the prototype is constructed in ANSYS software. Boundary condition in numerical modelling is applied based upon similar constraining condition existed in the experimental process. The loading condition of the numerical modelling is determined and calculated by similarity theory and dimensional analysis. Having successfully carried out the FE modelling, the results of it are, then, validated by the experimental results.

Comparing to the numerical modelling method, experimental method is expensive and time consuming to some extent. However, if the experimental results of validation agree well with that of the FE numerical modelling, it is no doubt that the methodology achieved in our study by using FEM will be able to be a promising efficient and economical solution to evaluate traction performance of various tread patterns design and further guide design studies in future.

7.2 Experimental Facility

Ahead of this project “Finite Element Analysis of Footwear and Ground Interaction”, an experimental device—soil slip rig had been designed, constructed and used for two-dimensional experimental test against two-dimensional analytical study at Salford University. Details of this experimental facility had been reported by Rachael Pisani¹ in her PhD thesis—“FOOTWEAR AND SOFT GROUND INTERACTION”.

The soil slip rig has been improved in this study and re-illustrated by Fig. 7.1. As

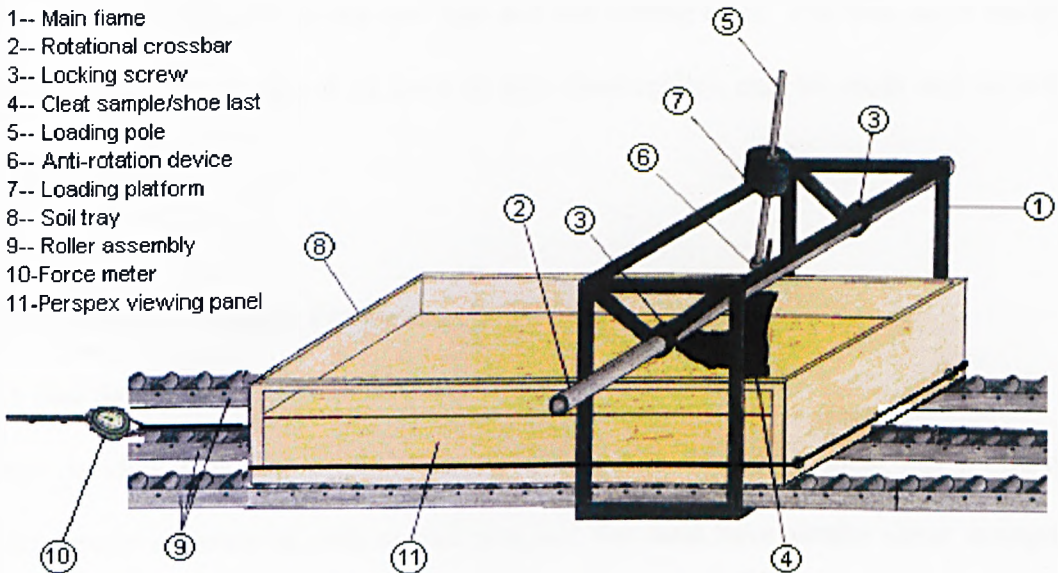


Fig. 7.1 Experimental device for validation of numerical modelling results

shown in Fig. 7.1, the rig consists of a main frame (1) and rotational cross bar (2). The rotational cross bar can be moved from side to side to enable a number of slip runs in one tray of soil which is carefully prepared. It is held by locking screws (3) at both ends and is used to pre-set the angle of contact of the cleat of tread pattern to the soil surfaces. A shoe last (4) to which footwear or scaled up cleat sample is attached is connected to a hardened steel pole (5) that slides through a bearing assembly located within the rotational bar. An anti-rotation device (6) has been fitted to the pole to maintain a consistent direction of the cleats during testing and also to assure no damage to the bearing assembly. The pole also has a loading platform (7) at its other end where the vertical load is applied using free weights. Having set the lateral position of the rotational bar and the contact angle of the tread, and having applied the vertical load using the weights, a soil tray (8) is pulled by weights and a pulley, a

force meter (10) enables the horizontal force to be measured. The horizontal force direction has been changed as shown in this figure which is different from that carried out by Rachael Pisani¹. The soil tray is mounted on a roller assembly (9) to simulate a state of no friction between the soil tray and supporting table. The tray has a Perspex viewing panel (11) on one of its sides so that observations may be made and recorded during a slip run.

7.3 Soil Selection and Its Properties

7.3.1 Soil Selection

It was decided in this research to begin testing with dry sand, since soil properties would remain constant as well as that wet and dry sand have similar shear strengths. Dry Leighton Buzzard sand is widely used in geotechnical laboratories and also found to be used in testing tyre traction. However, Leighton Buzzard sand was found to be unavailable in the laboratory within the engineering department at Salford University. Therefore, the kiln dried Congleton HST60 silica sand, that was purchased and used by Rachael Pisani¹, is selected in this study for the experimental validation.

The silica sand was supplied by Hepworth Minerals and Chemicals Ltd and its source is from Bent Farm, Congleton, Cheshire, UK. Silica sand is odourless, insoluble in water and stable under normal conditions. Its physical state is granule and in buff colour. The product information supplied by the supplier is that: Average grain size is 230 microns; Grain shape is well rounded; Loose bulk density is 1520 kg/m³; Clay content is 0.2% (Limits: 0.3% max.). The particle size is classified as a medium grained cohesionless soil.

7.3.2 Soil Properties

The soil properties had been tested and determined as follows. These parameters are used as input data for the FEM analyses.

7.3.2.1 Soil density

It was necessary to conduct the minimum and maximum density tests to find the full range of silica sand therefore the mid-density even though the supplier had supplied loose bulk density. The mid-density would then be reproduced during testing with the test rig and used as inputting density in numerical modelling.

The soil was prepared and tested according to BS 1377: part 1 (1990)¹²⁴ and BS 1377: part 4 (1990)¹²⁵. A 6 inch (one litre) California Bearing Ratio (CBR) mould was used for compaction testing to determine maximum dry density and a glass measuring cylinder was used to measure the minimum dry density of cohesionless soil.

Mould dimensions (without collar):

Diameter (d): 152mm

Height (h): 127mm

Volume of mould (without collar), V:

$$\frac{\pi d^2 h}{4} = 2.3 \text{ E}^{-3} \text{ m}^3$$

Minimum density (ρ_{\min}): Mass of sand (M_l): 3.564kg (loose)

Volume of mould (without collar), V: $2.3 \text{ E}^{-3} \text{ m}^3$

Density of sand (ρ_{\min}): $\frac{M_l}{V} = 1.55 \text{ E}^{-3} \text{ kg/m}^3$

Maximum density (ρ_{\max}): Mass of sand (M_c): 3.971kg (compressed)

Volume of mould (without collar), V : $2.3 \text{ E}^{-3} \text{ m}^3$

$$\text{Density of sand } (\rho_{\max}): \frac{M_c}{V} = 1.72 \text{ E}^{-3} \text{ kg/m}^3$$

The mid-density required for experimental validation is calculated by averaging the minimum and maximum densities.

$$\text{Mid-density } (\rho_{\text{mid}}): \quad \frac{1}{2} (\rho_{\min} + \rho_{\max}) = 1.635 \text{ E}^{-3} \text{ kg/m}^3$$

7.3.2.2 Soil friction angle

Based upon laboratory test results, the friction angle of soil (ϕ) is normally ranging

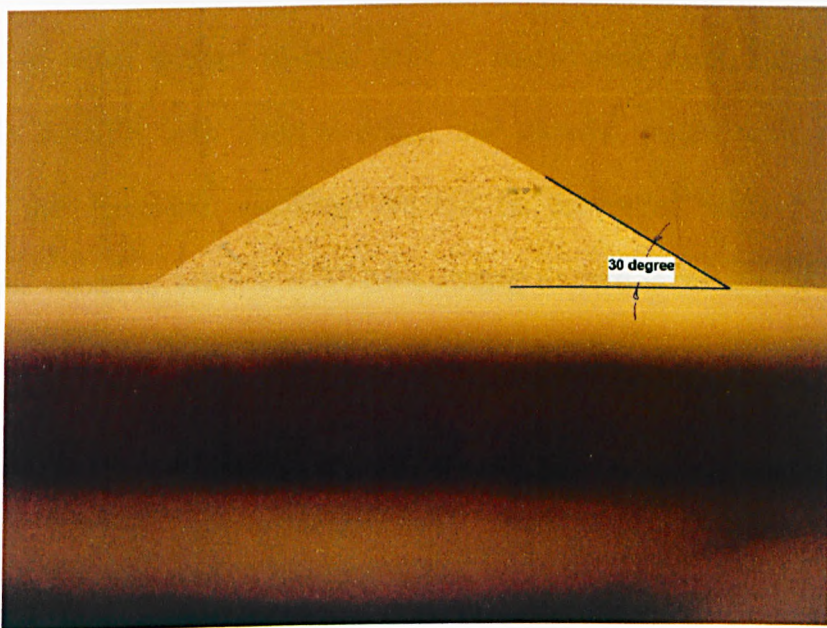


Fig. 7.2 Natural friction angle of silica sand

from 23.8° (degree) to 31.8° (degree) reported by Araya & Gao¹⁰ and Mouazen & Nemenyi¹¹, respectively. In this study, a simple method was employed to measure the

natural friction angle of silica sand as shown in Fig. 7.2. Several repeated measurements have been conducted and the mean friction angle was finally determined as $\phi = 30^\circ$ (degree).

7.3.2.3 Soil flow angle

As we know, a flow rule is applied to describe state of plastic flow. The flow angle of soil dilatation, β , allows the direction of principal plastic strain increments to be determined. If the flow angle, β , is equal to the angle of internal friction (ϕ) of soil, the plastic flow is fully associated. We assume the soil plastic flow is fully associated in this study of experimental validation, i.e. $\beta = \phi = 30^\circ$ (degree).

7.3.2.4 Soil cohesion

Under fully drained conditions, the cohesive strength of sand, c , is being zero from the results of either drained tri-axial tests or direct shear tests. However, the soil cohesion in ANSYS with Drucker-Prager soil material model must not be zero. Otherwise, the numerical modelling can not be proceeded further. Therefore, a relative small cohesion value, $c = 0.1$ kPa, closing to zero is selected to approximate the cohesive strength being zero for numerical modelling as well as experimental validation.

7.3.2.5 Young's modulus and Poisson's ratio

The Young's modulus, E , and Poisson's ratio, ν , are two fundamental mechanical parameters to reflect elasticity behaviour of material respect to elastic stress and elastic strain. These properties of soil (sand) used in this experimental validation study are determined as $E = 75000$ kPa and $\nu = 0.3$, by referring to that used in two-

dimensional case validation study in Chapter 4 (see sub-section 4.3.1). The Young's modulus could be decreased if clay content is raised. For instance, Mouazen & Nemenyi¹¹ reported the Young's modulus equals to 8067 kPa while clay content is 13.4% and silt content is 18.4%. The clay content of silica sand in this experimental validation study is 0.2%.

7.4 FE Modelling of Interaction between Scaled Up Model and Soil

As introduced in section 7.1, the FE model scaled up 10 times of a star-shape cleat has been constructed by using ANSYS package and in the mean time a physical model with same geometry has been designed and produced in laboratory. The FE modelling process and results will be reported in this section in detail.

7.4.1 Star-shape Cleat

The scaled up 10 times FE model of a star-shape cleat has been built up in ANSYS. The scaled up model drawings is also illustrated in appendix II. The scaled up 10 times physical model with star-shape is made of natural rubber as displayed in Fig. 7.3. As shown in Fig. 7.3, the whole block of physical model is composed of five layers of natural rubber with star-shape. Each layer has identical thickness of 11mm and sticks together by a patented powerful multi-purpose adhesive. Between the physical model and the shoe last/cleat attachment, a wooden model with the same geometry as rubber model except thickness is designed and produced to connect with them. The adhesive used to stick each layer of rubber models is also effectively

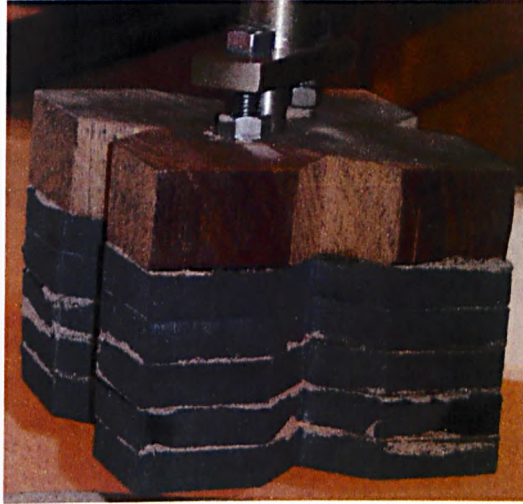


Fig. 7.3 Real model scaled up 10 times made of natural rubber

engaged in sticking wooden model and top layer of rubber model. Two bolts are fast embedded in the wooden model to be firmly fixed at the shoe last as shown in Fig. 7.3. Only the whole block of rubber models with a total of thickness 55~56mm joins in the interaction between the silica sand and the scaled up model in this experiment for validation purpose.

7.4.2 FE Modelling of Soil Interactive with Star-Shape Cleat

The soil FE model interactive with the star-shape cleat scaled up 10 times is shown in Fig. 7.4. The origin of coordinates is located at symmetrical center of bottom surface of the star-shape cleat scaled up 10 times.

7.4.2.1 Geometry size of the model

The soil is fully compressed before loading in the experimental validation. Full

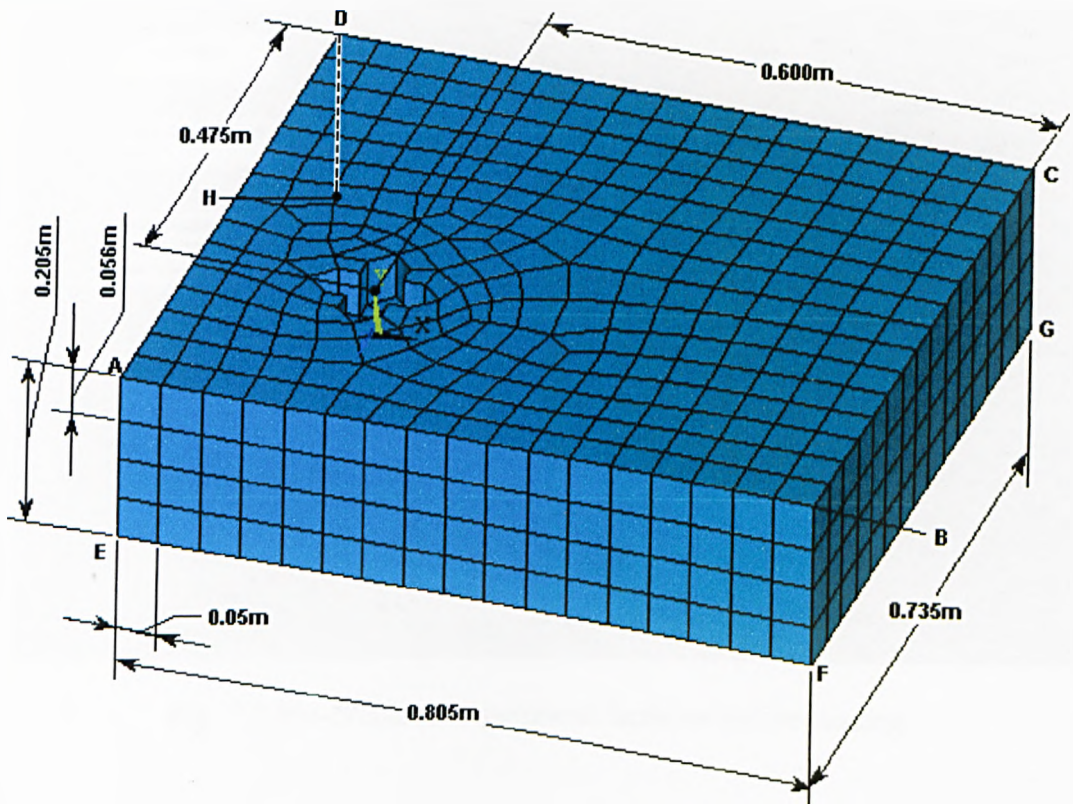


Fig. 7.4 The soil FE model interactive with star-shape cleat scaled up 10 times

sinkage is applied to star-shape cleat scaled up 10 times of forepart of outsole, that is, the depth of full sinkage equals to the height of scaled up cleat ($= 0.056\text{ m}$). As seen in Fig. 7.4, overall depth, length and width of the FE model are designed to be exactly same as that of experiment device shown in Fig. 7.5. The basic element size is optimized as 0.05m .

7.4.2.2 Soil properties and material model

The soil material parameters in FE modelling are same as that having been tested and determined in section 7.3.2, and summarized in Table 7.1.

Same as the material model used in Chapter 6, the Drucker-Prager material model is

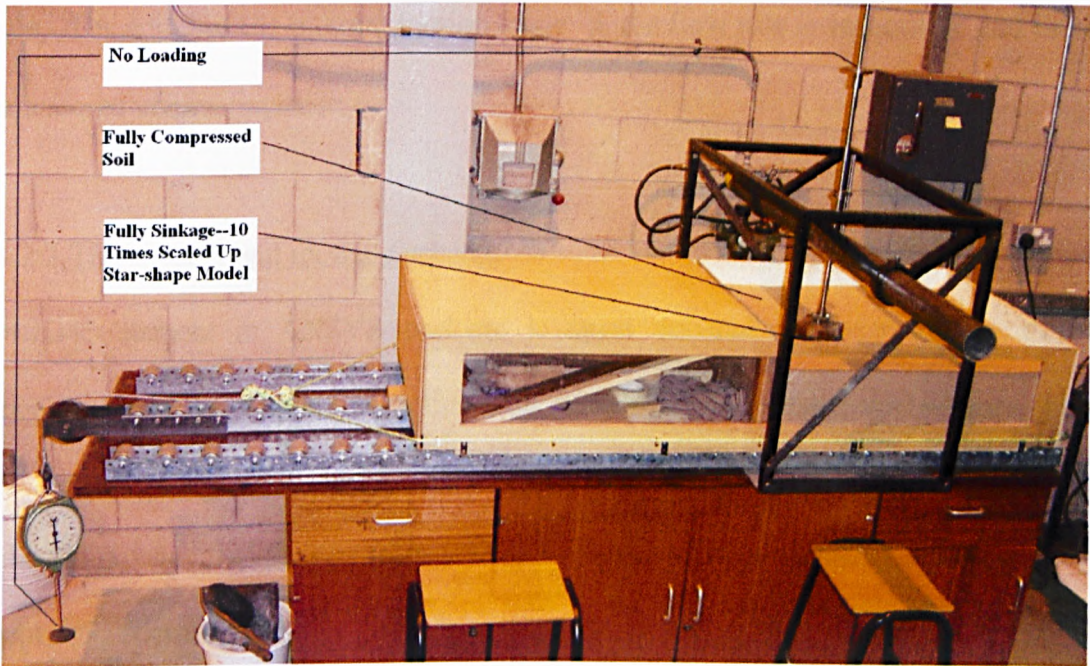


Fig. 7.5 Pre-prepared experiment facilities before loading

Table 7.1 Soil properties for FE modelling in experiment

Soil Properties	Value	Unit
Dry bulk density, ρ	1.635	$\text{k}\cdot\text{kg}/\text{m}^3$
Cohesion value, c	0.1	kPa
Internal friction angle, ϕ	30	deg.
Dilatancy angle, β	30	deg.
Poisson's ratio, ν	0.3	No dimension
Elastic modulus, E	75000	kPa

also employed to simulate the behaviour of elastic perfectly-plastic soil material in this experimental validation study. As shown in table 7.1, the dilatancy angle or flow

angle, β , is equal to the internal friction angle, ϕ , the flow rule is associative and there is a material volume increase.

7.4.2.3 The element and meshing scheme

SOLID45 element in ANSYS package is again selected to construct the three-dimensional soil FE model interactive with star-shape cleat scaled up 10 times. This type of element has been used for 3D cases validation studies as described in Chapter 5 and FE numerical modelling of interaction between soil and various tread patterns in Chapter 6 in detail.

A basic element size, that is 0.050 m, is optimized to mesh the whole block of soil volumes surrounding and being adjacent to the star-shape cleat scaled up 10 times. Total 61 key-points, 100 lines, 45 areas, 3 volumes, 1606 nodes, and 1144 eight-node SOLID45 elements are created. Fig. 7.4 shows the meshed volumes as well as elements.

...

7.4.3 Solution of the Soil FE Model Interactive with Star-Shape Cleat

7.4.3.1 Boundary conditions

Boundary conditions are applied to this three-dimensional model of soil problem. As shown in Fig. 7.4, referring to Fig. 7.5, the top surface ABCD is left free of any constraints in any direction. The horizontal negative displacement (x) of the surface ADHE and the horizontal positive displacement (x) of the surface BCGF are constrained, respectively. The lateral surfaces ABFE and DCGH are constrained in positive and negative z directions, respectively. The vertical y displacement of the bottom surface EFGH is also constrained.

7.4.3.2 Loading conditions

As described in section 6.3.1.2, vertical compressive and transverse shear forces are applied to the ground via the footwear during the process of gait. For this experimental validation study, a scaled up vertical load and a uniform horizontal displacement are acted on the model scaled up 10 times. The model, scaled up 10 times, is assumed to be a rigid body as its Young's modulus is more greater than that of the soil, that is, there is no deformation for the model assumed during the process of interaction between the model and soil. As the main interest of this study is to investigate soil plastic failure under transverse shear load and vertical load so as to evaluate traction performance of various tread patterns, the motion between the model and the soil is assumed to be frictionless, that is, interface friction between them is zero. Therefore, the loading conditions acted on the model are directly transferred to the soil through the model in the FE numerical modelling.

i) Transverse loads

As displayed in Fig. 7.6, the transverse loading condition is realised by applying a uniform horizontal displacement to all transverse surfaces of soil that are contacted with the model scaled up 10 times and sustained transverse shear forces.

Chi & Kushwaha^{3, 4} and Mouazen & Nemenyi¹¹ reported that the theoretical draught force increased with the agricultural tillage tool movement. After a number of increments, the draught force reached a maximum value at 0.050 m ~ 0.150 m of tool movement because of the failure of the soil structure. Consequently, a uniform horizontal displacement of 0.10 m is determined in this experimental validation study

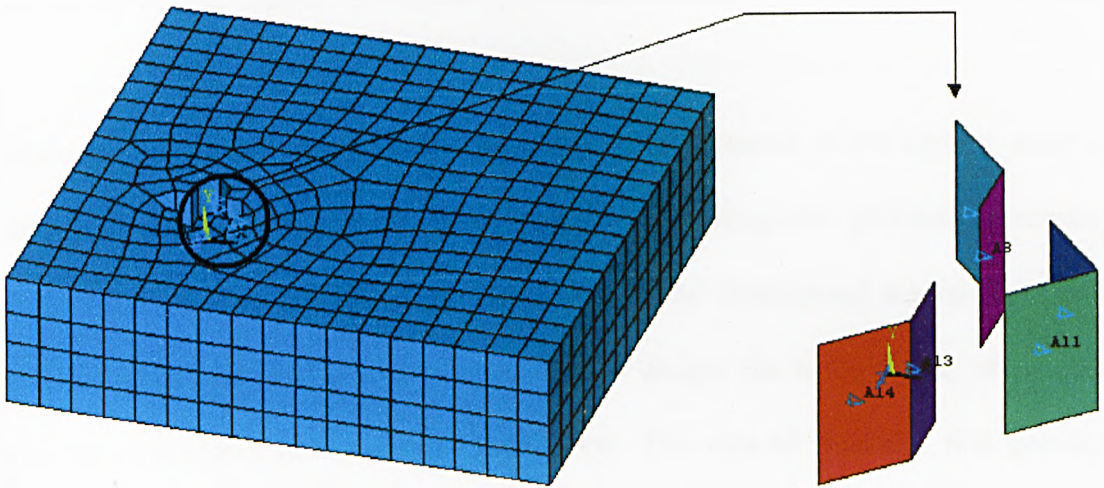


Fig. 7.6 Transverse loading conditions for the FE numerical modelling

including the FE numerical modelling to simulate the scaled up 10 times model's movement until the traction force reaches a maximum value when plastic flow occurs.

ii) Vertical loads

As reported in section 6.3.1.3 of Chapter 6, the average vertical pressure (P_v) acting on soil surfaces equals to 33.252 kPa for the first tread pattern (see formula 6.1). Therefore, the vertical load, F_* , acting on by any one star-shape cleat of the first tread pattern (see Fig. 6.10) can be calculated as follows:

$$F_* = P_v A_* = 33.252 \text{ kPa} * 0.00007788 \text{ m}^2 = 2.583 \text{ N} \quad (7.1)$$

where A_* is the area of horizontal surface of the star shape cleat.

For star-shape model scaled up 10 times, how to decide vertical pressure acted by it on the soil surfaces is a key factor to carry out the experimental validation study.

Similarity theory and dimensional analysis method in mechanics are employed to decide the vertical load for the scaled up 10 times model.

Similarity theory and dimensional analysis was encountered in the earliest study of physics in academies and in the initial stage of formulating new problems in research work. After entering 20 century, similarity theory and dimensional analysis have been widely studied and used in hydrodynamics, ship design, the many scaling effects that arise in wind tunnel or water tank testing, etc. The idea of similarity first gained a precise meaning in geometry. In Euclidean geometry two plane figures are similar when corresponding angles are equal and when corresponding sides are in a constant ratio. However, a physical body is more than an only geometric figure as it has mass and other physical attributes. Hence we regard two bodies or systems as similar only when their relevant physical properties are similarly distributed.

Physical Similarity and dimensional properties play a very important role in experiments and calculations in physics and engineering. Similarity theory and dimensional analysis determine the conditions the model experiments are to be carried out and the key parameters representing fundamental effects and processes. The modelling in experiments is to replace the study of the natural phenomenon by the study of an analogous phenomenon in a model of smaller or greater scale. It is obvious that the model in our experimental validation study is of a greater scale.

The concept of similarity in phenomena applies to both the static and dynamic behaviour of physical systems. Problems in static or dynamic reduce to the determination of certain functions and characteristic parameters. There are various

ways of defining physical similarity of static or dynamical problems. We adopt a definition of physical similarity in a form required in practical application and which is ready for direct use. Two phenomena are similar, if the characteristics of one can be obtained from the assigned characteristics of the other by a simple conversion, which is analogous to the transformation from one system of units of measurement to another. The “scaling factor” must be decided in order to accomplish the conversion. In our experimental validation study, the “scaling factor” is considered as 10. An example reported by Sedov⁶⁷ about analysing the problem of equilibrium of elastic structure is now re-introduced to make it clear how the vertical load is decided for the model scaled up 10 times in this study.

The elastic properties of a bridge girder are determined by two constants, Young’s modulus (E , N/m^2) and the non-dimensional Poisson’s ratio (ν), for this isotropic and homogeneous material. Considering geometrically similar structures, a series of characteristic parameters are formed. a) To assign a certain characteristic dimension B in order to define all the model dimensions. b) To select the gravity $\gamma = \rho g$ (N/m^3) as a characteristic parameter if the weight of the structure is essential in the equilibrium state. c) External loads must be considered as a characteristic parameter in addition to the weight of the structure which is determined by the force F (N). Then the system of characteristic parameters will be E , ν , B , F , ρg . For this case, three independent non-dimensional parameters will form the basis of mechanical similarity of elastic equilibrium state. These are:

$$\nu, \frac{E}{\rho g B}, \frac{F}{E B^2}$$

The similarity criteria demand that these three parameters are constant on the model and the prototype. If the model and the prototype are made from the same material, then the values of ρ , ν and E are identical on the model and the prototype. Consequently, the following conditions must be satisfied for mechanical similarity:

$$gB = \text{const.} \quad (7.2)$$

Under ordinary conditions, $g = \text{const}$; therefore, B must be a constant in order to conserve mechanical similarity.

Considering the stress τ (N/m^2) which develops in the deformation of an elastic structure under loading conditions of a weight and of a given load distribution, we can explain τ to be the maximum value of some stress component or, in general, to be a certain stress component acting on a specific element of the structure. The term τ/E is non-dimensional. As a result, we can write:

$$\frac{\tau}{E} = f\left(\nu, \frac{E}{\rho g B}, \frac{F}{EB^2}\right) \quad (7.3)$$

If the model and the prototype are produced from the same material, then $E = \text{const}$; consequently, the stress in corresponding points will be identical for mechanical similarity. If the magnitudes of the external loads are great but the intrinsic weight of the structure is small enough to be neglected, then the parameter $\gamma = \rho g$ and, therefore, the parameter $E/\rho g B$ is not essential. The preceding relation becomes:

$$\frac{\tau}{E} = f\left(\nu, \frac{F}{EB^2}\right) \quad (7.4)$$

and the similarity conditions will reduce to the only two conditions:

$$\nu = \text{const} \quad \text{and} \quad \frac{F}{EB^2} = \text{const} \quad (7.5)$$

Therefore, it follows that the external loads must be proportional to the square of the linear dimension when modelling with the material properties conserved.

Applying formula (7.5) to our experimental validation study, we have:

$$\frac{F_m}{E_m B_m^2} = \frac{F_*}{E_* B_*^2} = \text{const} \quad (7.6)$$

Where, the footnote “*m*” represents model scaled up 10 times; footnote “*” represents real cleat with star-shape, i.e. prototype. *F* is vertical load, *E* is Young’s modulus and *B* is characteristic dimension — linear dimension. As the model and the prototype are produced from the same material — natural rubber, $E_m = E_*$. Hence,

$$F_m = F_* \left(\frac{B_m}{B_*} \right)^2 = F_* \left(\frac{B_m}{B_*} \right)^2 \quad (7.7)$$

From formula (7.1), we have $F_* = 2.583 \text{ N}$, B_m/B_* is the “scaling factor” and equals to 10. So,

$$F_m = 2.583 * 10^2 = 258.3 \text{ N} \quad (7.8)$$

Therefore, the average vertical pressure (P^m_ν) acting on the soil surfaces by the model scaled up 10 times is:

$$P^m_v = \frac{F_m}{A_m} = \frac{258.3N}{0.009986m^2} = 25866N/m^2 = 25.866kPa \quad (7.9)$$

where A_m is calculated from Fig. 7.4 and Appendix II.

After the transverse and vertical loading conditions are applied and the solution controls are determined, a nonlinear numerical modelling is successfully conducted. The FE modelling results and discussion will be presented in the latter section 7.6 in detail by comparing to the experimental results.

7.5 Procedure of Experimental Validation

7.5.1 Soil Preparation

The mass of sand was calculated and the depth of sand in the tray, 0.205m, was determined to achieve the mid-density value as required for the experimental validation and the FE modelling. This depth, as shown in Fig. 7.4 and Fig. 7.5, was considered to be deep enough to eliminate the effect of the sand sliding against bottom surface of the tray. The sand with a total depth 0.205m was prepared by compacting four layers with depth of approximate 0.050m for each layer. The first layer was paved by pouring the sand into the base and evenly distributing it. A wooden board is placed over the sand layer and vibrated evenly for a period of time using an electric sander. At first the board was vibrated for 3 minutes, and then it was continuously vibrated until the required density was achieved. The next layer was then created like the first and vibrated. The tray was marked at the required depth of each layer. On completion of the soil preparation, the depth of soil was checked to ensure

the density was correct. The required density was achieved with an error of less than \pm 5%.

7.5.2 Installation of Scaled up Model

As shown in Fig. 7.3 and Fig. 7.5, the star-shape cleat model scaled up 10 times was fitted to the loading pole. The attachment was then secured at the shoe last by tightening the two bolts they were already fast embedded in the wooden model.

7.5.3 Positioning of the Model

Firstly, the soil tray was aligned with the rollers and fixed in the required position by inserting two wooden blocks into the gap between two rollers at positions of either left end of the tray or right end of it. The blocks were further secured by inserting one bolt into holes pre-drilled at the block and roller track. The bearing shaft was then set at the required angle (vertical to ground for all tests) and the horizontal crossbar was then locked to maintain this position. The model to be tested was then gently lowered onto the sand surface, correctly aligned and facing the correct direction. In order to make sure only the whole block of rubber models with total thickness 55~56mm to be joined in the interaction, a sinkage of 50mm was preset so as to the total 56mm sinkage could be achieved after vertical load was acted on later. The alignment device was then be secured to make ensure that the bearing shaft does not rotate during the experiment.

7.5.4 Application of Vertical Load

From calculated results in formula (7.8), the required weights, 258.3N (58.11lb), were gently placed on to the loading platform so not to disturb the prepared soil

unnecessarily. The locking device was then tightened thus securing the weights in position. Repeated tests had been done to ensure 50mm preset sinkage before the vertical loading can make the final sinkage equals to 56mm after the application of vertical load.

7.5.5 Application of Horizontal Load

After the application of vertical load, horizontal load was carefully acted on to the rig. First, the rig was checked to ensure everything was secure and in the correct position. The weight hanger was then connected to the soil tray pulling cord. The cord was checked to make sure it is aligned within the pulley. The weight hanger was correctly positioned at a distance 0.100m vertically from the end of it to the ground to ensure the distance of relative movement between the model and the soil was same as that in the FE modelling. The soil tray movement relative to the model was stopped when the end of weight hanger touches the ground as the horizontal pulling force, i.e. gravity of the weights was offset by ground.

Weights were then gently added to the weight hanger until the total weight of the weights was equal to 177.8 N (40 lb). Previous repeated tests had been done and found that the soil tray began to slide, that is plastic flow occurs, when the pulling force reached 177.8 N (40 lb). And then, the wooden block at the left hand side of the soil tray was removed at the same time the soil tray was firmly hold by hands to ensure no disturbance resulting from the taking away of the block. The applied horizontal load and vertical load are shown in Fig. 7.7.



Fig. 7.7 Loading conditions applied in the experimental validation

7.5.6 Observations and Measurements

Finally, the soil tray was moved under the horizontal load and vertical load as soon as after freeing the holding hands. The moving process of the soil tray was observed and recorded. Slip distance, i.e. distance of soil plastic flow as well as pattern of shear failure were also measured and recorded. These experimental validation results will be presented in detail in the following section comparing to the FE numerical modelling results.

7.6 Results and Discussion

The soil failure dimensions taken on the soil surfaces in the soil tray tests are reported in this section. The experimental data are compared with results of the FE modelling in order to validate the FEM model developed in this study. The final experimental results are shown in Fig. 7.8 after the soil tray moved 0.10m under the vertical and horizontal load and stopped when the pulling force is offset by the ground.

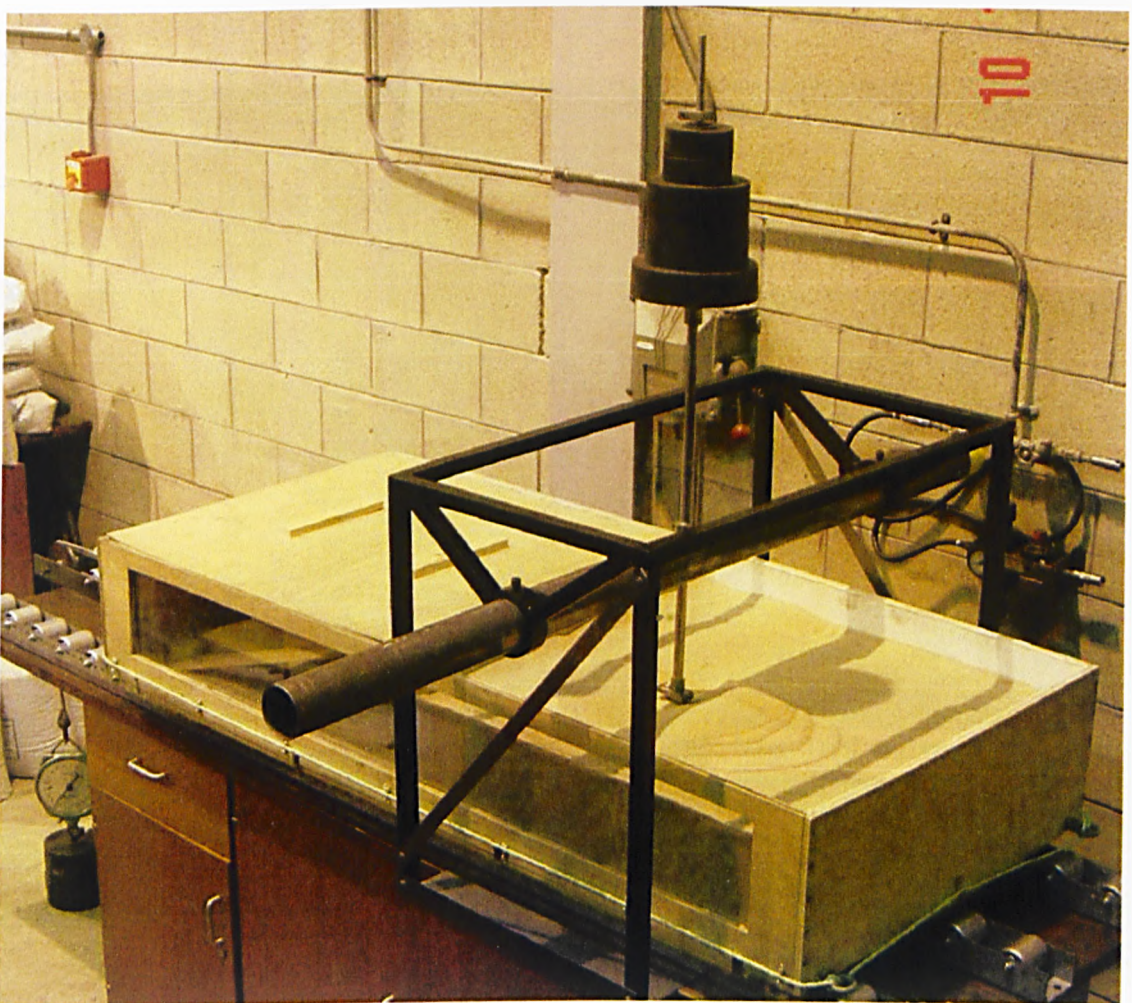


Fig. 7.8 Experimental results of soil failure in the soil tray test

It could be clearly observed that the soil was heaved up and moved forward in front of the cleat model, which is scaled up 10 times, as it slid along the soil surfaces. The soil

being heaved up by the model movement is the soil shear zone. The shape of the shear zone in front of the cleat model was seen to be approximately pattern of elliptical plateau, as illustrated by Fig. 7.8. These “elliptical plateaus” were considered as the amount of soil volume dilatancy resulting from the fully associated plastic flow.

The maximum forward, vertical and lateral soil movements are measured as displayed in Fig. 7.9.

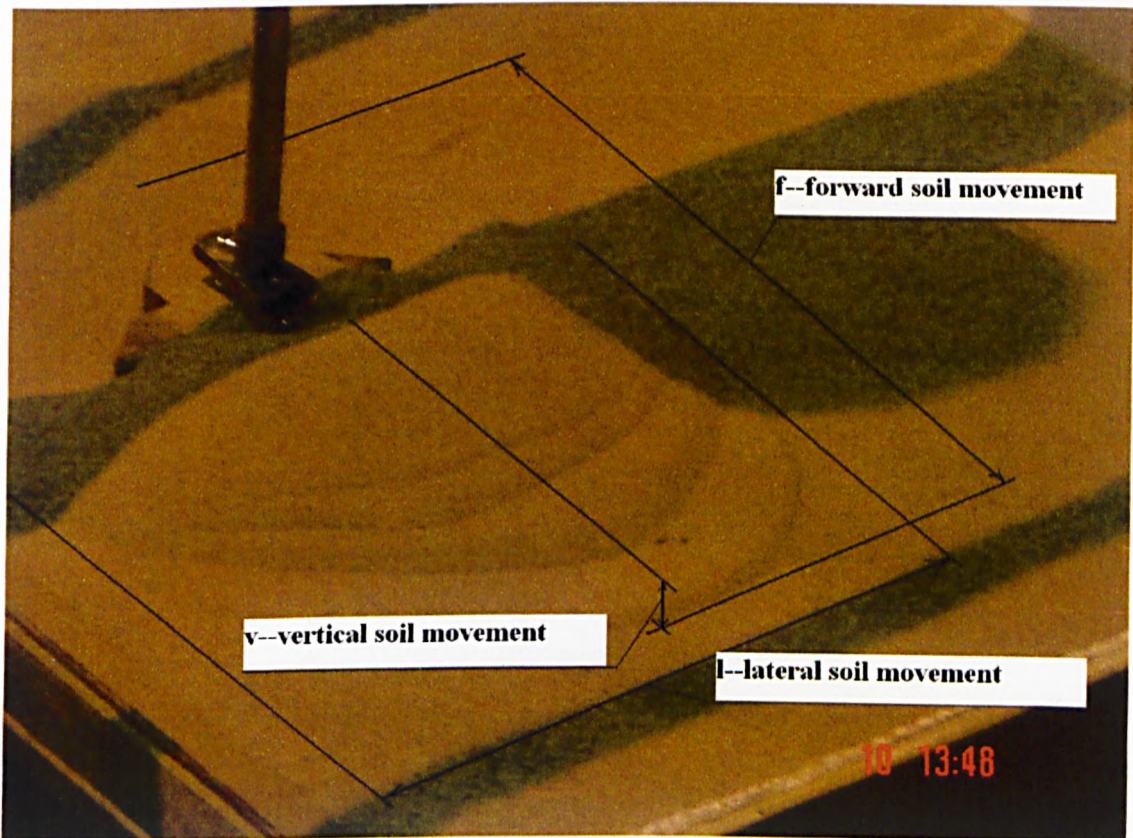
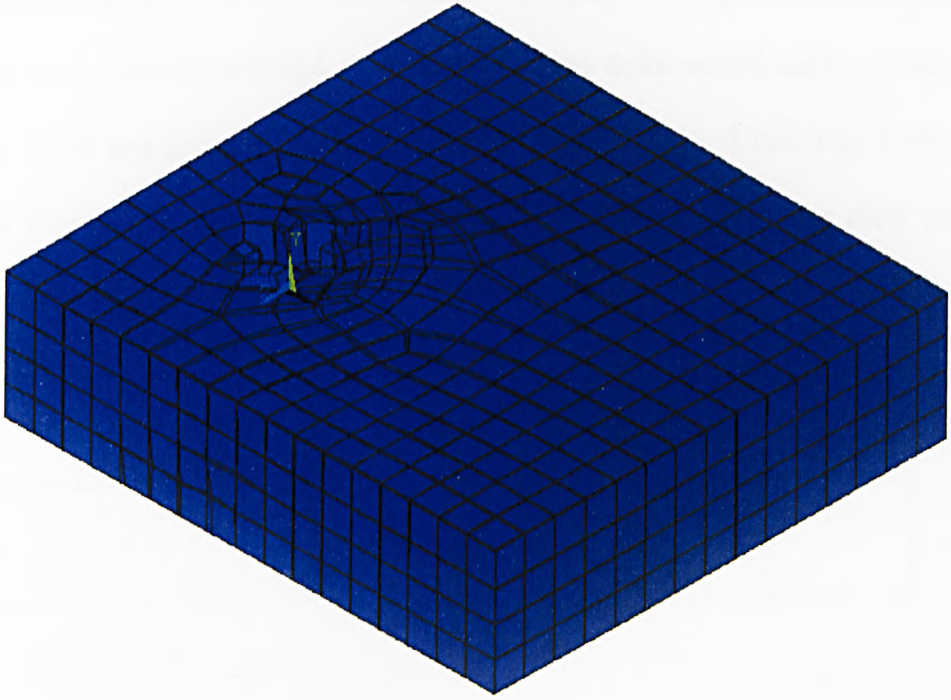


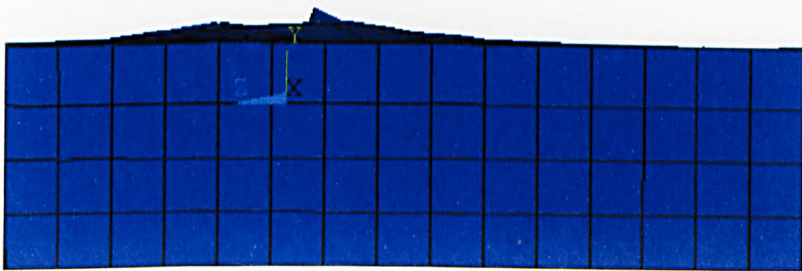
Fig. 7.9 The maximum soil failure distances measured in the experiment



a)



b)



c)

Fig. 7.10 The FE modelling results of soil deformation

The FE modelling results of soil deformation are displayed in Fig. 7.10 and Fig. 7.11. Fig. 7.10a is a three-dimensional picture of the soil deformation with undeformed edge; Fig. 7.10b is a projective picture from front view of Fig. 7.10a; Fig. 7.10c is a from right view projective picture of Fig. 7.10a. Fig. 7.11 shows vector plots of soil deformation at different directions of views.

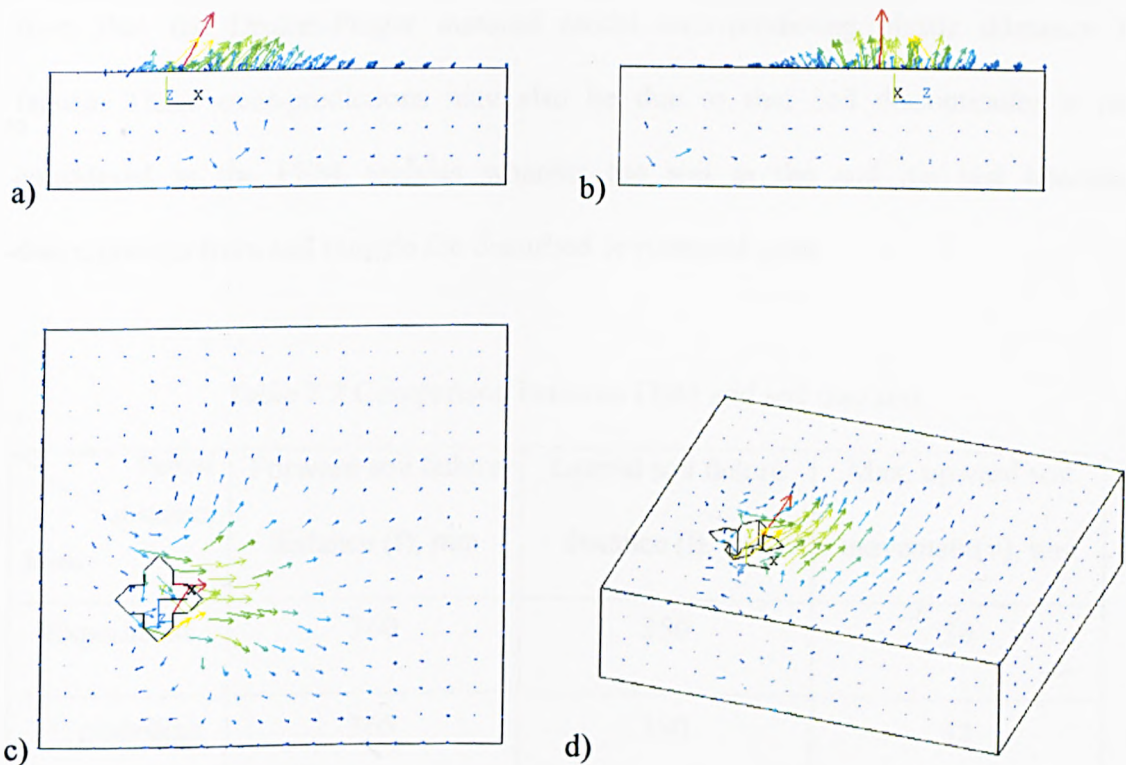


Fig. 7.11 Vector plots of soil deformation with the FEM

A comparison of the measured dimensions of soil failure in the experiment and predicated results by the FE modelling is summarized in Table 7.2.

It can be seen from Fig. 7.9, Fig. 7.10 and Fig. 7.11 that the soil deformation in the FE modelling results follows a similar failure pattern in the experiment. From Table 7.2, the FE numerical modelling provided a reasonable approximation of the forward soil failure distance (f), the maximum upward soil movement (v) as well as the lateral soil

failure distance (l) to the experimental results. The error between the FE modelling and the soil tray test for the forward soil failure distance (f) is 1.37%, therefore, shows a reasonably good agreement. The difference of the maximum upward soil movements (v) is 6.67% and not bad an agreement between the FEM and experimental validation study. The lateral soil failure distance (l) of the FE modelling is 11.43% larger than in the soil tray test. The causes of these errors may mainly result from that the Druker-Prager material model over-predicting plastic dilatancy at failure. These over-predictions may also be due to that soil discontinuity is not considered in the FEM analysis whereas the soil in the soil bin test becomes discontinuous from soil outside the disturbed or ruptured zone.

Table 7.2 Comparison between FEM and soil tray test

Items \ Failure distances	Forward soil failure distance (f), mm	Lateral soil failure distance (l), mm	Max. upward soil movement(v), mm
Experiment	360	350	30
FE modelling	365	390	32

7.7 Summary

A star shape model scaled up 10 times adopted from the first tread pattern is designed to perform experimental validation. A soil FE model interactive with the same scaled up size model is also constructed in ANSYS FE package. Boundary condition and loading condition in FE modelling is applied based upon the same conditions existed in the experiment. The dry Congleton HST60 silica sand is employed in the experiment and its mechanical properties are used as input data for the FE modelling.

The Drucker-Prager material model is employed to simulate the behaviour of an elastic perfectly-plastic soil material. SOLID45 element is selected to construct the soil FE model. A basic element size, 0.050 m, is optimized to mesh the FE model. A uniform horizontal displacement of 0.100 m is determined in this experimental validation study to simulate the scaled up 10 times model movement until the traction force reaches a maximum value when plastic flow occurs. Vertical loading conditions are determined by similarity theory and dimensional analysis. The experimental validation study shows that the FE numerical modelling provided a good agreement with the experimental results about soil failure pattern and the maximum various failure distances.

Chapter 8

Conclusions and Further Work

8.1 Introduction

This chapter is devoted to present general conclusions arisen from the overall outcomes of the project, and with some suggestions for future work that could continuously be carried out based upon this work. First, each chapter is conclusively reviewed and the main results from each are outlined; then general conclusions are remarked; finally, some proposals for further work are suggested.

8.2 Conclusive Review of Each Chapter of the Thesis

Chapter 1 introduced background and objective of this project, and outlined research contents addressed in chapters of this thesis.

Chapter 2 first specified what the problem of this project is, then presented the literature review focused on several relevant topics, such as soil-tillage tools interaction, soil-wheel interaction, soil-structure interaction, limit analysis, etc. as well as the main topic of footwear and soft ground interaction.

It was concluded that, from the reviewed literature, little work existed on the topic of footwear and ground interaction with soft surfaces, especially on work by using finite element method. A great number of studies concerning soil-tillage tool interaction have been performed since 1970s including quite a few using FEM. Soil-wheel interaction

study began from 1950's and a number of researches used FEM and Drucker-Prager nonlinear material model. Finite element analysis of soil-structure interaction has been applied to a number of types of soil mechanics and soil engineering problems since 1960s. Limit analysis method, a sort of analytical methods opposite to numerical methods, was widely applied in soil mechanics problems since it was established in 1950s. Some research concerning footwear and ground interaction with soft surfaces were reported that mainly by means of experiment methods with respect to artificial surfaces, such as Astroturf, and natural surfaces, for instance, football field. One works was reported by using FEM and hyper-elastic material model to study footwear function. Some texts and reference books are identified to be rather useful to this project.

Chapter 3 reviewed plasticity theory in soil mechanics. Five typical perfectly plastic models, including the Drucker-Prager material model we adopted, are selectively presented as well as flow theory and some fundamentals of solid mechanics. Each material failure model of them has both advantages and limitations. The well-known failure model—the Coulomb criterion is well established for many hydrostatic pressure sensitive soils, but is not mathematically convenient in three-dimensional modelling situation owing to the existence of corners. The Tresca and von Mises criteria are widely used for metals to determine the collapse or limiting state of a structure, but can not describe the shear strength of soils. The extended Tresca and the Drucker-Prager model (extended von Mises criteria) consider the effectiveness of mean normal stress, but the former still has the flaw of singularities. The Drucker-Prager model is available in computer codes and the simplest perfectly plasticity model approximating the Coulomb model. It may give

reasonable results for progressive failure analysis of soil with adequate assumption of the material constants. Its main limitation is over-estimate plastic dilatancy at yielding.

Chapter 4 presented the two-dimensional case validation study. A case of typical earth pressure problem was selected to redo by using the Drucker-Prager material model in ANSYS package to simulate soil behaviour. The 2-D 8-node structural solid PLANE82 element is selected to model soil structure. The earth pressure problem is simulated under plane strain conditions. Initial stress is considered in this case study and user routine is created to produce initial stress effect. Wall displacement is applied as a loading condition. A series of numerical modellings have successfully carried out and good agreement with published works has achieved. The 2-D case validation is successful and the ANSYS software with the Drucker-Prager material model is applicable to 2-D FE modelling for soil problems.

Chapter 5 reported three-dimensional cases validation study. Two cases of three-dimensional agricultural soil tillage problem were selected to be validation. The soil material properties are simulated by Drucker-Prager material model in ANSYS FE package. The SOLID45 8-node 3D structural solid element in ANSYS is chosen to construct soil structure. 0.15m and 0.10m wall displacements of subsoilers are applied to soil structures as loading conditions, respectively, in case 1 and case 2. For case 1 validation, good agreement respect to the deformation contour with published works has reached but no draught forces comparison due to the geometry size of the FE model was estimated. Case 2 validation studies show reasonable agreement with the published works

respect to the draught forces. Three-dimensional cases validation studies confirm ANSYS software is suitable to 3D FE modelling for the problems of soil and structure—tillage tool interaction.

Chapter 6 presented the study of finite element analysis of a total of five tread patterns and soft ground interaction in detail. Outdoor boots as well as military boots are firstly reviewed. Then, the methodology of constructing soil FE model interactive with the first tread pattern, meshing schemes, boundary conditions, and loading conditions is intensively presented step by step. Finally, numerical modellings are successfully conducted and the modelling results are presented. Traction performance of each tread pattern as well soil deformations, stresses, strains and influence of soil properties, etc. are analyzed and conclusive results are achieved.

The methodology of FE numerical modelling for footwear and soft ground interaction having created with ANSYS FE package in this study can be applied to footwear industry on the aspect of tread pattern design and assessment of it. The DP failure criterion with an associated flow rule was employed in this study, and a general size, 0.022m, of SOLID 45 elements has been optimized for successful meshing for the soil FE models interactive with the five tread patterns. The FE numerical results demonstrate that, the first tread pattern has the best traction performance among the five tread patterns, the third and the fourth tread pattern also show relative better traction effect. The second tread pattern show the poorest traction effect. The fourth tread pattern is the best one having lateral stability and to utilize shear capacity of soil as well as to enable gripping and pivoting

due to sinkage effect. In general, the significant deformation of soil occurs in the regions contacted by cleats of the tread pattern or nearby and under them. Flow angle and cohesion have influence on the extreme stresses with different regularity respect to the X or Y or Z components and particular tread pattern, but Young's modulus has no influence on them. A FEM analysis of a soil FE model interactive with heel of the first tread pattern is also conducted. The situation of soil deformation of it is different from that of with forepart as difference of loading conditions in magnitude.

Chapter 7 describes details of the experimental validation studies. A star-shape cleat model scaled up 10 times was designed, manufactured and used in the experimental work to enable soil movement observation and accurate measurement of the soil failure distances to be compared to the FE modelling results. Similarity theory and dimension analysis of mechanics was employed to decide the vertical loading conditions. The soil mechanical parameters in experiment were as the inputted data of the soil properties in the FE modelling. The FE modelling results were finally validated by the experimental results.

The Drucker-Prager material model is still employed to simulate the behaviour of elastic perfectly-plastic soil material. A basic size, 0.050 m, of SOLID45 element is optimized to successfully mesh the FE model. A uniform horizontal displacement of 0.100 m is determined by repeat tests in the experiment to simulate the scaled up model movement until when plastic flow of soil occurs. This prescribed displacement is adopted as the horizontal loading conditions for the FE modelling. The experimental validation study shows that the FE numerical modelling provided a good or reasonable agreement with the

experimental results about soil failure pattern and the various maximum failure distances. The error for the forward soil failure distance is 1.37%. The maximum upward soil movement of the FEM predictions is 6.67% over-predicting the experimental result. The lateral soil failure distance of the FE modelling is 11.43% larger than that in the soil bin test.

8.3 Conclusions

Through studies of the project “Finite Element Analysis of Footwear and Ground Interaction”, the following general concluding remarks arise from this investigation:

1. The finite element method has been successfully applied to the numerical modelling of footwear and soft ground interaction with different tread patterns.
2. The methodology created in this study can be commissioned to identify military boots’ performance about tread pattern design, and applied to footwear industry respect to outdoor sports and civilian recreation activity.
3. The FE analyses were successfully conducted with a series of non-linear, three-dimensional soil FE models based upon the elastic-perfectly plastic material characteristics, and the Drucker-Prager failure criterion of material models in ANSYS FE package has been employed to model the soil behaviour.
4. In total, five tread patterns of military and hiking boots interactive with soil have been simulated by FEM. The FE modelling results showed that the first tread pattern is the best design on the aspect of traction performance, and the fourth tread pattern design has the best performance of lateral stability and enabling gripping and pivoting due to sinkage effect.

5. Experimental validation for the FE modelling results has been successfully carried out using greater cleat model scaled up 10 times in a laboratory soil bin. The FE numerical models shows a good agreement with the experimental results about soil failure pattern and the forward soil failure distance as well as the maximum upward soil movement.
6. Effects of soil mechanical parameters versus the extreme stresses for the first and fourth tread patterns are comparatively investigated. The FEM analyses showed that flow angle and cohesion have influence on the extreme stresses of both tread patterns, but Young's modulus has no influence on them. The varying tendency of the extreme stresses versus flow angles for the first tread pattern is, generally, different from that of the fourth one, whereas the fluctuant regularity of stress peak value to cohesion are similar to each other for the both tread patterns.
7. Soil deformation and distribution of stresses and strains are complex for the five tread patterns due to complicated cleats configuration, geometry size, and transverse loading conditions. In general, significant soil displacements occur in the regions contacted by cleats at rear part of the tread pattern and zones under central part of the tread pattern.
8. Two and three-dimensional case validation studies have been successfully conducted and good agreements have achieved with results of published works. These validation studies have provided a reinforced foundation to continuously carry out this project and fulfill it successfully.

8.4 Future Work

This research has created a methodology of using Finite Element Method to analyze footwear and soft ground interaction, and provided a useful platform from which to carry out further investigation with FE numerical modelling techniques and experimental validation scheme used in this study. Therefore, the following suggestions are drawn for future work.

8.4.1 Consideration of Interface Friction

As this research is focused on what limit condition is when shear failure of soil mass happens mainly under transverse shear loads, which is initiated by vertical surfaces of cleats, and vertical pressure loads, friction of interfaces between the soil and surfaces of cleats and sole was assumed to be zero, that is, the motion is frictionless. It is recommended that the FE modelling of footwear and soft ground interaction be further developed considering interface friction. It would be more close to reality, but no doubt that the FE modelling process will become more complicated and time costing. It is suggested that for its simplicity in connecting two materials with a complex geometric interface, two-node, gap elements can be inserted between each couple of nodes of the soil and contacting surfaces of cleats and sole.

8.4.2 Dynamics Analysis of Footwear and Soft Ground Interaction

The problem of footwear and soft ground interaction including slip is basically a dynamic process. It is suggested that dynamics analysis of footwear and soft ground interaction subjected to dynamic loads may carry out in future be means of either numerical modelling methods or experimental methods. The numerical modelling methods may

employ either Finite Element Method, or Finite Difference Method, or Boundary Element Method, or Distinct Element Method, etc. The experimental methods may include a method by employing some sensors embedded into the soil to measure soil disturbance, and recording data by a computer-controlled system during the process of gait.

8.4.3 Advancement of Experimental Facility

The experimental validation work to date has been carried out by manual operation based on simple mechanical mechanisms using weights and pulleys. Some suggestions are given for future improvements of the experimental device. Force transducers can be used to measure the pulling force so as to reduce measurement error. The soil bin movement can be driven by a motor system that is available to accurately control the moving speed and distance. Variety of soils can be ordered and prepared to validate the FE modelling results for use with different type of cohesive soils. However, frequent measurement of soil mechanical parameters would also be required as their variability.

Appendix I

The FORTRAN programme—a user subroutine for producing initial stress with 2D case validation study

```
C PROGRAM AUTO
C
COMMON/BLOCK01/NX,NY,AX,AY
COMMON/BLOCK02/XF(300,300),YF(300,300)
COMMON/BLOCK03/X(8,200,200),Y(8,200,200)
COMMON/BLOCK04/FX(8,200,200),FY(8,200,200)
C
OPEN(7,FILE='istress.ist')
  AX=35.0
  AY=5.0
  NX=30
  NY=10
  DX=AX/NX
  DY=AY/NY
  AA=0.0
  DO 100 I=1,NX
  DO 100 J=1,NY
    XF(I,J)=DX/2.0+(I-1)*DX
    YF(I,J)=AY-DY/2.0-(J-1)*DY
100 CONTINUE
  DO 200 I=1,NX
  DO 200 J=1,NY
    X(1,I,J)=XF(I,J)-DX/2.0
    Y(1,I,J)=YF(I,J)-DY/2.0
    X(2,I,J)=XF(I,J)
    Y(2,I,J)=YF(I,J)-DY/2.0
    X(3,I,J)=XF(I,J)+DX/2.0
    Y(3,I,J)=YF(I,J)-DY/2.0
    X(4,I,J)=XF(I,J)+DX/2.0
    Y(4,I,J)=YF(I,J)
    X(5,I,J)=XF(I,J)+DX/2.0
    Y(5,I,J)=YF(I,J)+DY/2.0
    X(6,I,J)=XF(I,J)
    Y(6,I,J)=YF(I,J)+DY/2.0
    X(7,I,J)=XF(I,J)-DX/2.0
    Y(7,I,J)=YF(I,J)+DY/2.0
    X(8,I,J)=XF(I,J)-DX/2.0
    Y(8,I,J)=YF(I,J)
200 CONTINUE
  DO 300 J=1,NY
  DO 300 I=1,NX
  DO 300 K=1,8
    FY(K,I,J)=18.0*(5.0-Y(K,I,J))
    FX(K,I,J)=0.5*FY(K,I,J)
300 CONTINUE
  WRITE(7,1600)
1600 FORMAT('! ***** STRESS INITIALIZATION FILE FOR ANSYS
*****
$*****')
  WRITE(7,1700)
1700 FORMAT('!')
  WRITE(7,1800)
```

```

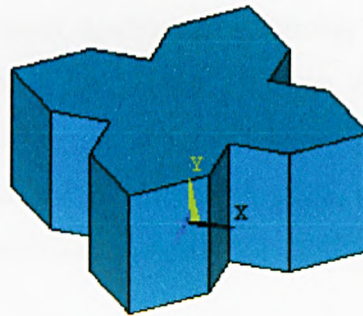
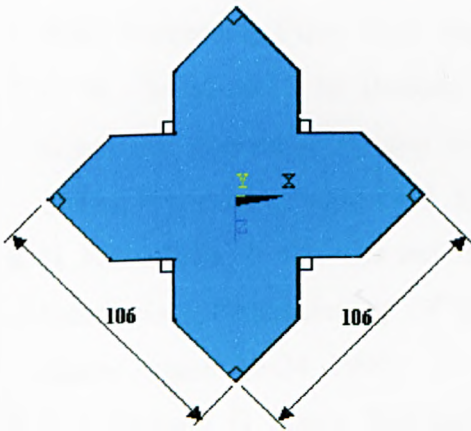
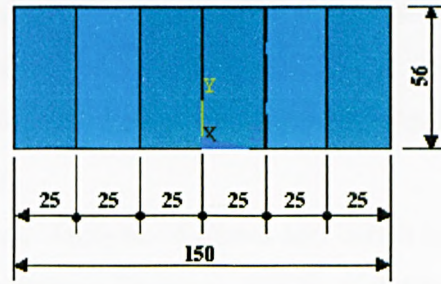
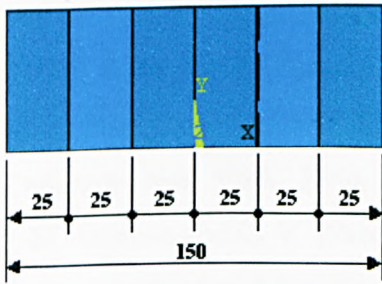
1800 FORMAT('! This file, istress.ist, contains initial stress
data')
WRITE(7,1900)
1900 FORMAT('! FOR 300 PLANE82 elements.')
WRITE(7,1700)
DO 400 I=1,NX
DO 400 J=1,NY
K=J+(I-1)*NY
WRITE(7,2000)K
2000 FORMAT('! Stress for element',I5)
WRITE(7,2100)
2100 FORMAT('!          Sx          Sy          Sz          Sxy          Syz
Sxz'
$)
WRITE(7,1500)K
1500 FORMAT('eis,',I5)
WRITE(7,1000)FX(1,I,J),FY(1,I,J),AA,AA,AA,AA
WRITE(7,1000)FX(3,I,J),FY(3,I,J),AA,AA,AA,AA
WRITE(7,1000)FX(5,I,J),FY(5,I,J),AA,AA,AA,AA
WRITE(7,1000)FX(7,I,J),FY(7,I,J),AA,AA,AA,AA
WRITE(7,1700)
400 CONTINUE
WRITE(7,2200)
2200 FORMAT('! End of initial stress file')
WRITE(7,2300)
2300
FORMAT('!*****')
$*****')
1000 FORMAT(G15.6,' ',',G15.6',' ',',F3.1',' ',',F3.1',' ',',F3.1,
$', ',',F3.1)
END
C
C

```

Appendix II

Dimensions of the Rubber Model Scaled up 10 Times

Sizes Unit: mm



References

1. Rachael Pisani, "FOOTWEAR AND SOFT GROUND INTERACTION", PhD Thesis, The University of Salford, UK, 2002.
2. R. N. Yong, and A. W. Hanna, "Finite element analysis of plane soil cutting", *Journal of Terramechanics*, 1977, vol. 14 (3): 103-125.
3. L. Chi and R. L. Kushwaha, Three Dimensional Finite Element Interaction between Soil and Tillage Tool, ASAE Paper No. 88-1611. ASAE, St. Joseph, MI 49085.
4. L. Chi and R. L. Kushwaha, A Non-Linear Finite Element Model for Predicting Soil Forces on Tillage Tools, *Proceeding of 10th International Conference of the ISTVS/ Kobe, Japan/ August 20-24, 1990*.
5. M. E. Harr, *Foundation of Theoretical Soil Mechanics*, McGraw-Hill Book Company, New York, 1966, N. Y. , USA.
6. J. M. Duncan and C. Y. Chang, Non-linear Analysis of Stress and Strain in Soils, *Journal of the Soil Mechanics and Foundations Division, ASCE, Vol. 96, No. SM5, Proceeding Paper 7513, Sept.1970, pp. 1629-1653*.
7. G. W. Clough and J. M. Duncan, Finite Element Analyses of Retaining Wall Behaviour, *Journal of the Soil Mechanics and Foundations Division, ASCE, No. SM12, Proceeding Paper 8583, December 1971, pp. 1657-1673*.
8. H. Nakashima, T. Taanaka and M. Yamazaki, Finite Element Analysis of Soil-Lug Interactions, *Proceeding of 10th International Conference of the ISTVS/ Kobe, Japan/ August 20-24, 1990*.
9. R. J. Godwin, G. Spoor, Soil Failure with Narrow Tines, *J. Agric. Engng. Res.* (1977) 22, 213-228.
10. K. Araya, R. Gao, A Non-linear Three-Dimensional Finite Element Analysis of Subsoiler Cutting with Pressurized Air Injection, *J. Agric. Engng. Res.* (1995) 61, 115-128.
11. Abdul M. Mouazen; Miklos Nemenyi, Tillage Tool Design by the Finite Element Method: Part 1. Finite Element Modelling of Soil Plastic Behaviour, *J. Agric. Engng Res.* (1999) 72, 37-51.
12. Abdul M. Mouazen; Miklos Nemenyi, etc., Tillage Tool Design by the Finite Element Method: Part 2. Experimental Validation of the Finite Element Results

- with Soil Bin Test, *J. Agric. Engng Res.* (1999) 72, 53-58.
13. Abdul M. Mouazen; Miklos Nemenyi, Finite element analysis of subsoiler cutting in non-homogeneous sandy loam soil, *Soil & Tillage Research*, 51 (1999) 1-15.
 14. Abdul M. Mouazen; Miklos Nemenyi, A Finite Element Model of Soil Loosening by A subsoiler with Respect to Soil Conservation, *Advances in Geo-Ecology*, 31, 549-556, Reiskirchen 1998. A cooperating Series of the International Society of Soil Science (ISSS). ISBN 3-923381-42-5.
 15. Abdul M. Mouazen; Miklos Nemenyi, Finite Element Modelling of Subsoiler Processes, *Advances in Geo-Ecology*, 32, 126-134, Reiskirchen 2000. A Cooperating Series of the International Union of Soil Science (IUSS). ISBN 3-923381-44-1.
 16. N. Renon, P. Montmitonnet and P. Laborde, Numerical Modelling of soil ploughing for military breaching, *Proceeding of 8th European Conference of the ISTVS/ UMEA, SWEDEN/ June 18-22, 2000.*
 17. Bekker, M. G. *Introduction to Terrain-Vehicle Systems*, The University of Michigan Press, 1969.
 18. K. Terzaghi, *Theoretical Soil Mechanics*, Wiley, New York, 1943.
 19. A. Oida, A. Satoh, H. Itoh and K. Triratanasirichai, Three Dimensional Stress Distributions on Tire-Sand Contact Surface, *Proceeding of 10th International Conference of the ISTVS/ Kobe, Japan/ August 20-24, 1990.*
 20. M. Ueno, K. Hashiguchi, Y. Nohse, F. Koyama, K. Uchiyama, H. Izumi, Analysis of Soil-Wheel Interaction by Elastic-plastic Finite Element Method, *Proceeding of 10th International Conference of the ISTVS/ Kobe, Japan/ August 20-24, 1990.*
 21. T. Aubel, FEM-SIMULATION OF THE INTERACTION BETWEEN AN ELASTIC TYRE AND SOFT SOIL, *Proceeding of 11th International Conference of the ISTVS Vol.2 S. 791-802, Lake Tahoe, 1993.*
 22. R. W. Clough, and R. J. Woodward, III, "Analysis of Embankment Stress and Deformations", *Journal of the Soil Mechanics and Foundation Division, ASCE*, Vol. 93, No. SM4, Proc. Paper 5329, July, 1967, pp. 529-549.
 23. W. D. L. Finn, "Static and Dynamic Behaviour of an Earth Dam", *Canadian Geotechnical Journal*, Vol. 4, No. 1, 1967.
 24. J. M. Duncan, and P. Dunlop, "Slopes in Stiff-Fissures Clays and Shales", *Journal of the Soil Mechanics and Foundation Division, ASCE*, Vol. 95, No. SM2, Proc. Paper 6449, March, 1969, pp. 467-492.

25. J. M. Duncan and C. Y. Chang, "Analysis of Soil Movement Around a Deep Excavation", *Journal of the Soil Mechanics and Foundation Division*, ASCE, Vol. 56, No. SM5, Proc. Paper 7513, Spet., 1970, pp. 1629-1653.
26. C. V., Girijavallabhan, L. C. Reese, "Finite Element Method for Problems in Soil Mechanics", *Journal of the Soil Mechanics and Foundations Division*, ASCE, Vol. 94, No. SM2, Proceeding Paper 5864, March 1968, pp. 473-496.
27. C. S. Desai, and L. C. Reese, "Analysis of Circular Footings on Layered Soils", *Journal of the Soil Mechanics and Foundation Division*, ASCE, Vol. 96, No. SM4, Proc. Paper 7408, July, 1970, pp. 1289-1310.
28. D. J. D'Appolonia, and T. W. Lambe, "Method for Predicting Initial Settlement", *Journal of the Soil Mechanics and Foundation Division*, ASCE, Vol. 96, No. SM2, Proc. Paper 7167, March, 1970, pp. 523-544.
29. I. M. Smith, "A Finite Element Approach to Elastic Soil-Structure Interaction", *Canadian Geotechnical Journal*, Vol. 7, No. 2, May, 1970.
30. N. R. Morgenstern, and Z. Eisenstein, "Methods of Estimating Lateral Loads and Deformations", *Preprint Proceedings*, 1970, Specialty Conference on Lateral Stresses in the Ground and Design on Earth-Retaining Structures, Cornell University, June, 1970, pp. 51-102.
31. T. W. Lambe, "Braced Excavations", *Preprint Proceedings*, 1970, Specialty Conference on Lateral Stresses in the Ground and Design on Earth-Retaining Structures, Cornell University, June, 1970, pp. 149-218.
32. R. L. Kondner, "Hyperbolic Stress—Stress Response: Cohesive Soils", *Journal of the Soil Mechanics and Foundations Division*, ASCE, Vol. 89, No. SM1, Proc. Paper 3429, 1963, pp. 115-143.
33. N. Janbu, "Soil Compressibility as Determined by Oedometer and Tri-axial Tests", *European Conference on Soil Mechanics & Foundations Engineering*, Wiesbaden, Germany. Vol. 1, 1963, pp. 19-25.
34. Potts, D. M. and Fourie, A. B., A numerical study of the effects of wall deformation on earth pressures, *Int. J. Num. Anal. Math. Geom.*, 10 (1986) 383-405.
35. Schweiger, H. F., On the Use of Drucker-Prager Failure Criterion for Earth Pressure Problems, *Computers and Geotechnics*, 16 (1994) 223-246.
36. D. C. Drucker, Limit Analysis of Two and Three Dimensional Soil Mechanics Problems, *Journal of the Mechanics and Physics of Solids*, 1953, Vol. 1, pp. 217

to 226. Pergamon Press Ltd., London.

37. W. F. Chen, *Limit Analysis and Soil Plasticity*, Elsevier Scientific Publishing Company, Amsterdam, 1975.
38. D. C. Drucker, H. J. Greenberg, and W. Prager, 1952. Extended limit design theorems for continuous media. *Q. Appl. Math.*, 9: 381-389.
39. A. V. Lyamin, and S.W. Sloan, Upper Bound Limit Analysis Using Linear Finite Elements and Non-linear Programming, *Techniques and Developments. Fifth International Conference on Computational Structures Technology and the Second International Conference on Engineering Computational Technology*. Civil-Comp Press. 2000, pp.131-45. Edinburgh, UK.
40. I. D. S. Pontes Fo., etc., An Approach to Limit Analysis with Cone-Shaped Yield Surfaces, *Int. J. Numer. Methods in Engng.*, 40 (1997) 4011-4032.
41. A. R. S. Ponter, etc., "Limit analysis for a general class of yield conditions", *Eur. J. Mech. A/Solids* 19 (2000) 401-421.
42. V. A. Babakov, etc., "Flat rigid die under a transverse load", *Journal of applied Mechanics and Technical Physics*, Vol. 35, No. 1, 1994, pp. 150-154.
43. E. B. Barry, and P. D. Milburn, "A mechanism explaining traction of footwear on natural surfaces", *Proc. 4th Symposium on Footwear Biomechanics*, 1999, pp. 22-23.
44. E. B. Barry, and P. D. Milburn, "A footwear traction measuring device", *Proc. 4th Symposium on Footwear Biomechanics*, 1999, pp. 20-21.
45. S. W. Valiant, *Sportverletz Sportschaden*, 7, 171-178, 1993.
46. T. W. Lambw, and R. V. Whitman, *Soil Mechanics*, 119-120, John Wiley, 1979.
47. S. W. Valiant, *Sports Res. Review*, Jan./Feb., Nike Inc., 1990.
48. J. Y. Wong, *Terramechanics and Off-Road Vehicles*, 72-80, Elsevier, 1989.
49. G. Baroud, etc., "A non-linear hyper-elastic finite element model of energy return enhancement in sport surfaces and shoes", *Proc. 4th Symposium on Footwear Biomechanics*, 1999, pp. 18-19.
50. A. C. Garcia, etc., "Development of a method for measuring horizontal forces in soccer boots studs during skills performance", *Proc. 4th Symposium on Footwear Biomechanics*, 1999, pp. 44-45.
51. K. Douglas, etc., "Cleat-surface friction on new and old Astroturf", *MEDICINE AND SCIENCE IN SPORTS*, Vol. 7, No. 2, pp. 132-135, 1975.
52. S. H. Robert, etc., "Differences in Friction and Torsional Resistance in Athletic

- Shoe—Turf Surface Interfaces”, *THE AMERICAN JOURNAL OF SPORTS MEDICINE*, VOL. 24, NO. 6, pp. 834-842, 1996.
53. P. Xu, J. Zhuang, and Z. Wang, EXPERIMENT AND ANALYSIS OF THE INTERACTION BETWEEN CAMEL FOOT AND SAND GROUND, 11th *International Conference of ISTVS*, Incline Village, USA, 1993.
 54. R. F. Craig, *Soil Mechanics*, 5th Edition. Chapman & Hall, 1992.
 55. G. N. Smith and Ian G. N. Smith, *Elements of Soil Mechanics*, 5th Edition. Blackwell Science, 1988.
 56. A. R. Jumikis, *Theoretical Soil mechanics*, American Book Company, 1969.
 57. R. N. Yong, and B. P. Warkentin, *Soil Properties and Behaviour*, Elsevier Scientific Publishing Company, Amsterdam, 1975.
 58. S. S. Rao, *The Finite Element Method in Engineering*, Pergamon Press Ltd., 1982.
 59. R. D. Cook, *Concepts and Applications of Finite Element Analysis*, 2th Edition, John Wiley & Sons, Inc. 1981.
 60. P. E, Lewis and J. P. Ward, *The Finite Element Method—Principles and Applications*, Addison-Wesley Publishers Ltd., 1991.
 61. Jean-Francois, etc., A micromechanical approach to the strength criterion of Drucker-Prager materials reinforced by rigid inclusions, *International Journal for Numerical and Analytical Methods in Geomechanics*, Volume 28, Issue 7-8, Pages 576-582, June 2004, Copyright © 2004 John Wiley & Sons, Ltd.
 62. R. Hill, *The Mathematical Theory of Plasticity*, Oxford University Press, 1950.
 63. J. Chakrabarty, *Theory of Plasticity*, McGraw-Hill, Inc., 1987.
 64. G. N. Smith, *An Introduction to Matrix and Finite Element Methods in Civil Engineering*, Applied Science Publishers Ltd., London, 1971.
 65. W. F. Chen, and E. Mizuno, *Non-linear Analysis in Soil Mechanics-- Theory and Implementation*. Elsevier Science Publishers B. V., 1990.
 66. W. J. Duncan, *PHYSICAL SIMILARITY AND DIMENSIONAL ANALYSIS*, EDWARD ARNOLD & CO., London, 1953.
 67. L. I. Sedov, *Similarity and Dimensional Methods in Mechanics*, INFOSEARCH LTD., London, 1959.
 68. K. L. Johnson, *Contact Mechanics*, Cambridge University Press, 1985.
 69. Z. Sun, M. Moatamedi, and D. Howard, the Designing for Load Carriage Systems, Symposium, Loughborough University, 2002, hosted by the UK Ministry of Defence.

70. Z. Sun, D. Howard, and M. Moatamedi, Military boots and Soft surfaces Interaction Mechanism, Proceedings of the International Society of Biomechanics XIXth Congress—The human Body in Motion, 2003, New Zealand.
71. Z. Sun, M. Moatamedi, and D. Howard, Finite Element Analysis of Footwear and Ground Interaction, Proceedings of the 2nd International Conference “Biomechanics of the Lower Limb in Health, Disease and Rehabilitation”, Salford University, 2003.
72. Drucker, D.C., Some Implications of Work Hardening and Ideal Plasticity, *Quart. Appl. Math.*, 7 (1950) 411-418.
73. Drucker, D. C. and Prager, W., Soil Mechanics and Plastic Analysis or Limit Design, *Quart. Appl. Math.*, 10 (1952) 157-165.
74. Fielke, J. M., Finite Element Modelling of the Interaction of the Cutting Edge of Tillage Implements with Soil, *J. Agric. Engng. Res.* 74 (1999) 91-101.
75. Griffiths, D. V., Failure criterion interpretation based on Mohr-Coulomb friction, *J. Geotech. Engng. ASCE*, 116 (1990) 986-999.
76. L. Chi and R. L. Kushwaha, A Non-linear 3-D Finite Element Analysis of Soil Failure with Tillage Tools, *Journal of Terra-mechanics*. Vol. 27. No. 4 pp. 343-366, 1990.
77. Drucker D. C.; Gibson R. E.; Henkel D. J., Soil mechanics and work-hardening theories of plasticity. *Proceedings of American Society of Civil Engineers*, 1955, 81 (798): 1-14.
78. Drucker D. C.; Providence R. I., Coulomb friction, plasticity, and limit loads. *Journal of Applied Mechanics*, 1954, 21 (1); 71-74.
79. G. Rajaram and D. C. Erbach, Soil Failure by Shear versus Modification by Tillage: A Review, *Journal of Terra-mechanics*, Vol. 33, No. 6, pp. 265-272, 1996.
80. R. L. Kushwaha, L. Chi and J. Shen, Analytical and numerical models for predicting soil forces on narrow tillage tools-A review, *Canadian Agricultural Engineering*, Vol. 35, No. 3, July/August/September 1993.
81. Z. X. Zhang and R. L. Kushwaha, Operating speed effect on the advancing soil failure zone in tillage operation, *Canadian Agricultural Engineering*, Vol. 41, No. 2, April/May/June 1999.
82. Goodman, R. E., Taylor, R. L., and Brekke, T. L., “A Model for the Mechanics of Jointed Rock”, *Journal of the Soil Mechanics and Foundations Division*, ASCE,

Vol. 94, No. SM3, Proc. Paper 5937, May 1968, pp. 637-659.

83. Banhazi, J., J. L. Jori, and P. Soos, "Investigation and Comparing of Soil Cultivation with Medium-Deep Subsoilers", *Hungarian Academy of Science*, Budapest, 1984.
84. Philippe Kolmayer, Bernard Cambou, Constitutive modelling of superficial soils, *Laboratoire de Tribologie et Dynamique des Systèmes UMR-5513, Ecole Centrale de Lyon, Ecully, France*.
85. Cécile NOUGUIER, Numerical simulations of interaction between a tool and granular soils, *LMGC CC048, Place E. Bataillon, 34095 Montpellier cedex 5, France*.
86. Wolfgang Fervers, Effects of Traction and Slip, Investigation with FEM, *Institute of Automotive Engineering (IKK), University of Federal Armed Forces Hamburg, Holstenhofweg 85, D-22043 Hamburg, Germany*.
87. Akira OIDA, Helmut SCHWANGHART, etc., SIMULATION OF SOIL DEFORMATION UNDER A TRACK SHOE BY THE DEM, *Laboratory of Agricultural Systems Engineering, Division of Environment Science and Technology, Graduate School of Agriculture, Kyoto University, Kyoto 606-01, Japan; Institute für Landmaschinen, TU München, 85747 Garching, BRD*.
88. Tanya Niyamapa, Kiyoshi Namika and V. M. Salokhe, SOIL FAILURE UNDER UNDRAINED QUASI-STATIC AND HIGH SPEED TRIAXIAL COMPRESSION TEST, *Journal of Terramechanics*, Vol. 29, No. 2, pp. 195-205, 1992.
89. J. A. Chamberlain, J. E. Sader, etc., Incipient plane-strain failure of a rectangular block under gravity, *International Journal of Mechanical Sciences* 43 (2001) 793-815.
90. Jaroslaw Pytka, Load effect upon soil stress and deformation state in structured and disturbed sandy loam for two tillage treatments, *Soil & Tillage Research* 59 (2001) 13-25.
91. Chang-New Chen, PLASTIC FAILURE ANALYSIS BY USING THE FINITE ELEMENT METHOD ALONG WITH A GLOBAL SECANT RELAXATION-BASED ACCELERATED ITERATION PROCEDURE, *Structural Engineering Review*, Vol. 6, No. 1, pp. 11-21, 1994.
92. P. C. F. Ng, I. C. Pyrah & W. F. Anderson, Assessment of Three Interface Elements and Modification of the Interface Element in CRISP90, *Computers and*

Geotechnics, Vol. 21, No. 4, pp. 315-339, 1997.

93. Th. Aubel, APPLICATION OF THE FINITE ELEMENT METHOD ON SOIL MECHANICAL PROCESSES, *University of the Federal Armed Forces Hamburg, Germany, Institute of Automotive Engineering*.
94. M. Yazdchi, N. Khalili, S. Valliappan, Dynamic soil-structure interaction analysis via coupled finite-element-boundary-element method, *Soil Dynamics and Earthquake Engineering* 18 (1999) 499-517.
95. Nathan M. Newmark, OPENING ADDRESS: FAILURE HYPOTHESES FOR SOILS, *ASCE Research Conference on Shear Strength of Cohesive Soils, Boulder, Colorado, June 1960*.
96. R. McNeill Alexander, Simple models of walking and jumping, *Human Movement Science* 11 (1992) 3-9.
97. Thomas Aubel, THE INTERACTION BETWEEN THE ROLLING TYRE AND THE SOFT SOIL, FEM-SIMULATION BY VENUS AND VALIDATION, *Institute of Automotive Engineering IKK, University of the Federal Armed Forces Hamburg, Germany*.
98. L. Chi, R. L. Kushwaha, THREE DIMENSIONAL NON-LINEAR FINITE ELEMENT ANALYSIS OF SOIL FAILURE UNDER A SIMPLE NARROW TILLAGE TOOL, *International Winter Meeting of the AMERICAN OF AGRICULTURAL ENGINEERS, Hyatt Regency Chciago in Illinois Center, December 15-18, 1987*.
99. Takeshi Tamura, Shoichi Kobayashi and Tetsuya Sumi, Rigid-plastic finite element method for frictional materials, *SOILS AND FOUNDATIONS*, Vol. 27, No. 3, 1-12, Sept. 1987, Japanese Society of Soil Mechanics and Foundation Engineering.
100. D. R. P. Hettiaratchi and A. R. Reece, SYMMETRICAL THREE-DIMENSIONAL SOIL FAILURE, *Journal of Terramechanics*, 1967, Vol. 4, No. 3, pp. 45 to 67. Pergamon Press Ltd.
101. Ray W. Clough, COMPARISON OF THREE DIMENSIONAL FINITE ELEMENTS, *Proceedings of the Symposium on Application of Finite Element Methods in Civil Engineering*. Vanderbilt University, Nashville, pp. 1-26, November 1969.
102. H. Jayalath Siriwaedane, (Ph.D. Dissertation) NOR-LINEAR SOIL-STRUCTURE INTERACTION ANALYSIS OF ONE-, TWO-, AND THREE-

DIMENSIONAL PROBLEMS USING FINITE ELEMENT METHOD, Virginia Polytechnic Institute and State University, November 1980, Blacksburg, Virginia, USA.

103. E. H. Davis, H. G. Poulos, Triaxial Testing and Three-dimensional Settlement Analysis, *Fourth Australia-New Zealand Conference on Soil Mechanics and Foundation Engineering*, University of Sydney.
104. C. H. Lee, S. Kobayashi, New Solutions to Rigid-Plastic Deformation Problems Using a Matrix Method, *Transactions of the ASME Journal of Engineering for Industry*, 1973. Mechanical Design, University of California, Berkeley, California, USA.
105. Hongsheng Zhu, Nabil Maalej, etc., An Umbilical Data-Acquisition System for Measuring Pressures Between the Foot and Shoe, *IEEE Transactions on Biomedical Engineering*, Vol. 37, No. 9, September 1990, Page 908-911.
106. Fendley, A. E., and Marpet, M. I., Required Coefficient of Friction Versus Walking Speed: Potential Influence of Footwear and Walkway Surfaces, *Journal of Testing and Evaluation*, JTEVA, Vol. 24, No. 6, Nov. 1996, pp. 359-367.
107. Wilson, M. P., "Development of SATRA Slip Test and Tread Design Guideliones," *Slips, Stumbles, and Falls: Pedestrian Footwear and Surfaces*, ASTM STP 1103, B. E. Gray, Ed., American Society for Testing and Materials, Philadelphia, 1990, pp. 113-123.
108. Filiz I. H., Akpolat A., Guzelbey I. H., DEFORMATIONS AND PRESSURE DISTRIBUTION ON MACHINE TOOL SLIDEWAYS, *International Journal of Machine Tools & Manufacture*, Vol. 37, No. 3, pp. 309-318, May 1997.
109. Joseph E. Saliba, Elastic-Viscoplastic Finite-Element Program for Modelling Tire/Soil Interaction, *J. AIRCRAFT*, Vol. 27, No. 4, pp. 350-357, April 1990. Copyright© 1989 American Institute of Aeronautics and Astronautics, Inc.
110. C. A. Coulomb, Sur une application des règles de maximis et minimis à quelques problèmes de statique relatifs à l'architecture. *Acad. R. Sci. Mém. Math. Phys. Par divers savants*, 7: 343-382, 1773.
111. W. J. M. Rankine, On the stability of loose earth. *Philos. Trans. R. Soc. London*, 147: 9, 1857.
112. J. Massau, *Mémoire sur l'intégration des equations aux derives partielles*, 1899. Reprinted as Edition du Centenaire, Delporte, Mons, 1952.
113. F. Kötter, Die Bestimmung des Druckes an gekrümmten Gleitflächen, eine

- Aufgabe aus der lehre vom Erddruck. *Monatsber. Akad. Wiss. Berlin*, 1903: 229-233.
114. W. Fellenius, 1926. *Mechanics of soils. Statika Gruntov*, Gosstrollzdat, 1933.
115. V. V. Sokolovskii, *Statics of Granular Media*. Pergamon Press, New York, 1965.
116. H. Tresca, Mémoire sur l'écoulement des corps solides. *Mémoires présentés par divers savants à l'Académie des Sciences*, 18: 733-799, 1868.
117. De Saint Venant B., Mémoire sur l'établissement des equations differentielles des mouvements intérieurs operas dans les corps solides ductiles au delà des limites où l'élasticité pourrait les ramener à leur premier état. *C. R. Acad. Sci., Paris*, 70: 473-480, 1870.
118. K. H. Roscoe, A. N. Schofield, and C. P. Wroth, On the yielding of soils. *Geotechnique*, 8(1): 22-53.
119. K. H. Roscoe, and H. B. Poorooshasb, A theoretical and experimental study of strains in triaxial compression tests on normally consolidated clays. *Géotechnique*, 13(1): 12-38, 1963.
120. O. C. Zienkiewicz, and D. J. Naylor, Elastoplastic stress analysis. A generalization for various constitutive relations including strain softening. *Int. J. Numer. Methods Eng.*, 5: 113-135, 1972.
121. Von Mises, R., Mechanik der plastischen Formänderung von Kristallen. *Z. Angew. Math. Mech.*, 8:161-185, 1928.
122. O. C. Zienkiewicz, and G. N. Pande, Some useful forms of isotropic yield surfaces for soil and rock mechanics. In: *Finite Elements in Geomechanics*, Ed. By G. Gudehus, John Wiley and Sons, New York (1977) 179-190.
123. A. M. Mouazen, M. Nemenyi, Application of the Drucker-Prager elastic-perfectly plastic material model for performing finite element analyses of deep tollage, [Conference Paper] *Mathematics and Control Applications in Agriculture and Horticulture*. Elsevier Science. 1997, pp. 79-84. Oxford, UK.
124. BS 1377: Part 1 (1990), *Methods of Test For Soils For Civil Engineering Purposes – Part 1: General requirements and sample preparation*.
125. BS 1377: Part 4 (1990), *Methods of Test For Soils For Civil Engineering Purposes – Part 4: Compaction related tests*.